TWO-DIMENSIONAL III-VIA SEMICONDUCTORS AND THEIR APPLICATIONS IN OPTOELECTRONIC DEVICES

QINGHUA ZHAO

Madrid, 2020

TWO-DIMENSIONAL III-VIA SEMICONDUCTORS AND THEIR APPLICATIONS IN OPTOELECTRONIC DEVICES

By

QINGHUA ZHAO

Supervised by

Dr. ANDRES CASTELLANOS-GOMEZ

Dr. RICCARDO FRISENDA

Tutor: Prof. NICOLAS AGRAIT DE LA PUENTE

Doctor of Philosophy

in Physics of Condensed Matter

Universidad de Autonoma de Madrid

Madrid, 2020

“If were to live the life twice.
I would like to be a tree.
Standing in the dust firmly, without happiness and sadness.
A half of my body will be sleeping in the earth peacefully.
A half of my body will be dancing with the wind joyfully.
A half of my body will be providing green shade for passers-by willingly.
A half of my body will be bathing in the sunshine warmly.
So quiet and proud …”

ACKNOWLEDGEMENTS

This thesis could not have been possible without the help and support from many people who have played important roles during the journey to pursue my PhD degree. Herein, I would like to express my sincere gratitude and appreciation.

Most importantly, I would like to thank my supervisor, Dr. Andres Castellanos-Gomez, and my co-supervisor, Dr. Riccardo Frisenda, for their patient guidance and steadfast support during my studying period at Instituto de Ciencia de Materiales de Madrid (ICMM-CSIC) and Universidad de Autonoma de Madrid (UAM). Both Dr. Andres Castellanos-Gomez and Dr. Riccardo Frisenda have solid background in two-dimensional materials and devices physics left a great impact on me. I truly appreciate the time and effort that they have committed to the achievement of this thesis. Moreover, their diligence and talent will always inspire me to move forward.

I would like to show my special appreciation to Prof. Wanqi Jie and Prof. Tao Wang from Northwestern Polytechnical University (NPU) in Xi’an, China. Their firm support and efficient collaboration have provided a guarantee for achieving fruitful progresses.

I would like to extend my thanks to Prof. Nicolas Agrait de la Puente from Universidad de Autonoma de Madrid for his kind help as my tutor, and also to my colleagues at ICMM-CSIC, Patricia Gant, Felix Carrascoso, Sergio Puebla, Hao Li, Wenliang Zhang, Begoña Morales, Carmen Munuera López, Mar García Hernández, and at IMDEA nanociencia, Yue Niu, David Perez de Lara for their help, support and friendship.

I also would like to thank my friends, Zi’ang Yin, Chen Sun, Dasheng Lu, Zhenyu Liu, Qihui Zhang, Lizhi Guan, Yong Xie, Wei Wang, Jie Li, Li Wang, Huan Zhang, Xuejun Lu for their help and accompany during the time in Madrid.

I gratefully acknowledge the support, patience and love from my family. This work could not have been achieved without their constant encouragement and motivation.

Finally, I would like to acknowledge the grant from China Scholarship Council (CSC) under No. 201706290035.

Qinghua Zhao

Madrid, September in 2020

ABSTRACT

Two-dimensional (2D) semiconductors, initialed by the isolation of graphene in 2004, have drawn a great research interest thanks to their remarkable mechanical, electrical, optical, and optoelectronic properties. Their layered structure, originating from the strong in-plane covalent bonds and weak out-of-plane van der Waals interactions, allows such materials being stable with atomically thin geometry. Thanks to the ultrathin nature and dangling-bond-free surface, various advanced heterostructures-based devices with superior performance have been demonstrated without being hampered by their lattice mismatch, which make them as promising candidates for future nano-electronic and optoelectronic applications. As novel 2D members from III – VIA semiconducting group, Gallium selenide (GaSe) and Indium selenide (InSe), are barely explored but recently both reach exciting promise in theory achievements and application research. Thanks to their unique electron band structures and strong light-matter interactions, they both are sensitive to external stimuli, which can be advantageous for certain applications but also brings drawbacks for others, thus motivates the goal of this thesis that exploring how the environment, light and strain play roles on the properties of these materials.

Two dimensional materials are especially sensitive to the environmental atmosphere and to external stimuli due to their layered structures and large surface-to-volume ratio. Thus, in the first part of this thesis, the interaction between air species and thin GaSe and InSe flakes has been discussed. Thin GaSe can be degraded completely after being exposed in the air for several days, during which macro- and micro-scope surface morphology evolution, chemical composition variation, and laser-induced degradation, as well as how it leads to the photodetector breakdown as a function of exposure time in air have been fully presented. On the contrary, thin InSe shows a different environmental interaction mechanism: the performance of InSe photodetector can be significantly modified, and even reaching a long-term stable behavior in air, without obviously changing the surface morphology and crystal lattice. Both these observations are related to the interaction between air species (*e.g.* O_2 and H_2O) and the defects (*e.g.* selenium vacancies) in the materials. The failure of GaSe photodetectors can be attributed to a full transformation from crystalline GaSe to amorphous Ga_2O_3 by air species, while the performance variation of InSe devices may be related to the passivation of selenium vacancies in the system. Based on these understandings, both long-term stable photodetectors based on thin GaSe and InSe have been realized using hexagonal boron nitride (h-BN) encapsulation protection (for GaSe) or controllable air exposure (for InSe).

Thanks to the dangling-bond-free surface of 2D semiconductors and the deterministic transfer methods, one can fabricate pure van der Waals (vdW) metal-semiconductor interfaces, without direct chemical covalent bonding that typically leads to chemical disorder and Fermi-level pinning (FLP). This kind of vdW metal-semiconductor is thus an ideal system to study the Schottky junctions. The defects passivation effect in InSe introduced by air species not only can modify the material properties but also reduces the fermi level pinning at the metal-InSe contact interface. Various Schottky contact based on thin InSe with different van der Waals electrical contacts have been investigated. The Schottky barrier height at the interfaces of Au-InSe, Pt-InSe and InSe-Gr (graphite) are determined to be approximately 460 meV, 540 meV and less than 100 meV, respectively. Taking advantage of the large contact barrier difference, the transport properties of Schottky diodes based on engineered asymmetric van der Waals contacts of thin InSe, including Au-InSe-Gr and Pt-InSe-Gr, have been investigated.

The dangling-bond-free nature of the surface of 2D materials leads to high mechanical resilience against mechanical deformation. This has motivated a whole sub-field of research focused on using mechanical deformation to tune the electronic properties of 2D materials. The mechanical properties of GaSe and InSe were barely explored at the moment of the elaboration of this thesis and thus to decide to measure the Young’s modulus of InSe to access its suitability in strain engineering applications. Using buckling metrology method, the Young’s modulus of InSe is experimentally determined to be 23 ± 5 GPa, which makes thin InSe one of the most flexible 2D materials. Subsequently, the biaxial strain tunability of thin InSe, including piezoresistance effect, band gap modulation, and strain engineered optoelectronic devices has been discussed. Interestingly, it is further demonstrated that how the strain tunable band gap can be exploited to tune the spectral response of InSe photodetectors.

This thesis demonstrates the great promise of 2D III-VIA semiconducting materials, especially GaSe and InSe, for future electrical and optoelectronic applications. These results, on the one hand, reveal the important role of traps induced by defects in tailoring the properties of devices based on 2D materials, on the other hand, show the reliability of electronic and optoelectronic properties of van der Waals Schottky contacts, which are both attractive for different applications, such as strain engineering and flexible electronics.

RESUMEN

La investigación en semiconductores bidimensionales (2D), iniciada con el aislamiento del grafeno en 2004, ha atraído un gran interés de la comunidad científica gracias a sus notables propiedades mecánicas, eléctricas, ópticas y optoelectrónicas. Su estructura en capas, que se origina a partir de los fuertes enlaces covalentes en el plano y las débiles interacciones de van der Waals fuera del plano, permite que dichos materiales sean estables con una geometría atómicamente delgada. Gracias a la naturaleza ultrafina y la superficie libre de enlaces desapareados, se han demostrado varios dispositivos avanzados basados en heteroestructuras con un rendimiento superior sin verse obstaculizados por diferencias entre sus parámetros de red, lo que los convierte en candidatos prometedores para futuras aplicaciones nanoelectrónicas y optoelectrónicas. El seleniuro de galio (GaSe) y el seleniuro de indio (InSe), como nuevos miembros 2D del grupo de semiconductores III-VIA apenas explorados, prometen emocionantes descubrimientos teóricos y en investigación aplicada. Gracias a sus estructuras electrónicas y sus fuertes interacciones luz-materia, ambos son sensibles a los estímulos externos, lo que puede ser ventajoso para ciertas aplicaciones pero también presenta inconvenientes para otras, por lo que motiva el objetivo de esta tesis que es explorar cómo el medio ambiente, la luz y la tensión juega un papel en las propiedades de estos materiales.

Los materiales bidimensionales son especialmente sensibles a la atmósfera ambiental y a los estímulos externos debido a sus estructuras en capas y su gran relación superficie-volumen. Así, en la primera parte de esta tesis, se ha discutido la interacción entre las especies atmosféricas y las láminas delgadas de GaSe e InSe. Los copos de GaSe se puede degradar completamente después de haber estado expuestos al aire durante varios días, durante los cuales la evolución de la morfología de la macro y micro-superficie, la variación de la composición química y la degradación inducida por láser, así como la forma en que GaSe fotodetectores se terminan descomponiendo con la exposición al aire se ha presentado. Por el contrario, copos delgados de InSe muestran un mecanismo de interacción ambiental diferente: el rendimiento de fotodetectores de InSe se modifica significativamente, incluso alcanzando un comportamiento estable a largo plazo en el aire, sin cambiar de forma evidente la morfología de la superficie y la red cristalina. Ambas observaciones están relacionadas con la interacción entre las especies presentes en el aire (por ejemplo, O_2 y H_2O) y los defectos (por ejemplo, las vacantes de selenio) en los materiales. El fallo

eléctrico de los fotodetectores de GaSe puede atribuirse a una transformación completa de GaSe cristalino a Ga_2O_3 amorfo por especies de aire, mientras que la variación de rendimiento de los dispositivos InSe puede estar relacionada con la pasivación de las vacantes de selenio en el sistema. Sobre la base de estos conocimientos, tanto los fotodetectores estables a largo plazo basados en GaSe delgado como en InSe se han realizado utilizando protección de encapsulación de nitruro de boro hexagonal (h-BN) (para GaSe) o exposición de aire controlable (para InSe).

Gracias a la superficie libre de enlaces desapareados de los semiconductores 2D y los métodos de transferencia determinista, se pueden fabricar interfases semiconductor-metal de tipo van der Waals (vdW) puras, sin enlaces covalentes directos que normalmente conducen al desorden químico y la fijación del nivel de Fermi (“Fermi level pining” FLP). Este tipo de contacto semiconductor-metal tipo vdW es, por tanto, un sistema ideal para estudiar las uniones Schottky. El efecto de pasivación de defectos en InSe introducido por especies atmosféricas no solo puede modificar las propiedades del material, sino que también reduce la fijación del nivel de Fermi en la interfaz de contacto metal-InSe. Se han investigado varios contactos de Schottky basados en copos delgados de InSe con diferentes contactos eléctricos de van der Waals. Se ha determinado que la altura de la barrera de Schottky en las interfaces de Au-InSe, Pt-InSe e InSe-Gr (grafito) es aproximadamente 460 meV, 540 meV y menos de 100 meV, respectivamente. Aprovechando la gran diferencia de barrera de contacto, se han investigado las propiedades de transporte de diodos Schottky basados en contactos asimétricos de van der Waals diseñados de InSe delgado, incluidos Au-InSe-Gr y Pt-InSe-Gr.

La naturaleza libre de enlaces desapareados de la superficie de los materiales 2D también conduce a una alta resiliencia mecánica contra deformaciones mecánica. Esto ha motivado todo un sub-campo de investigación centrado en el uso de la deformación mecánica para ajustar las propiedades electrónicas de los materiales 2D. Las propiedades mecánicas de GaSe e InSe apenas se habían explorado en el momento de la elaboración de esta tesis y por tanto se decidió medir el módulo de Young de InSe para debatir sobre su idoneidad en aplicaciones de ingeniería de deformaciones. Utilizando el método de metrología de pandeo, el módulo de Young de InSe se determina experimentalmente en 23 ± 5 GPa, lo que hace que el InSe delgado sea uno de los materiales 2D más flexibles. Posteriormente, se ha discutido la

capacidad de sintonización de deformación biaxial de InSe delgado, incluido el efecto piezoresistivo, la modulación de banda prohibida y los dispositivos optoelectrónicos de ingeniería de deformación. Curiosamente, se demuestra además cómo se puede aprovechar la banda prohibida sintonizable por deformación para ajustar la respuesta espectral de los fotodetectores InSe.

Esta tesis demuestra el potencial de los materiales semiconductores 2D III-VIA, especialmente GaSe e InSe, para futuras aplicaciones eléctricas y optoelectrónicas. Estos resultados, por un lado, revelan el importante papel de las trampas inducidas por defectos en la adaptación de las propiedades de los dispositivos basados en materiales 2D, por otro lado, muestran la fiabilidad y reproducibilidad de las propiedades electrónicas y optoelectrónicas de los contactos Schottky tipo van der Waals, que son atractivos tanto para aplicaciones, como la ingeniería de deformación y la electrónica flexible.

TABLE OF CONTENTS

1

INTRODUCTION

While the research on three-dimensional (3D) materials runs in parallel with the development of human society, research on two-dimensional (2D) materials can be traced back to only 80 years ago. In this chapter, the history including rising and development of 2D materials will be firstly discussed. Subsequently, a brief introduction of the state-of-the-art on 2D materials research, especially focusing on 2D gallium selenide (GaSe) and indium selenide (InSe), consisting of isolation, characterization, and their device applications. In the last part, the motivations of the research carried out in this thesis will be stressed.

1.1 The rising of 2D materials

1.1.1 From bulk materials to 2D materials

Anything made up of matter with one or several elemental constituents is termed as materials.[1] If a solid state material has three spatial dimensions with macro-scales (typically larger than 100 nm), we usually refer to it as a bulk or three-dimensional (3D) material. Within 3D materials, 3D crystalline materials are those whose constituents (atoms, ions or molecules) are arranged in a long range ordered microscopic structure, forming a crystal lattice that extends in all directions.[2] The properties of 3D crystals are mostly determined by the crystal lattices parameters and/or constituent periodic arrangements.

In the case of materials which have at least in one dimension in the sub ~100 nm scale they can be called low dimensional materials or nanomaterials.[3] The research field of nanomaterials was envisioned by Richard P. Feynman with the talk entitled “There is plenty of room at the bottom” in 1959.[4] From this point, nanomaterials can exist in zero-dimensional (0D), one-dimensional (1D) and two-dimensional (2D) forms,[5] as shown in **Fig. 1-1**. Zero-dimensional (0D) nanomaterials, the first type of discovered nanomaterials, refer to the materials wherein all the dimensions are within the nanoscale (smaller than 100 nm). The most common examples of 0D nanomaterial are nanoparticles and fullerenes.[6] One-dimensional (1D) nanomaterials, were explored 6 years later after the discovery of 0D nanomaterials in 1991,[7] and can be defined as nanomaterials with two dimensions in nanoscale (smaller than 100 nm), and the third dimension is beyond nanoscale. This leads to needle-like shaped nanomaterials, such as nanotubes, nano-rods, nanobelts and nanowires.[8] Two-dimensional (2D) nanomaterials exhibit plate-like shapes and they present thicknesses smaller than 100 nm.[9] 2D nanomaterials include nanofilms, nanolayers, nanomembranes, nanosheets and nanocoating.

Interestingly, it is not only size but also dimensionality itself that determines materials properties. This particularly applies to the case of sp2 carbon materials: 3D graphite, 2D graphene, 1D carbon nanotubes and 0D fullerenes.[10] All these materials exhibit very different properties: as the dimensions of the materials decrease, the electronic band structures change from continuous bands towards discrete levels. Also, when it comes to analyzing the chronological order of the findings of the different dimensional forms of a given materials, the case of the carbon is a representative examples: graphite has been known since the 16th century and has been widely used in industry for steel-making, as brake lining or as dry lubricant in some other devices. But it was not until 1985 when the discovery of fullerenes greatly expanded the number of known carbon allotropes and furthermore suggested the existence of its 1D form, carbon nanotube, which was first demonstrated in 1991.[6,7] Although the theoretical studies of graphite as starting material, it was not until 2004 that scientists were able to isolate a monolayer graphene sheet for the first time.[11] The recent blossoming of graphene literature evidences not only its basic scientific interests but also its potential technological impact.[12] Actually, two dimensional materials are expected to have a significant impact on a large variety of applications, ranging from electronics to gas storage or separation, catalysis, high performance sensors, support membranes and inert coatings, just to mention a few of them.

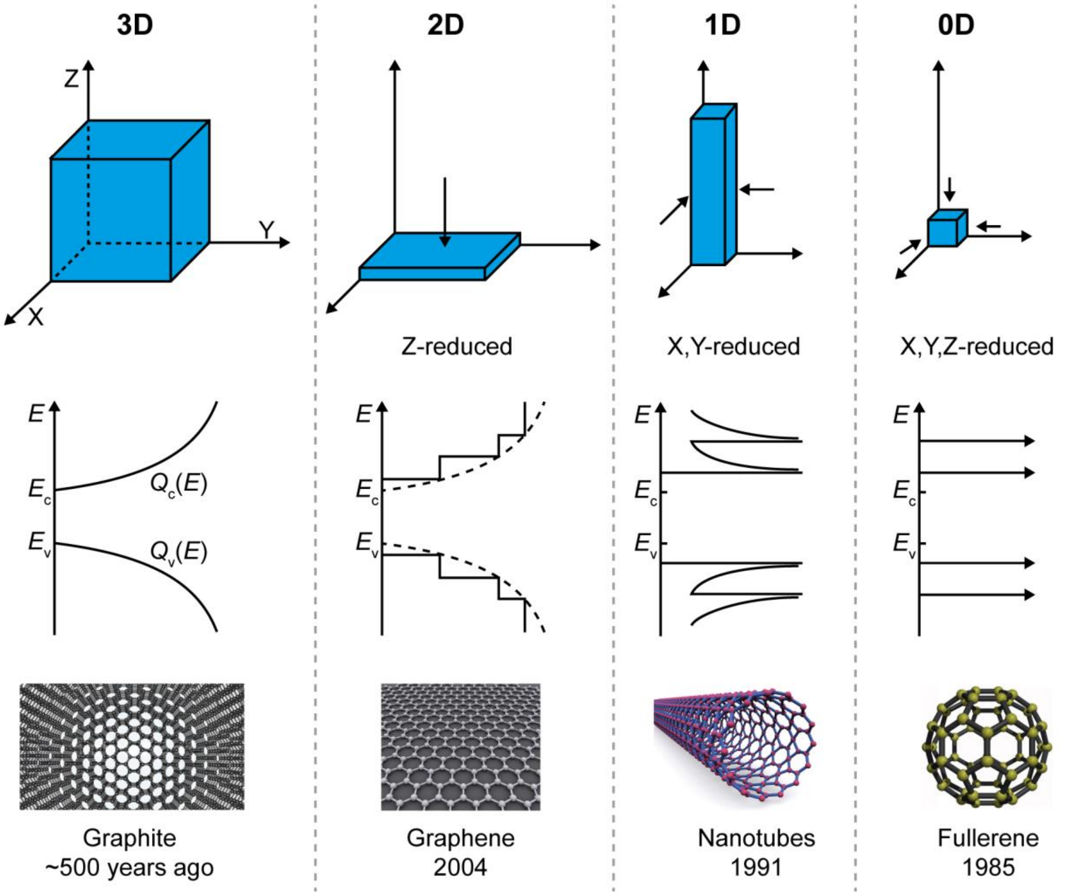

Fig. 1-1. Classifications of materials according to their dimensionality (top), energy band diagram (middle) and their representative species (bottom). 3D: Graphite; 2D: Graphene; 1D: Nanotubes; 0D: Fullerenes.[5,6,8,10]

When the dimensions of materials shrink to the nanoscale, classical properties are not applicable but they enter the world of quantum mechanics.[13] The qualitative changes in physical and chemical properties, such as reactivity, are connected to the ratio of surface atoms or molecules with respect to the total number of atoms/molecules forming the materials. The difference in properties of nanoscale materials in respect to bulk materials can be mainly attributed to two reasons:

1, Increase in surface area to volume. Nanomaterials have a relatively large surface area as compared to the same mass of materials produced in larger form. This makes materials more chemically reactive and affects their mechanical and electrical properties.

2, Quantum confinement.[14,15] In nanomaterials, electronic energy levels are not continuous as in the bulk but are discrete. This is due to the confinement of the electronic wave function in one, two or three physical dimensions of the materials and accordingly it can be classified as 1D, 2D or 3D confinement. This quantum effects can strongly change the behaviors of matter at the nanoscale affecting the optical, electrical and magnetic behaviors of materials, which are significantly different from their bulk counterparts. For instance, size-effect properties can be observed, such as surface plasmon resonance in metal nanoparticles,[16] quantum confinement in semiconductor particles and superparamagnetism in magnetic nanomaterials.[17,18]

In addition to the common characteristics of general nanomaterials, two-dimensional materials also possess certain special characteristics thanks to their unique structure features. First of all, most 2D materials are isolated based on layered van de Waals bulk crystals in which there is no covalent bonds between the layers along their thickness orientation (**Fig. 1-2**),[19] thus the fabricated 2D materials both can reach atomically thin sizes without breaking the in-plane lattice periodicity and have a naturally passivated surface. On the one hand, the ultrathin nature of these materials introduces quantum confinement in the vertical direction leading to large thickness-dependent band structure tunability and strong light-matter interactions in the ultrathin (< 10 layers) regime. On the other hand, the dangling bond free surface accompanied by the van der Waals interactions allows stacking different 2D materials beyond the constraint of crystal lattice mismatching, in order to realize novel artificial it is more advantage to combine with the state-of-the-art micro-, nano- processing technology than 0D and 1D nanomaterials. Based on the above mentioned characteristics, 2D materials, as a novel and isolated materials system, can both bridge the property advantages of nanomaterials and macroscopic 3D bulks, indicating various promising applications in the future world.

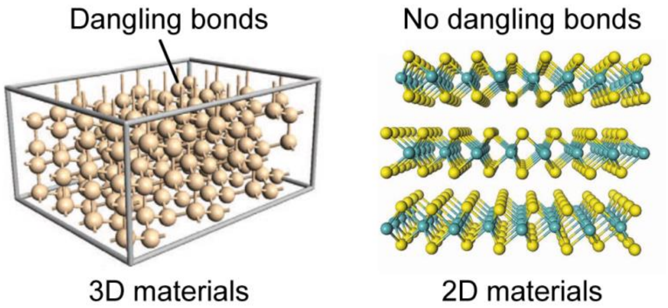

Fig. 1-2. The surface of 3D materials (left) and 2D materials (right) with and without dangling bonds.[19]

1.1.2 The development of 2D materials

During the first decades of the 20th century, the existence of two-dimensional materials was a highly debated issue in the physics community. The question whether a strictly two-dimensional (2D) crystal can exist, was first raised by Peierls and Landau.[20-23] They demonstrated that, in the standard harmonic approximation,[24] thermal fluctuations would destroy long-range order, resulting in melting of 2D lattices at any finite temperature. Furthermore, Mermin and Wagner proved that a magnetic long-range order could not exist in one or two dimensions and later they extended the proof to crystalline order in 2D geometry.[25,26] Importantly, numerous experiments on thin films showed agreement with the theoretical prediction, finding that below a certain thickness of dozens of atomic layers, the films became thermodynamically unstable (trend to segregate into island or decompose) unless they constitute an inherent part of a three-dimensional (3D) system (such as being grown on top of a bulk crystal with a matching lattice).[27-29]

Significantly, materials science had a major breakthrough in 2004,[11] when Novoselov and Geim isolated the first single-layer 2D material, graphene, through Scotch tape exfoliation of graphite. The importance of this achievement was rewarded in 2010, with the Nobel Prize for both their contributions. However, the physical structure of graphene - a single layer of carbon atoms densely packed in a honeycomb crystal lattice is still puzzling. On the one hand, graphene appears to be a strictly two-dimensional material, exhibiting such a high crystal quality that electrons can travel micrometer distances without scattering. On the other hand, perfect two-dimensional crystals cannot exist in the free state of 2D space, according to both theory and experiments.[20-23,25,26,30] Actually, a detailed analysis of the 2D crystal problem beyond the harmonic approximation has led to the conclusion that the interaction between bending and stretching long-wavelength phonons could in principle stabilize atomically thin membranes through their deformation in the third dimension.[31] The following studies by transmission electron microscopy (TEM) revealed that these suspended one atom-thick carbon sheets are not perfectly flat (see left panel in **Fig. 1-3**). In fact, they exhibit intrinsic microscopic roughness such that the surface normal varies by several degrees and out-of-plane deformations reach 1 nm in amplitude. The observed corrugations in the third dimension may provide subtle reasons for the stability of two-dimensional crystals, which are further confirmed by atomistic Monte Carlo simulations based on a very accurate interatomic potential of carbon.[32]

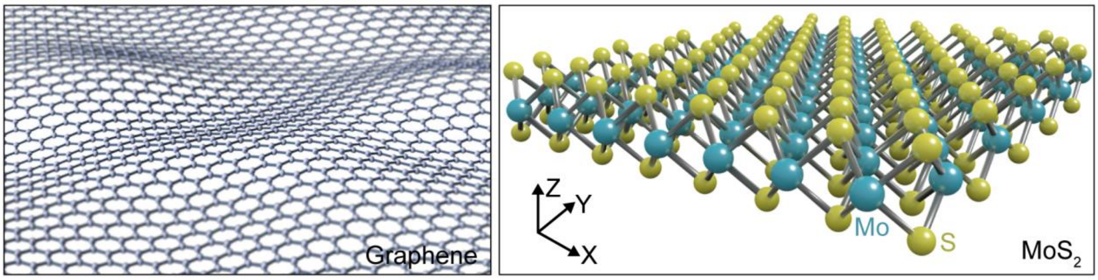

Fig. 1-3. The crystal structure models of a suspended graphene flake (left) and monolayer MoS_2 (right).

In general, this important discovery came at the background of a continuous ongoing quest raised the semiconductor industry committee to search for new semiconducting materials, engineering techniques and efficient transistor topologies to extend “Moore’s law” – an empirical observation pointed out in 1960s by Gordon Moore which claimed that the number of transistors on a complementary metal-oxide-semiconductor (CMOS) microprocessor chip and, hence, the chip’s performance, would approximately double every 24 months.[33-35] In fact, to enhance the density and performance on the chips, the semiconductor industry has been shrinking down the conventional CMOS transistors to nanometer regime.[36-41] However, during the last decades, the performance gains derived due to dimensional scaling down have been severely offset due to the detrimental short-channel effects (SCE) which cause high OFF-state leakage currents (due to loss of effective gate control over the charge carriers in the semiconducting channel and inability of the gate to turn the channel fully OFF) leading to larger static power consumption and heat dissipation, which introduce dire implications for Moore’s law.[42-47] With continued down-scaling (sub-10 nm regime), the SCE effect will get far worse and even state-of-the-art CMOS transistor architectures (such as MuGFET, UTB-FETs, FinFET, *etc.*) designed to enhanced gate controllability would face serious challenges in minimizing the overall power consumption. Thus, an urgent requirement that finds an appropriate transistor channel material which allows for a high degree of gate control at these ultra-short dimensions has been introduced.[48-51] In theory, based on the characteristic "channel length (L_{CH}) scaling" factor "λ", given by $\lambda = (t_{OX}t_{BODY}\varepsilon_{BODY})^{1/2}/\varepsilon_{OX}$, in which t_{OX} and t_{BODY} are the thicknesses of the gate oxide and channel, and ε_{BODY} and ε_{OX} are their respective dielectric constants;[52] natural ultrathin channel materials can help mitigate SCE in ultra-scaled FETs, thus enabling enhanced electrostatic gate control and carrier confinement versus 3D bulk semiconductors.[53] From this point, graphene has been thoroughly researched for its remarkable properties, such as 2D atomically thin nature, extremely high carrier mobility, superior mechanical strength, flexibility, optical transparency, and high thermal conductivity, which can be useful for a wide range of device design and fabrications.[53] Though graphene allows for excellent gate controllability thanks to its innate thickness, a major drawback of graphene is the absence of an electronic "band gap" nature, a necessary attribute any material must possess to be considered for electronic/optoelectronic device applications, which means a graphene transistor cannot be turned "OFF".[54,55]

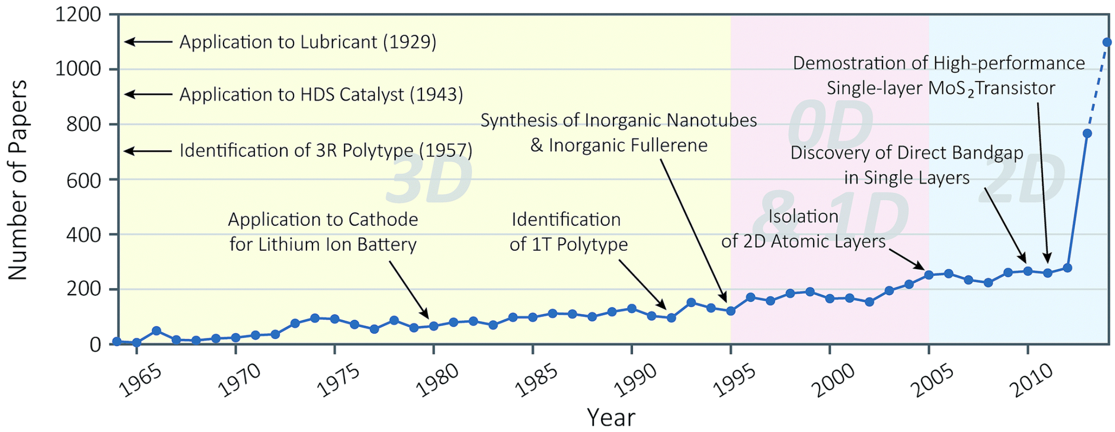

Fig. 1-4. History of molybdenum disulphide research for last 50 years (1964–2014).[56]

Graphene's shortcomings motivated to the search for alternative materials with similar yet complementary properties, which promote the emergence of a large catalogue of 2D layered materials ranging from insulators to semiconductors and metals.[10,57] Due to the natural availability and environmental/ambient stability, MoS_2 (shown by right panel in **Fig. 1-3**), as the first isolated monolayer 2D semiconductor, has been one of the most popular and widely studied materials by the research community, as witnessed in the exponentially rising number of publication on this subject in **Fig.**

1-4.[56] The bandgap variability, together with high carrier mobility, mechanical flexibility, and optical transparency, makes 2D MoS_2 extremely attractive for practical nano- and opto-electronic device applications on both rigid and flexible platform.[9,58-63]

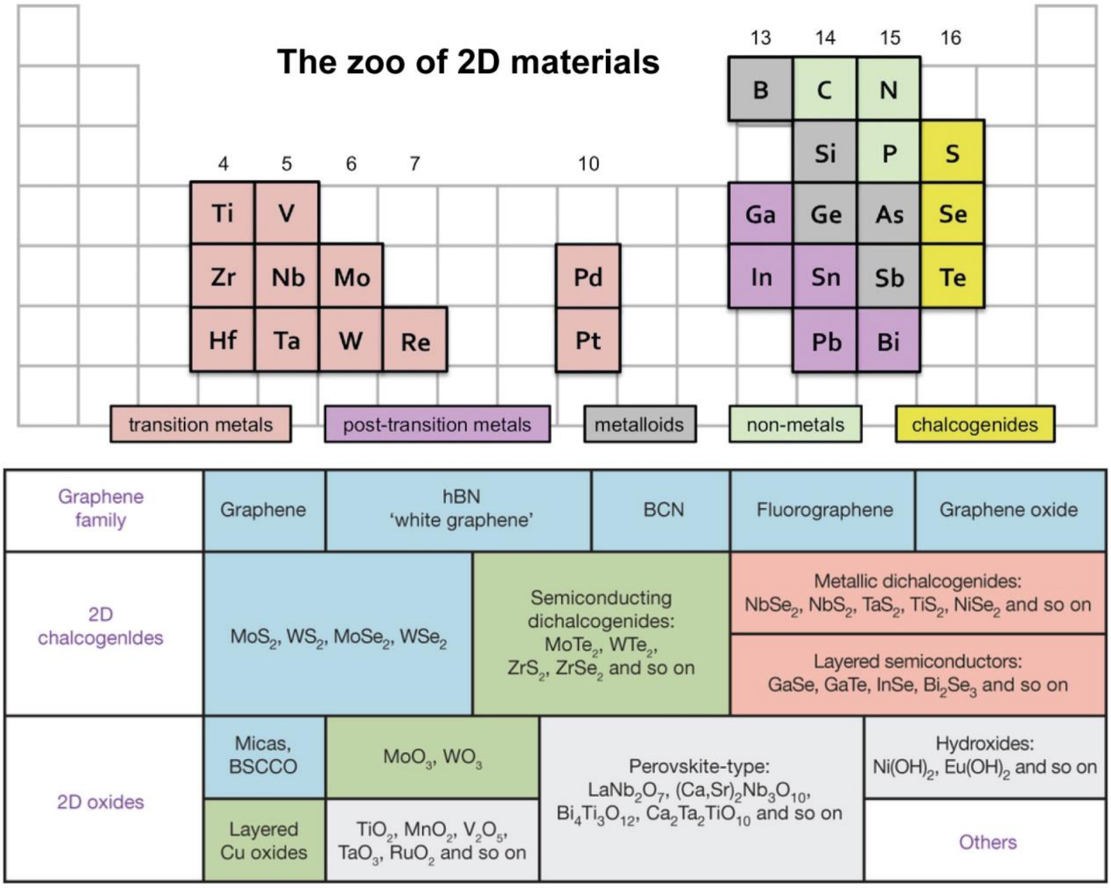

Graphene family	Graphene	hBN 'white graphene'	BCN	Fluorographene	Graphene oxide
2D chalcogenides	MoS_2, WS_2, $MoSe_2$, WSe_2	Semiconducting dichalcogenides: $MoTe_2$, WTe_2, ZrS_2, $ZrSe_2$ and so on	Metallic dichalcogenides: $NbSe_2$, NbS_2, TaS_2, TiS_2, $NiSe_2$ and so on		
			Layered semiconductors: GaSe, GaTe, InSe, Bi_2Se_3 and so on		
2D oxides	Micas, BSCCO	MoO_3, WO_3	Perovskite-type: $LaNb_2O_7$, $(Ca,Sr)_2Nb_3O_{10}$, $Bi_4Ti_3O_{12}$, $Ca_2Ta_2TiO_{10}$ and so on	Hydroxides: $Ni(OH)_2$, $Eu(OH)_2$ and so on	
	Layered Cu oxides	TiO_2, MnO_2, V_2O_5, TaO_3, RuO_2 and so on		Others	

Fig. 1-5. The zoo of 2D materials.[64-66]

One very important factor for the initial rapid development of the 2D materials field was the natural abundance of graphite and MoS_2 as common minerals/materials. After the initial studies, luckily it was discovered that also other layered materials could be synthesized and studied in the ultra-thin regime. Other important families of layered materials include the transition metal dichalcogenides (TMDCs) (*e.g.*, WS_2, $MoSe_2$), certain metal halides (*e.g.*, PbI_2, $MgBr_2$), and oxides (*e.g.*, MnO_2, MoO_3), perovskites (general form ABO_3), layered III-VIAs (*e.g.*, GaS, InSe), and V-VIAs (*e.g.*, SnS_2, $SnSe_2$) materials, layered silicates (clays, micas) and also elemental layer materials (*e.g.*, black phosphorous, silicene, antimonene).[64-66] In addition, the insulating hexagonal boron nitride (h-BN) system is another important layered material, one isostructural with graphite, but exhibiting very different properties. Currently, around 500 different layered materials have been identified, and a schematic description has been shown in **Fig. 1-5**.

1.2 Isolation of thin vdW materials and their properties

1.2.1 Preparation of 2D materials

Until now, many methods have been employed to prepare single- and multi-layer 2D nanomaterials. The top-down methods, which rely on the exfoliation of layered bulk crystals, include the mechanical cleavage method and liquid phase exfoliation method. Examples of bottom-up approaches are CVD growth and wet chemical synthesis. these four different types of method will be discussed in the following context.

- Mechanical exfoliation

Generally, there are two kinds of mechanical principles to exfoliate layered bulks into 2D (mono- or multi-layer) forms, *i.e.*, by the application of normal force and lateral force. One can exert normal force to overcome the van der Waals attractions when peeling two bulk layers apart, such as micromechanical cleavage by Scotch tape.[11,30] Taking advantage of layered bulks self-lubricating ability in the lateral direction, one can also exert lateral force to promote the relative motion between two bulk layers. These two mechanical principles are illustrated in **Fig. 1-6**, which are perquisite for the production of 2D flakes.

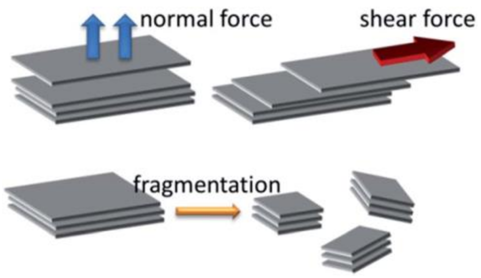

Fig. 1-6. The mechanism of mechanical exfoliation: mechanical cleavage and liquid exfoliation.[67]

A second process that can happen during exfoliation is the fragmentation effect. On one hand, it can reduce the lateral size of 2D flakes, which is not desirable for fabricating large-area 2D flakes. On the other hand, it can facilitate exfoliation, because smaller bulk particles are easier to exfoliate than larger ones thanks to the smaller collective van der Waals interaction forces between the layers in these particles. In the following, in terms of the above two mechanical routes, the micromechanical cleavage and liquid exfoliation techniques are discussed.

The micromechanical cleavage technique is a conventional method to fabricate thin flakes by exfoliation of layered bulk crystals, using Scotch tape (see **Fig. 1-7**).[68] The original idea of this technique is to apply mechanical force via Scotch tape to weaken the van der Waals interaction between the layers of bulk crystals without breaking the in-plane covalent bonds of each layer, hence peeling off single- or few-layers of 2D crystals.

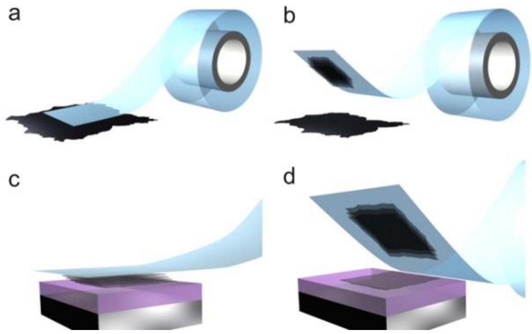

Fig. 1-7. Micromechanical cleavage of 2D crystals.[68]

In 2004, Novoselov, Geim, and co-workers first successfully isolated a single-layer graphene nanosheet from graphite by using the micromechanical cleavage technique.[11] Later, the same group demonstrated the extension of this technique for the exfoliation of other ultrathin 2D nanomaterials, including h-BN, MoS_2, $NbSe_2$, and $Bi_2Sr_2CaCu_2O_x$, from their parent layered bulk materials.[30] Since then, this method has been widely used to fabricate various kinds of ultrathin 2D nanomaterials. The exfoliated nanosheets range from TMDs (*e.g.*, TiS_2, TaS_2, $TaSe_2$, $MoSe_2$, WS_2, WSe_2, $MoTe_2$, ReS_2, $Mo_xW_{1-x}S_2$, $ReS_{2x}Se_{2(1-x)}$, etc.),[69-79] topological insulator (*e.g.*, Bi_2Te_3, Bi_2Se_3, and Sb_2Te_3),[80-82] $CuInP_2S_6$,[83] BP,[84-87] antimonene,[88] and metal phosphorous trichalcogenides (*e.g.*, MPS_3: M = Fe, Mn, Ni, Cd, and Zn) to h-BN.[89-91] Theoretically, this method is capable of producing all kinds of ultrathin 2D nanomaterials whose bulk crystals are layered compounds.

Although the micromechanical cleavage technique has many advantages, such as wide applicability, high crystal quality, clean surface, and larger lateral size of the obtained flakes, there are still several disadvantages that restrict its practical application in its current form. First, the production yield and rate of this technique are quite low, which makes it difficult to fulfill the demand for various practical applications, high-yield and large-scale production. Then, the size, the thickness and the shape of the produced ultrathin 2D nanomaterials are difficult to control because the exfoliation process is operated manually by hands, which lack the precision, controllability, or repeatability.

Layered bulk crystals also could be exfoliated into ultrathin 2D regime in liquid if proper mechanical forces are applied on the layered bulk crystals dispersed in liquid media. Sonication is the simplest and most common mechanical method that has been used for the exfoliation of layered bulk crystals into ultrathin 2D nanosheets in liquid media, as shown in **Fig. 1-8a**. The key factor for achieving efficient exfoliation of layered bulk crystals is matching the surface energy between the layered bulk crystal and the solvent system. This simple and effective method was first developed in 2008 by Coleman's group for the exfoliation of graphite into graphene,[92] which neither need any complicated equipment nor expensive chemicals, having paved a way for the high-yield and large-scale production of graphene at low cost in liquid phase. Besides graphene, in 2011, Coleman and co-workers further extended this method for exfoliation of other layered bulks into 2D nanosheets, including MoS_2, WS_2, $MoSe_2$, $NbSe_2$, $TaSe_2$, $NiTe_2$, $MoTe_2$, h-BN, and Bi_2Te_3. Both the experimental and theoretical results suggested that the good matching of the surface tension between the layered bulks, not only the choice of solvents, is also a key factor for the efficient exfoliation.[93] The solvent is also important in stabilizing the exfoliated nanosheets and prohibiting their restacking and aggregating as illustrated in **Fig. 1-8a**. To further promote the production rate of the sonication based liquid exfoliation and meet the requirement for industrial applications, several optimized liquid exfoliation strategies have been developed, such as shear force assisted liquid exfoliation,[94,95] ion intercalation-assisted liquid exfoliation (**Fig. 1-8b**),[96,97] ion-exchange-assisted liquid exfoliation (**Fig. 1-8c**),[98-102] oxidation-assisted liquid exfoliation,[103,104] and selective etching-assisted liquid exfoliation.[105-107]

As mentioned the above, the liquid exfoliation supports an efficient way for 2D nanosheets fabrication, while there are several disadvantages for this method. First, the yield of the single-layer nanosheets in the exfoliation suspension is typically low. As known, some of the extraordinary properties of 2D nanomaterials only can be observed in its single-layer form. Recently, Claudia Backes and co-worker demonstrated that the high efficient nanosheet size-selection and/or monolayer enrichment can be achieved using cascades centrifugation method.[108] Second, the lateral size of the produced nanosheet is relatively small due to the fragmentation effect. Third, for the sonication in aqueous polymer/surfactant solution, the residual polymer/surfactant absorbed on the exfoliated nanosheets is undesirable for some further applications, such as electronics, optoelectronics, electro-catalysis, and energy storage. Last the sonication process may induce some defects on the exfoliated nanosheets, which will affect the properties of the exfoliated nanosheets.

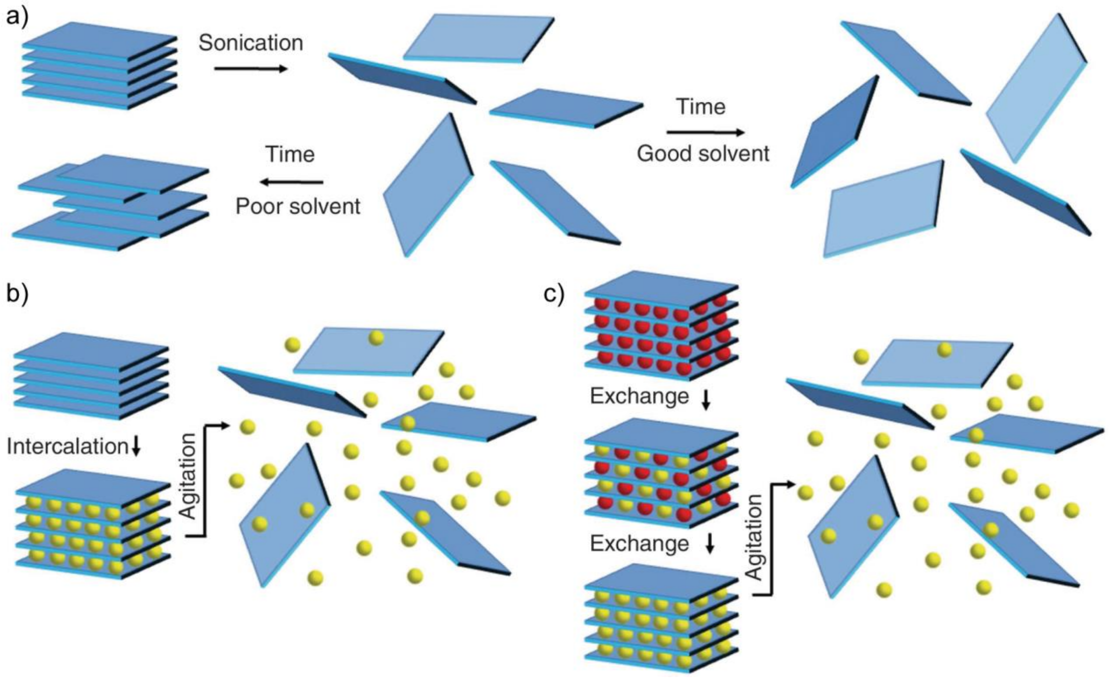

Fig. 1-8. Mechanism of liquid exfoliation. Sonication--assisted liquid exfoliation (a), ion intercalation-assisted liquid exfoliation (b), ion-exchange-assisted liquid exfoliation (c).[109]

- Chemical vapor deposition (CVD) growth

CVD is a conventional technique for the fabrication of high-purity materials or thin films such as W, Ti, Ta, Zr, and Si films on substrates.[110] Currently, as the key step for the production of single crystal silicon, CVD has been widely used for many modern technologies, such as electronics and solar cell devices.[111] During the past decades, CVD method has also been continuously developed and recognized as a reliable and powerful technique for producing a large number of ultrathin 2D nanomaterials.[110] In a typical process, the preselected substrates are mounted in a furnace chamber, and one or more gas/vapor precursors are cycled through the chamber, in which the precursors can react and/or decompose on the surface of substrates.[110] In this case, ultrathin 2D nanosheets can be obtained on the substrate with proper experimental growth window parameters.[110] In some growth processes, catalysts need to be used in the reaction process, for example, for growing graphene.[112] In 2006, Somani and co-workers first demonstrated the growth of thick multilayer-graphene from camphor pyrolysis on a Ni substrate by the CVD technique.[113] Although the graphene realized in this work is about 30 layers, it proved the possibility for the growth of single- or few-layer graphene by the CVD technique. Inspired by this work, many efforts have been spared to optimize experimental conditions to achieve the growth of single- or few-layer sheets. Beton and co-worker achieved the growth of single-layer graphene by CVD method on polycrystalline Ni film deposited on the SiO_2/Si substrate.[114] Note that the Ni film here not only acted as the substrate to support the growth of graphene, but also as the catalyst to facilitate the nucleation of precursors to form graphene sheets. Ruoff and co-workers demonstrated the growth of large-area single-layer graphene film up to 0.5 mm on copper foil by the CVD method using methane and hydrogen as gas sources.[115] It is worth to point out that the precursors, substrates, catalysts, temperature, and atmospheres are among the key factors in determining the structure features of the final graphene products in CVD growth. By fine-tuning those experimental parameters, the controlled growth of graphene with tunable layer number, crystallinity, and lateral size can be achieved on different substrates with different precursors by the CVD technique.[112] Likewise, CVD can be extended for the growth of many other 2D nanosheets on various substrates, such as h-BN nanosheets,[116,117] topological insulators (*e.g.*, Bi_2Se_3),[118-120] metal carbides,[121,122] silicene, borophene, and antimonene.[123-125]

Not only the aforementioned graphene nanosheets, single- or few-layer TMDs also have been achieved by the CVD technique on various substrates.[126] Although the growth of TMDs can date back to the 1980s,[127] the growth of ultrathin 2D TMD flakes was only achieved a few years ago. In 2012, Li and co-workers first demonstrated the growth of few-layer MoS_2 nanosheets on insulating substrates by the thermal decomposition of ammonium thiomolybdates that was dip-coated onto the substrates with a subsequent sulfurization using sulfur vapor (**Fig. 1-9**).[128] Alternatively, the CVD growth of large-area few-layer MoS_2 nanosheets was achieved by sulfurization of Mo metal film by sulfur vapor, in which the Mo film was previously deposited on the SiO_2 substrate using an electronic beam evaporator.[129] The size and thickness of the film can roughly be tuned by controlling the size of the substrate and the thickness of Mo metal film. TMOs and transition metal chlorides (*e.g.*, MoO_3 and $MoCl_5$) can also be used as the Mo sources to produce MoS_2 nanosheets by the CVD technique.[130-132] Up to now, many ultrathin 2D nanosheets of TMDs, including MoS_2, WS_2, $MoSe_2$, WSe_2, ZrS_2, ReS_2, $MoTe_2$, etc.,[133-144] and also some alloyed TMD nanosheets (*e.g.*, $MoS_{2x}Se_{2(1-x)}$, $Mo_xW_{1-x}S_2$, and $WS_{2x}Se_{2(1-x)}$) have been grown by the CVD technique from different precursors at different temperatures on various substrates under different atmosphere.[145-150]

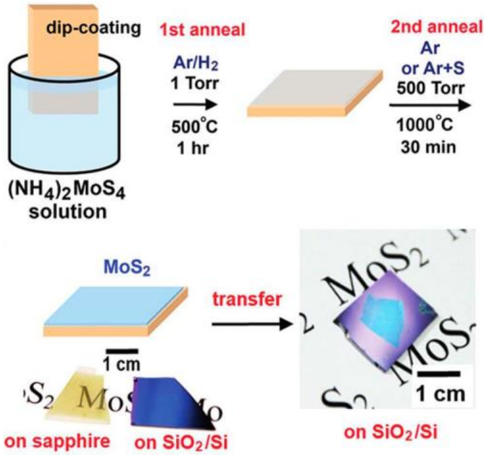

Fig. 1-9. Schematic illustration of the CVD method grown of MoS_2 thin layer on insulating substrate.[128]

The CVD technique allows researchers to prepare ultrathin 2D nanomaterials with high crystal quality, high purity, and limited defects on certain substrates with controllable size and thickness. More importantly, the electronic properties of ultrathin 2D nanomaterials, such as graphene and TMDs, are approaching those of mechanically exfoliated thin layers. Therefore, ultrathin 2D nanomaterials grown by the CVD technique are also promising candidates for the fabrication of high-performance electronic and optoelectronics devices. Unlike the low yield and low production rate of the micromechanical cleavage technique, CVD is capable of producing materials in industry scale. It is believed that CVD technique is a promising method with potential to produce ultrathin 2D nanosheets in industry applications for electronics and optoelectronics. However, the CVD method still has some disadvantages at its current form, for example ultrathin 2D nanomaterials grown by the CVD technique are always deposited on the substrates, needing to be transferred to other substrates for further investigation and applications. The CVD technique normally needs high temperature and inert atmosphere, leading to relatively high cost of production as compared to the solution-based methods.

- Wet-chemical syntheses

Wet-chemical syntheses also are good choices for the preparation of ultrathin 2D nanomaterials in high yield and larger amount.[151,152] Wet-chemical syntheses represent all the synthetic methods that rely on the chemical reactions of certain precursors at proper experimental conditions conducted in solution phase.[153] Because of their powerful controllability, wet-chemical syntheses have been considered as a class of convenient and reproducible strategies for the preparation of ultrathin 2D nanomaterials with controlled size and thickness, which are potentially scalable for industry applications. Particularly, wet-chemical syntheses have been widely used for preparing various non-layer structured ultrathin 2D nanomaterials that are unable to be realized by top-down methods.[152] The synthesized 2D nanomaterials can easily be dispersed in organic or aqueous media, which make them very suitable for various applications. Wet-chemical syntheses can be also used for the synthesis of ultrathin 2D nanosheets with layered structural features.[151] Unlike all of the methods discussed above, there are no general principles underlying each wet-chemical synthesis method. One wet-chemical synthesis method could be as different from the other. To classify, hydro/solvothermal synthesis, 2D-oriented attachment, self-assembly of nanocrystals, 2D-templated synthesis, hot-injection method, interface-mediated synthesis, and on-surface synthesis are a few routines and a brief summary as follows.

The hydro/solvothermal synthesis method is a typical wet-chemical synthesis strategy, using water or organic solvent as the reaction medium in a sealed vessel, in which the used reaction temperature is higher that the boiling point of the solvent.[154] When the reaction temperature of the closed system is heated above the boiling point of the solvent system, the solvent will be autogenerated in high pressure to promote the reaction and improve the crystallinity of the as-synthesized nanocrystals. Dou and co-workers employed this method for the synthesis of ultrathin 2D transition metal oxide nanosheets, including TiO_2, ZnO, Co_3O_4, WO_3, Fe_3O_4, and MnO_2, by using the poly(ethylene oxide) – poly(propylene oxide) – poly(ethylene oxide) (P123) and ethylene glycol as surfactants in ethanol.[155] Later, Xie and co-workers reported the preparation of few-layer defect-rich MoS_2 nanosheets by a facial hydrothermal method with the assistance of excess thiourea.[156] The 2D-oriented attachment is another typical wet-chemical synthesis method used for the synthesis of ultrathin 2D nanomaterials, in which adjacent nanocrystals are connected with each other and fused together to form single-crystalline 2D nanosheets by sharing a common crystallographic facet to eliminate the high energy facets and interfaces.[152] In 2010, Weller and co-workers developed this method for the synthesis of PbS nanosheets from tiny PbS nanocrystals.[157] Impelled by the development of nanocrystals synthesis and surface modification technologies, self-assembly of nanocrystals has been developed as one of the efficient ways to create nanoarchitectures with inner nanocrystals in ordered and steady manner, in which presynthesized nanocrystals spontaneously organize with each other by noncovalent interactions, such as van der Waals interactions, electrostatic interactions, and/or hydrogen bonds.[158] It has been demonstrated that the assembly of low-dimensional nanocrystals, such as nanoparticles and nanowires, is a promising strategy to prepare ultrathin 2D nanomaterials. And Acharya and co-workers prepared an ultrathin 2D PbS nanosheet via the coalescence of PbS nanowires.[159] Templated synthesis is an effective strategy for growth of anisotropic nanostructures, which refers to the use of the presynthesized nanomaterials or bulk substrates as templates to confine/direct the growth of specific nanostructures.[160,161] For instance, by using the GO nanosheet as template, Zhang and co-workers achieved the growth of hexagonal close-packed (hcp) Au square nanosheet with size between 200 and 500 nm and thickness of ~2.4 nm.[162] The hot-injection method, initially developed by Bawendi and co-workers for the synthesis of cadmium chalcogenide nanocrystals,[163] is a very attractive approach to prepare monodispersed colloidal nanocrystals with uniform size, shape, and high purity. As a typical example, a single-layer CdSe nanosheet was synthesized using this method by heating the reactants of $CdCl_2$ and Se powder in a mixture solution of octylamine and oleylamine.[164] The interface-mediated synthesis method is another typical wet-chemical synthesis method used for the synthesis of ultrathin 2D nanomaterials, especially for metal coordination polymers (CPs) and polymers. In 2011, Schlüter and co-workers first achieved the synthesis of single-layer CP nanosheet at the water/air interface.[165] The on-surface synthesis method has been developed as a promising way for the synthesis of ultrathin 2D COF nanosheets from monomers on solid substrates.[166,167] In a typical process, the monomers for a certain COF were casted in the surface of a solid substrate, which then reacted into COF nanosheets through the polymerization process due to the surface confinement of the solid substrate. As a typical example, Lei and co-workers first developed this method for the single-layer imine-based COF on the highly oriented pyrolytic graphite (HOPG) surface.[166]

1.2.2 Electrical, optical and mechanical properties

Two-dimensional (2D) materials are crystalline films with large ratio between their lateral size (> 1 μm) and thickness (< 1 nm). The structural lattice of bulk layered crystals, which facilitates their exfoliation to 2D layers, originates from the strong in-plane covalent (or mixed ionic-covalent) bonding and relatively weaker out-of-plane van der Waals (vdW) interactions with typical binding energies of 40-70 meV/atom.[168] The electronic transport, *i.e.*, conductivity, in layered materials is much more efficient within the layers (*i.e.*, in the plane perpendicular to the stacking axis) than it between the layers, typically by 3 or 4 orders of magnitude in natural MoS_2 bulks.[169] This is due to the strong charge carrier localization within the individual layers and simultaneous transport of charge carriers through multiple layers.[170] In the situation of 2D material regime, the in-plane conduction is dominant by band transport, while the out-of-plane conduction reduced due to the large interlayer van der Waals gap which does not allow a good hybridization of wave functions between different layers. A large number of layered materials with diverse properties based on the elements have been highlighted in **Fig. 1-10** were gradually exfoliated in 2D form.[64] In this part, a general discussion will be focused on the electrical, optical and mechanical properties of these 2D materials in a point of view of condensed matter physics employing graphene and TMDCs as examples.

- Crystal structure of 2D materials

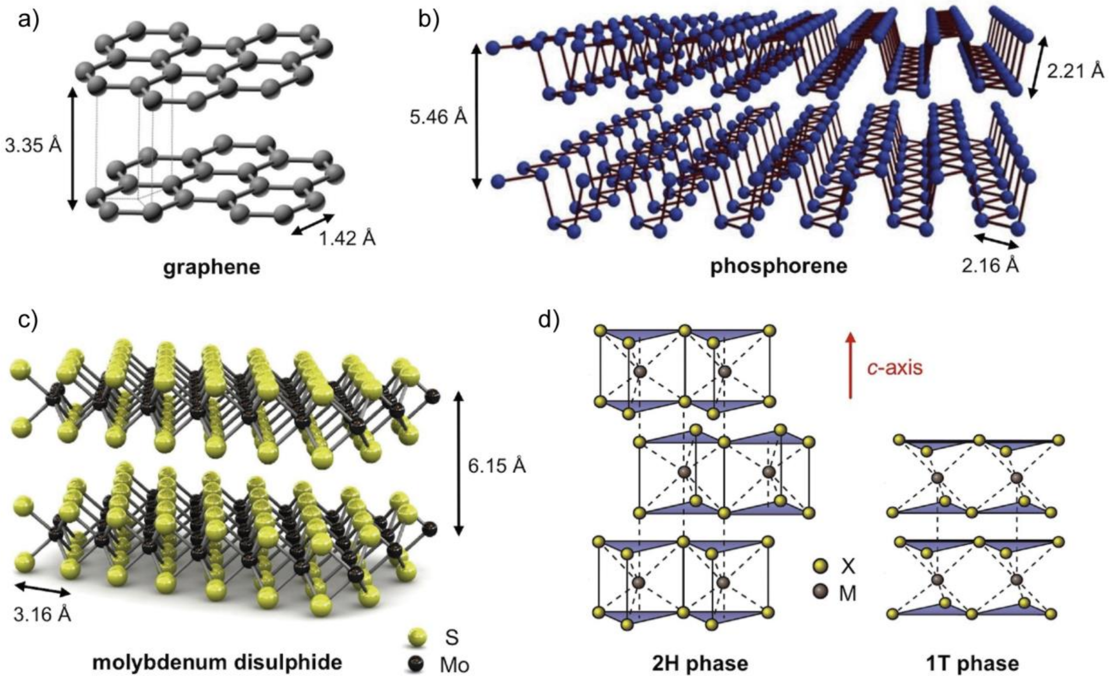

Fig. 1-10. Crystal structures of various 2D materials. a) graphene. b) black phosphorene. c) MoS_2. d) Two different stacking sequences of TMDCs.[64]

Monolayer graphene and hBN are two examples of 2D crystals which all the atoms are arranged in a hexagonal lattice and occupying the same lattice plane (**Fig. 1-10a**). Other single-element 2D materials such as phosphorene form buckled structures with the atoms arranged across more than one plane (**Fig. 1-10b**). Monolayer TMDCs are three atoms thick and comprise of an X-M-X (X = S, Se, Te; M = Mo, W, Re *etc.*) sandwich geometry (**Fig. 1-10c** and **d**) with either trigonal prismatic or octahedral coordination of the metal atom.[171] The d orbitals of M atoms and the p orbitals of X atoms facilitate their covalent bonding within an MX_2 monolayer, the atoms are arranged in a hexagonal pattern when viewed along the c-axis direction, and the individual layers are held by the weak vdW forces. Importantly, all the accessible orbitals of M and X at the basal surface are involved in the intralayer bonding, leaving only the high-energy antibonding orbitals for interlayer or external bonding, thus result in a complete absence of dangling bonds.[172] The metal coordination and stacking order between the individual layers defines the phase or the polytope of a TMDC (**Fig. 1-10d**). Common phases are 1T, 2H or 3R, where 1, 2, 3 defines the number of X-M-X sandwiches per unit cell in the c axis direction and T (tetragonal), H (hexagonal), R (rhombohedral) denotes the crystal symmetry.[173] The phase determines the properties of TMDCs: *i.e.*, MoS_2 exist either as 2H or 3R, which is a thermodynamically stable or metastable semiconducting phase with a bulk band gap of ~1.2 eV, or as 1T, which is a metastable metallic phase. The 2H and 1T phases can be transformed to one another by simple gliding of the atomic planes, demonstrated by an in situ electron microscopy,[174] or by chemical modification.[175] The coordination of the M atoms is a trigonal prismatic in the 1H and 3R phases and octahedral in the 1T phase (**Fig. 1-10d**).[171]

- Electronic, optical, and mechanical properties of 2D materials

Band diagrams describe the electronic structure of solids, whose multitude of electronic state lead to continuum-like bands of allowed energy levels.[52] Solids can be classified based on their electronic structure as metal, semimetals (with an overlap in energy between their valence band (VB) and conduction band (CB)), semiconductors and insulators (with a 1-4 eV and > 4 eV band gap between their VB and CB, respectively). Graphene, thanks to its zero-band gap semiconducting nature and a linear dispersion of charge carriers near the K and K’ points of the Brillouin zone, occupies a unique position amongst other 2D materials. This results in various interesting physical phenomena, such as relativistic-like charge carriers, wavelength-independent light absorption, Klein tunneling, and others.[176,177] Conductivity (σ) of graphene is intrinsically high due to the high charge carrier mobility (μ) in graphene, and it is readily tuneable through charge carrier density (n), according to $\sigma = ne\mu$, where e is the elementary charge. **Fig. 1-11a** demonstrates this ambipolar nature of graphene in the vicinity of the Dirac point.[11,178]

The charge carrier mobility of semiconducting 2D materials is strongly dependent on factors such as temperature, number of layers, substrate, charged impurities, localized states, defects, device geometry, contacts, and external electric-field induced charge carrier polarity. Thus, introducing large discrepancies in the literature reports about the electronic transport of mono- and few-layer MoS_2 with the mobility values ranging over 6 orders of magnitude, between 0.03 and 34000 $cm^2V^{-1}s^{-1}$.[70,179-181] The mobility generally increases upon the increased number of layers in TMDC FETs,[70,182,183] although exception to this have been reported and attributed to the interlayer resistance.[184,185] The charge carrier density depends on the intrinsic and extrinsic doping levels, electrical field, and density of traps levels and recombination centers. The typical values of $\sim 10^{12}$ cm^{-2} can be significantly increased to 10^{13} - 10^{14} cm^{-2} by ionic top-gating using polymer or ionic liquids.[186] Mobilities of graphene and group 5 TMDCs are summarized in **Table 1**.

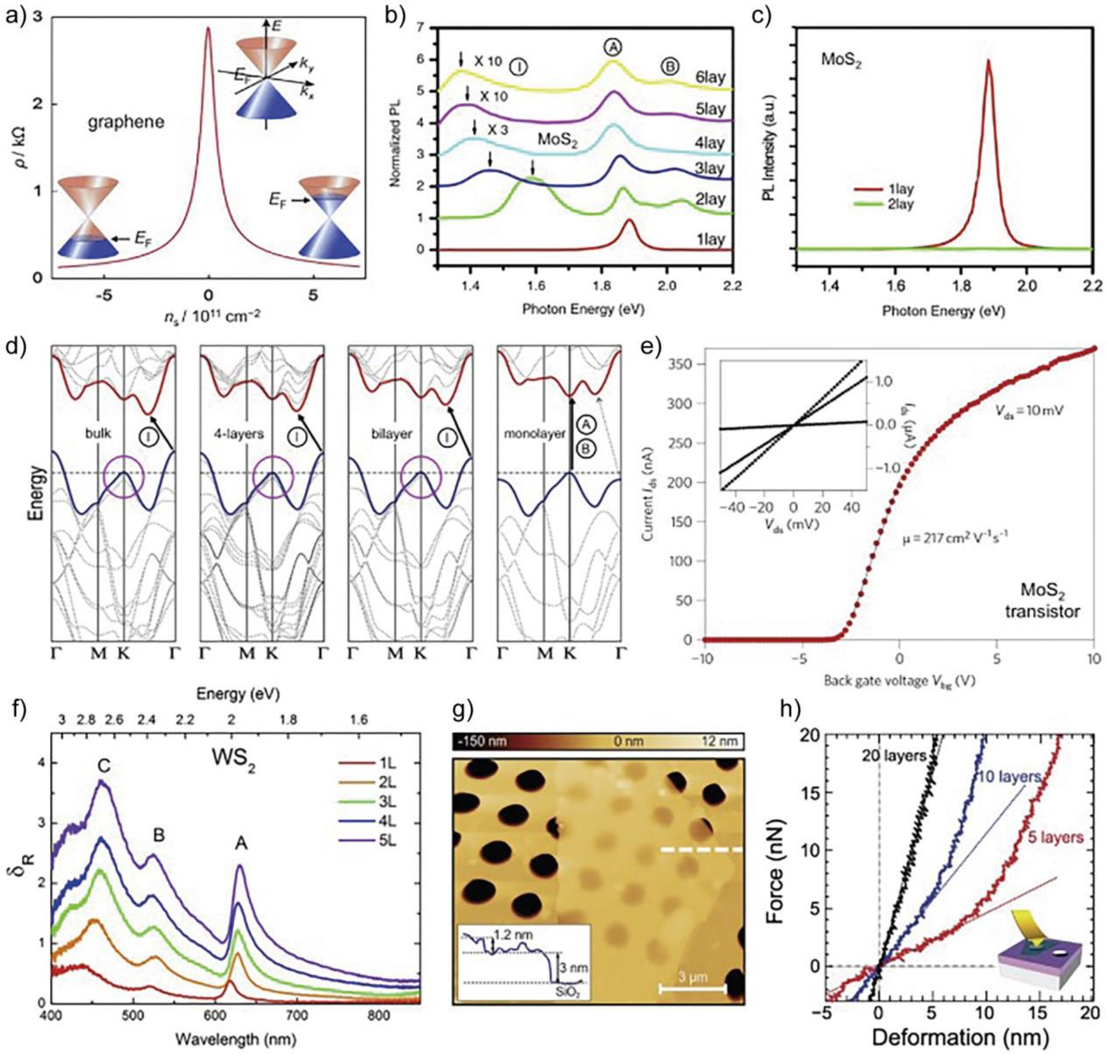

Fig. 1-11. Electronic, optical, and mechanical properties of 2D materials.[64,177,179,187-190]

As schematically shown in **Fig. 1-12a**, 2D semiconducting materials also experience strong enhancement of the Coulomb interactions among charge carriers and defects thanks to the quantum confinement and significantly reduced dielectric screening.[191,192] As a result of this effect, long-lived excitons and trions with spatial extent of several nm have been observed in mono- and few-layer TMDCs.[193,194] Their binding energies, *e.g.*, ~320 meV for excitons in WS_2 and ~20 meV for trions in MoS_2,[194,195] which are several times higher than those in bulk, imply high thermal stability of these quasiparticles at room temperature. Biexcitons with a binding energy of ~52 meV have also been recently reported in the emission spectra of monolayer WSe_2 at high exciton densities.[196] These results, which were previously only observed in exotic systems such as quantum wells at low temperatures,[197,198] open new experimental avenues for studying many body physical phenomena.

Table 1: charge carrier mobility in graphene and TMDCs.[135,170,179,183,186,199-203]

2D materials	Mobility ($cm^2V^{-1}s^{-1}$)	
	Bulk (> 10 layers)	Monolayer
Graphene	10000	> 140000
2H-MoS_2	60 - 200	> 200
2H-$MoSe_2$	160 - 250	50
2H-$MoTe_2$	40	-
2H-WS_2	20 - 100	0.2
2H-WSe_2	120 - 150	30 - 180
1T'-WTe_2	6000 - 44000	20 - 21000

Table 2: Band gap evolution of TMDCs.[187,189,204-207] ^{I} Indirect band gap, ^{D} Direct band gap.

2D materials	Band gap (eV)				
	Bulk	Tetralayer	Trilayer	Bilayer	Monolayer
2H-MoS_2	1.23^I	1.41^I	1.46^I	1.59^I	1.89^D
2H-$MoSe_2$	1.09^I	-	1.34^I	1.46^I	1.57^D
2H-$MoTe_2$	0.93^I	1.00^I	1.02^I	1.05^I	1.08^D
2H-WS_2	1.35^I	1.47^I	1.53^I	1.73^I	1.98^D
2H-WSe_2	1.2^I	1.42^I	1.45^I	1.54^I	1.66^D
1T'-WTe_2	Semimetal/metal (~0.5 eV overlap between W 5d and Te 5p bands)				

The strong interlayer coupling and quantum confinement, introduced by the strong hybridization between d orbitals of the M atoms,[187,208,209] further result in thickness-dependent electronic band structures in most 2D materials (**Figs.1-11b-d** and **1-12b**). For example, as shown in **Fig. 1-11d**, bulk group 6 2H-TMDCs possess an indirect band gap of 0.9 – 1.4 eV, originating from the transition between the VB maximum (VBM) at the Γ point to the CB minimum (CBM) halfway between the Γ and K points.[210,211] This indirect transition is strongly affected by the presence of neighboring layers because of the fact that the VBM states near the Γ point arise from a linear combination of the d and p orbitals of M atoms and X atoms and that the involved holes and electrons have lower out-of-plane masses. In contrast, the smallest direct band gap, which is larger in size than the indirect one, originates from the d-d metal orbital transitions at the K (and K') point of the VBM and CBM.[171,212,213] The direct transition remains almost unaffected by the interlayer interaction because the M d orbitals are nested inside the X-M-X sandwich and the holes and electrons at the K (K') point have much higher out-of-plane mass than free electrons.[188] As a result, the indirect band gap is strongly dependent on the number of layers, while the direct one is not (**Fig. 1-11d**). These changes are manifested by energy shifted in the TMDC photoluminescence (PL) spectra shown in **Fig. 1-11b**. Importantly for optoelectronics, this band structure evolution is accompanied by an enormous increase of PL intensity in monolayer TMDCs in comparison to thicker layers as shown in **Fig. 1-11c**.[187,188,205] For the group 6 TMDCs, the band gaps increase with the increasing size of transition metal atoms and decreasing size of chalcogen atoms, regardless of thickness,[208,214,215] as shown in **Table 2**, whereas the VBM and the CBM increase with the increasing size of both M and X.[193,216] Furthermore, the direct band gap comprise of two excitonic transitions, A and B, at energies between 1.1 and 2.4 eV, originating from the transition between the spin-orbit split VBM (indicated in **Fig. 1-11d** by magenta circles) and doubly degenerate CBM at the K (K') point, and further transitions are observed at higher energies (2.5 – 4.8 eV).[212,217-219] Due to a greater overlap between the outer orbitals of larger atoms, the size of the A-B energy splitting increases with the increasing size of M atoms and X atoms (**Table 3**).[218,219] 1T'-WTe_2 is an exception to this due to its perfectly-compensated semi-metallic character with a small overlap between the W 5d and Te 5p orbitals due to the distorted octahedral coordination discussed earlier.[199,204]

Table 3: A and B exciton in bulk TMDCs.[189,204,217,219]

2D materials	Bulk exciton energy (eV)		
	A	B	$\Delta_{A\text{-}B}$
2H-MoS_2	1.88	2.06	0.18
2H-$MoSe_2$	1.57	1.82	0.25
2H-$MoTe_2$	1.10	1.48	0.38
2H-WS_2	1.96	2.36	0.40
2H-WSe_2	1.62	2.19	0.57

The absorption spectrum of TMDCs is well matched to the solar spectrum and more than 95% of the sunlight can be absorbed even in polycrystalline films of sub-micrometer thickness, much thinner than the current photovoltaics standard.[220]

Theoretical calculations and experiments indicate that a TMDC monolayer can absorb ~5% - 10% of sunlight, equal to as much as 50 nm Si or 15 nm GaAs, and are able to generate about ten times larger photocurrent.[221] However, due to the complex electronic band structure of TMDCs, their absorption/reflectance is strongly dependent on the wavelength of the incident light,[218,219,222] as can be seen in the differential reflectance spectra shown in **Fig. 1-11f**. In contrast, graphene monolayer can absorb ~2.3% of light, a value, solely defined by the coupling between light and the relativistic-like electrons in graphene, and independent of wavelength in the visible range.[223] The wavelength-specific transmission/absorption scales linearly with the number of layers for most thin 2D materials but this proportionality breaks down in thick crystals.[187,223] The absorption coefficient between the infrared (IR) and near-ultraviolet (UV) is typically on the order of $\sim 10^4 - 10^6$ cm^{-1} and is generally larger for the W-based than Mo-based TMDCs.[215,217-219,222,224] Furthermore, the equivalent absorption coefficients of monolayer MoS_2 and graphene are 2 – 3 times higher than that of their bulk counterparts.[221]

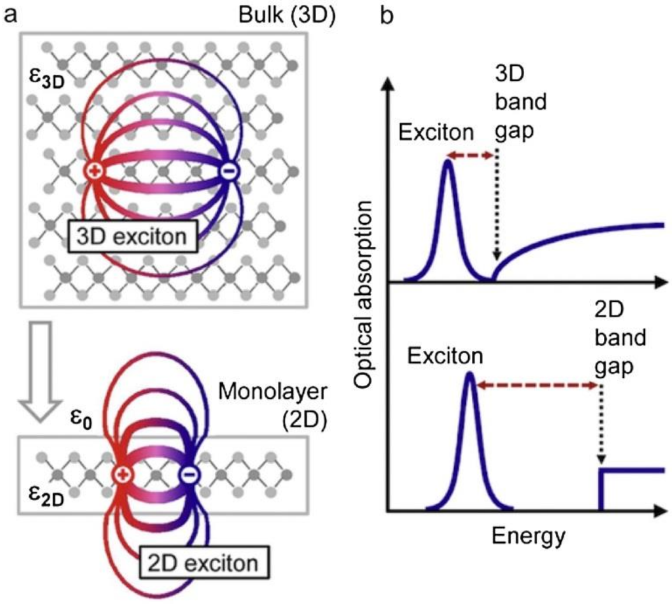

Fig. 1-12. Quantum confinement and reduced dielectric screening in 2D materials.[64]

Mechanical properties of 2D materials have also been studied extensively. Monolayer MoS_2 can withstand strain up to 11%, deformations up to several tens of nm without broken, and has a Young’s modulus that is comparable to that of steel (see **Fig. 1-11g** and **h**).[190,225] Such strength and elasticity makes it suited for applications where sturdiness as well as flexibility is both required. Ripples and wrinkles, which are known to form in 2D materials due to the localized strain and differing thermal expansion coefficient of the 2D material and substrate, were predicted to grow in size with temperature and decrease the size of the band gap in MoS_2.[226] These ripples have typical height of 1 – 25 nm, periodicity of 40 – 300 nm, and have been shown to be correlated with changes in the surface potential and charge.[227] Strong, thickness-dependent piezoelectricity, for the odd number of layers only, was also observed in mono- and few-layer MoS_2 with the strongest effect and ~5% mechanical-to-electrical energy conversion efficiency observed in monolayer.[228] Frictional properties of MoS_2 which are related to surface oxidation, moisture, and temperature also have been studied because of its use as a lubricant.[229] Moreover, the melting temperature of most 2D crystals generally decreases with the decreasing thickness, and, while sulfides and selenides tend to be more thermodynamically stable than tellurides (and most metallic) TMDCs.[66,230]

1.3 The advances of 2D GaSe and InSe

Group III–VI compounds $M^{III}X^{VI}$ (M = Ga, In; X = S, Se, Te) are one class of important 2D layered materials and are currently attracting increasing interest due to their unique electronic and optoelectronic properties and their great potential applications in various other fields. Similar to 2D layered transition metal dichalcogenides (TMDs), $M^{III}X^{VI}$ have the significant merits of ultrathin thickness, ultrahigh surface-to-volume ratio, and high compatibility with flexible devices. More impressively, in contrast with TMDCs, $M^{III}X^{VI}$ demonstrate many superior properties, such as thickness-independent direct band gap electronic structure, low mass conduction band electrons and high carrier mobility, p-type electronic behaviors (rare for TMDCs), high charge density, strong second harmonic generation (SHG), and so on. These unique characteristics allow for high-performance device applications in electronics, optoelectronics, and optics. Here, the following text will be employed for the discussion of the advances of 2D GaSe and InSe from the aspects of crystal structure, crystal fabrication, properties and applications.

- Crystal structure

Both GaSe and InSe are layered III-VI semiconductors that consist of covalent bonded stacks with top and bottom layers of Se and two layers of Ga or In ions in the middle, *i.e.*, in the sequence of Se-Ga-Ga-Se and Se-In-In-Se, with a lattice constant of a = b = 3.74 Å for GaSe and 4.005 Å for InSe, respectively.[231,232] **Fig. 1-13** shows the schematic representation of the typical hexagonal structures. The covalent bonded layers, named tetra-layers (TLs), are held together by a weak interaction of the vdW force, implying possibility of existence of 2D GaSe and InSe layers. The stacking sequence of the TLs both determines the polytypes of GaSe and InSe crystals. There are three most important classifications for GaSe crystals: *β*-GaSe, *ε*-GaSe, and *γ*-GaSe.[233] Among them, *γ*-GaSe has a 3R stacking sequence, belonging to non-centrosymmetric space group of C^4_{6v} with the lattice constant of c = 23.92 Å. Both *β*-GaSe and *ε*-GaSe are hexagonal symmetric with a 2H stacking and the lattice constant of c = 15.95 Å, which belong to the space groups of D^4_{6h} and D^1_{3h}, respectively. Similarly, four polytypes are defined as *β*, *ε*, *γ*, and *δ* for InSe crystals,[234-237] which are all layered structures. Among them, *β*-phase and *γ*-phase are two common forms of InSe. For *β*-phase, each primitive unit cell contains two quaternary layers, *i.e.*, 8 atoms. However, in the unit cell of *γ*-phase, there are three layers of Se-In-In-Se monatomic sheets (12 atoms), with lattice parameters of c = 24.961 Å.

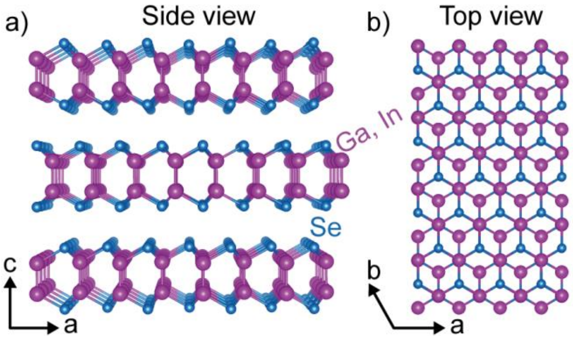

Fig. 1-13. Schematic of crystal structure of *ε*-GaSe and *ε*-InSe. a) Side view. b) Top view.

- Crystal fabrication

Both GaSe and InSe bulks can be mechanically exfoliated to mono- and few-layer geometry using the Scotch tape method thanks to their layered stacking structural features. Monolayer GaSe was firstly experimentally obtained in 2012 by Late *et al.* via the mechanical exfoliation method.[238] After the exfoliation of monolayer GaSe, many methods have been employed to grow these ultrathin crystals. The vapor-phase mass transport (VMT) method was firstly reported to prepare large-area atomically thin GaSe layers on insulating substrates in 2013 by Lei *et al.*, as illustrated in **Fig. 1-14**,[239] where thin GaSe layers can be obtained in triangle, truncated triangle, and hexagonal shapes on the SiO_2 substrate. The shape of the fabricated 2D flakes can be tuned by the distance from nucleation sites to the source. However, it is difficult to control the growth process because it is very fast. Then Zhou *et al.* proposed the controlled synthesis of high-quality single- and multi-layer GaSe crystals on flexible transparent mica substrates via the van der Waals (vdW) epitaxy method.[240] And Li *et al.* also used this method to grow GaSe layers with preferred orientation in graphene to fabricate vdW heterostructures.[241] Besides the aforementioned chemical deposition methods, some physical methods also have been employed to grow 2D layered GaSe, such as molecular beam epitaxy (MBE) and pulse laser deposition (PLD) methods. Yuan *et al.* reported layer-by-layer growth of 2D GaSe on n-type Si substrates by the MBE method.[242] And later, the 2D GaSe nanosheets also were prepared by highly pure Ga and Se via high-temperature process in a high-vacuum system through PLD technique.[243]

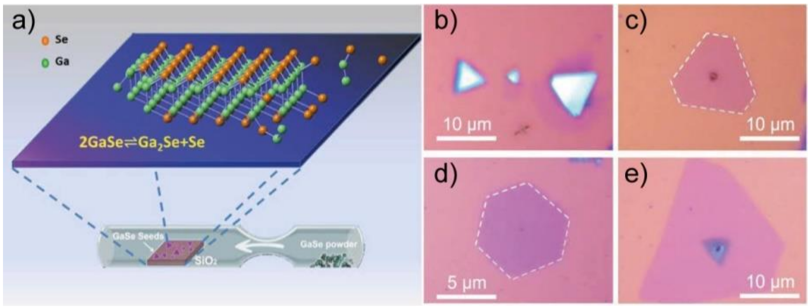

Fig. 1-14. Large-area atomically thin GaSe layers synthesized on insulating substrates using VMT method (a) and thin GaSe layers in triangle (b), truncated triangle (c), and hexagonal (d, e) shapes on the SiO_2 substrate.[239]

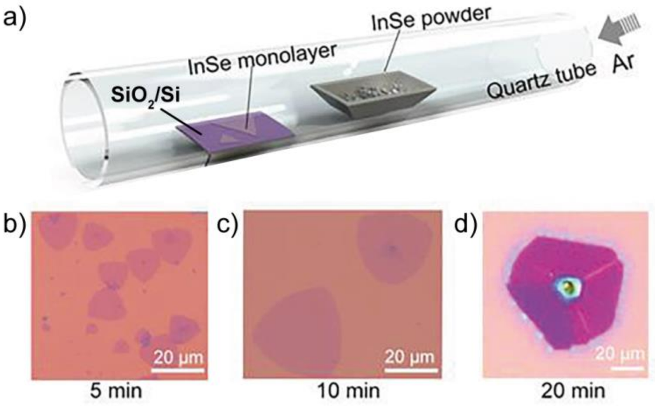

Fig. 1-15. PVD setup (a) and images of atomically thin InSe on SiO_2/Si substrate (b, c, d).[244]

As for InSe, the first 2D flake was obtained by Garry W. Mudd *et al.* using mechanical exfoliation method from the bulk single-crystal ingot in 2013.[245] Since then, most of the experimental investigations have been carried out based on mechanical cleavage method, which provides high-quality 2D InSe nanosheets. Four years later, Zhibing Yang *et al.* reported that wafer-scale synthesis of ε-InSe thin film has been achieved on SiO_2/Si substrate by PLD technique.[246] In 2018, Jiadong Zhou *et al.* reported the successful synthesis of monolayer InSe by physical vapor deposition (PVD) (**Fig. 1-15**).[244] Very recently, single- and few-layered InSe flakes are produced, with lateral sizes ranging from 30 nm to a few micrometers and thicknesses from 1 to 20 nm, by the liquid-phase exfoliation of β-InSe single crystals in 2-propanol by Elisa Petroni *et al.*,[247] obtaining stable dispersions with a concentration as high as 0.11 g L^{-1}. Zhongjun Li *et al.* also reported the results of the synthesized photoelectrochemical (PEC)-type photodetector using liquid-phase exfoliated 2D InSe nanosheets dispersions.[248]

- Properties and applications

Bulk GaSe has an indirect band gap of about 2.1 eV and a direct band gap of only about 25 meV higher.[249] When GaSe comes to 2D geometry, the electronic band gaps trend to be getting larger upon the decrease of thickness.[250] The band gaps of mono- and bi-layer GaSe are reported to be indirect and have a value of 3.001 eV and 2.426 eV, respectively, as shown in **Fig. 1-16**, calculated from the DFT-HSE06 function.[251]

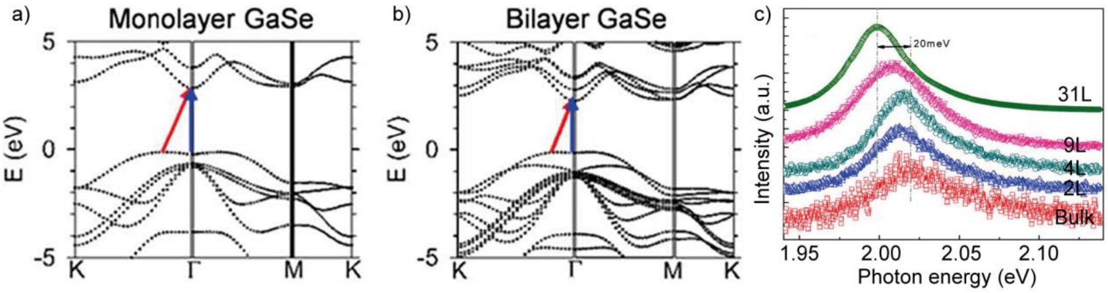

Fig. 1-16. Electronic band structure of monolayer (a) and bilayer (b) GaSe.[250,251]

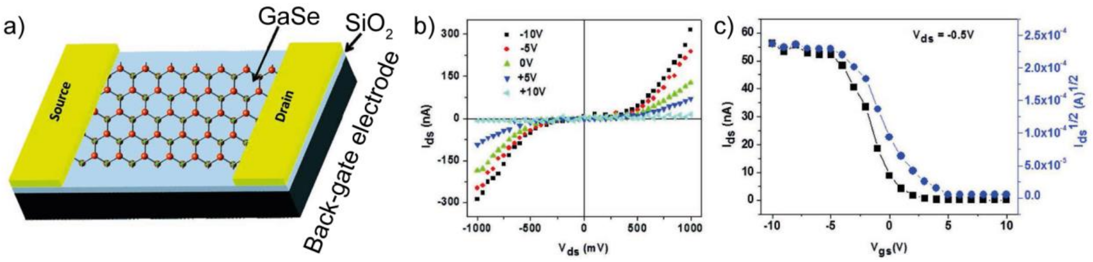

Fig. 1-17. Schematic of GaSe-based bottom-gated FET (a), room temperature output (b) and transport (b) characteristics of p-type GaSe-based FET.[252]

Following the roadmap of graphene and MoS_2, 2D GaSe flakes have also been used in transistors as the channel material. In 2012, Dravid's research group firstly reported mechanically exfoliated monolayer GaSe-based bottom-gated FETs by using 500 nm SiO_2 as gate dielectric, as schematically shown in **Fig. 1-17**.[252] The output and transport characteristics are shown in panel b and c, respectively, which indicate a p-type behavior with an on/off ratio of 10^5. The mobility was calculated to be about 0.6 $cm^2V^{-1}s^{-1}$, which is much lower than that of its bulk counterpart (~215 $cm^2V^{-1}s^{-1}$), and is comparable with previous reported bottom-gated MoS_2-based FETs.[179] Based on the aforementioned FET device, mechanically cleaved GaSe flakes were transferred onto a silicon substrate with an oxidized layer of 300 nm to fabricate a phototransistor (**Fig. 1-18a**).[250] As the wavelength of light decreases from 610 to 254 nm, there is a significant increase in photocurrent (**Fig. 1-18b**). The on/off switching ratio, photoresponsivity, external quantum efficiency (EQE) and response time extracted from the *I*-t curve (**Fig. 1-18c**) upon the illumination of 254 nm take the values of ~8, 2.8 A W^{-1}, 1367% and 0.0157 s. The reported photoresponsivity is higher than that of first monolayer MoS_2-based phototransistor with a photoresponsivity of 7.5 mA W^{-1}.[253] The operation speed is much slower than that of traditional metal-semiconductor-metal (M-S-M) photodetectors with a typical switching time on the order of 10^{-6} – 10^{-9} s, which is possibly caused by the interaction between the GaSe nanosheets and SiO_2 surface, because a large surface-to-volume ratio tends to induce defects and dangling bonds on the surface of GaSe. After that, a lower dark current in the order of pA and a higher on/off ratio than 100 also have been realized in few-layer GaSe phototransistors using the 2D GaSe grown by vapor phase mass transport (VMT) method and van der Waals (vdW) epitaxy.[239,240] Then, the photocurrent generated from GaSe flakes prepared by PLD and controlled vapor deposition methods was studied,[243,254] respectively. For the former, the photoresponsivity could be improved to 1.4 A/W by changing the illumination light from 700 to 240 nm. For the later, the photoresponsivity could be increased to 8.5 A/W by applying a gate voltage of -60 V to the FET-based phototransistor. Very recently, Cao *et al.* reported an ultra-high photoresponsivity of 2D GaSe-based phototransistor by reducing the lateral spacing distance, as schematically shown in **Fig. 1-18d**,[255] e and f, the fabricated phototransistor could achieve a significant high photoresponsivity of about 5000 A W^{-1}. Up to now, multilayer GaSe crystals are generally used in the application of FETs rather than single-layer one, a summary of the parameters of the fabricated phototransistors are shown in **Table 4**. Yuan *et al.* reported MBE-grown p-type GaSe flakes on n-type Si to fabricate a p-n junction (**Fig. 1-18g** and **h**), which can produce fast response with a rising photoresponse time of 60 μs and the decay time of 20 μs (**Fig. 1-18i**), which is an order of magnitude faster that the aforementioned phototransistor.[242]

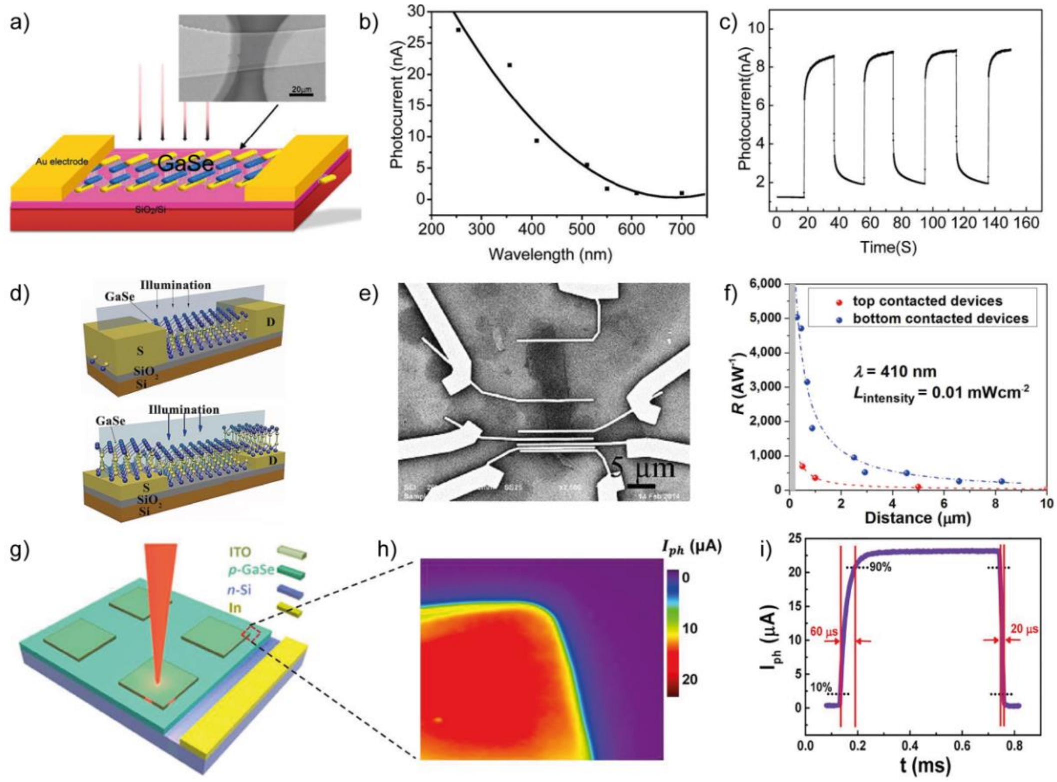

Fig. 1-18. 2D GaSe-based photodetectors.[242,250,253,255]

The evaluated the electronic band structures of monolayer, few-layer, and bulk γ-InSe are shown in **Fig. 1-19a**.[256] There is a drastic decrease in the electronic band gap of few-layer InSe compared to that of the monolayer, which is consistent with experimental photoluminescence (PL) measurements result (**Fig. 1-19b**). Another observation is that 2D InSe shows an indirect to direct band transition upon increasing layer thickness, which is opposite to the behavior of MoS_2.

Table 4 Parameters of 2D GaSe-based photodetectors.

Method	thickness	λ (nm)	R (A/W)	EQE (%)	On/OFF ratio	*t* (ms)	REF.
ME	Few-layer	254	2.8	1367	8	15.7	250
VMT	6-8	405	0.017	5.2	1000	--	239
vdWE	6	White light	0.6	--	110	--	240
CVD	Few-layer	White light	8.5	--	100	--	254
PLD	20	700/240	0.4/1.4	100/700	--	--	243
ME	20-30	410	5000	--	--	0.27	255

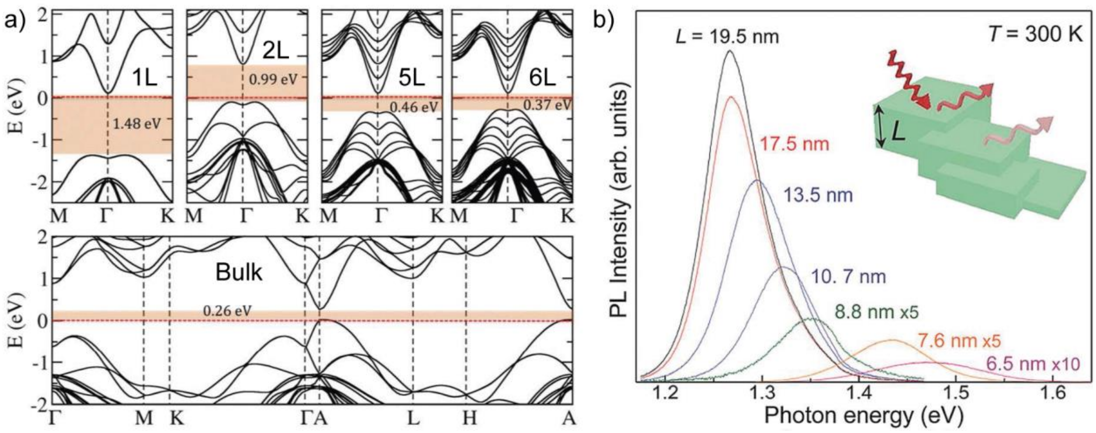

Fig. 1-19. a) Electron band structure of *N*-layer (*N* = 1, 2, 5, 6) and bulk InSe. b) PL spectra of 2D InSe as a function of thickness at room temperature.[245,256]

Initial investigations on InSe systems focused on mechanically exfoliated layers of samples grown using the chemical vapor transport method (**Fig. 1-19b**).[245] Based on the results from DFT and high-field magnet optics, Mudd *et al.* reported a significant smaller electron and exciton effective mass, which is weakly dependent on the layer thickness in few-layer InSe. In general, several studies have shown that typical room temperature mobilities of FETs fabricated using InSe flakes are a few tens of $cm^2V^{-1}s^{-1}$. A detailed list of mobility values is included in **Table 5**. Techniques that by using a bilayer dielectric of poly-(methyl methacrylate) (PMMA)/Al_2O_3 instead of using conventional SiO_2, a room temperature mobility of 1055 $cm^2V^{-1}s^{-1}$ can be achieved, as shown in **Fig. 1-20**.[257] Such back-gate engineering, according to this report, can also lead to InSe based FETs with high current On/Off ratio of 10^8 and strong current saturation over a broad voltage window. Similarly, investigations performed on few-layer InSe encapsulated in hexagonal boron nitride under an inert atmosphere showed carrier mobility of > 10^3 $cm^2V^{-1}s^{-1}$, at room temperature.[258] This article also reported the observation of a fully developed quantum Hall effect.

A large number of investigations also focused on the photoconductive properties of InSe based materials and a typical Au-InSe-Au photodetector and characterizations are shown in **Fig. 1-21a, b, c.**[246] Reports of InSe photoconductors showing very high responsivities of ~10^7 A W^{-1}, λ = 515.6 nm as well as InSe photoconductors showing responsivity of 34.7 mA W^{-1}, λ = 532 nm can be found in the literature.[235,246,259-265] A summary of the parameters, including geometry, sensing wavelength, photoresponsivity and response time, of 2D InSe-based photodetectors have been listed in **Table 6**, among which the photoresponsivity and photodetectivity of InSe photoresponse are superior to those of most other 2D materials, commercial Si and

InGaAs photodetectors.[266]

Table 5 Mobility of 2D InSe-based FETs. h – thickness, V_D – drain voltage, V_G – gate voltage, μ– field effect mobility

Method	Dielec. / d (nm)	h (nm)	V_D (V)	V_G (V)	μ ($cm^2V^{-1}s^{-1}$)	REF.
BT[a]	SiO_2/300	12	10	70	~0.1	260
CVD[a]	PMMA/Al_2O_3 200/50	33	1	7	1055	257
	PMMA/SiO_2 200/300	34	1	40	395	
	Al_2O_3/50	32	1	7	64	
	SiO_2/300	33	1	40	66	
CVD[a]	SiO_2/300	32	1	40	79.5	267
CVD[a]	SiO_2/300	33	1	40	162	259
BT[a]	SiO_2/285	30	2	40	32.6	268
PLD	SiO_2/300	1	1	0	10	262

[a] Mechanically exfoliated from bulk crystals. BT – Bridgman technique, CVD – Chemical vapor deposition, PLD – Pulsed laser deposition

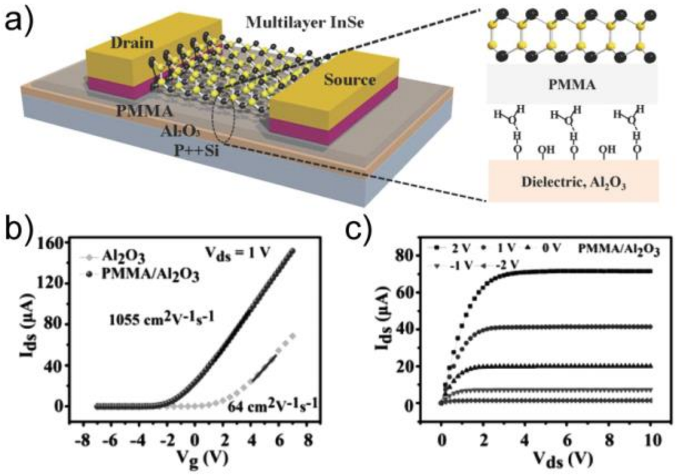

Fig. 1-20. a) The PMMA/Al_2O_3 double layer dielectric 2D InSe FET. b) Transfer and (c) output characterization of multilayer InSe FETs with PMMA/Al_2O_3 dielectric layer.[257]

Table 6 The photoresponsivity and response time of various thin InSe photodetectors with metal-InSe-metal geometry found in literature.

Device geometry	Wavelength	Response time	Responsivity	REF.
Al-InSe-Al	543 nm	87 μs	---	259
Metal-InSe-metal	532 nm	488 μs	34.7 mA W^{-1}	235
Cr/Au-InSe-Cr/Au	450 nm	50 ms	6.9 – 157 A W^{-1}	260
Cr/Au-InSe-Cr/Au	515.6 nm	---	~10^7 A W^{-1}	261
Cr/Au-InSe-Cr/Au	700 nm	5 ms	~10^4 A W^{-1}	262

Au-InSe-Au	370 nm	0.5 s	27 A W^{-1}	246
Ti/Au-InSe-Ti/Au	500 nm	5.63 s	700 A W^{-1}	263
Pt/Au/Pt	325 nm	---	~10^{7} A W^{-1}	264
G-InSe-G	500 nm	120 μs	60 A W^{-1}	263
G-InSe-G	633 nm	1 ms	4000 A W^{-1}	265

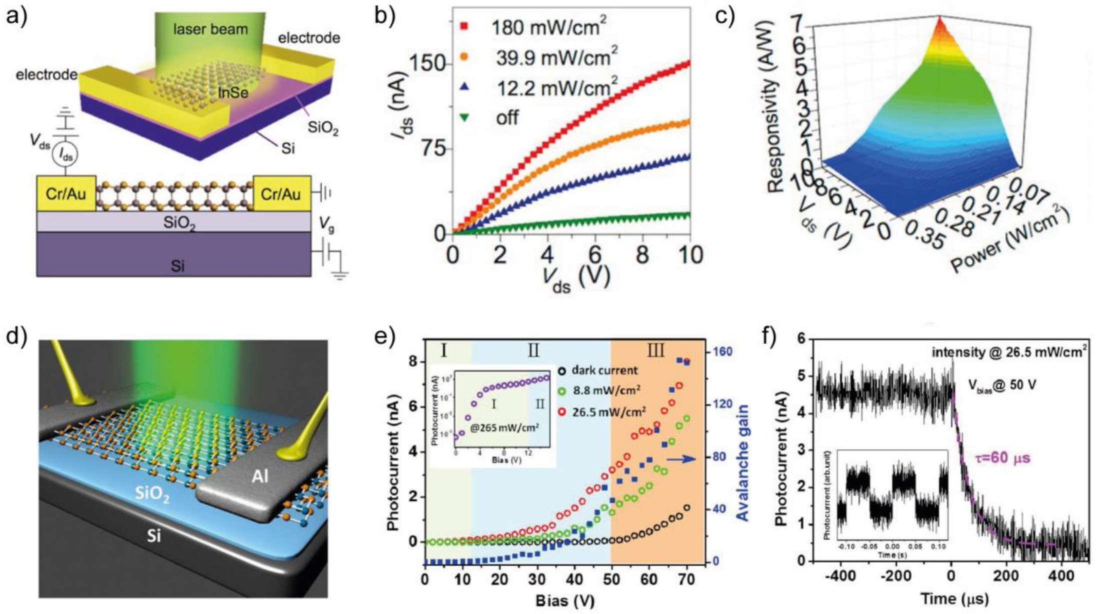

Fig. 1-21. a, b, c) A typical schematic (a), *I*-*V* characteristics (b), and bias-dependent photoresponsivity (c) of few-layer Au-InSe-Au photodetector. d, e, f) Schematics (d), bias-dependent photocurrent (e), and *I*-t curve (f) of Al-InSe-Al photodetector.[246,259]

Actually, for a photodetector, responsivity is not the only factor that needs to be considered because the amplification circuit can be used to improve them. However, the signal-to-noise ratio (S/N) which is related to detectivity, and response time cannot be tuned by using the signal process, which is problematic in practical applications. Lei *et al.* designed and demonstrated an avalanche Al-InSe-Al photodetector (**Fig. 1-21d, e**).[259] By utilizing the avalanche effect, the performances of InSe photodetectors were enhanced largely, with improved photoresponsivity, low dark current and fast response time. An external quantum efficiency of 334%, an ultrafast response time of 60 μs (faster than most reported 2D layered material photodetectors) and a high avalanche gain of 47 were achieved, as shown in **Fig. 1-21f.** The avalanche effect led to photo generated carriers being utilized more efficiently, but the number of photo generated carriers was not enhanced. This study has demonstrated that plasmonic Al disk nanoantennas patterned on the InSe flakes can improve the light absorption, which introduces a large photocurrent. The combination of the avalanche effect and the plasmonic effect can work together and similar strategies can also be used in other 2D material based photodetectors.

Heterostructures based on 2D InSe have been also fabricated. The most studied system is graphene/InSe in which graphene is used as the Schottky barrier free and high conductive electrode. Mudd *et al.* reported planar and vertical vdW graphene/InSe heterostructures, and both responsivities of the InSe-based photodetectors have been significantly enhanced, as shown in **Fig. 1-22a-d**.[265] Especially in the vertical stacks, a photoresponsivity up to 10^5 A W^{-1} at 633 nm illumination has been observed. In another kind of graphene/InSe heterostructures demonstrated by Chen *et al.*,[269] monolayer graphene covers an ultrathin InSe flake. Then, source/drain electrodes are deposited on graphene, as illustrated in **Fig. 1-22e**. The top graphene can supply a tight cover making ultrathin InSe flake stable as well as plays an important role in transporting photo-excited electrons. **Fig. 1-22f** gives the corresponding band structure diagram of a graphene/InSe heterostructure at different gate voltages. Compared to separate InSe-based photodetectors, the graphene/InSe photodetector exhibits a much better performance in photoresponsivity and external quantum efficiency.

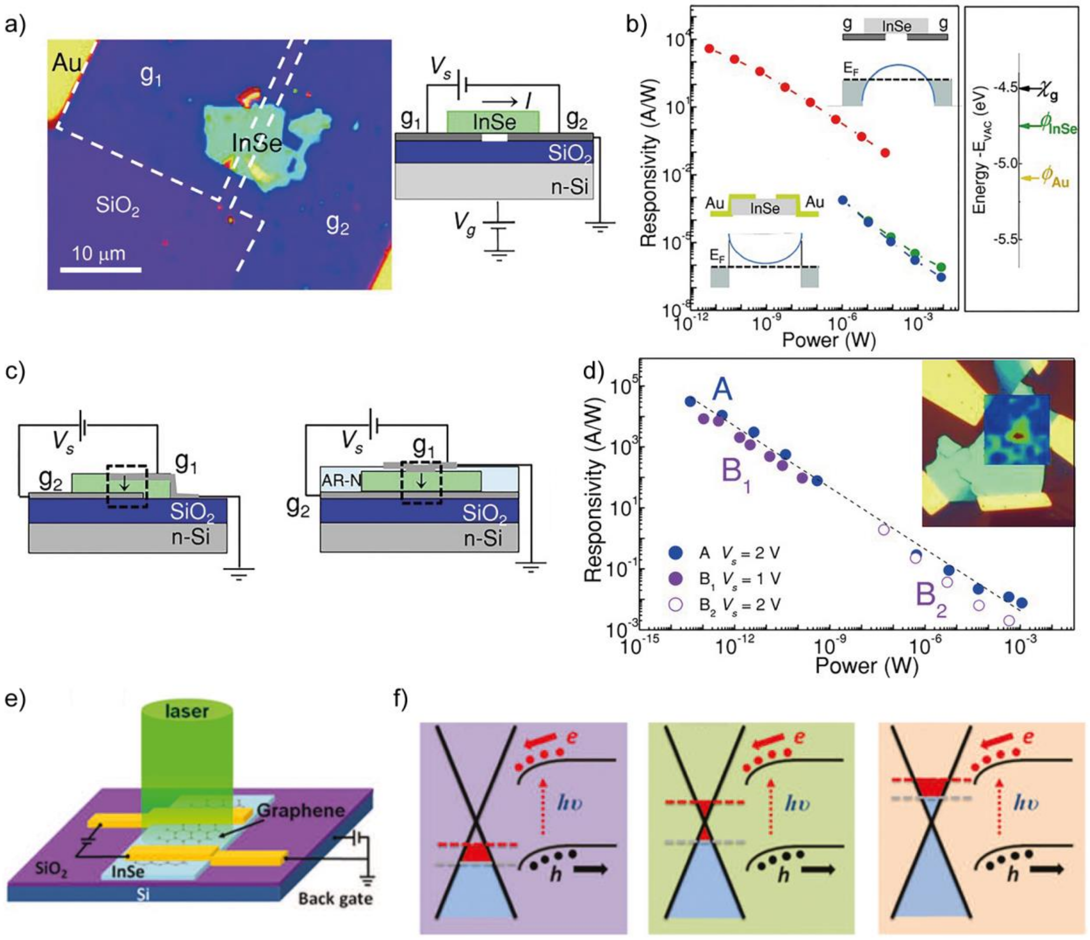

Fig. 1-22. a, b) Schematic representation of planar van der Waals graphene/InSe heterostructures (a), Photoresponsivity, band alignment of graphene/InSe/graphene and Au/InSe/Au heterostructures, as well as their work functions (b). c, d) Schematic structures of two kinds of vertical graphene/InSe/graphene devices (c) and the corresponding photoresponsivity (d). e, f) Photodetectors based on graphene/InSe heterostructures. (a) Schematic diagram and optical image of the device. (b) The corresponding band structure diagram of a graphene/InSe heterostructure at different gate voltages.[265,269]

Besides the superior electrical and optoelectronic properties, it should be noted that one of the most important properties of 2D GaSe and InSe is the nonlinear optical properties due to the absence of the inversion symmetric center. For 2D GaSe, recently, Karvonen *et al.* reported nonlinear optical properties of SHG and third harmonic generation (THG) in multilayer GaSe crystals with thickness more than seven layers.[270] W Jie *et al.* also studied the nonlinear optical properties of atomically thin GaSe flakes with thickness from bilayer to multilayer by using fs laser with a wavelength of about 800 nm.[271] It should be mentioned that we can get the emission from bilayer flakes. This suggest that SHG can be produced in both odd and even number layers, different from the SHG in 2D TMDCs and BN which is dependent on the parity of the layer number. Very recently, Zhou *et al.* reported strong SHG in CVD-grown monolayer GaSe under nonresonant excitation and emission condition.[272] **Fig. 1-23a** shows SHG intensity from monolayer GaSe and MoS_2 under the same illumination condition, the SHG intensity of GaSe is about 1-2 order of magnitude higher than that from MoS_2. Interestingly, Qiaoyan Hao *et al.* recently reported the optimal SHG intensity from multilayer pure ε-InSe and alloys is even superior to that of ε-GaSe with the same thickness at the excitation wavelength from 800 nm to 1200 nm.[273] Similarly, Jiadong Zhou *et al.* also discovered that the SHG signal from monolayer InSe shows large optical second order susceptibility is three times of largest value reported for monolayer GaSe, which is the strongest among all the monolayer 2D crystals (**Fig. 1-23b, c**).[244]

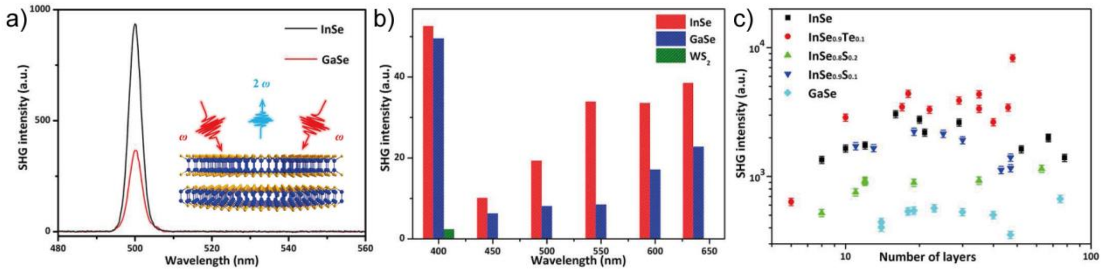

Fig. 1-23. Comparison of SHG intensity of 2D GaSe, InSe and TMDCs (*e.g.*, WS_2).[273]

1.4 Motivations

As mentioned above, 2D GaSe and InSe possess superior electrical, optical and optoelectronic properties due to their unique electron band structures and strong light-matter interactions, which make them the promising candidates for photo-sensing applications. However, several fundamental questions, which motivate the works in this thesis, still remain to be answered and as following listed:

1) Both 2D GaSe and InSe crystals are known to show poor environmental stability. But how the materials properties and optoelectronic devices performance evolve during the ambient degradation processes still is an open question. Also the fabrication of long-term stable optoelectronic devices based on 2D GaSe and InSe is an open challenge Thus, the degradation mechanism of 2D GaSe and self-passivation effect of InSe in ambient conditions will be investigated in chapter 3.
2) Typically, the 2D based optoelectronic devices consist on two main components: 1) the active channel parts for sensing and 2) the electrodes for carrier collection. Both components determine the device performance. However, in most of the cases, the connection between 2D semiconductors and 3D metals is usually realized using conventional metal deposition techniques. This fabrication process can introduce defects in the 2D crystal lattice or at the M-S interfaces, which can degrade the transport characteristics and induce Fermi level pinning, masking the intrinsic properties of the 2D semiconductors. In chapter 4, by taking the example of 2D InSe and using deterministic transfer technique, the role of the van der Waals contact between 2D InSe and metals and graphite will be discussed, and the transport properties of these heterostructures will be analyzed.
3) Strain engineering, the modification of the optical, magnetic, electrical, and optoelectronic properties of a given material by applying an external mechanical deformation to its crystal lattice, is establishing itself as one of the most prospective strategies to controllably modify the properties of two-dimensional (2D) materials. Although the DFT calculations predicted that the 2D InSe possesses superior mechanical properties and strain tunability, their experimental realizations are still lacking. The mechanical property, e.g., Young’s modulus, will be thus characterized and the flexible optoelectronic devices based on 2D InSe will be introduced in chapter 5.

Moreover, the experimental method section, as a complementary part, including the growth and characterization of bulk GaSe and InSe crystals, 2D GaSe and InSe preparation and characterization processes, and optoelectronic devices fabrication and testing tools will be provided in chapter 2. Finally, a brief summary will be given in the conclusion and outlook part as chapter 6.

The research field of 2D materials is novel, active and with rapid development, in which most of the investigations focus on the explorations of novel materials, interesting phenomena and theories, and advanced applications. However, the gap between laboratory level researches and practical applications has not been bridged due to the insufficient fundamental investigations. This thesis belongs to applied basic research field, and several points are listed as follows. Firstly, two kinds of typical environmental stability of 2D semiconductors, *e.g.*, degradation and self-passivation, have been thoroughly discussed, which helps to establish the correlations between materials variation and devices performance during the environmental aging process for the first time. Secondly, the investigations of transport properties of van der Waals engineered contact can enrich the horizons of novel optoelectronic applications. Finally, the explorations of straintronics applications suggest 2D InSe is one of the most promising candidates for flexible sensing.

2

EXPERIMENTAL METHODS

Due to the ultrathin nature and relatively large lateral dimensions of 2D materials, the investigations of 2D materials require both conventional characterization tools and specially designed testing systems. Thus, in this chapter, the synthesis and basic characterization methods of single crystal GaSe and InSe bulks, used for 2D nanosheets fabrication, will be firstly introduced. Then the optical microscopy (OM), atomic force microscopy (AFM), and Raman Spectroscopy techniques will be used to characterize the mechanically exfoliated 2D GaSe and InSe. Finally, a home-made deterministic transfer setup, a specially designed optoelectronic testing system, and the setup employed for scanning photocurrent measurements for 2D material-based devices fabrication and characterization will be discussed.

2.1 Synthesis and characterizations of single-crystal GaSe and InSe bulks

In this section, both GaSe and InSe bulks have been synthesized using a two-step Bridgman method. And then, the crystal structure, chemical composition homogeneity, macro- and micro- surface morphology, optical and electrical properties of GaSe and InSe single crystals are subsequently characterized using a set of test techniques, which include X-ray diffraction (XRD) and transmission electron microscopy (TEM), scanning electron microscopy (SEM), infrared-transmission spectroscopy (IR), absorption spectroscopy, photoluminescence (PL), and Hall effect measurement. Note that this section is mainly based on the published paper “High-quality GaSe single crystal grown by the Bridgman method” in Materials and the submitted manuscript “ε-InSe single crystals grown by a Horizontal Gradient Freeze method” both where I am one of the contributors.[274] I summarize these results here since they are relevant results for the rest parts of this thesis.

2.1.1 GaSe single crystals growth

The GaSe single crystals are grown through a two-step method. Firstly, the melting Ga and Se were mixed completely and to fabricate polycrystalline GaSe bulks. And then, the crucible that contains polycrystalline GaSe was transferred into vertical Bridgman crystal growth furnace for single crystals fabrication.

- Synthesis of polycrystalline GaSe

To prevent adhesions between the Ga-Se melting compound and quartz under high temperature conditions, a quartz ampoule coated with a carbon film on the inner surface was used as the polycrystalline GaSe growth container. High-purity Ga (6N, 99.9999%) and Se (6N, 99.9999%) granules from Emei Corp., Ltd. (Emei, China) were selected as the raw materials. Firstly, Gallium was baked at 673 K for 4 h under high vacuum (~10^{-5} Pa) to remove the surface oxide layer. Then, Ga and Se were mixed with a stoichiometric ratio and sealed in the quartz ampoule at the vacuum level of 10^{-5} Pa. A single-temperature zone rocking furnace shown in **Fig. 2-1a** was used for this synthesis process.

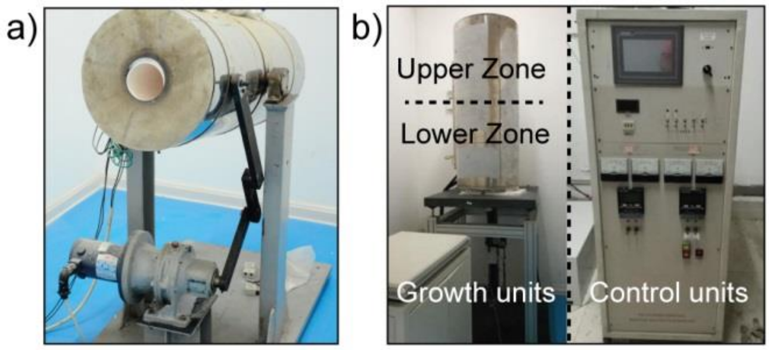

Fig. 2-1 Single-temperature zone rocking furnace (a) and vertical Bridgman crystal growth system (b) using for growth of single-crystal GaSe and InSe bulks. The vertical Bridgman crystal growth system consisted of a growth unit (left panel) and a control unit (right panel).

- Growth of single-crystalline GaSe

A two-temperature zone vertical Bridgman crystal growth system (**Fig. 2-1b**) was used for GaSe single crystals growth. A boron nitride (BN) crucible with an inner diameter of 22 mm was used to accommodate polycrystalline GaSe and thus later for the GaSe single crystals growth. The upper and lower zones (highlighted in **Fig. 2-1b**, growth unites) were set with temperature of 1293 K and 1173 K, respectively, and the temperature gradient was 10 K/cm. The growth rate was set to be 0.5 mm/h.

2.1.2 Characterizations of GaSe bulks

- Crystalline structure and composition

A GaSe ingot with diameter of 22 mm and length of 20 mm was obtained, the optical picture is shown in **Fig. 2-2a**. The crystal is transparent and shows rufous color under white light illumination. **Fig. 2-2b** shows the sample cleaved along the (001) layer direction from as-grown ingots without polishing or additional treatment of the surface. The twin-boundary free surface indicates that there is only one large grain along the cleavage plane, though several voids can be found at the surface. **Fig. 2-2c** shows a GaSe single crystal wafer with the dimension of 7 mm × 10 mm × 1 mm, and it can be easily exfoliated thanks to the weak interlayer van der Waals interaction. The phase and lattice structure of the as-grown GaSe crystals were analyzed by X-ray diffraction technique based on an Empyrean X-ray diffraction machine (PANalytical, X'Pert Pro, Eindhoven, the Netherlands). **Fig. 2-2d** shows the X-ray diffraction pattern of powder sample formed by grinding the as-grown GaSe crystals. The good matching agreement between the experimental results and the theoretical curve of

GaSe (JCPDS: 37-0931) indicates that the obtained single crystal GaSe has a hexagonal lattice with cell parameters a = b = 3.749 Å, and c = 15.907 Å, which corresponds to space group D^1_{3h} and ε-GaSe, as mentioned in paragraph 1.3 in chapter 1. Generally, the symmetry of the X-ray rocking curve is directly related the structural uniformity of the crystals. **Fig. 2-2e** shows the X-ray rocking curve of the (004) lattice plane from the as-grown GaSe crystals. The peak has a symmetric shape with a FWHM (full-width-at-half-maximum) of ~46 arcs, which is the smallest values ever reported for GaSe crystals (0.15 ° in [273],[275] split peaks in [274],[276] 0.07 ° in [275],[277] and 0.04 ° in [276][278]). The composition distributions from the tip to the tail of GaSe ingot also have been analyzed by an electro-probe microanalyzer (EPMA; JXA-8100, JEOL, Tokyo, Japan), as shown in **Table 7**. The Ga/Se ratio of both parts across the ingot are near 1:1 and it is more close to stoichiometric ratio than the previously reported GaSe single crystals,[278,279] which indicates a good crystalline homogeneity. Slight Ga rich in composition is probably resulted from the loss of Se during synthesis and growth process due to its high vapor pressure. All above results indicated the as-grown crystals have a good crystalline quality.

Table 7 The composition measured by EPMA.

Sample	Se (Atom %)	Ga (Atom %)
1	49.5613	50.4387
2	49.5203	50.4797
3	49.6189	50.3811
4	49.5266	50.4734

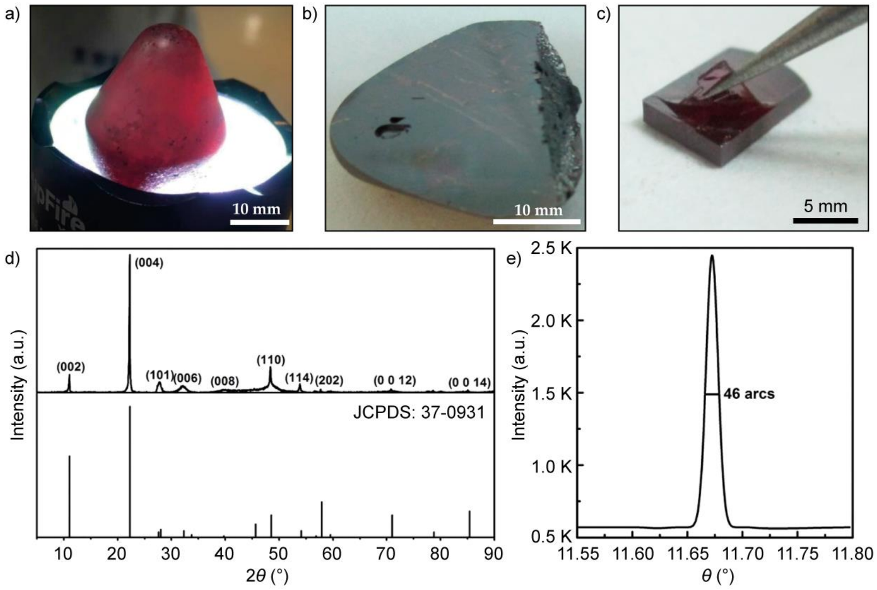

Fig. 2-2 The single crystalline GaSe and structure characterizations. a, b, c) Optical pictures of single crystalline GaSe ingot (a), cleaved sample along the (001) plane (b),

the mechanically exfoliated GaSe wafer (c). d) The X-ray diffraction pattern of powder GaSe sample and the PDF database of ε-GaSe (JCPDS: 37-0931). e) The rocking curve of (004) face from GaSe single crystals.

- Optical measurements

The infrared-transmission spectrum recorded by a Nicolet Nexus Fourier Transform Infrared Spectrometer (Nexus 670, Nicolet, Waltham, MA, USA) of as-grown GaSe single crystals is shown in **Fig. 2-3a**, and a record high infrared transmittance of ~66% over the all range from 500 cm^{-1} to 4000 cm^{-1} has been determined, which is the highest value among the reports for GaSe crystals grown by the Bridgman method in the literature.[275-278] And the absorption coefficient was calculated to be an ultralow value of 0.18 – 0.2 cm^{-1} in the range of 0.9 – 1.4 μm, indicating the superior optical quality of GaSe sample. The room temperature optical band gap of GaSe crystals was measured using a UV-3150 ultraviolet visible/near-infrared spectrometer (Shimadzu, Kyoto, Japan), and the ultraviolet-visible-near-IR spectrum of GaSe over the wavelength range from 200 nm to 2600 nm is shown in **Fig. 2-3b**, from which the band gap is determined to be about 2.005 eV. The photoluminescence (PL) spectrum was measured using an argon ion laser with the wavelength of 488 nm and the luminescence signals were recorded with the spectrometer of TRIAX 550 (Jobin Yvon, Paris, France). **Fig. 2-3c** shows the photoluminescence (PL) spectrum recorded at 9.2 K of the as-grown GaSe crystals. A dominant peak at 2.1046 eV can be attributed to the free exciton recombination. The strong and narrow peak with FWHM of 11 meV indicates excellent crystalline quality.

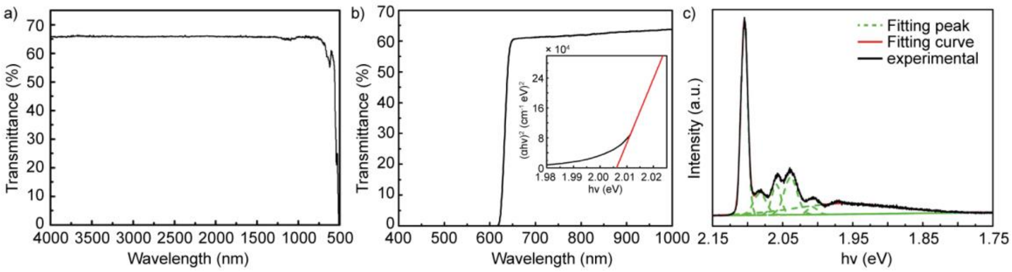

Fig. 2-3 Typical IR transmittance spectrum (a), ultraviolet-visible-near IR spectrum (b), and low-temperature (9.2 K) photoluminescence recoded from GaSe sample.

- Electrical measurements

Table 8 shows the Hall measurements of three GaSe samples taken from the tip to the tail from the GaSe ingots. All samples displayed p-type conductivity with a hole concentration of ~10^{15} cm^{-3}, and the mobility has been determined to be ~20 cm^{2}V^{-1}s^{-1}. The p-type conductivity may be introduced by the gallium vacancies (V_{Ga}), interstitial selenium atoms (Se_I), and gallium atoms on selenium sites (Ga_{Se}).[280] Since Ga atoms are slightly richer than Se atoms in as-grown GaSe crystals according to the composition analysis, which probably promotes the existence of defects Ga_{Se} in GaSe, thus results in a p-type conductivity.

Table 8 The transport properties of GaSe single crystals (*T* = 295 K).

Sample	Conduction type	Carrier concentration (cm^{-3})	Resistivity ($\Omega\cdot cm$)	Mobility ($cm^2V^{-1}s^{-1}$)
1	p	2.9894×10^{15}	1.1295×10^{2}	18.484
2	p	1.4701×10^{15}	2.3322×10^{2}	18.204
3	p	1.6830×10^{15}	1.6220×10^{2}	23.492

2.1.3 InSe single crystals growth

The InSe single crystals also are grown through a two-step method, including polycrystalline InSe synthesis and single crystalline InSe growth. However, due to the high chemical activity of In element and the complex In-Se phase diagram, the fabrication of high-quality InSe single crystals requires both high-purity synthesis conditions and accurate growth parameters setting. Thus, for the first step, a physical vapor transport technique was employed to reach a high-purity and homogeneous polycrystalline InSe synthesis. And then, the single crystalline InSe are grown by vertical Bridgman technique with good parameters setting.

- Synthesis of polycrystalline InSe

A physical vapor transport (PVT) setup used for polycrystalline InSe synthesis has been shown in **Fig. 2-4a**. And **Fig. 2-4b** shows the schematics of the synthesis process using PVT techniques. To prevent the chemical reaction and adhesions between melting In and quartz, two Pyrolytic Boron Nitride (PBN) crucibles, named A and B, are fixed with a distance of 600 mm at the both ends of a quartz ampoule and are used as reaction containers. And then, high-purity Se (6N, 99.9999%) and In (6N, 99.9999%) granules from Emei Corp., Ltd. (Emei, China) were selected as the raw materials, which are respectively placed in A and B with a sub-stoichiometric ratio of Se : In = 48.5 : 51.5. Subsequently, the quartz ampoule was sealed at the vacuum level of 10^{-5} Pa. The temperature of B crucible was firstly increased up to 890 ℃ to obtain In melt, and later heating the A crucible up to 690 ℃. Keep the insulation for 24 hours until Se vapor and In melt have fully contacted, diffused, mixed and reacted. Then, keeping the temperature of crucible A fixed and slowly reducing the temperature of crucible B. The crystallization of InSe bulks begins at 630 ℃ and ends at 550 ℃, and final polycrystalline InSe will be collected in crucible B.

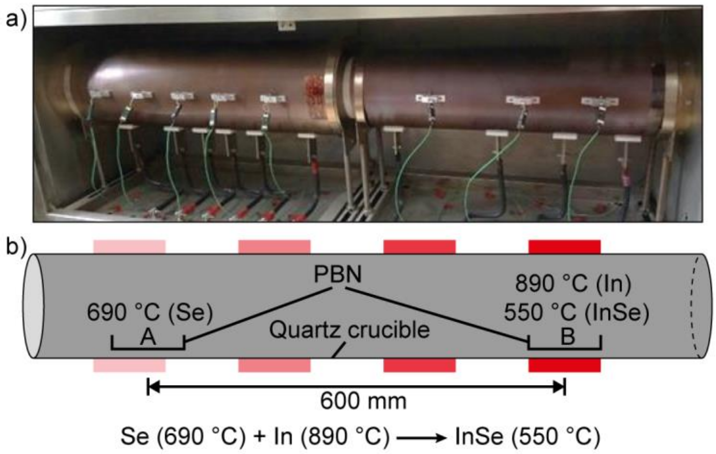

Fig. 2-4 PVT setup (a) and schematics of polycrystalline InSe synthesis process (b).

- Growth of single-crystalline InSe

The single crystalline InSe growth is a similar process to that of GaSe. A quartz ampoule with an inner diameter of 14 mm was used for the InSe single crystals growth based on the PVT synthesized polycrystalline InSe bulks. The upper and lower zones (highlighted in **Fig. 2-1b**, growth unites) were set with temperature of 720 ℃ and 490 ℃, thus a temperature gradient of 18 K/cm was obtained. The growth rate was set to be 0.3 mm/h.

2.1.4 Characterizations of InSe single crystals

- InSe single crystals

The image of the InSe crystal ingot with diameter of 14 mm and length of ~50 mm has been shown in **Fig. 2-5a**. There is no crack, and few grain boundaries can be easily observed from the ingot surface, which indicates that the whole crystal ingot consists of several large single crystalline InSe grains. **Fig. 2-5b** shows a few InSe single crystal wafer obtained from the InSe ingot. In **Fig. 2-5c**, an image of freshly cleaved surface of one of the InSe wafers was recorded by scanning electron microscope (SEM, Zeiss Supra 55). Both the polishing surface and clear steps indicate the InSe crystals can be easily exfoliated thanks to its layered nature, which further confirms the high crystallinity of InSe. Panel d shows the result of composition analysis by energy dispersive X-ray Spectroscopy (EDX) and the ratio of In and Se is near to 1:1, which indicates a good homogeneity of the elements distribution in the studied samples. Both the sub-stoichiometric ratio between Se and In and the loss of

Se during the growth process may lead to the slightly In rich in the composition.

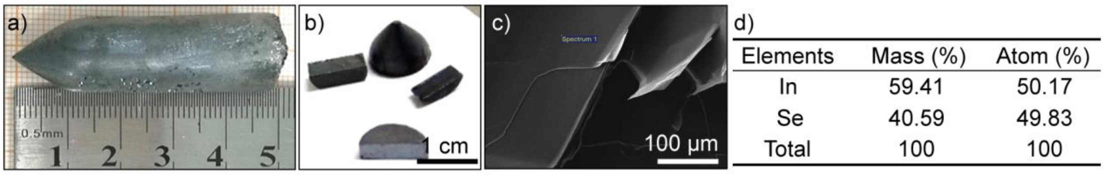

Elements	Mass (%)	Atom (%)
In	59.41	50.17
Se	40.59	49.83
Total	100	100

Fig. 2-5 InSe crystals grown by vertical Bridgman technique. InSe Crystal ingot (a), InSe single crystalline wafers (b), image of cleaved InSe surface taken by SEM (c), and corresponding elements composition (d).

- The identification of InSe phase

As introduced in 1.3 (*i.e.*, the advances of 2D GaSe and InSe), there are three basic polytypes including *β*-InSe, *ε*-InSe, and *γ*-InSe, which differ in the symmetry and structure of the crystal lattice, and present totally different nonlinear optical properties. Thus it is important to determine the phase structure for the studied InSe. **Fig. 2-6a** shows the X-ray diffraction (PANalytical, X'Pert Pro, Eindhoven, the Netherlands) pattern from the as-grown InSe crystal powder samples. The good matching agreement between the experimental results and the theoretical pattern of InSe (JCPDS: 34-1341) indicates that the obtained single crystalline InSe has a hexagonal lattice with cell parameters a = b= 4.005 Å, and c = 16.96 Å.[281] To further determine the phase of InSe crystals, the transmission electron microscope (TEM, FEI Talos F200X) technique has been used, and a picture taken from the perpendicular direction of a thin InSe flake on the TEM grid has been shown in left inset panel in **Fig. 2-6b**. And thus, a representative selected area electron diffraction (SAED) pattern of InSe crystal can be obtained, as shown in **Fig. 2-6b**. Both the arrangement and intensity of the diffraction spots are highly consistent with the theoretically calculated electron diffraction pattern based on *ε*- or *β*-InSe crystal lattices (right inset panel in **Fig. 2-6b**).[273,282] Based on the results of XRD and TEM analysis, the InSe crystals can be attributed to *ε*- or *β*- phase stacking blocks. Then Raman spectroscopy and infrared (IR) adsorption spectroscopy were used to identify the stacking phase of InSe crystals since both they are sensitive to the crystal lattice vibrations. The Raman spectrum and IR adsorption spectrum acquired from InSe crystal samples are shown in **Fig. 2-6c** and **d**, respectively. Three Raman active in-plane modes A_1'(1), A_2''(1) and A_2'(1) located at ~113 cm^{-1}, ~198 cm^{-1} and ~226 cm^{-1}, and one out-of-plane E''(2) located at ~176 cm^{-1} are observed under a 532 nm laser excitation. While there is only one peak centered at ~200 cm^{-1} observed in IR absorption spectrum, which is also related to the vibration mode A_2''(1).[282-284] The observation of both Raman and IR active peak centered at ~200 cm^{-1} appeared on A_2''(1) mode is consistent with hexagonal crystal structure of ultrathin InSe with ε stacking sequence.

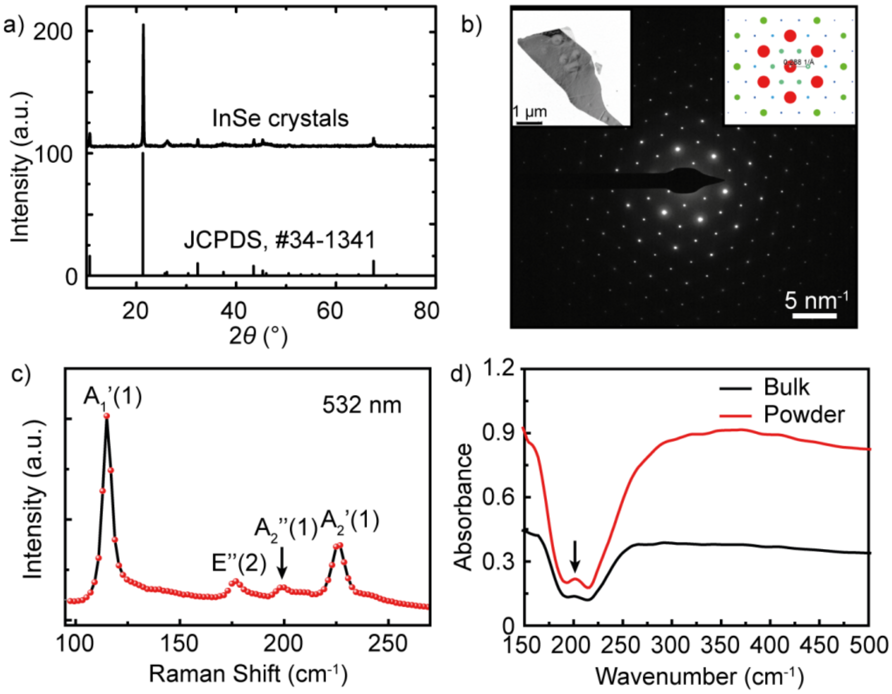

Fig. 2-6 Identification of InSe phase. a) The X-ray diffraction pattern of powder InSe sample and the PDF database of ε- or β-InSe (JCPDS: 34-1341). b) Selected area electron diffraction pattern of InSe flake. A InSe flake on TEM grid and theoretically calculated electron diffraction pattern of ε- or β-InSe are shown in left and right inset panels, respectively. c, d) Raman spectrum (c), and IR absorption spectrum (d) of InSe crystals.

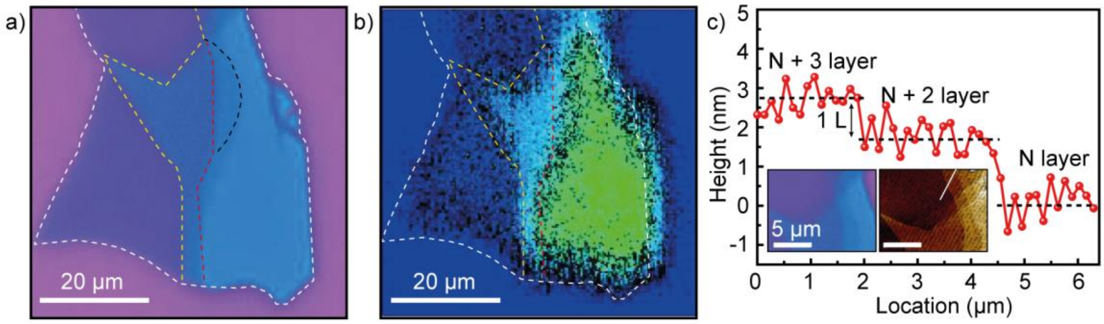

Fig. 2-7 SHG mapping of InSe with different layers. a, b) optical picture (a) and SHG generation distribution (b) of a InSe flake with various thicknesses on 300 nm SiO_2/Si substrate. c) A step with height of 1L (~0.8 nm) measured by AFM. The optical picture and AFM characterization of selected area are both shown by the inset panels.

Then the second harmonic generation (SHG) characterization performed on the studied InSe crystals since the ε-InSe has different thickness-dependent SHG behavior from β-InSe. For even-layer β-InSe, it belongs to the D^4_{6h} space group, the existence of an invert center would suppress the SHG signal, while in odd-layer β-InSe the symmetry would be broken, then the SHG signal would appear due to the lack of invert center in the crystals.[285] However, ε-InSe, which belongs to the D^{1}_{3h} space group, has no invert center in any layers, thus, there is no thickness limitation for SHG in ε-InSe.[286] Then a SiO_2/Si substrate based InSe flake with various thick areas has been used for SHG mapping analysis. And the optical picture and the SHG signal as a function of thickness on the selected InSe flake are shown in **Fig. 2-7a** and **b**, respectively. In general, the SHG signal can be collected throughout the whole flake regardless of the thickness. More importantly, both (N + 2) and (N + 3) layers thick InSe have the SHG emission as shown in the selected area of the inset panel in **Fig. 2-7c**. A one-layer high step was confirmed by atomic force microscope (AFM, Dimension Fast Scan and Dimension Icon, Bruker) in **Fig. 2-7c**. SHG both can be observed on odd- and even-layer InSe sample indicates the studied InSe has a ε phase.

- Optical characterization

The room temperature optical band gap of InSe crystals was determined using a UV-3150 ultraviolet visible/near-infrared spectrometer (Shimadzu, Kyoto, Japan), and the ultraviolet-visible-near-IR spectrum of GaSe over the wavelength range from 200 nm to 2600 nm is shown in **Fig. 2-8a**, from which the band gap is determined to be about 1.26 eV. The photoluminescence (PL) spectrum was measured using an argon ion laser with the wavelength of 488 nm and the luminescence signals were recorded with the spectrometer of TRIAX 550 (Jobin Yvon, Paris, France). **Fig. 2-8b** shows the photoluminescence (PL) spectrum recorded at 4.2 K of the single crystalline InSe sample, which can be fitted to 5 isolated peaks, centered at 1.336 eV (P1), 1.332 eV (P2), 1.329 eV (P3), 1.327 eV (P4), and 1.324 eV (P5), respectively. The P1 at 1.336 eV with a FWHM of ~3 meV can be attributed to the free exciton recombination, which indicates excellent crystalline quality.[287-290]

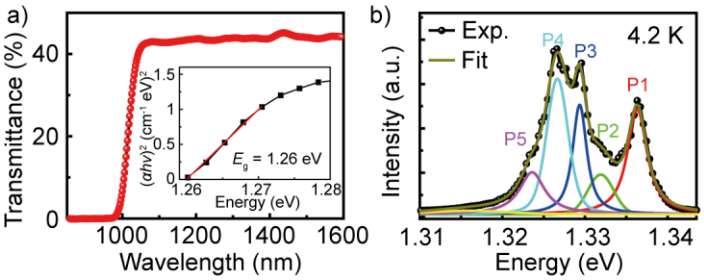

Fig. 2-8 Ultraviolet-visible-near IR spectrum (a), and low-temperature (4.2 K) photoluminescence (b) recoded from InSe crystals.

- Electrical measurements

Table 9 The transport properties of InSe single crystals (T = 295 K).

Sample	Conduction type	Carrier concentration (cm^{-3})	Resistivity ($\Omega \cdot cm$)	Mobility ($cm^2V^{-1}s^{-1}$)
1	n	7.84×10^{13}	134.4	591.97
2	n	4.63×10^{14}	20.4	658.00
3	n	9.72×10^{14}	7.3	870.21

Table 9 shows the Hall measurements of three InSe samples taken from the tip to the tail from the InSe ingots. All samples displayed n-type conductivity with electron concentration level of ~10^{14} cm^{-3}, and the mobility has been determined to be ~590 to ~870 $cm^2V^{-1}s^{-1}$, which is higher than the mobility value (~500 $cm^2V^{-1}s^{-1}$) reported in the literature.[291,292]

2.2 2D GaSe and InSe fabrication and optical identification

2.2.1 2D GaSe and InSe fabrication

Based on the high-quality single crystalline GaSe and InSe grown in Northwestern Polytechincal University by Bridgman method, 2D GaSe and InSe materials have been fabricated both in Institutos Madrileños de Estudios Avanzados (IMDEA) Nanoscience and Instituto de Ciencia de Materiales de Madrid (ICMM) in Madrid (Spain) using mechanical exfoliation method. The typical fabrication processes are shown in **Fig. 2-9** and described as follows: Firstly, a bulk GaSe or InSe has been deposited onto the sticky surface of Nitto tape (Nitto Denko® SPV 224). And then, keep folding and separating the Nitto tape until the GaSe or InSe thin film are distributed over the entire surface. Subsequently, a commercially available polydimethylsiloxane (PDMS) supplied by Gel-Pak (WF 4x Gel-Film) are used for transferring some of the flakes onto the PDMS by gently pressing the tape against the stamp and peeling off slowly. Finally, 2D GaSe or InSe can be deposited on the Gel-Pak film.

Then an optical microscope (Motic® BA310 MET-T, **Fig. 2-10a**) with transmission mode is used for 2D flake inspection. **Fig. 2-10b** shows a picture of general morphology of the Gel-Film surface after depositing thin InSe (GaSe) flakes by splicing the panels that are recorded with a 10X objective while changing the manual X-Y stage. One can qualitatively judge the thickness and uniformity of InSe (GaSe) flakes directly from the observed color and the target flake can be then selected. In **Fig. 2-10c-e**, three panels of a selected InSe flake recorded by the objectives with 10X, 20X, and 50X have been shown.

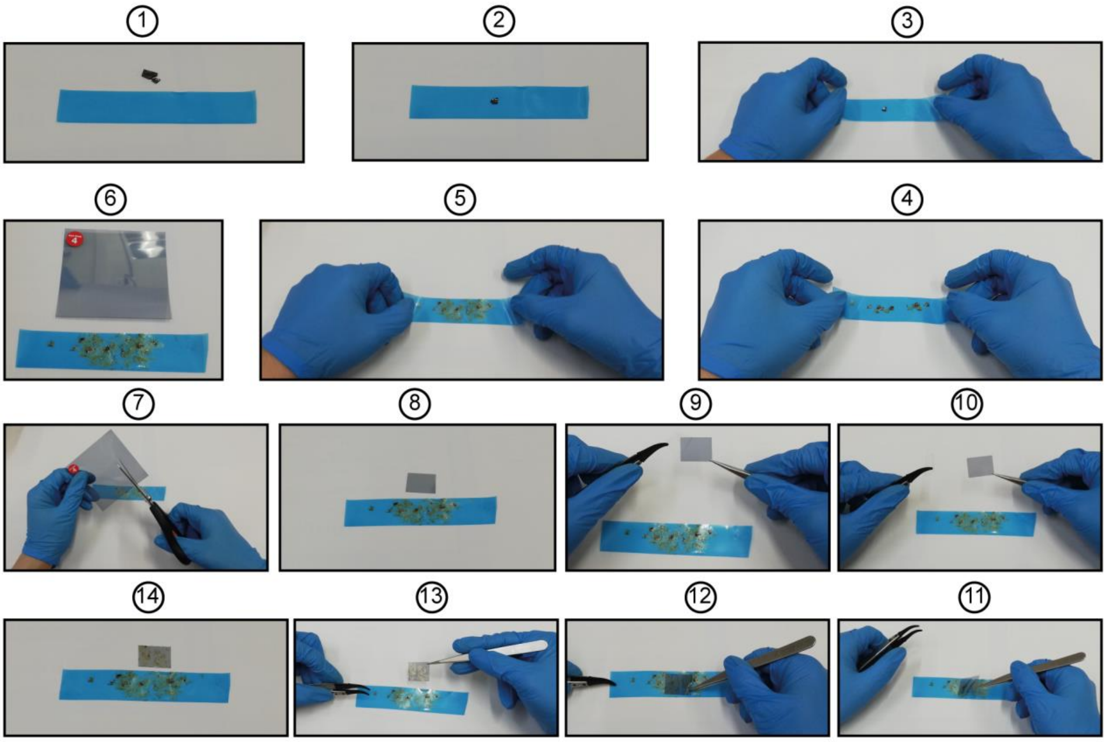

Fig. 2-9 An illustrative procedure of the Nitto-tape and Gel-film based micromechanical cleavage of GaSe and InSe.

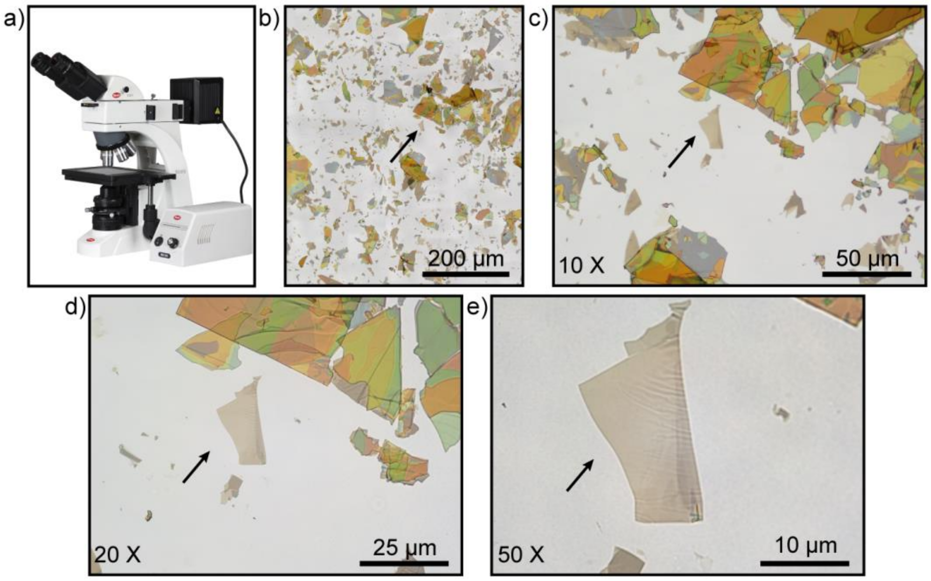

Fig. 2-10 a) Optical microscope used for 2D GaSe and InSe flakes inspection. b-e) Search of an InSe flake on PDMS substrate under transmission mode scanning with 10X objective (b), zooming in with 10X (c), 20X (d), and 50X (e) objectives, respectively.

2.2.2 Thickness identification by optical methods

The sensitivity of optical properties of 2D flakes on their thickness can be utilized to identify the layer number of them once the relation between spectral parameters of optical properties and their layer number is established. The thickness of 2D materials is a serial of discrete value, which indicates the thickness of an *N*-layer 2D flake is *N* times that of monolayer flake. In principle, once layer number of the 2D flakes is identified by optical techniques, its thickness is thus determined. In fact, atomic force microscopy (AFM) has been widely used to measure the thickness of 2D flakes. The tapping mode is usually utilized to minimize sample damage. However, on the one hand, AFM technique is time-consuming and not suitable for a rapid measurement for selected spots over a large area.[293] On the other hand, AFM cannot also be used for thickness determination of suspended samples. Furthermore, the different interactions of the AFM tip with the flake and substrate can lead to large thickness discrepancy when testing ultrathin flakes and introduce artifacts in the measurement.[245,294-298] Thus, in this thesis, four different optical microscopy methods, as fast and non-destructive methods, that are used to estimate the thickness of InSe flakes deposited on different substrate have been summarized. Note that this section is mainly based on the accepted manuscript in Advanced Photonics Research “Thickness identification of thin InSe by optical microscopy methods” where I am the first author.

- Optical transmission

Fig. 2-11a shows transmission mode optical images of two InSe flakes that have been deposited onto the Gel-film substrate recorded using an optical microscope equipped with a color CMOS digital camera. In the transmission mode images the regions covered with InSe flakes are darker as the InSe flakes absorb part of the incoming light. The intensity on the InSe flakes depends monotonically on their thickness. Actually, the optical images are composed of three separate color channels which give information of the light transmitted in the red, green and blue regions of electromagnetic spectrum. The transmittance (*T*) at a given position of the image can be calculated, for each channel, by dividing the intensity by the average intensity of the bare substrate. **Fig. 2-11b** shows the line profiles of 1-*T* versus the positions (indicated by the solid lines with arrows in panel a), extracted from the blue channel intensity of the images. The line profiles reach lowest values (0 percent) in the bare Gel-film regions. In the flake regions, the values of 1-*T* tend to increase upon the thickness growth of the thin InSe. The 1-*T* value allows us to quantitatively determine the thickness of thin InSe flakes. Optical pictures of tens of different InSe flakes were recorded and then the transmittance value (taken from the blue channel images) of each flake was extracted. In order to measure their thickness, all the InSe flakes were subsequently deposited onto 270 nm SiO_2/Si substrates with a dry-transfer method, and an AFM was employed to determine their thicknesses in dynamic mode. The data collected from 18 different thickness regions in thin InSe flakes used to correlate the 1-*T* values to their height measured with AFM have been presented in **Fig. 2-11c** (the top x-axis indicates the InSe thickness). From the plot it is evident that the data, in the thickness range experimentally probed, follow a linear trend and a linear regression has been used to fit them. Thus, a slope of 1.4 ± 0.1 %/nm and an offset of around 5 nm of flake thickness can be determined. Note that when testing an ultrathin flake with AFM, the offset between 2D flakes and substrate can be as large as several nanometers, which can be explained by the different interactions of the AFM tip with the InSe flake and SiO_2/Si substrate as well as the adsorbates on the InSe surface and interfaces.[294-297,299] To further demonstrate the easiness of using this calibration to determine the thickness of thin InSe, the number of layers of the investigated InSe flake in **Fig. 2-11a** has been marked in left axis of panel b, where assuming a value 0.8 nm for a InSe single layer. It is worth to note that this method also can be used for the thickness determination of freely-suspended InSe samples.

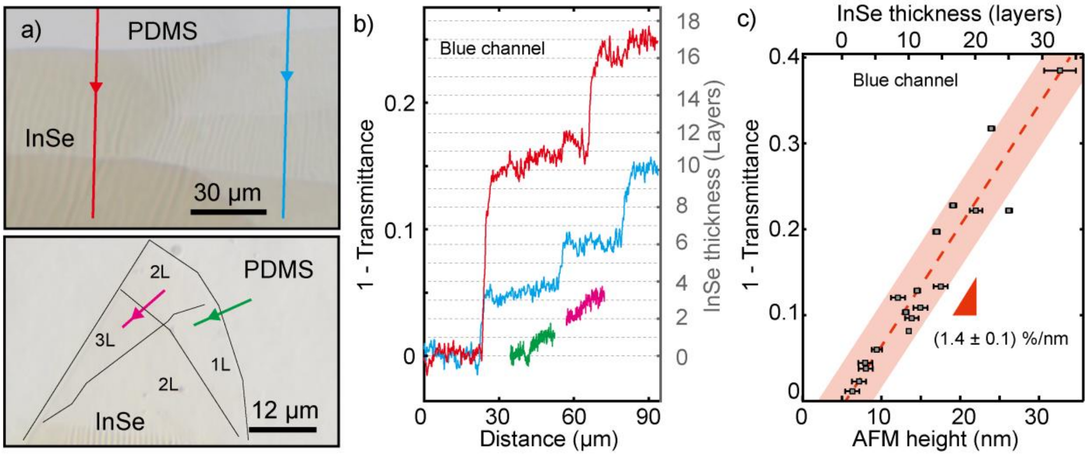

Fig. 2-11 a) Optical image of two mechanically exfoliated thin InSe flakes on the Gel-film recorded with an optical microscopy working under transmission mode. The colored lines in the image correspond to the intensity profiles in panel (b). b) The normalized blue channel intensity line profiles of 1-transmittance recorded as a function of InSe flake regions with various thicknesses indicated upon the arrows in (a). Note that the bare Gel-film takes a unity transmittance. c) The relationship between InSe flake heights determined by atomic force microscopy (AFM) versus the 1-transmittance.

- Apparent color

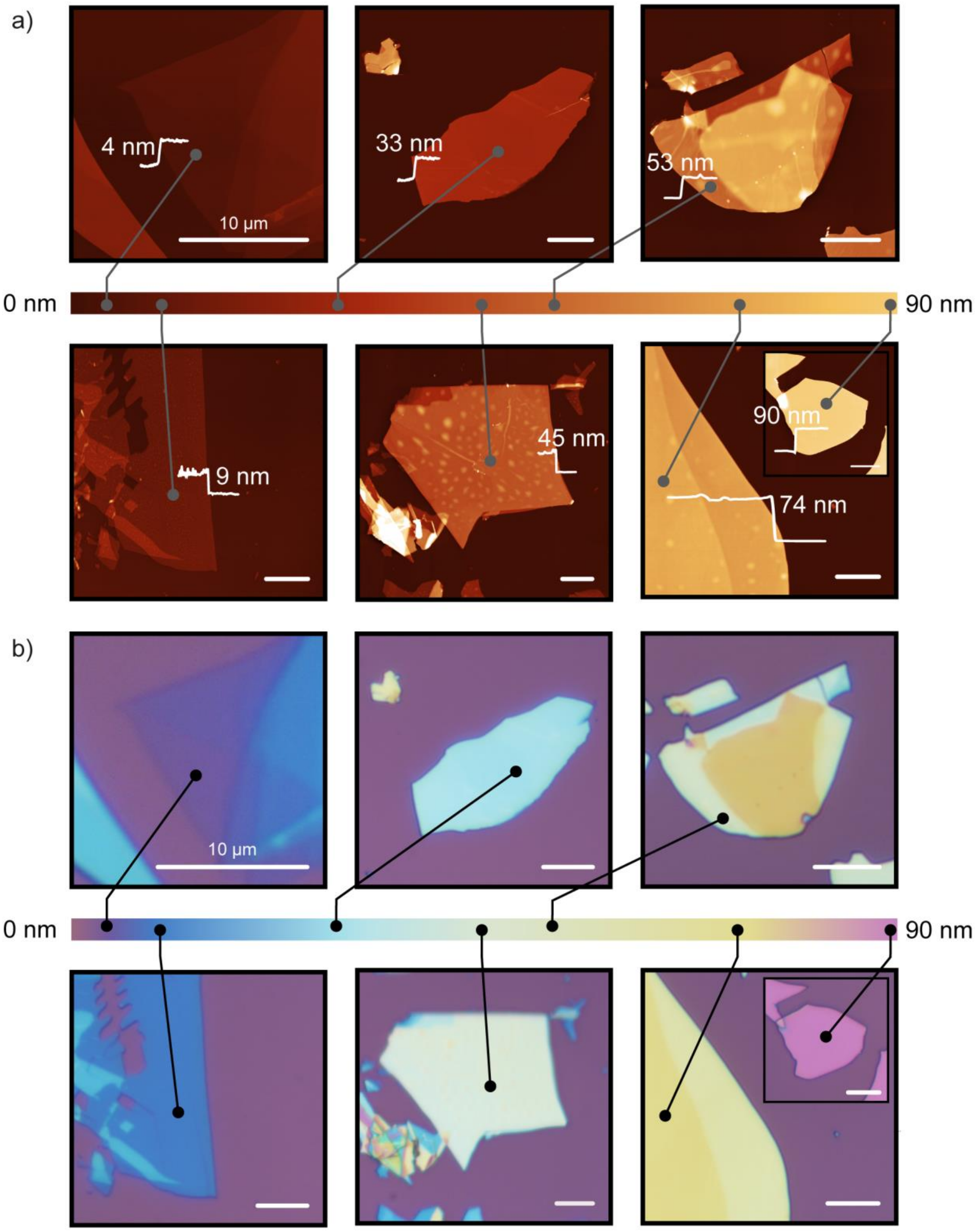

Fig. 2-12 a) Atomic force microscopy (AFM) characterizations of the exfoliated thin InSe flakes with different thickness deposited on 270 nm SiO_2/Si substrates. b) Optical pictures of the thin InSe flakes shown in panel (a) and the color bar indicates the apparent color dependency of thin InSe upon the flake thickness up to 90 nm. All the scale bars are 10 μm.

It is well known that graphene, transition metal dichalcogenides (TMDCs), TiS_3, franckeite, mica, antimonene and MoO_3 flakes deposited on a SiO_2/Si substrate presents different colors depending on their thickness and on the SiO_2

thickness.[115,300-305] A comprehensive analysis of the apparent colors can yield a quick guide to estimate the thickness of 2D materials in a similar fashion as the thickness of SiO_2 capping layers on Si wafers is estimated from its interference color. **Fig. 2-12a** shows the atomic force microscopy (AFM) topography of seven InSe flakes with thicknesses ranging from ~4 nm to ~90 nm, and **Fig. 2-12b** shows their corresponding optical microscopy images on 270 nm SiO_2/Si substrate (the SiO_2 thickness has been experimentally determined by reflectometry with ± 0.5 nm uncertainty). By comparing the AFM thickness and the optical image colors of these InSe flakes, one can build up a color-chart correlating the apparent color of the InSe deposited on the top of 270 nm SiO_2/Si substrate with their corresponding thickness. Since the interference colors of the thin InSe flakes have a strong dependence on the underlying substrate thickness, it is necessary to use the substrates with specific SiO_2 thickness (the provided case with a thickness color chart that will be valid for 270 nm SiO_2/Si substrates).

- Optical contrast analysis

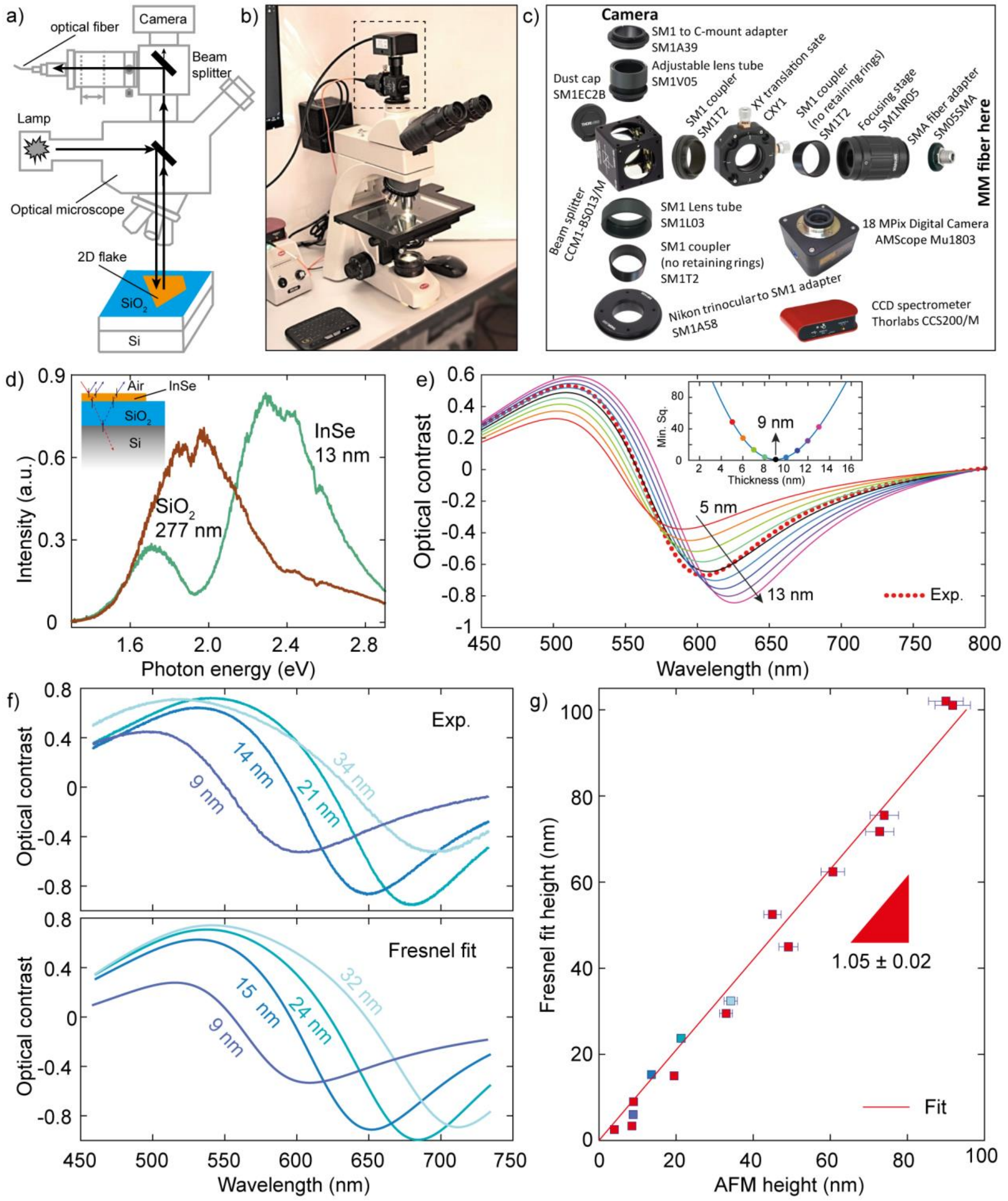

Fig. 2-13 Optical contrast analysis. a) Schematic diagram of the optical path of the system operated in reflection mode. b) Photograph of the Motic BA310 MET-T optical microscope equipped with the modified trinocular to perform optical contrast measurement on 2D flakes. The modified trinocular has been highlighted using a dashed square. c) Detailed scheme of the assembly process of the modified trinocular tube. d) Reflectance spectra recorded from bare 277 nm SiO_2/Si substrate (redish brown) and 13 nm 2D InSe flake (cyan). The inset is schematic drawing of the four-media system (air/InSe/SiO_2/Si) from which the optical contrast spectra calculated. e) Comparison between experimental optical contrast spectrum of a 9 nm thick InSe flake (red dot line) and the calculated ones (colored solid lines), with the thickness ranging from 5 nm to 13 nm, and deposited on 270 nm SiO_2/Si substrates.

The inset shows the minimum square value as a function of flake thickness. f) Experimental optical contrast spectra of thin InSe flakes with different thickness on 270 nm SiO_2/Si substrates (top panel) and the corresponding Fresnel fits (bottom panel). g) Comparison between the thickness determined with AFM measurements and Fresnel fit. The experimental data represented by the red squares, the error bars demonstrates the uncertainty of the AFM measurements, and the red line guides a fit with a slope of 1.05 ± 0.02.

The number of layers of InSe flakes that have been deposited on the SiO_2/Si substrate can be further determined more accurately by quantitatively analyzing their reflection spectra. **Fig. 2-13a** shows the schematic setup diagram to measure OC(λ) of 2D flakes by a microsystem in a backscattering geometry at room temperature. **Fig. 2-13b** shows a photograph of the optical contrast setup, which has been developed to characterize 2D materials in the group in ICMM. The setup consists of a Motic BA310 MET-T metallurgical microscope, a modified trinocular (marked with the dashed square), and a fiber-coupled CCD spectrometer. A 90:10 beam splitter is connected to the C-mount trinocular in order to divide the trinocular light beam into two paths. In one of the paths (10% of the intensity) a COMS camera is placed at the image plane of the optical system to acquire images of the studied sample. In the other path (90% of the intensity), a multimode fiber is placed, also at the image plane, projecting an image of the studied sample on the surface of the fiber end. **Fig. 2-13c** shows all the components and details (including their part numbers) required as well as how to assembly a modified trinocular. Based on the above setup, one can measure the differential reflectance spectra in normal incidence on InSe flake and SiO2/Si subtract (see **Fig. 2-13d**), then the optical contrast (C) of four-media air/InSe/270 nm SiO_2/Si optical system can be calculated from the spectra measured on the bare substrate (I_{sub}) and the one measured on the InSe flake (I_{InSe}):

$$\mathrm{C} = \frac{I_{InSe} - I_{sub}}{I_{InSe} + I_{sub}}. \tag{2-1}$$

The optical contrast of this kind of multilayer system can be also modelled with high accuracy using a Fresnel law-based model that takes into account the light reflected and transmitted at the different interfaces.[306] The reflection coefficient in a Fresnel model with four media can be expressed as:[307]

$$r_{InSe} = \frac{r_{01}e^{i(\Phi_1+\Phi_2)} + r_{12}e^{-i(\Phi_1-\Phi_2)} + r_{23}e^{-i(\Phi_1+\Phi_2)} + r_{01}r_{12}r_{23}e^{i(\Phi_1-\Phi_2)}}{e^{i(\Phi_1+\Phi_2)} + r_{01}r_{12}e^{-i(\Phi_1-\Phi_2)} + r_{01}r_{23}e^{-i(\Phi_1+\Phi_2)} + r_{12}r_{23}e^{i(\Phi_1-\Phi_2)}}, \tag{2-2}$$

where the subscript 0 refers to air, 1 to InSe, 2 to SiO_2 and 3 to Si. Under normal incident condition, $\Phi_i = 2\pi\tilde{n}_i d_i/\lambda$ is the phase shift induced by the propagation of the light beam in the media i, in which $\tilde{n}_i$, d_i and λ are the complex refractive index, thickness of the media and wavelength, respectively; $r_{ij} = (\tilde{n}_i - \tilde{n}_j)/(\tilde{n}_i + \tilde{n}_j)$ is the Fresnel coefficient at the interface between the media i and j.

The reflection Fresnel coefficient in a three media (the case of the bare substrate without being covered by InSe flake) is expressed as:

$$r_{sub} = \frac{r_{01}+r_{12}e^{-i2\Phi_1}}{1+r_{01}r_{12}e^{-i2\Phi_1}} \tag{2-3}$$

Where sub index 0 is air, 1 is SiO_2 and 2 is Si. Using equations (2-2) and (2-3), one can calculate the optical contrast by firstly calculating the reflected intensity of both situations as

$$R_{InSe} = |\overline{r_{InSe}}r_{InSe}|, R_{sub} = |\overline{r_{sub}}r_{sub}|. \tag{2-4}$$

Then the optical contrast can be obtained through the following equation (2-5) that correlates the reflected intensity by the bare substrate (R_{sub}) with the reflected intensity by the InSe flake (R_{InSe}) as:

$$\mathrm{C} = \frac{R_{InSe}-R_{sub}}{R_{InSe}+R_{sub}}. \tag{2-5}$$

Interestingly, it was found that using the thickness of the SiO_2 layer (determined by reflectometry), the thickness of the InSe flakes (measured with AFM), the reported refractive indexes for air, SiO_2 and Si, and assuming a thickness independent refractive index $\tilde{n}_i = 2.7 - i0$ for the InSe flakes we can reproduce the experimental optical contrast spectra accurately.[308-310] Moreover, by considering that the thickness of the flake is an unknown parameter we can determine the thickness of the InSe flakes by calculating optical contrast spectra for different InSe thicknesses and computing which thickness provides the best matching with the experimental data. **Fig. 2-13e** shows how to compare the optical contrast experimentally measured in an InSe flake (9 nm thick according to the AFM measurement) with the modelled optical contrast assuming a thickness in the range of 5-13 nm. There is a clear best match for a thickness of 9 nm, illustrating the potential of this method to determine the thickness of InSe flakes. The inset in **Fig. 2-13e** shows the square of the difference between the measured contrast and the calculated one as a function of the thickness assumed for the modelling. The plot shows a well-defined minimum centered at a thickness of 9 nm. In **Fig. 2-13f** the experimental optical contrast curves obtained from other three InSe flakes with thicknesses of 14 nm, 21 nm and 34 nm (top panel) are further compared the fit curves (bottom panel) with the Fresnel-based model. One can find that the fitted flake thicknesses of 15 nm, 24 nm and 32 nm are consistent with the flake heights measured by AFM, with a small error of ± 2 nm. In order to benchmark this thickness determination method for InSe, a comparison between the flake height values determined with AFM from 16 flakes from 4 nm to 90 nm thick and the value obtained following the discussed optical contrast fit method has been presented in **Fig. 2-13g**. In this plot, one can find a slope value of 1.05 ± 0.02 marked by the straight line indicates the good agreement between the thicknesses of thin InSe flakes measured by AFM and the fit to the Fresnel law-based model (a perfect agreement in this representation would yield a linear trend of slope equal to 1). Finally, it is worth to mention that the choice for the thickness-independent refractive index is motivated by the negligible variation of the band structure of InSe with the thickness in the range probed experimentally (4-90 nm).

- Photoluminescence (PL)

Photoluminescence (PL) is another important method to identify the thickness of 2D semiconducting flakes. In contrast to MX_2 (M = Mo, W; X = S, Se, Te), layered InSe exhibits a direct-to-indirect band gap transition while reducing the flake thickness from bulk to monolayer regime.[187] The large quantum efficiency supported by direct band gap in few-layer InSe regime indicates the PL can be employed for layer number n determination of thin InSe in a larger thickness range at room temperature.[245,311] **Fig. 2-14a** shows the photoluminescence spectra that are collected from four InSe flakes with the thicknesses of 6 nm, 9 nm, 12 nm and 22 nm, respectively. With the increase of the flakes thickness, one can observe an obvious redshift of the maxima of the PL peak: from 1.34 eV (6 nm) to 1.27 eV (22 nm). Note that the PL peak emission energy from the spectra were determined using a Gaussian fit. More importantly, such well-shaped PL spectra can be collected both on the InSe flakes deposited on the transparent (*e.g.* polycarbonate, PC) and opaque (*e.g.* SiO_2/Si) substrates. In **Fig. 2-14b**, it shows the results of a statistical analysis of the PL emission peak as a function of InSe flake thickness extracted from 42 different InSe flakes deposited on PC and SiO_2/Si substrate. The thickness dependence of the exciton optical transition and hence the optical band gap of InSe flakes, as obtained from the PL-peak maxima, follows a trend that seems to be nicely described in terms of quantum-size confinement effects on the direct band gap of InSe. Thus one can follow this PL emission energy (E_{PL}) as a function of thickness of InSe flake (h, nm) using the equation based on the quantum well confinement effect,[15]

$$E_{PL} = \frac{a}{h^2} + b, \tag{2-6}$$

which the black line indicates the best fit to the present data points with the parameters are determined to be $a = 3.25 \pm 0.44$ eV•nm^2, $b = 1.27 \pm 0.01$ eV.

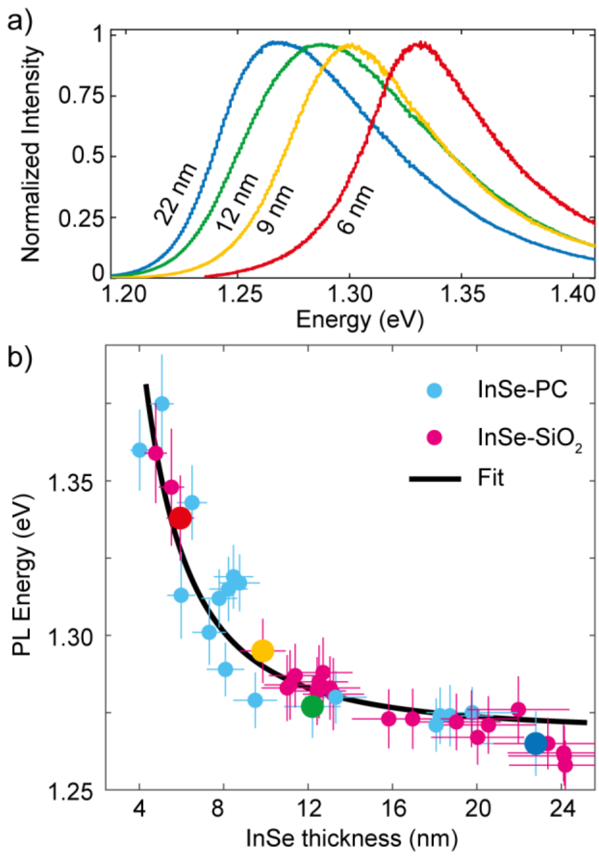

Fig. 2-14 a) Photoluminescence spectra of thin InSe flakes with different number of layers. b) Emission energy of the PL spectra as a function of InSe flake thickness extracted from 42 different InSe flakes deposited on PC (red dots) and SiO_2/Si (blue dots) substrates. The error bars come from the uncertainty of the thickness determination and extraction of the PL emission energy. The black line indicates a best fit based on quantum well confinement effect.

2.3 Complementary characterization technics: AFM, Raman

- Atomic force microscopy

Since it was invented by Binning et al in 1986, atomic force microscopy (AFM) has played a crucial role in nano-scale science and technology.[312] AFM is a microscopic technique imaging a surface topography by using attractive and repulsive interaction forces between a few atoms attached at a tip on a cantilever and a sample, as shown in **Fig. 2-14a**. In the case of attractive forces, there are three contributions causing AFM. These are short-range chemical force, van der Waals force and electrostatic force. As the effective ranges of these forces are different, one of them is dominant depending on distance. Atomic force spectroscopy is the force-versus-distance measurements when using AFM. The atomic force can be detected by cantilever bending caused by a tip-sample interacting force, which is called static AFM. Also, the atomic force can be detected by using the resonant properties of a cantilever, which is called dynamic AFM. Under the on-resonant condition, the frequency, amplitude or phase of the dynamic will be shifted by the interaction force. While the force can be estimated in static AFM, for dynamic AFM it requires complicated formalism to evaluate the force from measured amplitude, phase or frequency data. Recently developed techniques for ultra-high resolution imaging unveil sub-atomic features of the sample, which are facilitated by low temperature, ultra-high vacuum environments together with a stiff cantilever. In this thesis, the thickness and surface morphology of thin GaSe and InSe flakes was measured by an ezAFM (by Nanomagnetics, **Fig. 2-14b**) operated in dynamic mode in ICMM in Madrid. The cantilever used is a Tap190Al-G by BudgetSensors with force constant 40 Nm^{-1} and resonance frequency 300 kHz.

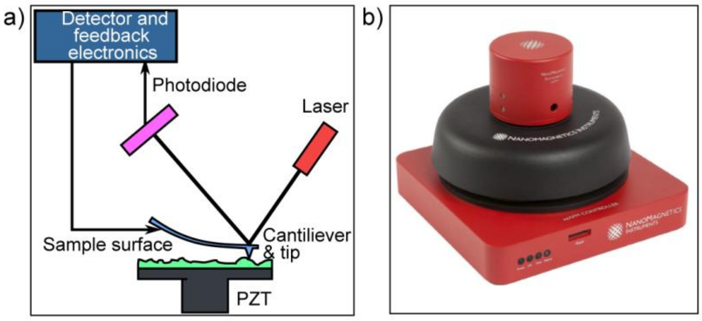

Fig. 2-14 a) The diagram block of AFM. b) Optical picture of ezAFM.

- Raman spectroscopy

Raman spectroscopy is an analytical technique where scattered light is used to measure the vibrational energy modes of a sample.[313] It is named after the Indian physicist C. V. Raman who, together with his research partner K. S. Krishnan, was the first to observe Raman scattering in 1928. Raman spectroscopy can provide both chemical and structural information, as well as the identification of substances through their characteristic Raman ‘fingerprint’. Raman spectroscopy extracts this information through the detection of Raman scattering from the sample.

As shown in **Fig. 2-15a** and **b**, when light is scattered by molecule, the oscillating electromagnetic field of a photon induces a polarization of the molecular electron cloud which leaves the molecule in a higher energy state with the energy of the photon transferred to the molecule. This can be considered as the formation of a very short-lived complex between the photon and molecule which is commonly called the virtual state of the molecule. The virtual state is not stable and the photon is re-emitted almost immediately, as scattered light. In the vast majority of scattering events, the energy of the molecule is unchanged after its interaction with the photon;

and the energy, and therefore the wavelength, of the scattered photon is equal to that of the incident photon. This is called elastic (energy of scattering particle is conserved) or Rayleigh scattering and is the dominant process. In a much rarer event (approximately 1 in 10 million photons) Raman scattering occurs, which is an inelastic scattering process with a transfer of energy between the molecule and scattered photon. If the molecule gains energy from the photon during the scattering (excited to a higher vibrational level) then the scattered photon loses energy and its wavelength increases which is called Stokes Raman scattering. Inversely, if the molecule loses energy by relaxing to a lower vibrational level the scattered photon gains the corresponding energy and its wavelength decreases; which is called Anti-Stokes Raman scattering. Quantum mechanically Stokes and Anti-Stokes are equally likely processes. However, with an ensemble of molecules, the majority of molecules will be in the ground vibrational level (Boltzmann distribution) and Stokes scatter is the statistically more probable process. As a result, the Stokes Raman scatter is always more intense than the anti-Stokes and for this reason, it is nearly always the Stokes Raman scatter that is measured in Raman spectroscopy.

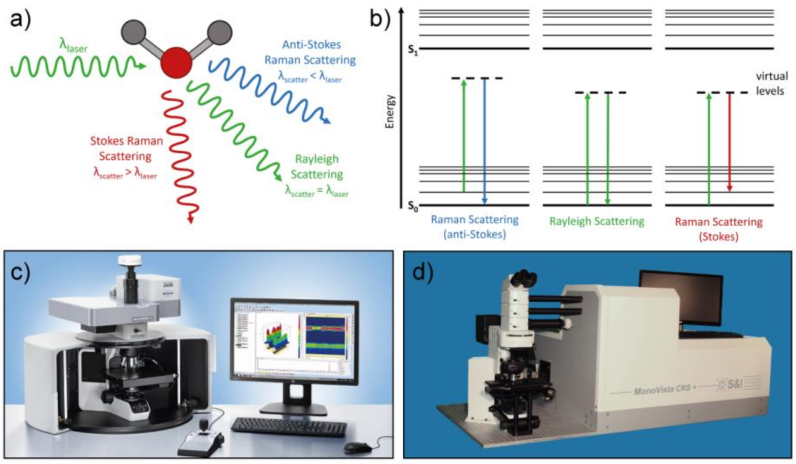

Fig. 2-15 a) Three types of scattering processes that can occur when light interacts with a molecule. b) Diagram showing the origin of Rayleigh, Stokes and Anti-Stokes Raman Scatter. c, d) Two Raman spectroscopy systems used for measurements in this thesis.

It is clear from the above, the wavelength of the Raman scattered light will depend on the wavelength of the excitation light. This makes the Raman scatter wavelength an impractical number for comparison between spectra measured using different lasers. The Raman scatter position is therefore converted to a Raman shift away from excitation wavelength:

$$\Delta\nu(cm^{-1}) = (\frac{1}{\lambda_0(nm)} - \frac{1}{\lambda_1(nm)}) \times \frac{(10^7 nm)}{(cm)}$$

$\Delta\nu$ is the wavenumber Raman shift in cm^{-1}, λ_0 is the wavelength of the excitation laser in nm, and λ_1 is the wavelength of the Raman scatter in nm.

In this thesis, two Raman spectroscopy systems were used for 2D GaSe and InSe characterization. **Fig. 2-15c** shows a Bruker Senterra confocal Raman microscopy setup (Bruker Optik®, Ettlingen, Germany) in IMDEA nanoscience and a MonoVista CRS+ confocal Raman microscopy system in ICMM (Spectroscopy & Imaging GmbH) is shown in panel **d**. Both the Raman spectra of thin GaSe and InSe flakes were obtained by with a 532 nm laser excitation focused in a 1 μm diameter spot.

2.4 Deterministic transfer

After successfully isolating graphene and other two-dimensional (2D) materials from 2004-2005,[11,30] the transfer methods that can deterministically place 2D materials at specific locations with high accuracy have been widely used for the research of 2D materials, especially for electrical and optoelectronic devices fabrication and artificial van der Waals heterostructures build-up.[91,314-318] Thus, we also establish a deterministic transfer setup in our group in ICMM to fabricate 2D materials devices and heterostructures. Interestingly, our fully functional deterministic transfer setup is much cheaper (the cost is less than 900€) than the systems are based on retrofitted metallurgical microscopes or probe stations that have been reported in literature (approximate 7000 - 8000€) or the commercial available versions. In this section, both the installation details of this setup and how to use it to fabricate 2D materials based devices and heterostructures will be demonstrated. Note that this section is mainly based on the published paper “An inexpensive system for the deterministic transfer of 2D materials” in Journal of Physics: Materials where I am the first author.[319]

Fig. 2-16 Step-by-step assembly of the low-cost deterministic transfer system.

- Assembly of low-cost transfer system

Fig. 2-16 shows a step-by-step assembly process of the low-cost deterministic transfer system, which includes all the components required and mounting details. And a picture of the presented system used for transferring 2D materials has been shown in **Fig. 2-17a**. As one can see, the system is basically consisted of a coaxial illumination zoom lens, a XY + rotation manual stage (sample/substrate stage) and a XYZ manual stage (stamp stage). A 21-megapixel digital camera with HDMI output has been mounted on the top of the zoom lens as a supplementary part and all the components are placed on a magnetic breadboard. The manual stages are attached to the breadboard through magnets glued at the base of the stages to realize quasi-rigid fixation. A close-up picture of the sample and stamp stages has been shown in **Fig. 2-17b,** in which one can find how the stamp is mounted. Note that a rectangular piece of Gel-Film (WF x4 6.0 mil, by Gel-Pak®), the polydimethylsiloxane (PDMS) -based gel material bonded to a flexible and quasi transparent backing polyester substrate, with approximate dimensions of 5 mm × 10 mm was employed as viscoelastic stamp. Then a 'cantilever-like' geometry structure of the stamp that the Gel-Film stamp is glued to a glass slide with Scotch tape, leaving most of the stamp overhanging (protruding from the glass slide as shown in **Fig. 2-17c**), were subsequently fabricated. After that, double-side tape (Scotch® Restickable Tabs) is used to fix the glass slide to the stamp stage and the sample to the sample stage. **Table 10** summarizes all the different parts needed to implement the system and the details of their corresponding distributors and prices have also been presented.

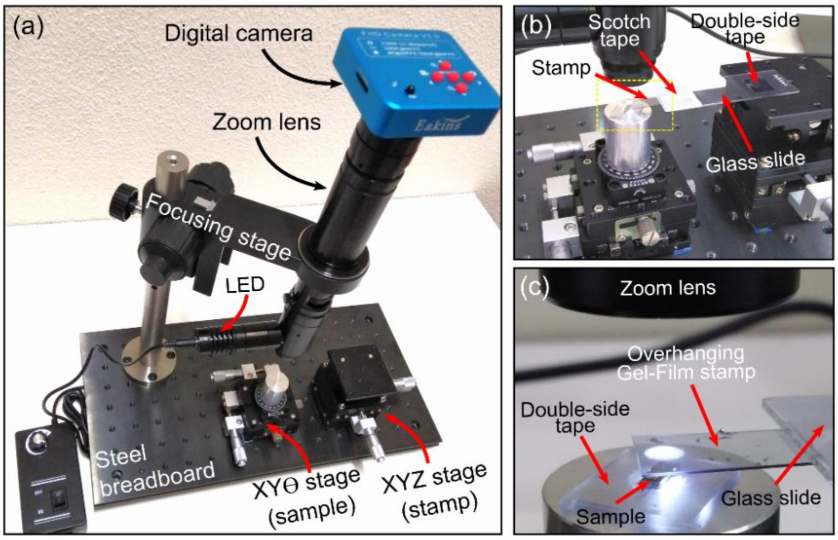

Fig. 2-17 a) Picture of the assembled low-cost system to transfer 2D materials, highlighting some of the key components and details used for deterministic transfer process. b) Zoomed in picture showing details of the stamp clamping and fixture to the XYZ stage. c) Zoomed in image of the area highlighted with a dashed yellow rectangle in (b) where the sample and stamp fixture are displayed.

Table 10 Summary of the components of the proposed system.

Description	Distributor	Price (€)

System base	Ferromagnetic steel optical breadboard	Standa	1BS-2040-015	130.00
	Rubber damping feets (set of 4)	Thorlabs	RDF1	4.92
Imaging system	Ø25.0 mm pillar post	Thorlabs	RS300/M	53.25
	Mounting post base	Thorlabs	PB1	22.44
	Focusing stage for zoom lens		Aliexpress	56.96
	400 × zoom lens with coaxial illuminator		Aliexpress	174.83
	Auxiliary 3.5x magnification lens		Aliexpress	34.36
	21 MPix digital camera		Aliexpress	74.70
	22” HDMI monitor		Amazon	89.99
Sample and stamp stages	Manual rotation stage (for sample)	Thorlabs	MSRP01/M	66.53
	XY manual stage (for sample)		Banggood	63.14
	XYZ manual stage (for stamp)		Banggood	81.18
	Magnets (for sample and stamp stages)		Amazon	7.15
				859.45

- Van der Waals heterostructures fabrication

To demonstrate the potential feasibility of the as-assembled deterministic placement system, **Fig. 2-18** shows how to use this inexpensive transfer system to fabricate van der Waals heterostructures by presenting the example of a fully encapsulated InSe flake between two hexagonal boron nitride (h-BN) flakes, and the sequence of transfer has been shown in panel a. As can be seen from left to right, the first step is that a h-BN flake has been transferred in the middle of a pre-pattern cross-hair marker structure on 300 nm SiO_2/Si substrate. Then a InSe flake is transferred onto the bottom h-BN flake that can be demonstrated as the second step. The final step is that transferring another h-BN flake to sandwich the InSe flake between h-BN sheets. **Fig. 2-18b** shows the pictures of resulting van der Waals heterostructure.

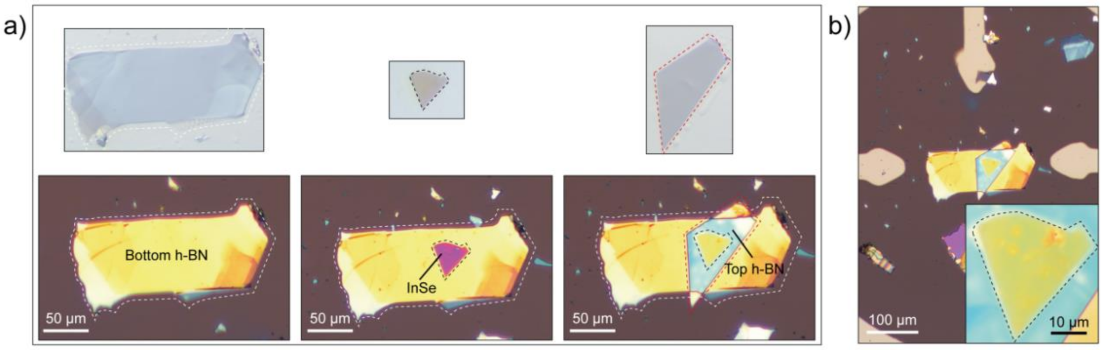

Fig. 2-18. Fabrication process of a fully encapsulated InSe flake heterostructure with

h-BN onto a pre-defined location on a SiO_2/Si substrate. a) Sequence of stacking bottom h-BN (left), thin InSe (middle) and top h-BN (right) by the deterministic transfer method. b) The overall resulting h-BN/InSe/h-BN heterostructure in the middle of a pre-patterned cross-hair and a zoom-in image of the fully encapsulated InSe flake (inset panel).

- Device Fabrication

The inexpensive transfer setup also has been tested for 2D based devices fabrication, and two fabrication examples have been presented as follows. A sequence of optical microscopy images shown in **Fig. 2-19** have been recorded with this deterministic transfer setup during the fabrication of a Au-InSe-Au field effect transistor device. Firstly, a SiO_2/Si substrate (285 nm of SiO_2) with pre-patterned electrodes (Ossila®, S221) separated by 30 µm was used. Then a thin InSe flake with uniform thickness and regular shape has been selected by focusing on the surface of the stamp. Subsequently, the stamp is brought closer to the surface of the sample and at the same time the flake is aligned with the electrodes employing the XYZ stamp stage micro-positioner. Next, lower the stamp gently until it contacts the surface of the sample. Then, peel off the stamp slowly (steps 5 to 7) until it is completely removed and finally the InSe has been successfully transferred bridging the two electrodes (step 8). **Fig. 2-20** demonstrates a second example that how one can use this inexpensive transfer setup to fabricate fully-encapsulated electronic devices, in which the steps needed for the assembly of a InSe device, fully encapsulated between h-BN flakes have been presented.

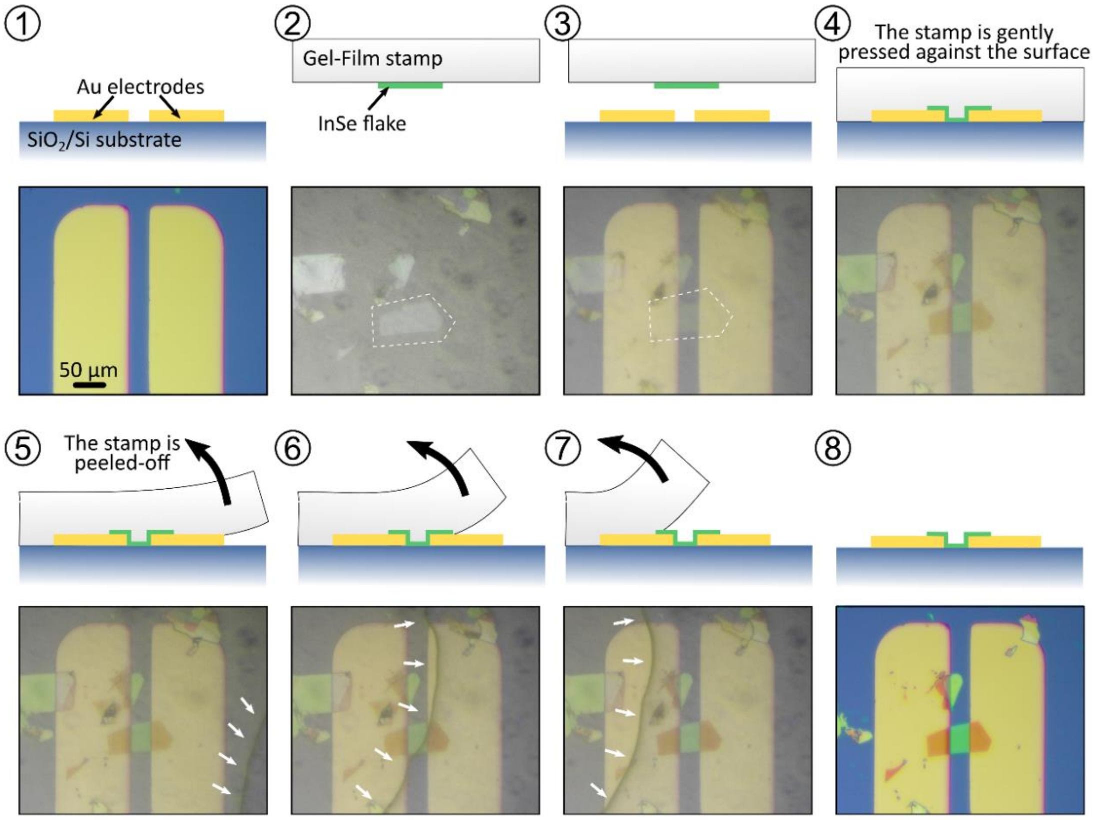

Fig. 2-19 Schematics and transfer process of bridging a thin InSe flake onto the pre-patterned gold electrodes on a 285 nm SiO_2/Si substrate, including empty pre-patterned gold electrodes (1), isolated thin InSe flake on the surface of the Gel-Film stamp (2), alignment of the flake with the electrodes (3), the stamp is gently pressed against the target sample (4), the stamp is slowly peeled off (5, 6, 7, white arrows indicate the stamp/air interface) and final device (8).

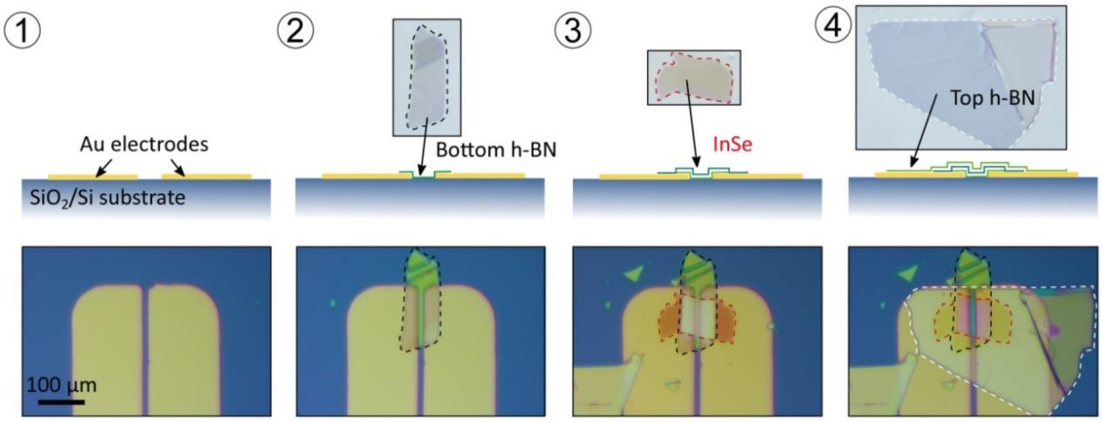

Fig. 2-20 Fabrication steps of a InSe device fully encapsulated between h-BN flakes. Pre-patterned gold electrodes on SiO_2/Si substrate (1), bottom h-BN flake is transferred (2), InSe flake is transferred bridging the two gold electrodes (3) and transfer of a top h-BN to complete the full encapsulation.

2.5 A setup for the characterization of optoelectronic devices

After the fabrication of 2D GaSe and InSe based devices, the following work is to characterization their electronic and optoelectronic properties. However, both thin GaSe and InSe present a strong sensitivity to environmental conditions and trends to degrade the device performance, thus characterization of these devices requires measurement systems operating in high-vacuum. Unfortunately, conventional optoelectronic probe-station testing systems are not compatible with high vacuum operation and vacuum-compatible versions are rather expensive. Thus, a high vacuum system specifically has been designed and implemented in our group in ICMM to test electronic and optoelectronic devices based on 2D materials with low budget. This system is mostly based on the assembly of commercially available standard vacuum, optic components, and several home-made parts. Despite the simplicity of this system full capabilities have been demonstrated to characterize optoelectronic devices in a broad range of wavelengths with fast pumping/venting speed and possibility of modulating the device temperature (room temperature to ~150 ℃). Note that this section is mainly based on the published paper "A system to test 2D optoelectronic devices in high vacuum" in Journal of Physics: Materials where I am the first author.[320]

- Assembly of the high-vacuum optoelectronic system

The details of commercially available components, indicating distributor and part-number, necessary for the assembly of the devices have been summarized and are collected into **Tables 11, 12** and **13**, which correspond to vacuum chamber components, optical accessories, as well as source meter unit and vacuum pumping station, respectively. A scheme of the high vacuum parts (with model information) needed to assemble the vacuum chamber is shown in **Fig. 2-21a** and **2-21b** shows the actual photograph of the assembled setup fixed on a manual X-Y placement platform that can travel in a range of 30 mm × 30 mm with a 1 μm adjustment accuracy. Two KFA25/50A reducers are mounted at the bottom of the chamber and are used for the connection of molecular turbo pumping station (indicated as "air out" in the schematics) and venting valve ("air in"), which allows fast chamber atmosphere switching between vacuum and air. After removing the cap, one can see the interior of the chamber. As shown in **Fig. 2-21c**, a machined cylinder piece which is marked by squared gray dash line is placed inside the chamber that can both reduce the pumping volume and place the sample much closer to optical window of the system. Based on the previous experience, though a smaller chamber size would provide an even faster pumping speed, that can also result in uncomfortable for the operators. Thus, an ISO-100 standard size has been selected to base the design in order to both facilitate the sample and probe placement operations. The home-built electrical feedthroughs (see **Fig. 2-23**) allows connecting the electronic components to perform the electrical measurements, which includes source measure unit for electrical characterization of devices, programmable benchtop power supply to control the heater mounted on sample stage and multi-meter to test the thermistor resistance.

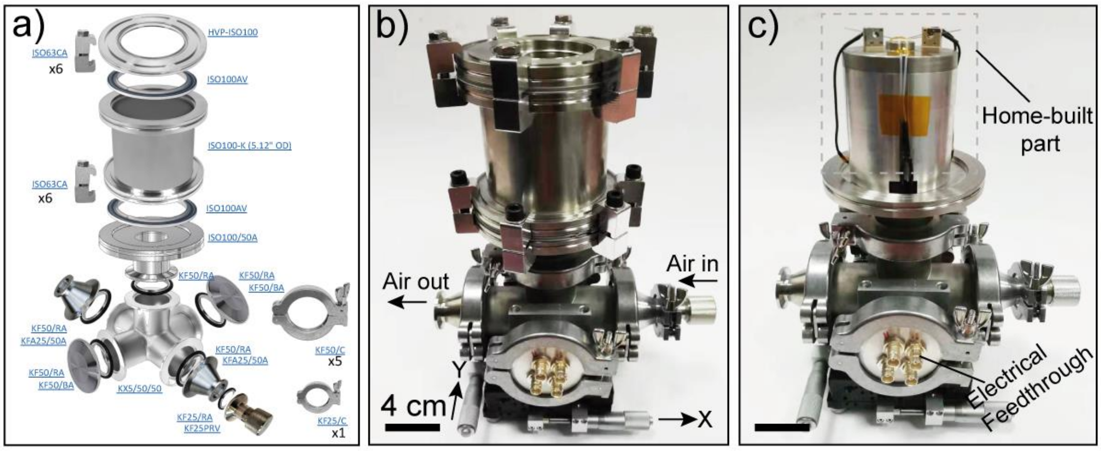

Fig. 2-21 a) Scheme of the commercial high-vacuum parts used for vacuum chamber building. b, c) Photographs with (b) and without (c) the cap of the assembled vacuum chamber mounted onto a XY stage. The home-built parts are highlighted in panel (c).

Table 11 Summary of the components needed for the assembly of the small vacuum chamber.

Vendor	Quantity	Part number	Description	Unit price
Hositrad	1	ISO100/50A	ISO-K 100 to NW50KF adaptor	97.00
	2	ISO100AV	ISO-K 100 centering ring	16.50
	12	ISO63CA	ISO-K 100 clamps	1.90
	1	KX5/50/50	NW50KF 5-way cross	240.00
	5	KF50/RA	NW50KF centering ring	5.00
	5	KF50/C	NW50KF clamps	6.00
	2	KFA25/50A	NW25KF to NW50KF (reducer)	18.00
	2	KF50/BA	NW50KF blanks	6.00
	1	HVP-ISO100	NW100 ISO-K viewport	195.00
	1	KF25/RA	NW25KF centering ring	2.25
	1	KF25/C	NW25KF clamps	2.50
USA lab	1	KF25PRV	KF25 Venting Valve	59.00

Lesker	1	ISO100-K (5.12" OD)	Full Nipple, Clamp Style	138.70
RS	7	295-7942	Hermetic BNC connector	7.97
Optics-Focus	1	MAXY-125L-25	XY placement platform	180.00
Linkam	3	---	Magnetic probe-tip holder	280
			Total (€):	1967.78

Table 12 Summary of the components needed for the assembly of the optical system used for inspection/illumination of the devices.

Vendor	Quantity	Part number	Description	Unit price
AMScope	1	SKU: SA-HG-2	Solid Aluminum Single-arm Boom Stand	202.99
Aliexpress	1	ZOOM_LENS	400x zoom lens with coaxial illuminator	185.99
	1	DIGI_CAM	21 MPix HDMI + USB camera	77.88
Thorlabs	1	M530F2	High-power fiber coupled LED source (λ = 530 nm, other wavelengths available)	371.82
	1	LEDD1B	LED driver	294.11
	1	M28L01	Multimode optical fiber (core 400 µm, other core sizes available)	84.59
	1	SCP05	Miniature XY translator stage for the optical fiber (see Figure 5b3)	146.49
	1	SM05SMA	Adapter from optical fiber to miniature XY stage (see Figure 5b3)	27.54
			Total (€):	1391.41

Table 13 Summary of the auxiliary equipment used here to pump down the chamber and to perform the electrical measurements.

Vendor	Quantity	Model	Description	Unit price
Keithley	1	Keithley 2450	Source measurement unit for the electrical measurements of devices	5250.00
Edwards	1	T-Station 85H Dry NW40	Turbo pump station with wide range pressure gauge	6700.00
			Total (€):	11 950.00

Fig. 2-22 and **Fig. 2-23** show the details of two home-built parts, the sample stage and

electrical feedthrough, necessary to complete the vacuum chamber system, respectively. **Fig. 2-22a** shows a sketch of the home-built sample stage that sits inside the vacuum chamber and the corresponding dimensions are marked in the left panel. A close-up picture of the home-built sample stage cylinder that consists of the top (magnetic) steel part and the bottom supporting aluminum cylinder part has been shown in **Fig. 2-22b**. A ceramic heater plate that is used for heat up the devices (up to 200 ℃) has been mounted on the top surface of steel part, and a thermistor is used for temperature sensing that limits the maximum operation temperature to 150 ℃. In **Fig. 2-22c,** it is shown that three miniature probes (Linkam) attached with magnets are used to contact the electrical pads of the devices to establish the source, drain and gate connections. The heater, the thermistor and the three probes are connected to a home-built BNC electrical feedthrough through coaxial cable (RG 178, BELDEN). An example of that how to fabricate such an electrical feedthrough has been shown in **Fig. 2-23**. Briefly, two holes are drilled on a blank KF50 flange and hermetic BNC nut-jam connectors are screwed to ensure a vacuum tight sealing.

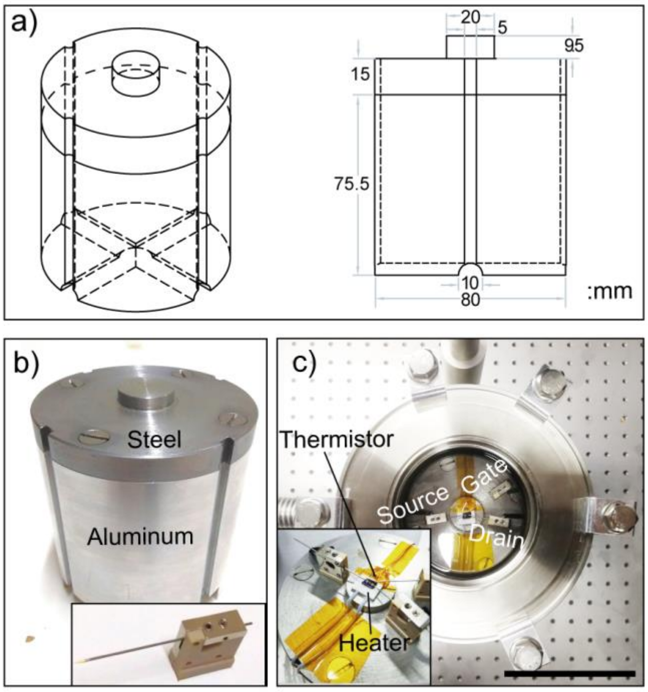

Fig. 2-22 Home-built sample stage. a) Isometric 3D sketch of home-built sample stage (left panel) and side view with indicated the corresponding dimensions in millimeters (right panel). b) Close-up photographs of the as-machined home-built sample stage and the miniature probe with bottom magnets. c) Top view of the sample stage surface as seen through the optical window. The inset is a close-up image of the ceramic heater, thermistor and three miniature probes (source, drain and gate). The scale bar is 50 mm.

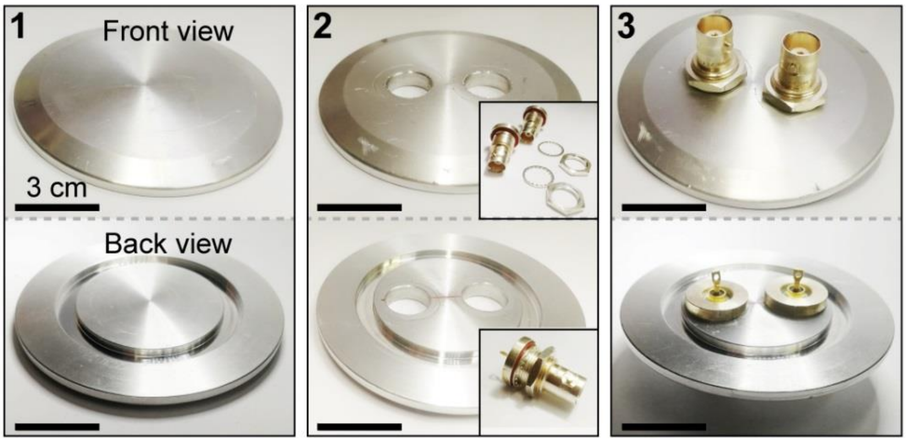

Fig. 2-23 Fabrication process of an electrical feedthrough. The front view and back view of a KF50 flange (1), the KF50 flange with two drilled holes (2) and two hermetic BNC nut-jam connectors are screwed on the KF50 flange (3).

- Calibration of optoelectronic testing system

After the assembly of the vacuum and optical components together, the calibration of the system thus follows. **Fig. 2-24a** shows how the pressure inside the chamber evolves as a function of pumping time when connected to a molecular turbo pumping station (Edwards, T-station 85H). Thanks to the reduced pumping volume by using the machined cylinder mentioned in **Fig. 2-22a**, the chamber reaches low enough internal pressure within relatively short period of time. It can be estimated that the internal pressure of chamber can be reduced from atmospheric pressure to ~10^{-4} mbar within less than ~30 minutes of pumping time. Note that upon pumping over longer periods of time (typically 10 hours overnight), the pressures that are lower than 10^{-5} mbar can be regularly achieved. **Fig. 2-24b** shows the calibration results of the ceramic heater both in ambient (red circles) and in vacuum (black squares) conditions by controlling the heater working power, the temperature values are recorded from room temperature up to ~150 ℃. The good agreement between the experimental data points and the linear fit (blue line) confirm that the heater temperature occupies a linear dependency on the heater working power both in ambient and in vacuum conditions. From the linear fits one can find the heater calibration values 13.2 ℃/W in air and 25.1 ℃/W in vacuum. To test the temperature response time of the system, the temperature has been recorded as a function of time while changing the heater working power in increasingly large steps, from 0 W to 4 W, every 600 seconds. It can be observed from **Fig. 2-24c** that after turning up or down the heater power a fast temperature raise or drop is followed by a stable temperature level. Figure 4c shows the details on the heating and cooling temperature change in left and right inset panels, respectively. Both of the processes are well fitted to an exponential growth/decay function while taking the time parameters $\tau \approx 16.4\text{-}17.8$ s.

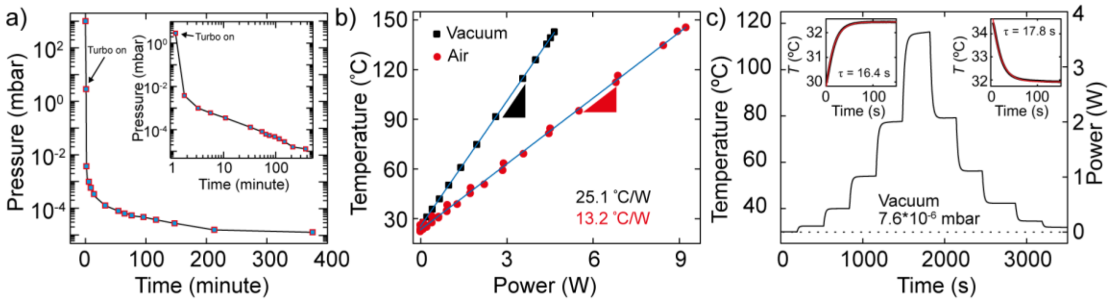

Fig. 2-24 Pressure and temperature calibration of the vacuum chamber. a) Recorded pressure in the chamber as a function of molecular turbo pumping time. The inset is the plot of pressure versus time in log-log scale. b) Relationship between surface temperature and working power of heater measured under atmosphere and vacuum (~10^{-5} mbar) condition. c) Continuous temperature control recorded in time as a function of working power of heater under high-vacuum ($7.6 \cdot 10^{-6}$ mbar) condition. The insets are exponential growth/decay fits of the heating (left) and cooling (right) temperature as a function of time.

The following step is to study the optoelectronic response of devices by placing the vacuum chamber under a long working distance zoom lens which allows one both imaging and shining light on the devices. An optical image after mounting the chamber under the zoom lens imaging/illumination system has been shown in **Fig. 2-25a**. A home-built part (highlighted with a red dashed square in **Fig. 2-25a**) that holds a multimode optical fiber has been employed to supplement the coaxial zoom lens system, which allows photo-exciting the devices with a controlled illumination. . **Fig. 2-25b** shows the details about the home-built fiber holder by a close-up picture (left panel) and the three isolated components can be found in the right panels, the corresponding sketches with fabrication details have been shown in **Fig. 2-26**. One can place the fiber core on the image plane of the zoom lens system through the fiber holder, thus a circular spot with uniform power density can be produced on the sample surface by projecting an image of the fiber core on the sample. Note that the optical fiber core size and the magnification of the zoom lens system both determine the size of the circular spot. In **Fig. 2-25c**, it is shown that a comparison of the spots acquired by connecting 5 optical fibers with the core sizes of 25 µm, 50 µm, 100 µm, 200 µm and 400 µm. Then one can obtain a linear relationship between the projected illumination spot size (on a 285 nm SiO_2/Si substrate) and the optical fiber core diameter (for a fixed magnification of the zoom lens). In addition, highly homogenous and speckle-free spots can be yielded using such projection of the fiber core on the sample in combination with high-power fiber coupled LED sources (Thorlabs) that result very convenient to determine the figures-of-merit of a photodetector, like photoresponsivity and detectivity. **Fig. 2-27** addresses a comparison between the intensity profile obtained with this illumination method with respect to a Gaussian-shape laser spot. Moreover, By using this illumination method one can realize the change of the illumination wavelength easily without substantially changing the spot size and shape. As can be seen from **Fig. 2-25d**, a Au-InSe-Au device illuminated by projecting the core of a 400 μm fiber coupled LED illuminators with 505 nm, 530 nm, 740 nm, and 850 nm of central wavelength.

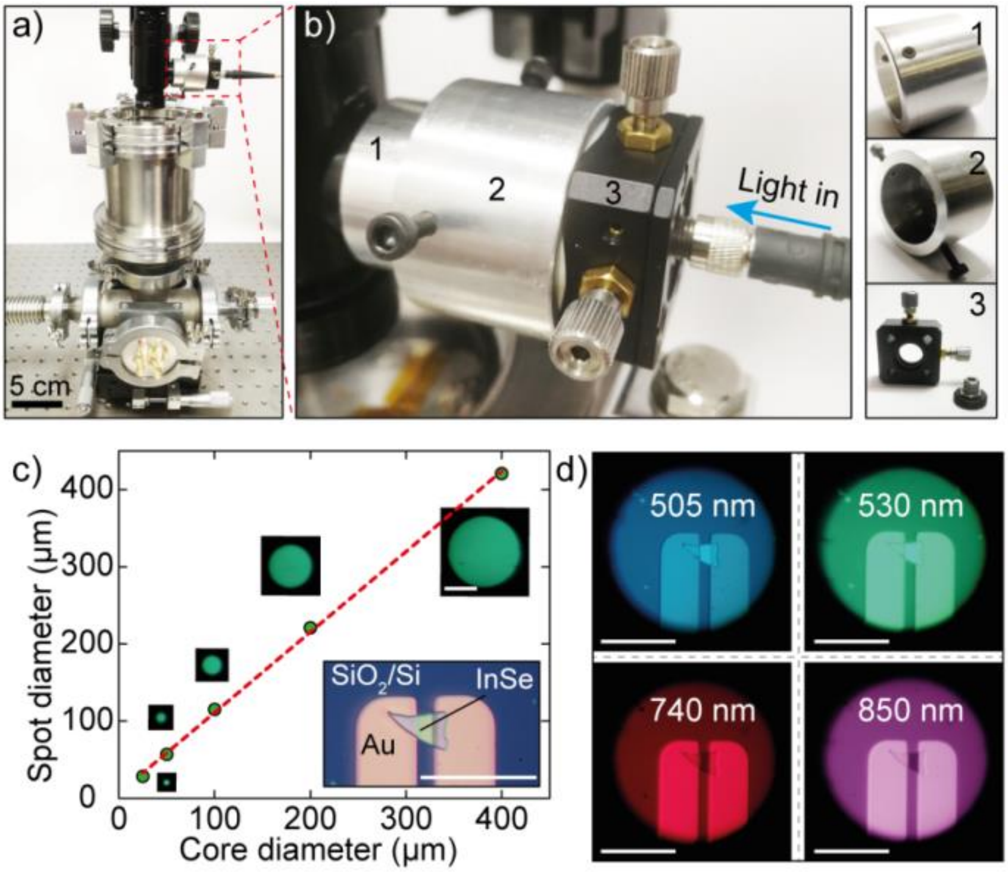

Fig. 2-25 a) Optical image of the optoelectronic measurement system. b) Close up pictures of a home-made fiber holder, highlighting the three components separately. c) Calibration of the illumination spot size as a function of core size of the optical fiber with a fixed zoom lens magnification. The inset is a Au-InSe-Au device under global illumination with a white LED source. d) Photographs of the Au-InSe-Au device being illuminated respectively with 505 nm, 530 nm, 740 nm and 850 nm LED illuminators by projecting the core of a 400 μm fiber onto the sample surface. All the scale bars in panel (c) and (d) are 200 μm.

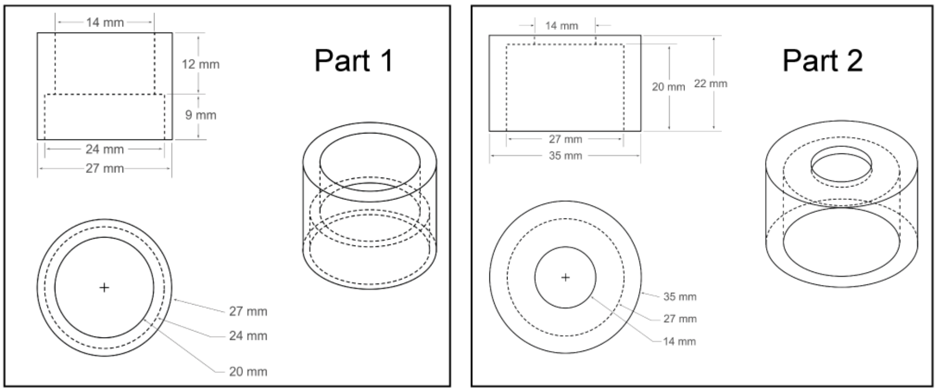

Fig. 2-26 The fabrication dimension of the home-made parts (highlighted by “1” and “2” in Figure 5b) of the fiber holder.

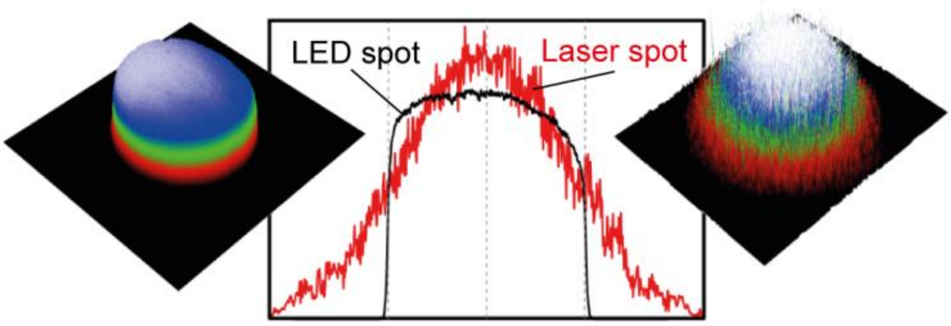

Fig. 2-27 Comparison between the intensity profile obtained with LED illumination method with respect to a Gaussian-shape laser spot.

In the following, an example of characterizing the optoelectronic properties of the Au-InSe-Au photodetector (shown in the inset in **Fig. 2-25c**) has been employed to illustrate how to operate this system. The device was assembled by deterministic placement of an InSe flake onto pre-patterned gold electrodes and the measurements were carried out under high vacuum condition at room temperature using a source measurement unit (Keithley 2450) to perform electrical measurements on the device in the dark state and upon illumination, respectively. Current-voltage (*I-V*) and current-time (*I-t*) curves are typical characteristics for measuring optoelectronic properties of photodetectors. **Fig. 2-28a** shows the result of source-drain current recorded as a function of voltage of a pristine Au-InSe-Au photodetector both in dark and under 530 nm illumination. In dark condition, there is negligible current flowing through the device, while an obvious increase in current can be observed once the device was illuminated thanks to the photogeneration of charge carriers in the device.[321] The appearance of hysteresis in the current-voltage curve recorded under illumination suggests the existence of traps in pristine InSe crystals when measured under vacuum condition. The response of the device to light is then studied by measuring the source-drain current flowing through the device at the fixed bias voltage as a function of time while switching the illumination ON and OFF. **Fig. 2-28b** shows a set of this kind of measurement that recorded under 530 nm illumination with various power density, which allows determining both the photocurrent (the difference between the current value with light ON and light OFF) and the response time of the device. The response time of a photodetector can be usually extracted by measuring the time that it takes, either in the rising or falling edge, to go from the 10% to the 90% (or from the 90% to the 10%) of the generated photocurrent under modulated excitation illumination.[321] A repeat measurement using different illumination wavelength (470 nm, 530 nm, 595 nm, 660 nm, 740 nm, and 850 nm) with the same power (100 μm) has been shown in **Fig. 2-28c**, from which one can extract that how the photocurrent varies of the device as a function of illumination wavelength.

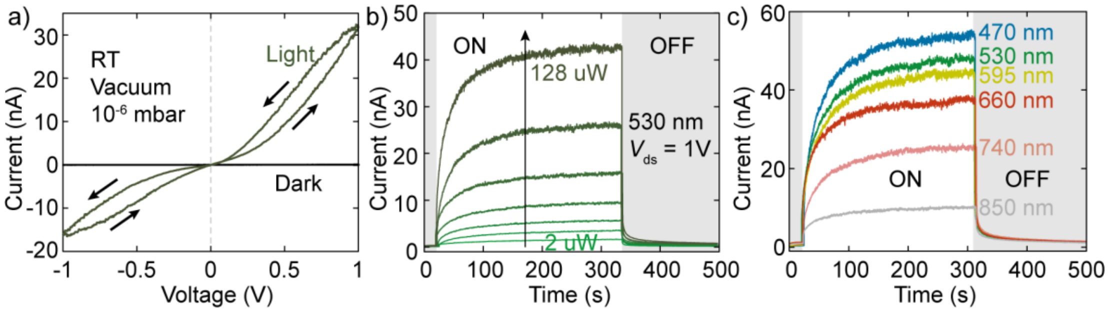

Fig. 2-28 Optoelectronic characterizations of a Au-InSe-Au photodetector in vacuum at room temperature. a) Current-voltage characteristics of a pristine Au-InSe-Au photodetector recorded in dark and under 530 nm LED illumination. b, c) Current recorded at the V_{ds} = 1V as a function of time while switching ON and OFF the 530 nm LED illuminator with different power (b) and with the LEDs of different wavelength (470 nm to 850 nm) with a fixed power of 100 μW (c).

In order to demonstrate the temperature control of the setup, a set of electronic characterization of an Au-InSe-Au device kept in dark has been carried out by varying the testing temperature. **Fig. 2-29a** presents a linear plot of current-voltage characteristics of the Au-InSe-Au photodetector recorded at 300 K and 430 K in dark condition, respectively. Noise-level current flows through the device at 300 K while the current increases noticeably when the temperature is heated up to 430 K. The temperature dependency of the *I*-*V* curves of the device recorded in dark are also plotted in semi-logarithmic scale and are reported in **Fig. 2-29b**. One can see that the current increases both at positive and negative bias voltages as well as an increase of the symmetry from the I-Vs recorded while increasing the temperature from T = 300 K to T = 430 K. Based on the I-Vs recorded in dark, the current values at V_{ds} = 0.25 V have been extracted and are plotted as a function of temperature in **Fig. 2-29c**. The dark current flowing through the device increases with the temperature in an exponential way (that appears linear in the semi-logarithmic representation of **Fig. 2-29c**), this could be attributed to an increase of carrier density by thermal excitation in the InSe or to a lowering of the contact resistance.[52,322,323]

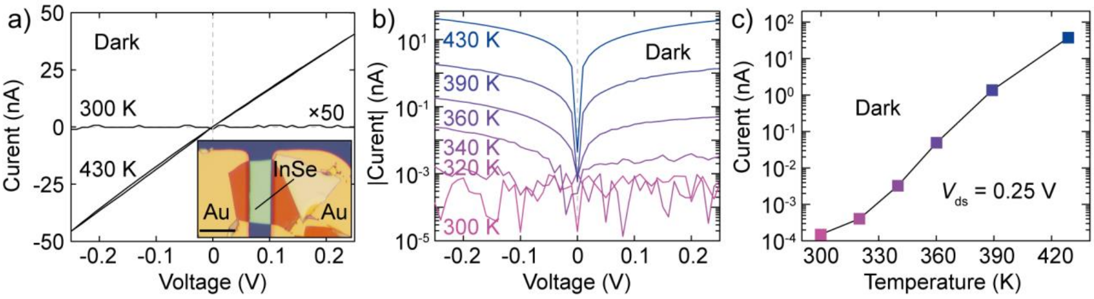

Fig. 2-29 Temperature-dependent characterization of a Au-InSe-Au photodetector in vacuum. a) Current-voltage characteristics of a Au-InSe-Au photodetector recorded at 300 K and 430 K in dark. The inset in panel (a) shows an image of the Au-InSe-Au photodetector. b) Current-voltage characteristics recorded in dark as a function of temperature. c) Current as a function of temperature recorded in dark at V_{ds} = 0.25 V.

2.6 A setup for scanning photocurrent microscopy

Thanks to the strong light-matter interaction, 2d semiconductors are considered prospective candidates for novel optoelectronics application and various photodetecting work units with ultrahigh responsivity, atomically thin body dimension, and ultrafast operating speed properties have been demonstrated during the past few years. Among most of the studies, wide-field illumination (light spot larger than the device lateral dimensions) are usually employed for extracting the information like the responsivity and response time constant collected from a global device.[324,325] Nevertheless, given the rich plethora of mechanisms involved in the photocurrent generation process in 2D system, some physical effects cannot be studied with this kind of measurements. Scanning photocurrent microscopy (SPCM) is a powerful experimental technique that can provide a wealth of information from a micro prospective, including internal electric field, charge transport and recombination dynamics happening in the semiconductors and semiconductor-metal (S-M) interfaces.[326] In general, the focused beam locally excites a semiconductor into non-equilibrium, from which point the injected electrons and holes go through a relaxation process which includes thermal relaxation, recombination, diffusion, and drift in the semiconductor. If these injected charge carriers can reach the nearby electrodes before they combine, a photocurrent is measured. This technique yields a spatial mapping of photocurrent as a function of excitation position and provides rich information that can be used to explore optoelectronic properties of semiconductors. Thus, in this thesis, a home-built scanning photocurrent microscope in our lab in ICMM has been employed for the investigation of electrical transport characteristics of 2D InSe based photodetectors and Schottky diodes.[327]

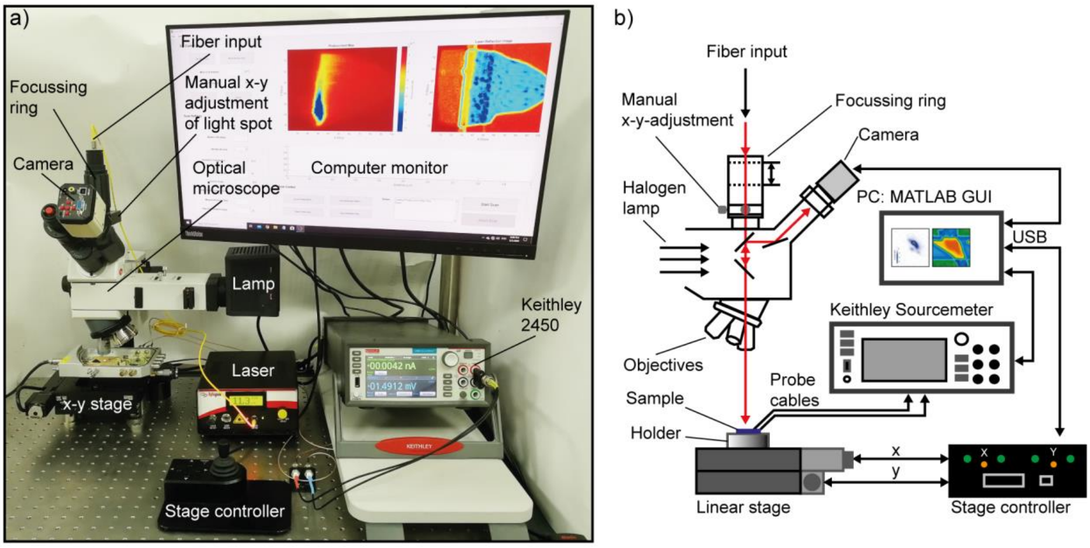

Fig. 2-30 a) Pictures of the components of the scanning photocurrent setup with the main units indicated. b) Schematics of the setup circuitry and of the optical path.

Fig. 2-30a shows a photograph of the setup for scanning photocurrent characterization which is based on a Motic BA310 MET-T metallurgical microscope equipped with a USB CMOS camera, a motorized X-Y stage, a Optogear^{TM} LED-660-5-X laser source, a Keithley 2450, and a modified spot illumination port, and **Fig. 2-30b** displays a schematic drawing. The camera is connected to one of the eyepiece ports of the microscope and the C-mount port is used as an input of the illumination that is going to be focused onto a small-diameter spot on the sample, which brought into the microscope through a multimode fiber. The modified spot illumination port is equipped with a focusing ring that allows one to modify the position of the optical fiber until the fiber core end is exactly placed at the image plane of the lens system. Under this condition, an image of the circular fiber core end (reduced accordingly to the magnification of the objectives) is projected onto the surface of the sample.

Therefore, one can easily adjust the diameter of the spot illumination by either selecting a multimode fiber with a core diameter or by switching the objectives with different magnification. The spot illumination port is also supplemented with an X-Y manual stage that allows one to move the position of the spot in the sample plane, being a useful addition for the initial alignment of the spot in the camera's field of view. The source of the spot illumination can be any fiber-coupled light source and a Optogear^{TM} LED-660-5-X laser source has been implemented.

The sample is mounted on a rotational sample holder fixed on a motorized X-Y stage. The two motorized axes have a travel range of the 25 mm with a resolution of 1.25 μm in full steps and 0.156 μm in 1/8 steps with a maximum speed of 6 mm/s. The X-Y stage can be controlled through a USB driver unit, connected to the computer. Whilst scanning sample, illuminated by a laser spot, the device electrical properties are measured with Keithley 2450 source meter unit as a function of the spot position. The data acquisition and motion control are managed through a home-made written in Matlab. A crucial part of the scanning photocurrent measurements is to correlate the photogenerated current with the device geometry. To do so, the signal from USB camera is directly employed to construct the reflectivity map. At each step of the scan, a snapshot is recorded with the camera and then the intensity of the spot would be extracted using the Matlab program. Based on this simple yet powerful tool, some example cases and analysis have been shown in the following chapters.

2.7 Conclusions

In summary, the experimental methods and characterization tools employed in this thesis have been fully introduced. The high-quality single crystalline GaSe and InSe bulks have been synthesized both using a two-step Bridgman method, and their crystal structures, composition homogeneity, optical and electrical properties are confirmed by a set of basic characterizations. Then the mechanical exfoliation method has been introduced to fabricate 2D GaSe and InSe flakes based on their bulk counterparts and three optical methods, including transmission, optical contrast, and photoluminescence (PL), are employed to quantitatively determine their thicknesses. In addition, atomic force microscopy (AFM) and Raman Spectroscopy techniques also have been used to characterize the mechanically exfoliated 2D GaSe and InSe. The 2D GaSe and InSe optoelectronic devices and heterostructures are fabricated using an inexpensive home-built deterministic transfer setup, and subsequently the transport properties and photoresponse performance are characterized using a specially designed high-vacuum optoelectronic testing system. To further understand the photocurrent generation mechanism in these devices, a microscope-based scanning photocurrent system supplemented with self-developed Matlab program has been employed. In one word, this chapter has established a rather completed platform for the investigations based on 2d materials.

3

INFLUENCE OF ENVIRONMENT ON THIN GASE AND INSE DEVICES

Two dimensional materials are especially sensitive to the environmental atmosphere and to external stimuli due to their large surface-to-volume ratio. In this chapter, two investigation cases about environmental influence on thin GaSe and InSe will be introduced. This work was motivated by previous observations reported in literature of poor stability of both of them in ambient conditions. Nonetheless, there was a large discrepancy between the results reported in those previous making it crucial to study ourselves the role of environmental exposure on our materials.

In the first part, the environmental induced degradation of thin GaSe, including macro- and microscopic surface morphology evolution, chemical composition variation, and laser-induced degradation, as well as how it leads to the photodetector breakdown as a function of exposure time in air will be fully presented. In the second part, I will focus on InSe that has a different environment-materials interaction mechanism: the environmental induced trap-passivation by air species. This process significantly affects the transport properties of InSe photodetectors, will *be investigated in detail. Finally, based on these understandings, both long-term stable photodetectors based on thin GaSe and InSe have been realized using hexagonal boron nitride (h-BN) encapsulation protection or controllable air passivation.*

3.1 Environmental induced degradation and breakdown: the case of GaSe

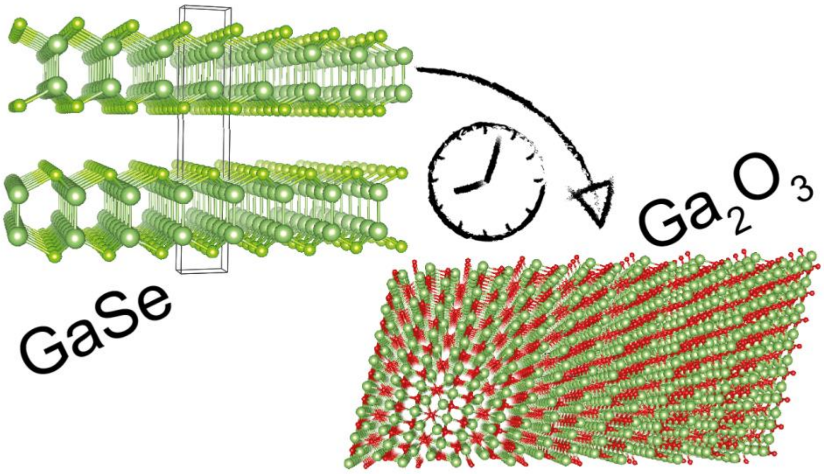

A combination of atomic force microscopy (AFM), Raman spectroscopy and optoelectronic measurements in photodetectors based on thin GaSe has been employed to study its long-term environmental stability. It was found that the GaSe flakes exposed to air tend to decompose forming firstly amorphous selenium (α-Se) and Ga_2Se_3 and subsequently Ga_2O_3. While the first stage is accompanied by an increase in photocurrent, in the second stage a decrease in photocurrent has been observed, which leads to the final failure of GaSe photodetectors. Additionally, it was found that the encapsulation of the GaSe photodetectors with h-BN can prevent the GaSe from degradation and can help to achieve long-term stability of the devices. Note that this section is mainly based on the published paper “Toward Air Stability of Thin GaSe Devices: Avoiding Environmental and Laser-Induced Degradation by Encapsulation” in Advanced Functional Materials where I am the first author.[328]

3.1.1 Background

Environmental degradation processes in 2D materials are common at ambient conditions and the origin is in part due to their sheet-like structure. In fact, although the very large surface-to-volume ratio of 2D materials has been beneficially exploited for surface chemical functionalization and physisorption of molecules or nanoparticles,[329,330] it also makes these materials very sensitive to the environmental atmosphere and to external stimuli in general. The mostly reported example of unstable 2D material is black phosphorous (BP),[331-333] which is a promising p-type layered material that exhibits high hole mobility at room temperature and thickness-dependent bandgap spanning from 0.35 eV to more than 1 eV.[84,87,334,335] Quickly after its isolation in ultra-thin form, it was found that the degradation of mechanically exfoliated few-layer BP is a layer-by-layer etching process, along with an expansion of volume due to the condensation of moisture of water in the air.[331-333] Photo-oxidation has been identified as the main cause of degradation and this process, which is faster in the case of thinner flakes, can be accelerated by increasing the concentration of oxygen or the illumination power.[331-333] Moreover, the air-degradation process was also reported in few-layer GaTe and $MoTe_2$.[336,337] Generally, the degradation in air of these compounds is described as a complicated oxidation process,[338] which comes along with the quenching of optical properties and changes in chemical composition, induced by O_2 and atmospheric humidity, and can be promoted by increasing environment temperature and by illuminating with above-bandgap light sources. Surprisingly, it was also found that in CVD-grown TMDCs (MoS_2, WS_2) a slow aging process is present, which is absent in mechanically exfoliated flakes, and it was attributed to grain boundaries and defect sites in the TMDCs films.[339]

Table 14. Summary of various experiments concerning the degradation of thin GaSe.

Reference	Substrate	Flake thickness	Time of complete degradation	Laser wavelength and power density used [mW/μm^2]
[340]	SiO_2(100nm) /Si	45 nm	30 min	532 nm, 6 (Raman)
[341]	SiO_2(300nm) /Si	14 nm	--	532 nm, 15.6 (Raman)
[342]	HOPG	3-8L	5 h (self-limited)	638 nm, 0.234 (Raman, 700s×3)
[343]	SiO_2/Si	10-25 nm	100 h	532 nm, 0.637 (PL)
[344]	SiO_2(300nm) /Si	10-40 nm	~120 h	532 nm, 0.127 (PL)
[345]	SiO_2(285nm) /Si	50 nm	> 2 weeks	514nm, 7.643(PL)
This work	Au(60nm)/SiO_2/Si	14 nm	192.5 h	532 nm, 0.11 (Raman, 20s×2)

The degradation process of GaSe flakes with different thickness has been investigated by various groups using Raman and photoluminescence (PL) spectroscopy and a comparison of the results in the literature has been presented in **Table 14**.[340-346] The general observation of these studies is that thin GaSe flakes tend to degrade over time (in a time-scale that goes from hours to days) when left in air. The scattering in degradation time reported in these studies can be explained by the differences in parameters such as the thickness of samples, the illumination power density and/or wavelength, the number and nature of defects, or the environmental humidity.[340-346] This large scattering further motivates this study of the particular GaSe materials source.

Moreover, photo-induced degradation of GaSe can even happen during the Raman spectroscopy characterization.[340-346] The long integration time and high excitation laser power used in the Raman spectroscopy experiments could decrease the degradation time to only a few seconds.[347] Among these reports, encapsulation methods, such as plasma-enhanced chemical vapor deposition (PECVD, Si_xN_y, 32nm) and atomic layer deposition (ALD, Al_2O_3, 50nm),[340-346] were proposed to protect the GaSe flakes and maintain their optical properties intact. While most of these reports are mainly focused on the influence of the degradation on the optical properties of the materials, an experimental study of the environmental stability of the electrical and optoelectronic properties of GaSe-based photodetectors is still lacking in literature.

3.1.2 Sample Fabrication

Few-layer GaSe flakes are fabricated by mechanical exfoliation in air with Nitto tape (SPV 224) from bulk GaSe crystals. The growth and characterization details of the bulk GaSe as well as the mechanical exfoliation process have been fully presented in chapter 2. **Fig. 3-1a** shows the optical microscopy image of a GaSe flake on a Gel-Film substrate recorded under transmission mode. The flakes on the PDMS can be then easily transferred onto another arbitrary substrate with micrometric precision by using a deterministic transfer setup described in chapter 2.4. **Fig. 3-1b** shows the same flake of **Fig. 3-1a** after being transferred onto a SiO_2/Si substrate and bridging two pre-patterned gold electrodes. The two regions in the flake that show different colors in the transmission-mode picture of **Fig. 3-1a** correspond to different thicknesses of the GaSe. The thinnest region which form the channel of the device is 14 nm thick as found from atomic microscope force (AFM) measurements, corresponding to approximately 14 layers. After the fabrication, all the samples have been annealed in vacuum to remove the surface adsorbates as well as to improve the contact between the GaSe flakes and gold electrodes. **Fig. 3-2** shows that the annealing does not introduce any surface or crystal structure changes, as indicated by the microscope pictures and the Raman spectra, but it leads to an improvement of device conductivity (in the case of panel (c) the conductivity increases of a factor 4).

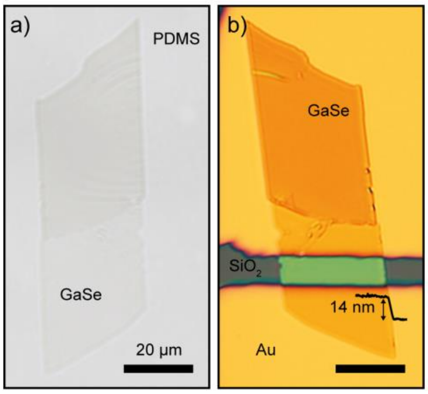

Fig. 3-1 Optical pictures of few-layer GaSe exfoliated onto PDMS (a) and deterministically transferred onto pre-patterned electrodes (b).

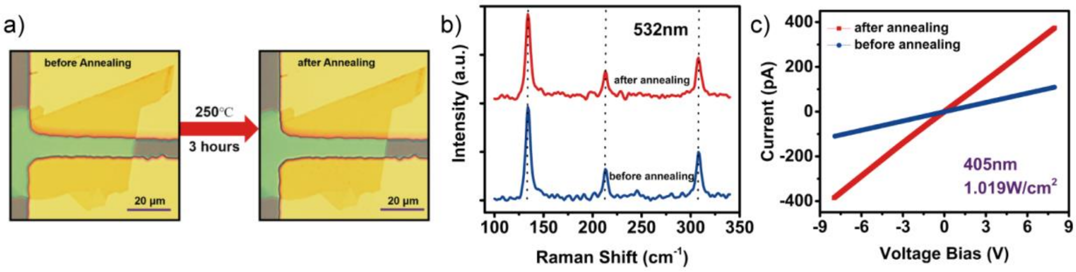

Fig. 3-2 Vacuum annealing of GaSe photodetectors. Surface morphology (a), Raman spectrum (b) and *I*-*V* curve (c) of the device before and after annealing.

3.1.3 Surface morphology

After the fabrication, **Fig. 3-3** shows two transferred GaSe devices were inspected by optical microscopy as a function of time to look for changes in the appearance of the flakes that would indicate their degradation. As indicated by the first sample shown in **Fig. 3-3a**, no obvious changes could be observed even after several hours of exposure to ambient conditions and the first symptoms of degradation could be observed after approximately 3 days. **Fig. 3-3b** shows sequence of the optical images of a second sample kept in air over a longer time period and a significant change in GaSe surface can be observed after 100 days. Interestingly, also at 44 days some degradation is visible, but localized mostly at the edges of the flake.

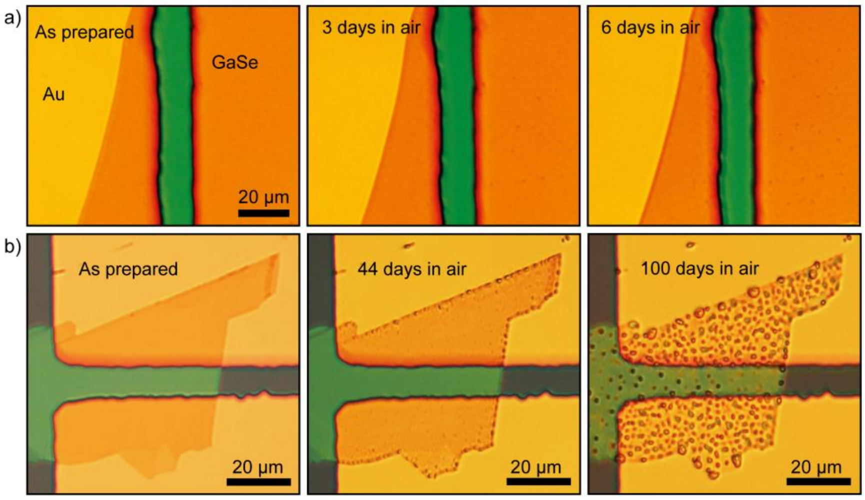

Fig. 3-3 Surface morphology evolution of two GaSe samples in air followed by optical microscopy.

To further understand the degradation of thin GaSe flake from a microscopic perspective, the AFM characterization was employed to probe subtle topographical changes that could not be resolved with the optical microscope. **Fig. 3-4a** shows the optical microscopy image of a pristine GaSe flake onto SiO_2/Si whose topographical properties have been studied as a function of exposure time to ambient conditions. **Fig. 3-4b** shows the topography of the region highlighted with a white dashed rectangle in panel (a). The surface of GaSe is uniform over a large scale with atomically flat large terraces and 1-2 nm high steps. **Fig. 3-4c** shows the topography of the region highlighted in **3-4b** with a black dashed square as a function of time. By inspecting the images, one can see that, at the initial state, the surface of the as-exfoliated GaSe presents many elongated bubbles of ~7 nm in height and an area of ~12000 nm^2. Such topographic features were also reported by Tonndorf *et al.*[348] The second AFM image, recorded after 5 hours, presents a smaller number of bubbles characterized by a circular shape and with an area of ~6000 nm^2 and height of ~20 nm. This topographic evolution seems to indicate that the original bubbles are probably due to adsorbates trapped between the flake and the substrate during the transfer process that diffuse at the flake/substrate interface over time to coalesce into larger bubbles. Similar behavior has been observed in graphene transferred onto h-BN after thermal annealing.[349,350] In the six subsequent images, recorded between 9 and 30 hours after the fabrication, the individual bubbles grow in dimensions, with the average diameter increasing from 100 nm to 500 nm and the height from 10 nm to 60 nm. From the top panel of **Fig. 3-4d**, which shows the evolution of the average height of the bubble extracted from a statistical analysis of the AFM images as a function of time, the height of the bubbles steadily increases at a rate of ~1.6 nm/h. This process can introduce strain in the atomic lattice thus modifying the optical and electronic properties of GaSe.[340-346,351] A second observation is that the number of bubbles increases in time as shown by the bottom panel of **Fig. 3-4d**. The initial formation and growth of an individual bubble is shown in **Fig. 3-4e** by the cross section of the AFM images taken in the region highlighted by the arrows in panel (c).

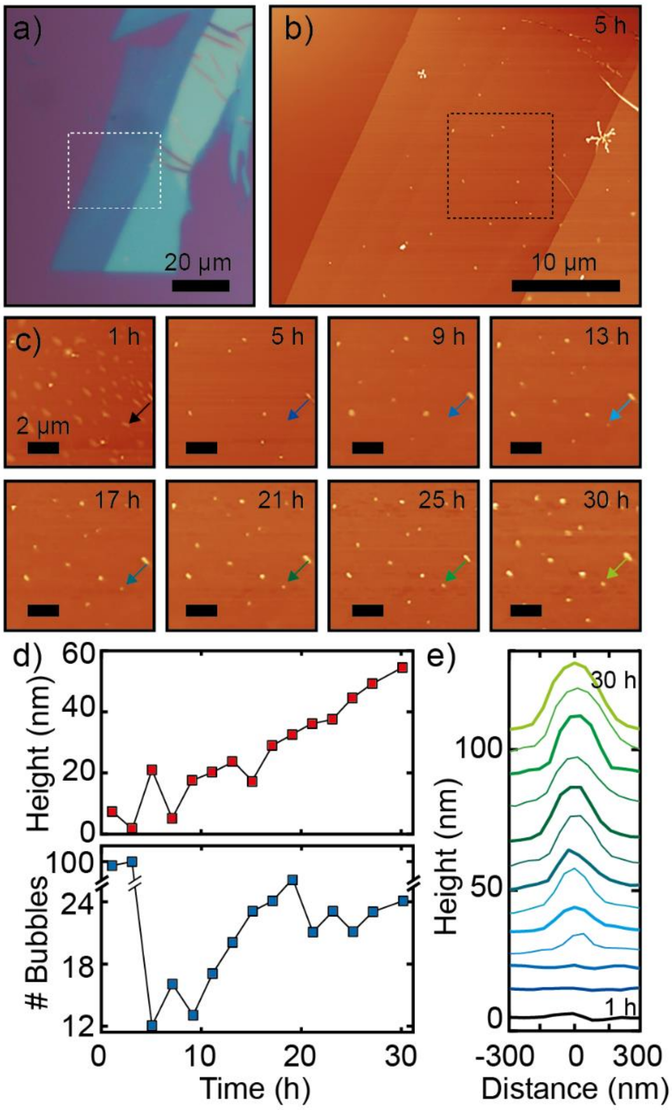

Fig. 3-4 Surface morphology evolution in ambient condition characterized by AFM. a) Optical image of a GaSe flake transferred onto the SiO_2/Si substrate. The area marked with white dashed square was selected to perform the long-term (30h) AFM analysis. b) A typical surface morphology of selected area on the GaSe flake after exposed 5 hours in air. The black dashed square area was used for following statistics analysis in panel (d). c) The surface morphology evolution of selected area on GaSe flake from 1h to 30h in air. d) The mode height and number of bubbles versus time from 1h to 30h. e) A typical evolution of cross-section shape of a bubble grown by spontaneous nucleation appeared at the 9th hour. The selected bubble was marked by arrows with

corresponding colors.

As a control experiment, the evolution of the AFM topography of a GaSe flake in N_2 atmosphere also has been analyzed. As shown in **Fig. 3-5,** the as-deposited thin GaSe flake on the SiO_2/Si substrate is firstly kept in N_2 atmosphere and then exposed to the air. From the **Figs. 3-5a-b**, one can see that even after 125 hours of N_2 exposure, the surface of the flake shows multiple elongated bubbles with small height and no signs of tall circular bubbles, a topography similar to the one observed in the initial stages of the GaSe flakes in air. After 125 hours of exposure to N_2 atmosphere, the flake was exposed to air and the topographic changes were continuously followed. **Figs. 3-5c-e** show that rapidly after the exposure to air the low elongated bubbles start to coalesce into tall circular bubbles similar to what is shown in **Fig. 3-4**. An abrupt change in the surface roughness and in the flake height can be observed right after the exposure to air of the flake in **Fig. 3-5f** and **g**, respectively. Given these observations, the nucleation and appearance of the tall circular bubbles can be attributed to the interaction of GaSe with O_2 or H_2O present in the air.

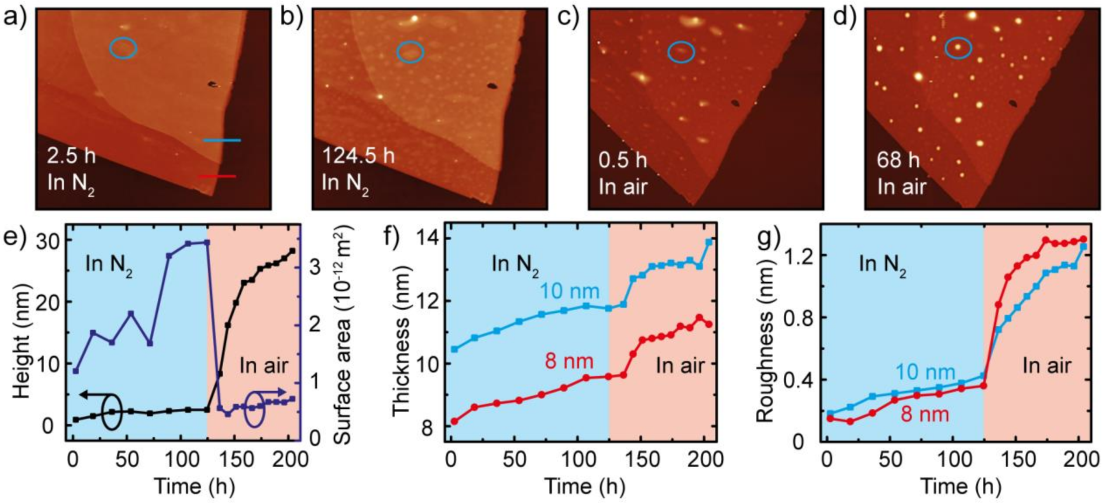

Fig. 3-5 Surface morphology evolution in time of GaSe flake in N_2 and then in air followed by AFM scanning. a-d) The surface morphology of a GaSe flake on SiO_2/Si substrate kept in N_2 atmosphere for 2.5h (a), 124.5h (b) and then in air for 0.5 h (c) and 68 h (d). The blue circles highlight a typical bubble. e) The evolution of height and surface area of the bubbles as a function of time. f-g) Thickness (e) and roughness (f) variation in time of the thinner (8nm) and the thicker (10nm) part of the GaSe flake as a function of time.

3.1.4 Chemical composition and laser-induced degradation

To get an insight about a possible chemical and/or structural transformation of the exfoliated GaSe associated with the observed topographical changes, Raman spectroscopy measurements of a GaSe flake were performed over a period of approximately 200 hours. A sequence of Raman spectra acquired on a 14 nm thick GaSe flake kept in air as a function of time (the flake used is the same one shown in **Fig. 3-1**) is shown in **Fig. 3-6a**. The spectrum acquired from the freshly cleaved GaSe shows three prominent peaks centered at 134 cm^{-1}, 214 cm^{-1} and 308 cm^{-1} that can be attributed to the A_1' (1), E' (TO), and A_1' (2) vibrational modes of crystalline GaSe, respectively (see **Fig. 3-6b**).[352-354] Upon atmospheric exposure the peak at 214 cm^{-1} (E' (TO)) gets less and less defined because of the development of three broad peaks related to the appearance of Ga_2Se_3, Ga_2O_3, and α-Se (amorphous selenium) chemical species in the sample that contribute with Raman modes centered at 155 cm^{-1}, 202 cm^{-1} and 236 cm^{-1},[355-359] respectively. **Fig. 3-6c** shows how the spectrum of the sample exposed to environmental conditions can be fitted to identify the presence of other species different from pristine GaSe. The evolution of these six peaks can be monitored in time during the degradation of GaSe. In **Fig. 3-6d**, the total area of the three peaks corresponding to pristine GaSe (134cm^{-1}, 214cm^{-1} and 308cm^{-1}, labelled as 'GaSe' in the figure) are displayed and the peaks corresponding to other species that appear upon air exposure (155 cm^{-1}, 202 cm^{-1}, and 236 cm^{-1}, labelled as 'aged' in the figure). The decrease of the 'GaSe' signal and the increase of the 'aged' one suggest that the GaSe is being converted into Ga_2Se_3, α-Se, and Ga_2O_3. Interestingly, it was also found that these 'aged' species do not appear all at the same time. **Fig. 3-6e** displays the time evolution of the area of the peaks associated to 155 cm^{-1}, 202 cm^{-1}, and 236 cm^{-1} demonstrating that while α-Se and Ga_2Se_3 appear almost right after the exfoliation, and Ga_2O_3 starts showing up and growing after that the sample was kept for approximately 40 hours in air.

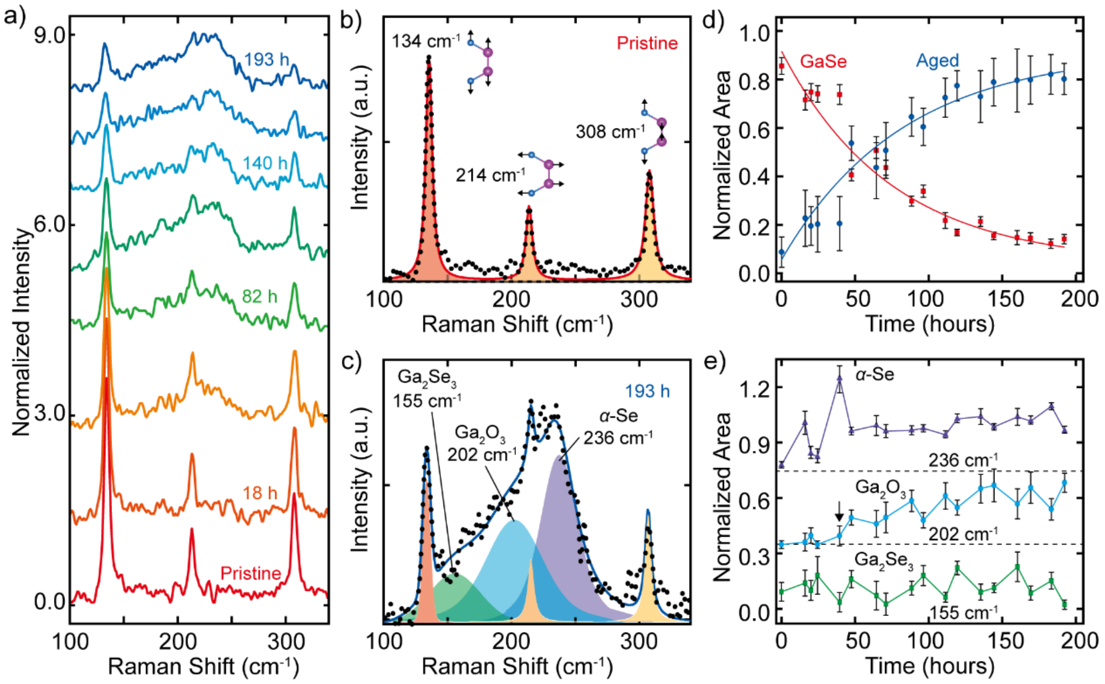

Fig. 3-6 Long-term Raman measurements of GaSe. a) Raman spectra of 14-nm thick GaSe recorded with 532 nm laser and power density 0.11 mW/µm^2. The curves have been offset vertically for clarity. b-c) Raman spectra of pristine (b) and aged (c) GaSe. The thick lines represent the total fit to the data and the filled areas are the different peaks that compose each fit. d) Evolution in time of the total area of the GaSe related peaks 134 cm^{-1}, 214 cm^{-1} and 308 cm^{-1} (red squares) and of the aged peaks 155 cm^{-1}, 202 cm^{-1} and 236 cm^{-1} (blue circles). The solid lines are guidelines for the eye. e) Evolution in time of the area of the of the aged peaks 155 cm^{-1}, 202 cm^{-1} and 236 cm^{-1}. The arrow highlights the appearance of Ga_2O_3 in the sample.

Raman measurements similar to the ones discussed above have the risk of damaging the GaSe flakes, thus introducing artifacts in the interpretation of the environmental degradation data. The left panel of **Fig. 3-7a** shows a sequence of Raman spectra acquired upon increasing integration time while keeping the incident power density 0.11 mW/µm^2, on a 14 nm thick GaSe flake deposited on SiO_2/Si substrate. For short integration time the spectra only show the features corresponding to pristine GaSe indicating that no laser-induced degradation is introduced. For integration times of 20 s or more the spectra start to develop new broad features and by optically inspect the flake after the measurement its surface seems to have been damaged as can be seen in the microscope picture shown in **Fig. 3-7b**. This fast degradation can help to explain previous results from the literature that reported fast degradation times on the order of few minutes when using a high excitation power laser and/or a long integration time. It was found that by transferring the flake onto a gold surface this laser-induced degradation can be reduced. The central panel of **Fig. 3-7a** shows how for the GaSe flake on gold integration time of up to 30 s does not show up any laser–induced degradation. This could be related to a more efficient heat management because of the higher thermal conductivity of gold.[360,361] However, for longer integration times the flakes suffer a similar laser-induced ablation (see the optical image in **Fig. 3-7b**) and the spectra develop again extra features not expected for pristine GaSe. Moreover, apart from the differences in laser-induced degradation time on Au and SiO_2 we also observe that the broad peak due to amorphous selenium (for GaSe/Au centered at 236 cm^{-1}) shifts at higher energies in the case of GaSe/SiO_2 (256 cm^{-1}), in the spectra recorded with an integration time larger than 60s. Such phenomenon can be explained by photo-crystallization of amorphous selenium.[362,363] Interestingly, as shown in the right panel of **Fig. 3-7a**, a partial encapsulation with h-BN is an effective method to completely prevent this laser-induced damage as evidenced by the Raman spectra that illustrates how a GaSe deposited on Au and capped with a h-BN flake does not present any laser-induced damage even for the longer integration times used in our experiment. This result suggests that the laser-induced degradation requires the presence of air, indicative of a photo-oxidative process. A further comparison has been presented in **Fig. 3-8**. **Fig. 3-8a** shows two Raman spectra of GaSe on SiO_2 and on Au/SiO_2 substrates both recorded with integration time 5 s and same incident power density (0.11 mW/μm^2). The minor difference between the spectra on the two substrates indicates that there is no enhancement of the GaSe Raman signal on Au. Hence, with integration time 20 s, the observable difference between the Raman intensity shown in **Fig. 3-8b** can be attributed to the faster degradation of thin GaSe on SiO_2 substrate. **Fig. 3-8c** presents that, under the same laser excitation power and with the increasing integration time, how the photo-induced damage level on the GaSe structure on SiO_2 and Au/SiO_2 substrate in air is much higher than that in the h-BN/GaSe/Au geometry as a function of integration time. The faster degradation of few-layer GaSe on SiO_2 may be caused by the O_2 species present in the substrate combined with inefficient thermal dissipation.

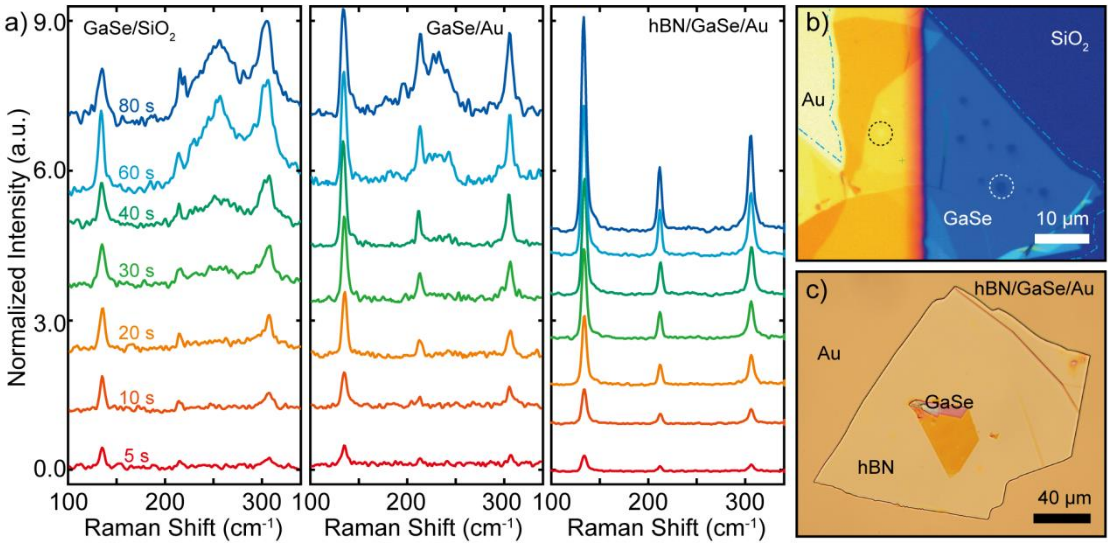

Fig. 3-7 Laser-induced degradation of GaSe. a) Raman spectra of a GaSe flake deposited onto gold (left), SiO_2/Si (center) and encapsulated with a boron nitride flake. b) Microscope image of a GaSe flake deposited onto gold and SiO_2 captured after the laser degradation experiment. The light blue dashed line highlights the contours of the GaSe flake. The spots that are visible on the flake (two of them highlighted by the dashed lines) are induced by the laser irradiation and were absent in the pristine flake. c) Microscope image of a GaSe flake deposited onto gold and then covered by a boron nitride flake.

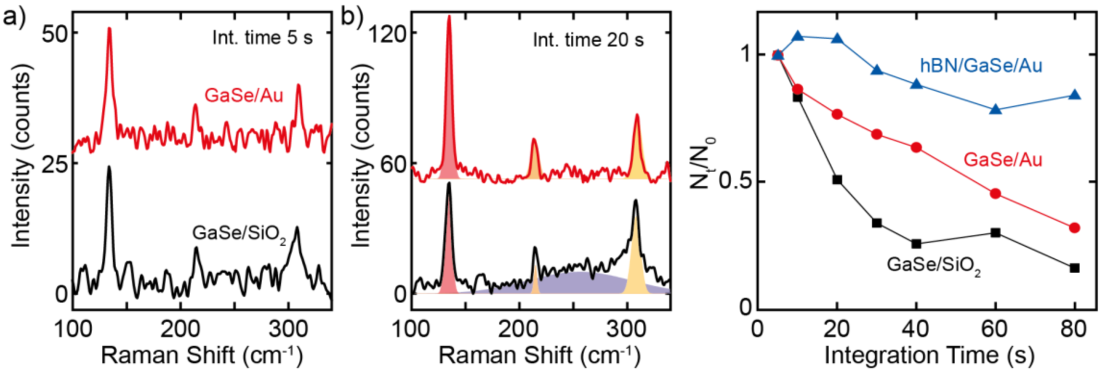

Fig. 3-8 Laser-induced degradation speed on different substrates of GaSe. Raman spectra of a GaSe flake on Au and SiO_2/Si with the integration time 5s (a) and 20s (b), respectively. c) Time-dependent normalized population of emitted photons per unit time of Raman signal from the GaSe flake deposited onto gold, SiO_2/Si and encapsulated with a h-BN flake. N_0 and N_t is the population of emitted photon per unit time with the integration time 5s and the increasing time (10s, 20s, 40s, 60s, 80s).

3.1.5 Optoelectronic performance

In the following, the study of environmental exposure effect on the optoelectronic properties of GaSe devices has been carried out. As shown in **Fig. 3-1b**, the GaSe photodetectors were fabricated by directly transferring GaSe flakes bridging two gold electrodes pre-patterned on a SiO_2/Si substrate, as described in sample fabrication section. **Fig. 3-9a** shows the current-voltage (*I*-*V*) characteristics of one GaSe device. In the dark state, the device is highly resistive and its dark current is within the noise level of testing setup showing a resistance of 420 GΩ. Upon global illumination with light at 405 nm of wavelength and a power density of 1.02 W/cm^2 the device builds up a sizeable photocurrent with the *I*-*V*s being linear and symmetric in bias voltage.[364,365] As can be seen in the plot after 72 hours in ambient conditions the device generates more photocurrent than the pristine one, while after 144 hours the photocurrent largely decreased. The resistance under illumination of the device is 1.5 GΩ, 1.1 GΩ and 20 GΩ in the pristine, after 72 hours and 144 hours, respectively. In **Fig. 3-9b,** the photoresponse of the device to modulated illumination (*I*-*t* curves) recorded with a bias of 8 V, has been presented.

To further investigate the role of the environmental induced degradation in the optoelectronic performance of the devices the long-term evolution of the photocurrent of devices kept in different environmental conditions has been followed. **Fig. 3-9c** shows the time evolution of the photocurrent (I_t) normalized to the photocurrent of the pristine device recorded right after fabrication (I_0) for four GaSe photodetectors kept in different environmental conditions. Interestingly, upon air exposure (green circles) the photocurrent increases steadily until almost triplicating its initial value at 39.5 hours. Importantly this change in photocurrent occurs before the appearance of Ga_2O_3 in the device revealed by Raman spectroscopy (the device tested in air exposure is the same one studied in **Figs. 3-1** and **3-6**). The initial increase of photocurrent is also observed in a device measured in pure O_2 atmosphere (red triangles), indicating that O_2 plays a critical role on the initial increase of the photocurrent. Indeed, according to our previous electronic probe microanalysis (EPMA) characterization, the atom ratio of Se and Ga is slightly smaller than 1 (Se:Ga = 49.5:50.5) in GaSe bulks (see the elements distribution analysis in **Table 7**), which indicates that in pristine GaSe flakes Se vacancies are already present that may act as effective sites for O_2 adsorption.[366]

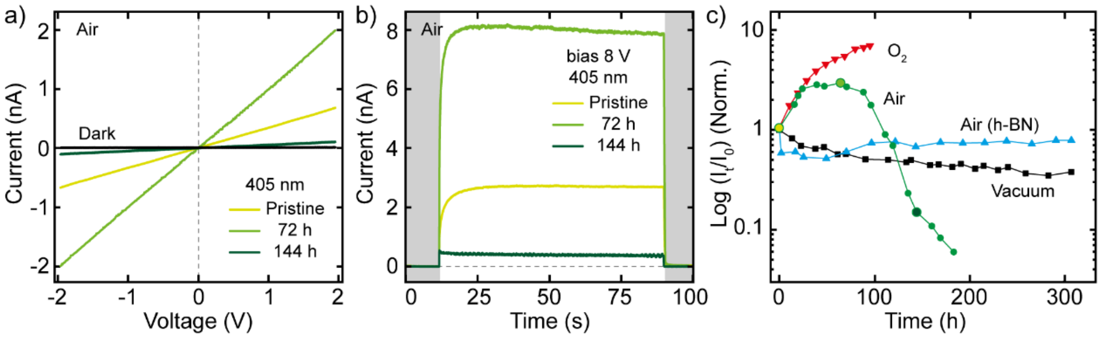

Fig. 3-9 Optoelectronic performances of GaSe photodetectors. a) *I-V* curves of a GaSe photodetector after 0h, 72h and 144h in the air with the illumination of a 405nm light source and under dark condition. b) *I-t* curves of a GaSe photodetector kept in air after 0h, 72h and 144h. The light at 405nm is modulated with a square wave. c) Normalized photocurrent evolution versus time of GaSe photodetectors in the dry-oxygen (red), air (green, blue) and vacuum atmosphere. The blue line was obtained with an h-BN encapsulated GaSe device.

Continuing the discussion of the photodetector exposed to air, after the initial increase, the photocurrent saturates between approximately 40 and 70 hours and then it decreases. At the same time the Raman spectra show a reduction of the amount of GaSe present in the device and the appearance of Ga_2O_3 among the aged components. Being a wide bandgap insulator (the bandgap is approximately 5 eV in bulk corresponding to 250 nm), Ga_2O_3 is not expected to yield photoresponse at 405 nm illumination and thus the conversion of GaSe to Ga_2O_3 is expected to reduce the total photocurrent generated in the device in the visible range.[367] The continuous oxidation process leads to the further increasing of Ga_2O_3, which results in the drop of photocurrent and the final device failure. The photocurrent evolution of a device kept in vacuum (5×10^{-4} mbar) and a device that has been capped by transferring an h-BN flake right after fabrication also has been studied (black squares and blue triangles). In both cases, the initial increase of photocurrent is not observed which agrees with the importance of O_2 to observe this photocurrent increase and with the AFM measurements of **Fig. 3-4**. Interestingly, while the device measured in vacuum shows a small (but noticeable) decrease of photocurrent over time, the h-BN encapsulated device displays a constant photocurrent. The slow decrease of the photocurrent of the device in vacuum can be attributed to its exposure to gases coming from the outgassing at the surrounding surfaces contrarily to the device encapsulated with h-BN that has a physical protective barrier. To further demonstrate how the h-BN encapsulation can be able to realize a long-term stable thin GaSe photodetector, the schematics of side view (top) and top view (bottom) of an h-BN encapsulated GaSe device have been shown in **Fig. 3-10a**. **Figs. 3-10b-c** shows the optical pictures of the h-BN encapsulated GaSe devices recorded in pristine state and after being exposed to the air for 40 days. Remarkably, **Fig. 3-10d-e** shows how an h-BN encapsulated GaSe photodetector exhibits an optoelectronic performance comparable to the initial device even after 40 days after its fabrication (The initial current decrease can be attributed to the air species trapped at InSe and h-BN interface, after that there is a negligible reduction in the current over 40 days). This solution is quite convenient if one compares it with fully encapsulated devices, sandwiched between two h-BN flakes, that requires more complex fabrication process to contact electrically the sandwiched flakes.

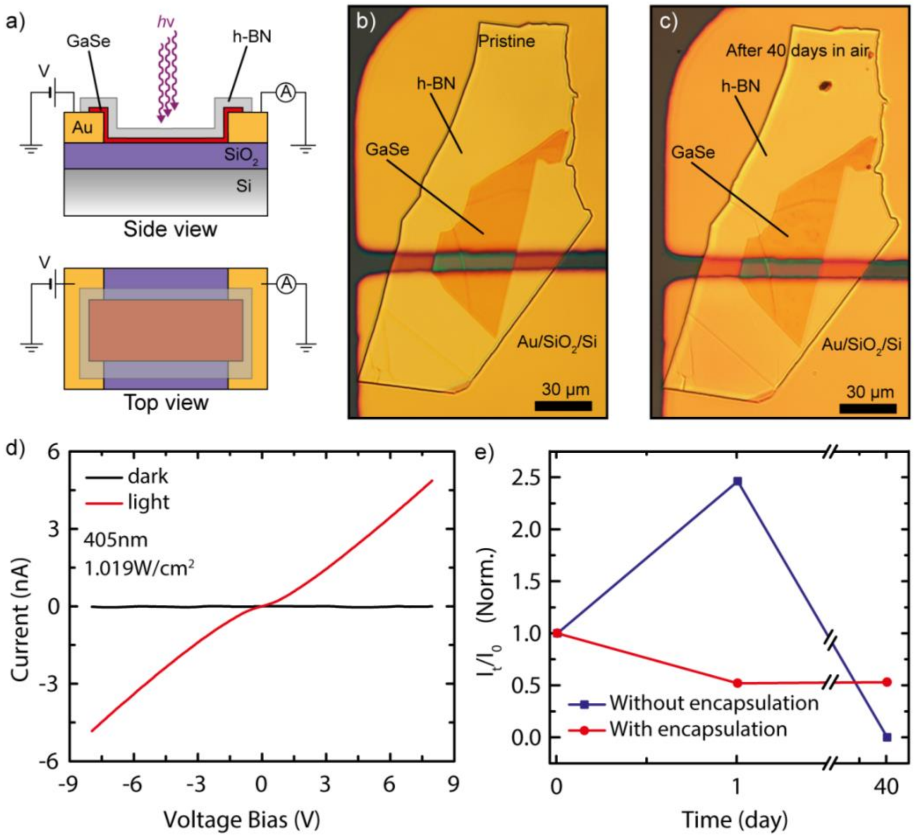

Fig. 3-10 h-BN encapsulated device. a) Schematic of a h-BN encapsulated GaSe photodetector. b-c) Optical micrographs of a h-BN encapsulated GaSe photodetector recorded just after fabrication (b) and after 40 days in air (c). d) *I*-*V* characteristic of the GaSe photodetector encapsulated with h-BN after 40 days in air. e) The long-term photocurrent evolution of GaSe photodetector with and without h-BN encapsulation in air.

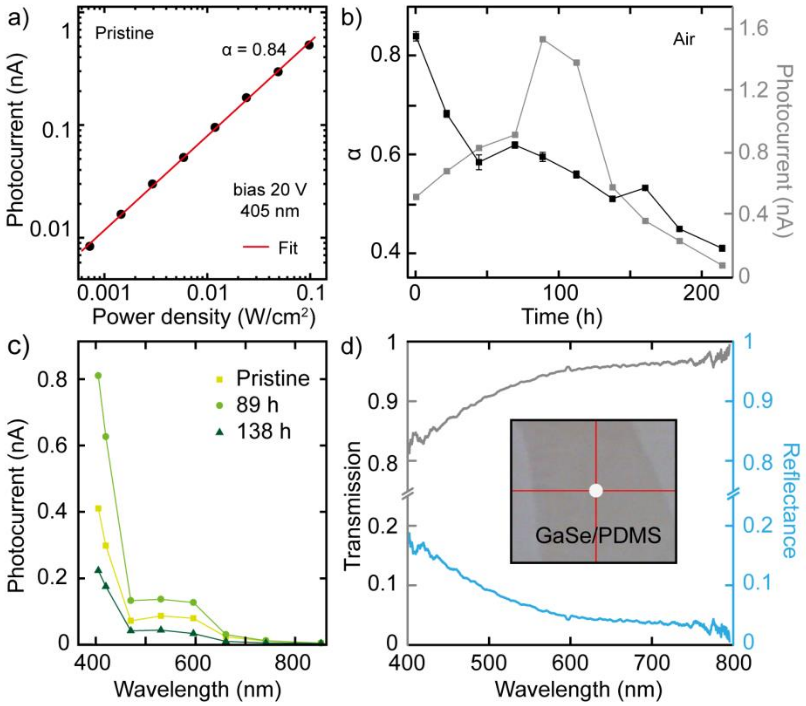

Fig. 3-11 a) Photocurrent of a GaSe device as a function of incident optical power in log-log scale. The red line is a fit to a power law. b) Time evolution of the power law exponent α (left y-axis) and of the photocurrent (right y-axis) for the device of panel (a). c) Wavelength-resolved photocurrent for the pristine device and after being kept in air for 89 hours and 138 hours. d) Transmission (left axis) and reflectance (right axis) spectrum of a thin GaSe flake. The inset shows the optical picture of the thin GaSe flake deposited onto the PDMS substrate and the white spot indicates the illumination position.

To gain further information on the degradation of GaSe, the power dependency of the photocurrent as a function of time in a second GaSe photodetector kept in air was studied. **Fig. 3-11a** shows the results of such power dependency measurements performed on the pristine device. As can be seen from the graph, the photocurrent generated in the device grows when increasing the incident optical power. The data plotted in a log-log scale appears linear, which is a sign of a power law dependency,[368] which can be fitted to the equation $I_{\mathrm{ph}} = A \cdot P^{\alpha}$, where α is a dimensionless fitting parameter and A is a quantity related to the responsivity. The power exponent α contains information about the traps present in the system and is expected to be equal to 1 in the case of a traps-free photodetector and becomes smaller in the presence of traps.[369] **Fig. 3-11b** shows the evolution of the exponent α (left axis) together with the photocurrent recorded in the device at a fixed optical power (right axis). As can be seen from the plot, the photocurrent increases in the first 100 hours and then decreases, which is in agreement with the device discussed previously. On the other hand, α displays a monotonous decreasing behavior, passing from 0.84 to 0.42 in approximately 200 hours. The observed behavior of α can be explained by an increase in the number of trap states between the valence and conduction bands as a function of time.[368,369] Finally, the wavelength-dependency of the photocurrent and its evolution over time were studied. **Fig. 3-11c** shows three photocurrent spectra recorded in the pristine device and after 89 hours and 138 hours of exposition to air. At short wavelengths the photocurrent can reach hundreds of pA and it rapidly decreases for longer wavelength. Eventually it goes to zero for wavelengths larger than 800 nm, which resembles the features of GaSe transmission and reflectance spectra shown in **Fig. 3-11d**. Despite the change in magnitude of the photocurrent, the three spectra feature a similar shape suggesting that the photocurrent generation is dominated by the absorption of GaSe.

3.1.6 Discussion: degradation mechanism

The results that have been discussed until now indicate that degradation process of thin GaSe has very important consequences on the properties of optoelectronic devices based on this material. The Raman measurements discussed in **Fig. 3-6** and **3-7** indicate that GaSe degrades into various components, mainly α-selenium, Ga_2Se_3 and Ga_2O_3. Since the photocurrent spectrum of the device is dominated at all the stages by the GaSe photon absorption (as can be seen in **Fig. 3-11c**), it can be proposed that the non-monotonous evolution of the photocurrent in devices kept in air is due to a competition between various mechanisms that can influence the photocurrent: (1) the decrease of the GaSe present in the device and the increase of Ga_2O_3 can lead to a decrease of the total photocurrent, (2) adsorbed oxygen and selenium vacancies can increase or decrease the photocurrent due to photogating effects, (3) the appearance of Ga_2Se_3 and α-Se can increase the photoresponse due to built-in electric-fields and/or the introduction of strain the GaSe lattice. Moreover, the presence of these materials can perturb the GaSe lattice and introduce strain, which may change the photoresponse.[340-346,351]

Recently, Shi *et al.* reported calculations showing that photo-excited electrons in GaSe can be effectively transferred to O_2 molecules adsorbed on the surface and create O_2^- anions.[340-346] The anions can then react with GaSe and replace Ga-Se bonds by Ga-O bonds leading to the formation of the oxidation products Ga_2O_3 and elemental Se. This process is consistent with the Raman measurements of GaSe of **Fig. 3-6** and can explain the evolution of the photocurrent observed in **Fig. 3-9c** and **3-11b**.

The trapping of electrons by O_2 molecules can induce an increase of the photocurrent thanks to the photogating effect (2), as observed in the first 100 hours of exposition of GaSe to air. The influence of photogating on the photoresponse of the device is also confirmed by the decrease of the power exponent α as a function of time. Part of this initial increase in photocurrent may also be caused by the introduction of strain (3), as suggested by the AFM measurements in **Fig. 3-4**. Finally, the decrease of the photocurrent after approximately 100 hours in air can be explained by a reduction of the amount of GaSe in favor of Ga_2O_3 because of the oxidation process (1), which has a lower photon absorption and larger electrical resistivity under illumination of 405nm light source.[367]

3.2 Environmental induced trap-passivation: the case of InSe

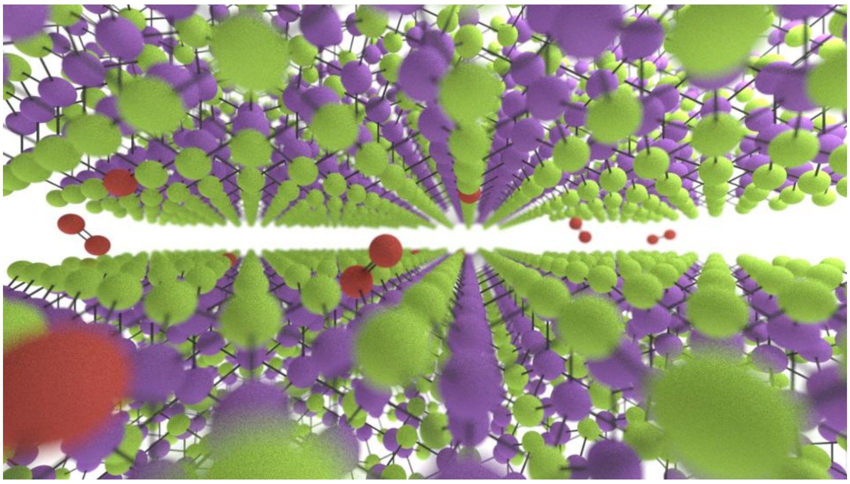

A set of experiments aimed at explaining the strong scattering in the photoresponsivity values reported in the literature in thin InSe photodetectors have been presented. By performing optoelectronic measurements on thin InSe-based photodetectors operated under different environmental conditions it is found that the photoresponsivity, the response time and the photocurrent power dependency are strongly correlated in this material. This observation indicates that the photogating effect plays an important role for thin InSe flakes, and it is the dominant mechanism in the ultra-high photoresponsivity of pristine InSe devices. In addition, when exposing the pristine InSe photodetectors to the ambient environment, a fast and irreversible change in the photoresponse has been observed, with a decrease in the photoresponsivity accompanied by an increase of the operating speed. This photodetector performance change (upon atmospheric exposure) can be attributed to the decrease in the density of the traps present in InSe, due to the passivation of selenium vacancies by atmospheric oxygen species. This passivation is accompanied by a downward shift of the InSe Fermi level and by a decrease of the Fermi level pinning, which leads to an increase of the Schottky barrier between Au and InSe. This study reveals the important role of traps induced by defects in tailoring the properties of devices based on 2D materials and offers a controllable route to design and functionalize thin InSe photodetectors to realize devices with either ultrahigh photoresposivity or fast operation speed. Note that this section is mainly based on the published paper "The role of traps in the photocurrent generation mechanism in thin InSe photodetectors" in Materials Horizons where I am the first author.[370]

3.2.1 Background

The presence of defects in 2D semiconductors, such as chalcogen vacancies in layered metal chalcogenides, can act as preferential sites for physical/chemical adsorption of environmental species (that can initiate the degradation process of 2D materials, as has been observed in thin GaSe) and/or may introduce additional scattering of the carriers (that could act as harmful active traps in working devices).[338,339] For instance, the mobility of 2D semiconducting transistors kept in vacuum or encapsulated with boron nitride (processed in inert atmosphere) is typically more than one order of magnitude larger than the mobility measured in the air.[371,372] Especially, in the case of single-layer and bilayer MoS_2, among the various reports, the device mobility at room temperature ranges from 0.1 $cm^2V^{-1}s^{-1}$ in air to tens of $cm^2V^{-1}s^{-1}$ in vacuum or with top/bottom deposited protection materials.[179,373,374] In addition, the existence of photo active traps in the 2D semiconductors can perform a significant effect on the photocurrent generation process as a photodetecting device takes response to the external illumination, and the variation of trap levels and density in the active channel materials may introduce a large scattering of photoresponse values, as have been observed in thin InSe photodetector. As mentioned in chapter 1.3 (the advances of GaSe and InSe), various photodetectors based on thin InSe flakes (as the active channel part), including metal-semiconductor-metal (M-S-M) geometry and graphene based van der Waals heterostructures, have been reported in literature with responsivities going from 0.035 A W^{-1} to ultrahigh values of ~10^7 A W^{-1} and detectivity up to ~10^{15} Jones (see **Table 6**), which are among the best performances reported for 2D photodetectors. In the case of InSe, the defects related to In adatoms and Se vacancies, which can be related to the In-rich atmosphere in which high-quality InSe crystals are grown (see chapter 2.1.4, **Fig. 2-5**),[375,376] may play important roles during the photocurrent generation process in thin InSe photodetectors.[375-378] Interestingly, the presence of defects in InSe crystals, especially selenium vacancies (V_{Se}),[379] is predicted to promote the physical adsorption and chemical dissociation of O_2/H_2O molecules and V_{Se} can act as preferential sites for the adsorption of these molecules.[375-378] This phenomenon can help in explaining the performance degradation reported in various works on thin InSe devices.[261,366,376,377,380] Recently, both theoretical calculations and experimental scanning transmission electron microscopy (STEM) reported that the selenium vacancies V_{Se} in InSe crystals can be passivated by chemical dissociation of O atoms at these sites.[376,377,379] Similarly, Po-Hsun *et. al.* demonstrated that the change of Raman and X-ray photoelectron spectra (XPS) of pristine InSe flakes exposed to ambient air is comparable to that observed when exposing InSe to dry oxygen atmosphere. The authors attribute these observations to the formation of a superficial $InSe_{1-x}O_x$ layer that encapsulate the InSe beneath and promote a long-term stability of thin InSe devices.[381] Despite the large amount of work on InSe photodetectors, an important question that remains unanswered is how this passivation influences the optoelectronic properties of photodetectors based on thin InSe.

3.2.2 InSe photodetector fabrication

Thin InSe photodetectors are fabricated by deterministic placement of InSe flakes (thicknesses going from ~6 nm to ~20 nm) mechanically exfoliated from ε-InSe bulk crystals grown by Bridgman method. The details of InSe bulk crystals and deterministic transfer method can be found in section 2.1 and 2.4, respectively. **Fig. 3-12a** shows a microscopic picture of a thin InSe flake isolated onto Gel-Film (top panel) and a picture of the final photo-detecting device (bottom panel), formed by the same flake after being transferred bridging two pre-patterned electrodes (5 nm thick chromium sticking layer and 50 nm thick gold) evaporated on a SiO_2/Si substrate (with a SiO_2 thickness of 280 nm). The differently colored regions of InSe deposited onto Gel-Film visible in **Fig. 3-12a** are due to different thicknesses of the material. From AFM topography measurements, it can be determined that the thinnest region of the flake, which forms the channel in the final device, is 9.1 nm thick corresponding to approximately 11 layers.[258] Following the same fabrication processes, five more thin InSe photodetectors have been fabricated and their corresponding thicknesses have been marked in **Fig. 3-12b**.

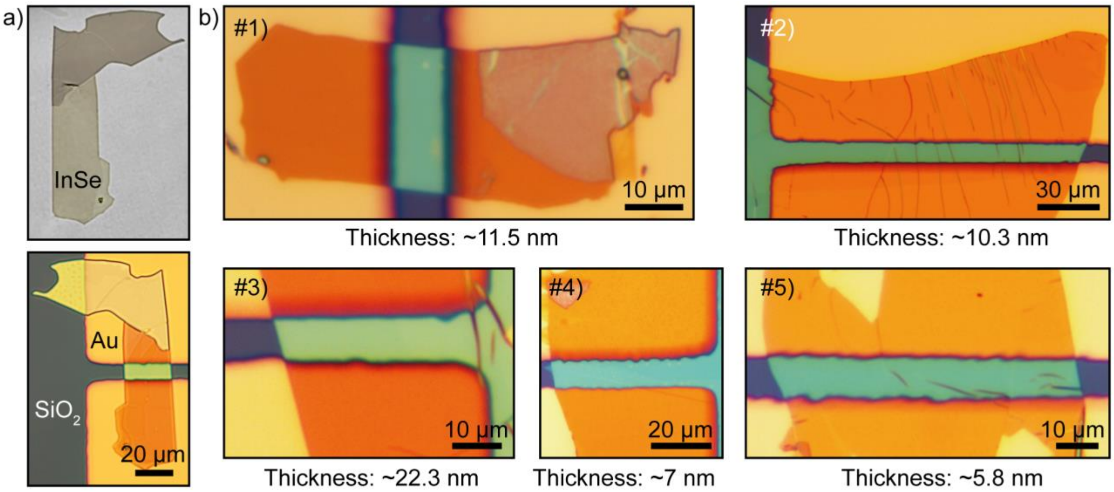

Fig. 3-12 Thin InSe photodetectors. a) Optical pictures of few-layer InSe exfoliated onto PDMS (top) and deterministically transferred onto pre-patterned gold electrodes (bottom). b) Optical pictures of five investigated thin InSe photodetectors with various thicknesses and labeled #1 to #5.

3.2.3 Surface morphology and structural stability

After the sample fabrication, the surface morphology variation of InSe photodetectors before and after being exposed to the air was first followed in both macro and micro perspectives. **Fig. 3-13a** shows the optical pictures recorded from an InSe photodetector in pristine state (left) and after being exposed in the air for 1 month (right). No obvious change is visible on the InSe flake according to the comparison of optical contrast, shape, as well as the surface morphology apart from the appearance of some bubbles-like structures. **Fig. 3-13b** shows a comparison of topography of an InSe flake deposited on Au substrate recorded using AFM before and after being exposed in the air. By inspecting the images, one can see that, at the initial state (left panel in **Fig. 3-13b**), the as-exfoliated InSe presents a smooth surface. The second AFM image (right panel in **Fig. 3-13b**), recorded after 2 days, and presents an increase in number and size of bubbles characterized by a circular shape. The similar topographical variation also has been observed on the aged InSe flakes that were deposited on graphite, Pt, and SiO_2/Si substrates (see **Figs. 3-13c-d**). This topographic evolution on thin InSe seems to be related to the adsorbates on the flake surface instead of the degradation that has been observed on thin GaSe flakes after being exposed in the air.

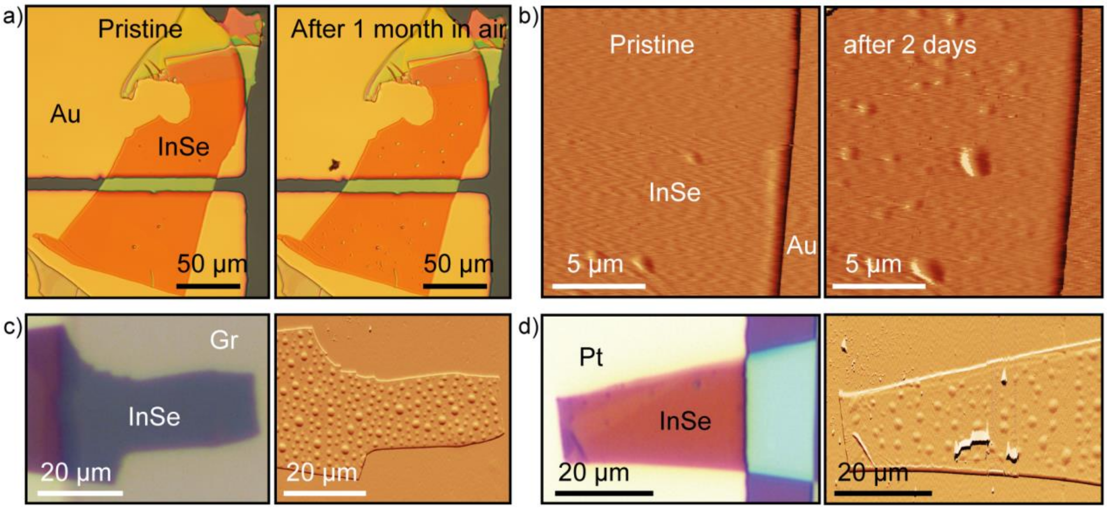

Fig. 3-13 a) Optical pictures of a InSe photodetector recorded in pristine state (left) and after being exposed in the air for 1 month (right) by microscope using reflection mode. b) Surface morphology of a thin InSe flake deposited on Au substrate recorded in pristine state (left) and after being exposed in the air for 2 days (right)using AFM. c-d) Typical surface topology of aged InSe flakes deposited on graphite (c) and gold (d) substrates.

Raman spectroscopy measurements are then employed to investigate the chemical composition or/and crystal structure change of the InSe flake during the degradation process. **Fig. 3-14a** shows the Raman spectrum acquired just after the fabrication of the device on the region of the flake located above the gold electrode (indicated in **Fig. 3-12a**, bottom panel). The spectrum shows three prominent peaks centered at 116 cm^{-1}, 178 cm^{-1}, and 227 cm^{-1}. These three peaks are due to vibrational modes of InSe and they can be attributed respectively to A'$_1$, E'' and A'$_1$. A fourth peak is visible at 200 cm^{-1} and is due to A''$_2$, which is sensitive to the crystalline phase.[282-284] Since the degradation of 2D materials is a common phenomenon, the stability of the InSe flake was tested by repeating the Raman measurements after two weeks of exposure to ambient conditions. As can be seen from **Fig. 3-14a** the Raman spectra of the pristine flake and the one of the aged flake are very similar, the only difference being a ~15% reduction of the intensity of the peaks in the aged spectrum, similar results also were obtained on additional flakes in **Fig. 3-14b-c**. These observations are consistent with previous Raman and XPS studies from literature.[269,343,381-383] Then from the **Fig. 3-14d** it can be estimated that the reduction of the Raman signal corresponds to the degradation of the top ~1-2 layers. Therefore, both the surface morphology inspection in **Fig. 3-13** and Raman measurements in **Fig. 3-14** indicate that the slight structure change of mechanically exfoliated thin InSe flakes may induced by the normal surface adsorbates upon exposure to ambient air, a different behavior from thin black phosphorous or GaSe.[328,331]

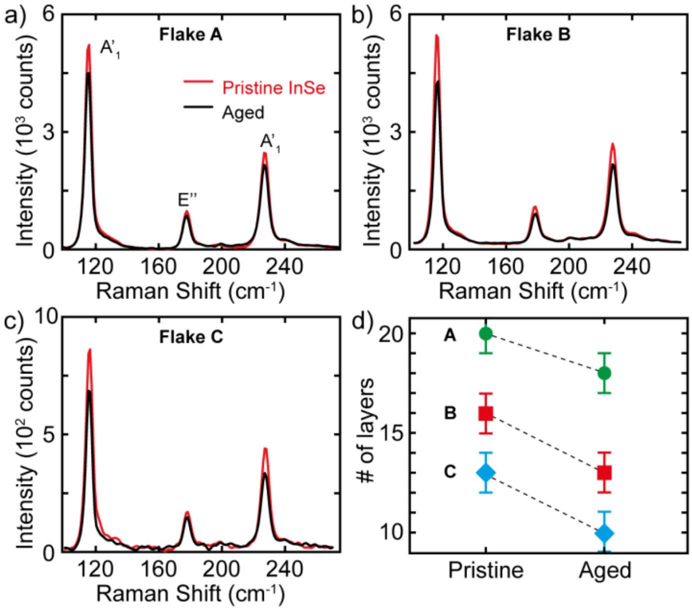

Fig. 3-14 a-b) Raman spectra (532 nm laser, power density 0.11 mW µm^{-2}) of two InSe flakes in pristine conditions and after 10 days in air. (c) Estimation of the thickness (number of layer) of pristine and aged InSe flakes. In average a loss of 2-3 layers after aging the sample in air has been observed.

3.2.4 Optoelectronic performance of pristine InSe photodetectors

To investigate the properties of pristine InSe photodetectors, optoelectronic measurements are performed on a freshly prepared device kept in vacuum (sample #1 in **Fig. 3-12b**). The measurements were carried out in a home-made vacuum probe-station (described in section 2.5 in chapter 2) connected to a turbomolecular pumping station capable of reaching a base vacuum level of $\sim 1 \times 10^{-6}$ mbar, and the two gold electrodes (used a source and drain) are connected to a sourcemeter (Keithley® 2450) and the silicon substrate (heavily p-doped) is connected to a voltage source and used as a back gate. All the measurements presented in this part were performed at room temperature (T = 300 K). **Fig. 3-15a** shows the transfer curve of the device, that is the source-drain current recorded while slowly changing the gate voltage V_G. This measurement was performed with a bias voltage V_{DS} of 1 V and keeping the device in dark conditions. The device shows negligible current at negative gate voltages (off state, $V_G < V_T$) and starts to conduct current for positive voltages (on state, $V_G > V_T$). These observations indicate that the InSe channel is n-doped and from the plot a threshold voltage V_T = 10 V has been determined, which is in agreement with previous reports on InSe transistors.[258,381,382,384,385] From this transfer curve one can also estimate the electron mobility using the equation:

$$\mu_{\mathrm{n}} = \frac{L}{W C_{\mathrm{OX}} V_{\mathrm{DS}}} \left(\frac{dI_{\mathrm{DS}}}{dV_{\mathrm{G}}}\right), \tag{3-1}$$

where L = 10 μm and W = 24 μm are the channel length and width of the InSe photodetector, C_{OX} = 115 μF m^{-2} is the capacitance per unit area of 280 nm thick SiO_2 and dI_{DS}/dV_G is the transconductance. Using the transconductance extracted from the linear regime of the transfer curve, one can find a calculated mobility of ~0.06 cm^{2}V^{-1}s^{-1} at a bias voltage V_{DS} of 1 V. Compared with the reported results based on the InSe transistors fabricated by lithography method, this smaller value may be caused by a larger contact resistance in our case that does not involve the thermal evaporation of the electrodes onto the InSe flake.[314] In **Fig. 3-15b**, the black curve shows the same transfer curve of panel a represented with a semi-logarithmic scale. From this graph, one can see that when passing from the off state to the on state the current flowing through the device increases of more than two orders of magnitude. The steepness of the current in the on-off transition region can be quantified by the subthreshold swing S, which is defined according to:

$$S = \frac{dV_{\mathrm{G}}}{d(\log_{10}(I_{\mathrm{DS}}/V_{\mathrm{DS}}))}, \tag{3-2}$$

from the data of **Fig. 3-15b**, S ~10 V/decade was determined, a value that is much larger than the ideal MOSFET (metal-oxide-semiconductor FET) subthreshold swing of 60 mV/decade and that is comparable to values reported previously for atomically thin high-gain photodetectors.[325] This large value for S points to the existence of trap levels in the device.[386]

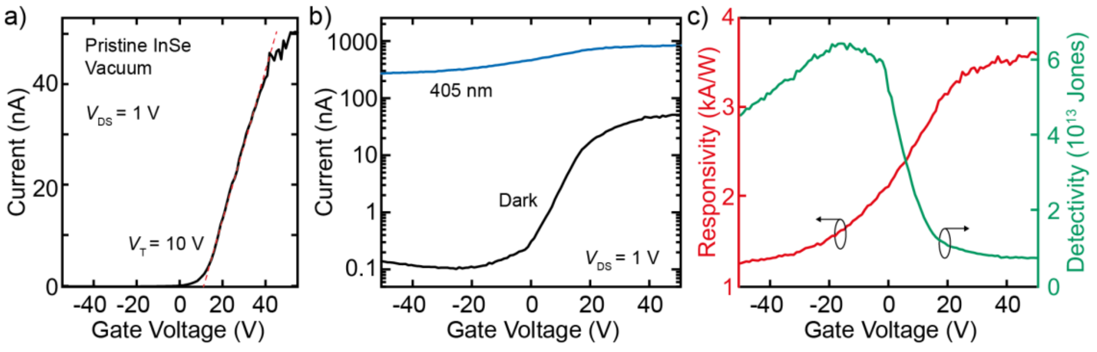

Fig. 3-15 Gate voltage tunability of optoelectronic properties of a pristine InSe photodetector (# 1) in vacuum. a) Current versus back gate voltage transfer curve at V_{SD} = 1 V of a pristine InSe photodetector kept in vacuum and in dark. b) Current

versus gate voltage in dark and under illumination at 405 nm (power density 0.92 mW m^{-2}) represented in semi-logarithmic scale. c) Responsivity (R, left axis) and detectivity (D^*, right axis) of pristine InSe extracted from the curves in panel (b).

After the characterization of the InSe photodetector in dark conditions, its optoelectronic properties and response to external illumination with the gate bias control are tested. The blue curve in **Fig. 3-15b** corresponds to the transfer curve of the device under external illumination with a light source of wavelength 405 nm and power density of 0.1 mW cm^{-2}. Under these conditions, the current passing through the device increases to a maximum of 1000 nA in the on state and to more than 200 nA in the off state, corresponding to an increase from the dark current of more than one order of magnitude in the on case and of three orders of magnitude in the off state. From the current measured while keeping the device in dark (I_{dark}) and under external illumination (I_{light}), one can calculate the responsivity R and the detectivity D^* of the photodetector using the following equations:[387,388]

$$R = |I_{\mathrm{ph}}| / (P\,A), \tag{3-3}$$

and

$$D^* = \quad R\,A^{1/2} / (2\,e\,I_{\mathrm{dark}})^{1/2}, \tag{3-4}$$

where I_{ph} is the photocurrent calculated as (I_{light} - I_{dark}), P is the external illumination density, A is the active area of the photodetector (that it is assumed equal to the InSe channel area) and e is the elementary charge. Note that the formula to calculate the detectivity of Eq. 3-4 assumes that the photodetector is limited by shot noise,[321] which is a common mistake in the community that has been spotted by Fang Yanjun, *et al.*[389] These two figures of merit R and D^* as a function of gate voltage are shown in **Fig. 3-15c**, calculated using the data of **Fig. 3-15b**. The responsivity follows the same behavior of the photocurrent, reaching its maximum at positive gate voltages in the 'ON' state and decreasing when the transistor is in the 'OFF' state. On the other hand, the detectivity is not monotonous and it reaches its maximum at a gate voltage of approximately -20 V and decreases for both large positive voltages and negative voltages. The values of R and D^* reported here are comparable to the highest values reported in literature for thin InSe photodetectors,[261,262] confirming the excellent performances of InSe as an active material in the fabrication of photodetectors. As a final comment, both the photocurrent and the responsivity show a decrease at negative gate voltages when the device is in the 'OFF' state. This can be explained by the presence of trap states for majority carriers near the conduction band of InSe whose occupation is controlled by the position of the Fermi level.[325] The measurements discussed up to this point, which have been performed in vacuum, indicate that trap levels are present in material and that these can influence the photodetection mechanism of InSe photodetector.

The complementary optoelectronic performance of a InSe device in pristine state characterized under vacuum conditions can be found in **Fig. 3-16**. **Fig. 3-16a** shows the current-voltage characteristics (*I*-*V*s) recoded in dark as a function of gate bias (V_g), and both the current at the positive and negative bias condition start to increase as the V_g is switched from -50 V to 50 V, which indicates the device operation is transferred from ‘OFF’ state to ‘ON’ state. The properties that how the device response to the external illumination are shown in panel b and four *I*-*V* curves recorded without gate bias control under illumination of 405nm, 470 nm, 530 nm, and 660 nm have been presented, respectively. **Fig. 3-16c** shows the results of power dependency measurements performed on the pristine device and a typical the photoresponse of the device to modulated illumination (*I*-*t* curves) recorded with a bias of 1 V, has been presented in the inset panel. As can be seen from the graph, the photocurrent generated in the device grows when increasing the incident optical power. **Fig. 3-16d** shows a photocurrent spectrum that is the photocurrent varies as a function of the illumination wavelength.

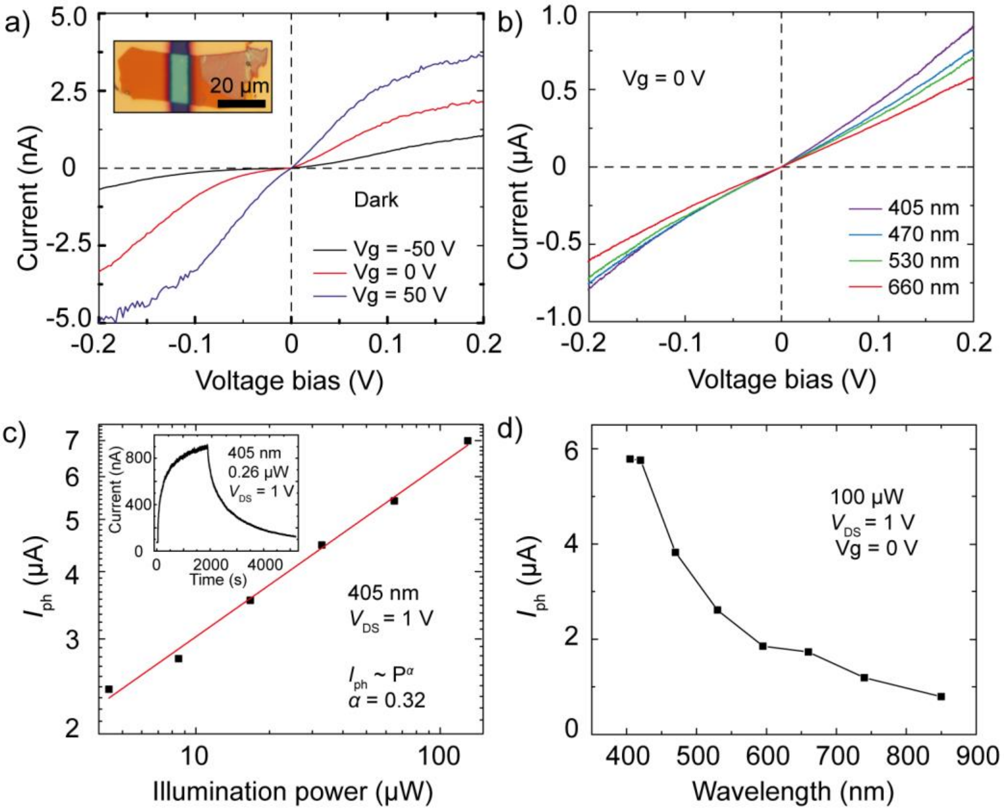

Fig. 3-16 Basic optoelectronic characterization in vacuum (0.5×10^{-6} mbar to 1×10^{-6}

mbar) of the InSe photodetector (#1). a) The *I-V* curves of the InSe photodetector in dark condition with the gate voltage V_g = -50 V, 0 V, and 50 V, respectively. b) The *I-V* curves of the InSe photodetector under various illumination wavelengths with the same power density of 35.4 mW cm^{-2}. c) The photocurrent versus illumination intensity (~4 – 128 μW) plotted in log-log scale with the 405 nm illumination. The inset figure is an *I*-t curve for the InSe photodetector. d) The photocurrent evolution with different wavelength under the illumination density of 35.4 mW cm^{-2} at V_{DS} = 1 V.

3.2.5 Environmental influence on performances of InSe photodetectors

In the following, the influence of air on the performances of InSe photodetectors will be investigated. Just after the device fabrication, a pristine InSe photodetector (sample #2 in **Fig. 3-12b**) was stored in high vacuum (pressure ~10^{-6} mbar) and the optoelectronic performance was measured. To characterize the device in this case its response in time to external square-wave modulated illumination was studied. The red curve in **Fig. 3-17a** shows the current flowing in the device at V_{DS} = 1 V as a function of time (*I*-*t*) while switching on and off a 530 nm light source focused onto the surface of the device. The two curves of **Fig. 3-17a** have been recorded with two illumination power densities, 45 mW cm^{-2} and 22.5 mW cm^{-2}. When switching on the illumination at around 30 s with power 45 mW cm^{-2} the current starts to slowly increase from ~400 pA to ~43 nA in approximately 100 s giving a responsivity of 0.09 A W^{-1}, while in the case of 22.5 mW cm^{-2} the current reaches a value of ~25 nA and the responsivity is 0.11 A W^{-1}. This increase of the responsivity for decreasing illumination power densities points to the presence of traps for minority carriers (holes) in the device and more details of the power dependent measurements will be discussed later in this chapter.[321,390]

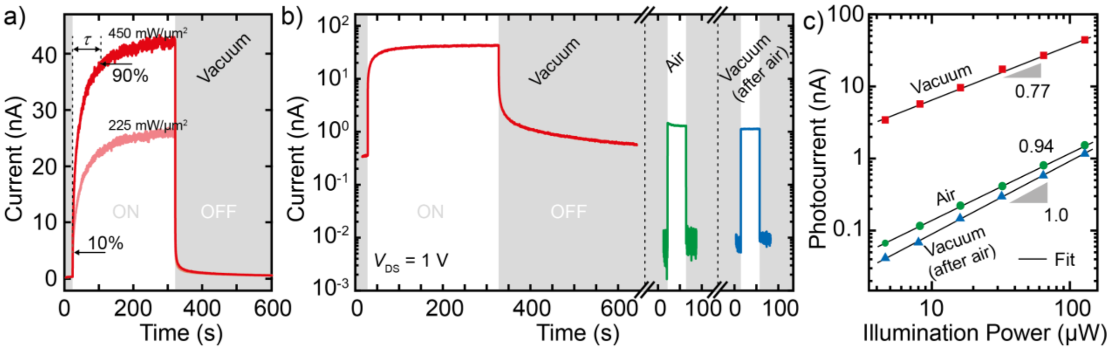

Fig. 3-17 Evolution in the air of an InSe photodetector (# 2). a) Current at V_{SD} = 1 V recorded in an InSe photodetector as a function of time while turning on and off a 530 nm light source with two different illumination powers. b) Current at V_{SD} = 1 V recorded in an InSe photodetector as a function of time while turning on and off illumination at 530 nm (power density 45 mW cm^{-2}). The device was kept first in vacuum (pressure ~10^{-6} mbar), then it was transferred into the air for ~20 hours (~10^{3} mbar) and finally it was kept again in vacuum. c) Photocurrent as a function of illumination power at 530 nm recorded in the three environments of the panel (b).

The slow response of the photocurrent to external illumination shown in **Fig. 3-17a** can be quantitatively characterized by the response time, which can be estimated using the 10%-90% criterion. Here the response time is defined as the time that it takes for the current to increase from 10% of the saturation value to 90%. From the current vs. time traces (*I*-*t*) at 45 mW cm^{-2} a rising time τ_{on} = 77 s and a decay time τ_{off} = 3.2 s are determined.[321] **Fig. 3-17b** shows the data just discussed plotted in semi-logarithmic scale, where the small dark current of ~400 pA is visible. After carrying out the measurements in vacuum then the device was exposed to air in ambient conditions for approximately 20 hours and then repeated the *I*-*t* measurements. The green curve in **Fig. 3-17b** is the corresponding *I*-*t* measured in air with the same illumination parameters used for the *I*-*t* in vacuum. As can be seen from the plot, both the dark current I_{dark} and the current under illumination I_{light} recorded in air conditions are much smaller than the initial values recorded in vacuum and the photocurrent I_{ph} becomes ~1.2 nA, a ~40 times reduction. At the same time, a decrease of both the rising and decay time of the device was observed, which becomes smaller than ~60 ms, approximately 2 or 3 orders of magnitude smaller than the initial values. Subsequently, after measuring the device in the air, the chamber was evacuated reaching again a pressure of ~10^{-6} mbar and the same optoelectronic characterizations were repeated. From the blue curve shown in **Fig. 3-17b**, one can see that both I_{dark} and I_{light} remain at the same level recorded in the air indicating that the device underwent an irreversible transformation after being exposed to air for ~20 hours. The extracted responsivity is 0.002 A W^{-1} and both the rising and the decay time are equal to ~40 ms. From these measurements, it can be found that by exposing the device to air, the InSe photodetector evolves from an initial state characterized by larger responsivity but slower time response to a final state with smaller responsivity and faster time response.

In a photodetector, important information about the mechanism behind the photocurrent generation can be extracted from the power dependency of the photocurrent.[328,391] During the *I-t* measurements discussed above, the photocurrent for different light intensities going from 45 mW cm^{-2} to 450 mW cm^{-2} also was measured. For each value of light intensity, the maximum photocurrent was extracted and the results were plotted in **Fig. 3-17c**. The photocurrent as a function of the illumination power density is shown in a log-log representation and the three datasets correspond to the three states of the device (**1** pristine in vacuum, **2** after 20 hours of exposure to air, **3** in vacuum after being exposed to air). From the graph, one can see that each of the three datasets follows approximately a straight line, indicating that the photocurrent and the illumination power are connected by a power law. This relation can be expressed by the equation:

$$I_{ph} = A \cdot P^{\alpha}, \tag{3-5}$$

where α is the dimensionless exponent of the power law and A is a parameter related to the photodetector responsivity. The value of the exponent α provides the information of traps present in the photodetecting system. In fact, in an ideal trap-free photodetector, the exponent α is equal to 1 meaning that the photocurrent scales linearly with the illumination power and the responsivity is constant as a function of power. Note that the equation 3-5 also has been introduced to explain the traps in GaSe in section 3.1. When trap states (for minority carriers) are present in the system α becomes smaller than 1 and the responsivity depends sub-linearly on the illumination power (as for high powers most of the traps are already filled in and further illumination power cannot effectively increase the photogain), effectively decreasing for higher illumination powers. As can be seen from **Fig. 3-17c**, by fitting the data to equation (5) it is found that the InSe photodetector in its pristine state in vacuum (**1**) is characterized by α = 0.77. This value increases to 0.94 after that 20 hours of exposure of the device to air (**2**). The final measurements performed on the device in vacuum after being exposed to air (**3**) show a value for α of 1.0. The observed evolution of α indicates that in pristine InSe photodetectors trap states play a role in the photocurrent generation process and that these trap states can be modified and eventually irreversibly removed after exposing the InSe photodetector to air.

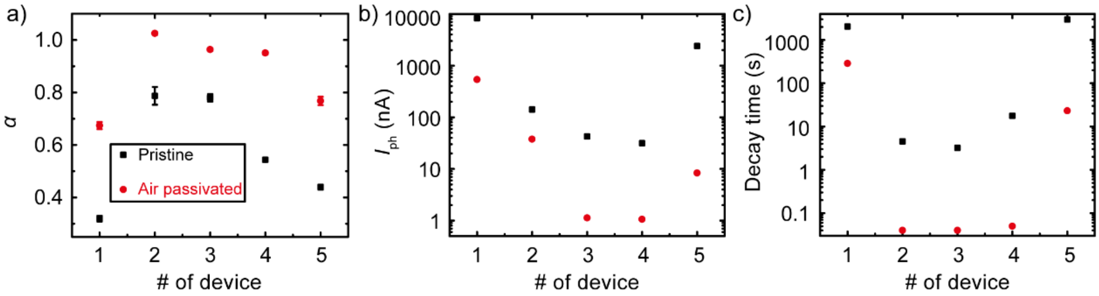

Fig. 3-18 Statistic results of five InSe photodetectors (in **Fig. 3-12b**) before and after air passivation. *α* (a), photocurrent (b), and decay time (c) of five InSe photodetectors with pristine state and after air passivation under the same measurement conditions. All the tested InSe photodetectors share the same manner when exposed to air.

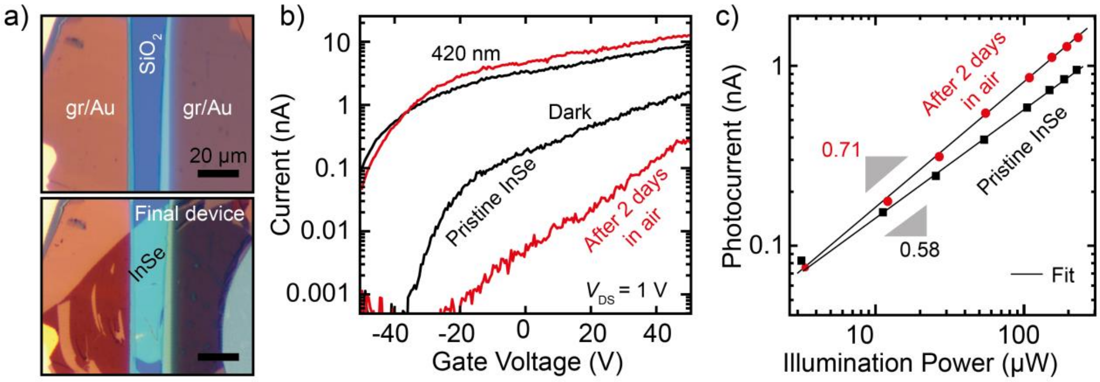

Fig. 3-19 Time-dependent performance of a graphite-InSe-graphite photodetector when exposed to air.

To further confirm the increase of *α* and operation speed, and the decrease of photoresponsivity in InSe photodetectors exposed to air, discussed above for a single device, a statistical analysis that is based on all the five investigated Au-InSe-Au devices has been shown in **Fig. 3-18**. Moreover, a similar increase in *α* has been observed also in graphite-InSe-graphite devices (see **Fig. 3-19**). Obviously, this common behavior is independent on the initial parameters of the measured devices such as responsivity, *α* or response time. This fact has been illustrated in **Fig. 3-20a** and **b** where the results of five different devices (shown in **Fig. 3-12b**) measured in the pristine state and after several exposure times to air has been further collected. **Fig. 3-20a** shows a semi-logarithmic graph of the decay time of the five devices plotted as a function of the exponent *α*, extracted from power-dependent *I*-*t* measurements similar to the ones shown in **Fig. 3-17a**. The different devices are represented by data-points with different shapes and colors. As can be seen from the statistical plot, among all the investigated InSe photodetectors the exponent α can take values between ~0.3 and 1 and correspondingly, the decay time goes from thousands of seconds when α is smaller than 0.5 (photogating dominated devices) to values smaller than 0.1 s (a value that could be limited by the experimental resolution of 0.04 s) when α tends to 1 (purely photoconductive (PC) devices). The plot shows a clear dependency of the decay time on the power exponent α for all the InSe photodetectors and indicates that the two variables are inversely proportional related. A second statistical correlation can be observed between the responsivity R and the decay time τ_{off} as shown in **Fig. 3-20b**. In this log-log plot, the decay time of the five different InSe photodetectors is plotted versus the photoresponsivity extracted for each device. In this case, the measured responsivity values going from 10^{-3} A W^{-1} to 10^{2} A W^{-1} corresponding to decay times going from less than 0.1 s to more than 1000 s. The graph shows a correlation between the two with the data-points following approximately a straight line, which indicates that the two variables are connected by a power law. The black dashed line represents a power law with an exponent equal to 1, corresponding to a linear relationship between the responsivity and the response time. As can be seen from the plot, for large values of both R and τ_{off}, the data-points follow perfectly the linear relation, suggesting that the photogating effect is the dominant mechanism for InSe photodetectors with large responsivities. In fact, in photogating dominated devices the minority carriers get trapped in long-lived charge traps that limits in an effective way the response time of the device (they are typically slower than photoconductive devices) but provides an external source of photogain (when the channel drift time of the charge carriers is much shorter than the charge trapping time the device presents a photogain proportional to τ_{off}/τ_{drift}).[321,325] For lower values of R and τ_{off}, the data-points start to deviate from the linear relation and present larger scattering, which could be due to the photocurrent generation mechanism being less dominated by photogating. In fact, while in the PG regime R and τ_{off} are dependent variables (linked by the carrier drift time), in the PC regime the responsivity is limited to a finite value according to:

$$R = \eta \cdot \lambda / 1240, \qquad (3\text{-}6)$$

where η is the efficiency and λ is measured in nanometers. On the other hand, the response time is not limited to a finite value and can be indefinitely large (since it depends on the drift and diffusion time of photogenerated carriers and on the RC time constant of the total circuit).

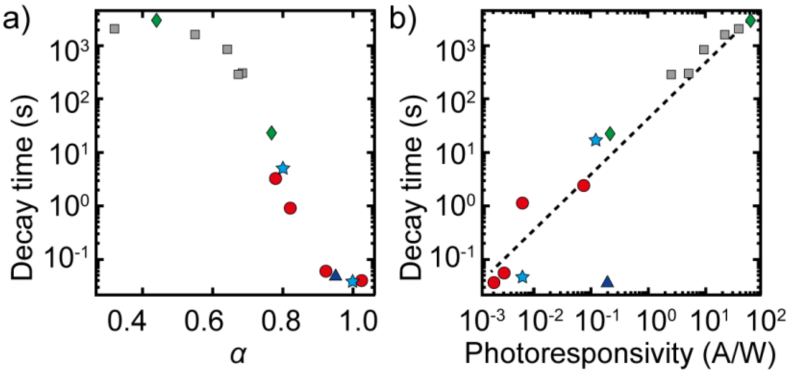

Fig. 3-20 a) Decay time as a function of the exponent *α* of the photocurrent-power scaling law extracted from all the investigated InSe photodetectors. b) The relationship between decay time and photoresponsivity in various InSe photodetectors. All the dots in the same shape and color were measured with the same device after different air exposure times.

After exploring the correlation between α, R and τ_{off}, a last set of experiments that highlight the change in the electronic structure of InSe after the exposure to air will be discussed. After the initial optoelectronic characterization of device #1 in vacuum (transfer curves, current-voltage characteristics (*I*-*V*s) and photocurrent power dependency at 405 nm, see **Fig. 3-15** and **Fig. 3-16**), the device was exposed to air in dark environment for 2 hours and then the vacuum chamber will be evacuated again and perform the optoelectronic measurements. These measurements will be repeated during air-vacuum cycles until the performances of InSe photodetector become stable (approximately after 16 hours of air exposure) and the results are shown in **Fig. 3-21**. **Fig. 3-21a** shows three transfer curves at V_{SD} = 1 V of a InSe photodetector kept in vacuum and in dark recorded after being exposed to air 0 h, 2 h, 11 h, from which one can find a decrease of dark current accompanied by the positive shift of threshold gate voltage upon air exposure time increase. **Fig. 3-21c** demonstrates how the photocurrent versus power evolves with 405 nm illumination as a function of air exposure time. In **Fig. 3-21c** the exponent α (left axis), extracted from the power dependency of the photocurrent shown in panel b, and the threshold voltage V_T (right axis), extracted from the transfer curves in panel a, both are plotted as a function of the exposure time to the air. As can be seen, the exponent α increases from 0.32 to 0.67, indicating the reduction in the trap states density and the change in the photocurrent generation mechanism from PG (α = 0.32) to PC (α = 0.67). At the same time V_T (recorded in dark conditions) increases from ~10 V to ~50 V, a clear sign of the incremental p-doping of the InSe channel.[381,383] The additional measurements under illumination after time-controlled air exposure can be found in **Fig. 3-22**.

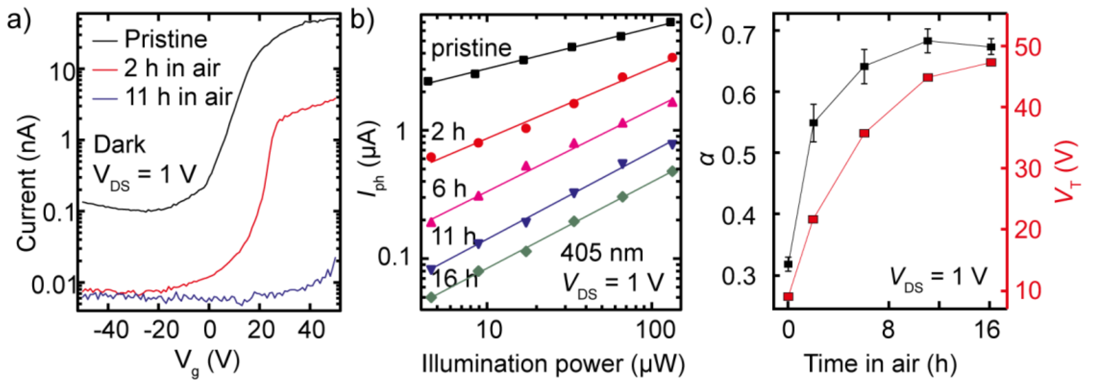

Fig. 3-21 Time-dependent performance of the InSe photodetector (#1) when exposed to air. a) Current versus back gate voltage transfer curves at V_{SD} = 1 V of a InSe photodetector kept in vacuum and in dark recorded after being exposed to air 0 h, 2 h, 11 h. b) Photocurrent versus illumination power of 405 nm light as a function of exposure time in air. c) Photocurrent exponent α (left axis) and threshold voltage V_T (right axis) recorded in a device (#1) exposed to air as a function of time.

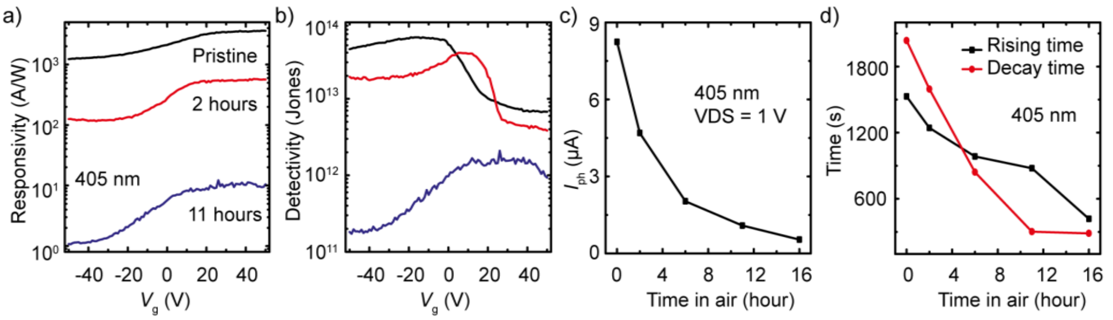

Fig. 3-22 Additional optoelectronic characterizations of the InSe photodetector (#1) when exposed to air. a-b) Photorespinsivity (a) and detectivity (b) versus back gate voltage recorded at V_{SD} = 1 V of a InSe photodetector kept in vacuum after being exposed to air 0 h, 2 h, 11 h. c-d) Photocurrent (c), rising and decay time (d) as a function of exposure time in air extracted from *I*-t curves recorded at V_{SD} = 1 V with modulated 405 nm illumination.

In a second experiment, the evolution of the spatially resolved photocurrent in device #4 (see **Fig. 3-12**) using scanning photocurrent microscopy has been studied in **Fig. 3-23**. Briefly, in this technique a 650 nm laser is focused in a ~1 μm^2 circular spot onto the surface of the InSe photodetector and moved across the sample while recording for each position the source-drain current and the intensity of the reflected light, the testing setup details can be found in section 2.6 and **Fig. 2-30**. **Fig. 3-23a** shows an optical picture of the investigated area selected from device #4 and intensity of the laser reflection from the sample recorded during the scanning photocurrent measurements of panel c and d is shown in **Fig. 3-23b**. The average current recorded in device #4 while scanning the laser spot from the source to the drain electrode in steps of 0.5 µm in pristine conditions (blue curves) and after 10 days of exposure to air (red) are shown in **Fig. 3-23c** and **Fig. 3-23d**. The line-profile of the pristine device at V_{DS} = 1 V (left) and -1 V (right) show broad and high photocurrent intensity regions over the entire InSe channel area. On the contrary, the aged device presents a strong and sharp photocurrent peak located near the source contact at the end of the device channel both at V_{DS} = 1 V (left) and -1 V (right), which is consistent with the presence of Schottky barriers at the InSe/gold contacts (the detailed properties of Schottky barrier at the InSe/gold will be discussed in chapter 4).[392,393]

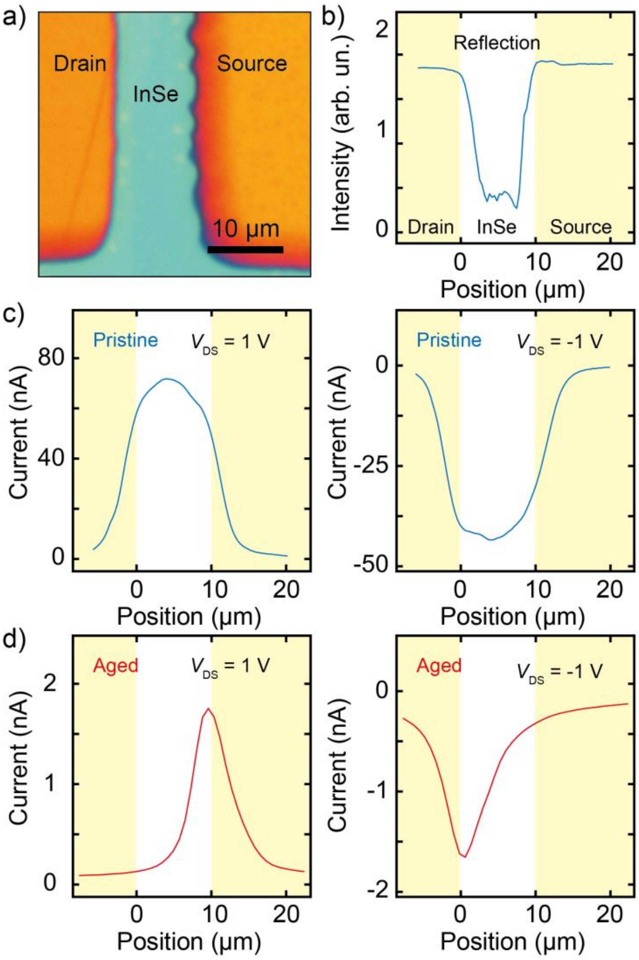

Fig. 3-23 a) Optical image of device #4. b) Intensity of the laser reflection from the sample recorded during the scanning photocurrent measurements of panels c and d. c-d) Spatially resolved photocurrent at V_{ds} = ±1 V of device #4 recorded just after fabrication (blue) and after 10 days in air (red).

Before discussing a model that can explain the photocurrent generation mechanism in thin InSe photodetectors it is instructive to summarize the experimental observations presented above. In summary, five different InSe photodetectors have been studied in their freshly fabricated pristine state, and after the exposure to ambient conditions.

1. From electrical measurements in a field effect transistor configuration, it is found that pristine InSe photodetectors are n-type doped (**Fig. 3-15a**).
2. The optoelectronic figures-of-merit of pristine InSe photodetectors are excellent, with responsivities of the order of 10^3 A W^{-1} and detectivities of ~10^{13} Jones. The responsivity depends on the gate voltage, decreasing when the InSe photodetectors are operated in the off state (**Fig. 3-15b-c**).
3. From time-resolved measurements it is found that the time response in pristine InSe photodetectors is slow and can be on the order of thousands of seconds (**Fig. 3-17a-b**).
4. After exposing the InSe photodetectors to the air, a decrease of both the dark current and the current under illumination has been observed, accompanied by a decrease in response time (**Fig. 3-17b**). Statistically, the responsivity and the response time across all the investigated photodetector are strongly correlated (**Fig. 3-20**).
5. The exposure to the air also affects the way in which the photocurrent depends on the illumination power density. While pristine InSe photodetectors show a sublinear dependency of I_{ph} on P, with the power law exponent α taking a value lower than 1, the exposure to air increase the linearity of this relation, with the power law exponent α increasing toward 1 (**Fig. 3-17c**).
6. Scanning photocurrent measurements (**Fig. 3-23**) shows that the interface between gold and pristine InSe shows lower Schottky barriers than that of aged InSe.

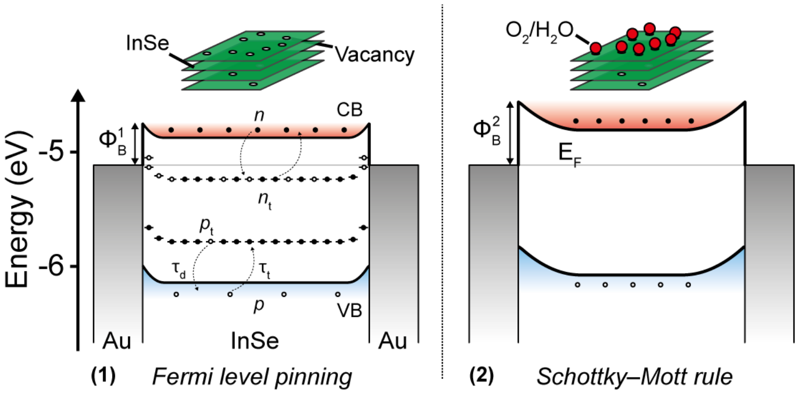

Fig. 3-24 Schematic band diagram of InSe in dark conditions with traps and Fermi level pinning (**1**, left) and in absence of traps with the alignment predicted by the Schottky-Mott rule (**2**, right). Depicted there are the valence (VB) and conduction band (CB) of InSe, the gold electrodes and the Fermi energy (E_F) and a set of hole trapping levels (whose density is P_t) and electron trapping level (density N_t). The density of free electrons, free holes, trapped electrons and trapped holes are

respectively *n*, *p*, n_t. and p_t.

The n-type doping observed in the transfer curves of pristine thin InSe photodetectors measured in dark and in vacuum conditions has been observed in different experiments apart from the ones presented in this thesis.[258,381,382,384,385] This behavior can be attributed to the presence of defects in the crystal such as selenium vacancies and indium interstial adatoms (I_{In}) that can be caused by the In-rich atmosphere in which high-quality InSe is grown (as mentioned in chapter 2.1).[375,376] These intrinsic defects are expected to modify the density of states of InSe and theoretical calculations predict the appearance of trap states linked to these defects. While V_{Se} can introduce two sets of trap levels, the first one is located closer to the conduction band minimum (CBM) and the second is closer to the valence band maximum (VBM), the trap levels due to I_{In} are located only closer to CBM.[376,394] A schematic band diagram of the system composed by InSe is shown in **Fig. 3-24**, with the conduction band CB and the valence band VB displayed, and two gold electrodes acting as electrons reservoirs. The Fermi energy of the electrodes E_F is closer to CB in agreement with the n-type conduction observed in the experiments. The majority carriers traps levels, which are closer to the conduction band, have a density N_t and can act as pinning centers for the Fermi level of the device at zero bias. On the other hand, the minority carrier traps with density P_t are expected to play a dominant role in the photocurrent generation process since they can generate photogain.[376-378,394] In dark conditions the InSe channel has a density of free electrons *n* (located in CB) and of free holes *p* (VB) and, as a consequence of the position of the Fermi level, there is a small density of trapped holes p_t (meaning that most of the trap levels are occupied by electrons, density n_t). A free hole in VB (free electron in CB) has a certain probability of getting trapped by a trap level with rate τ_t^{-1}. The opposite process also is possible and a trapped hole (electron) can jump from a trap level to VB (CB) with rate τ_d^{-1}. In general, the trapping and detrapping rates τ_t^{-1} and τ_d^{-1} can be different and there can be also a difference between the rates relative to holes and electrons.

The band diagram of **Fig. 3-24** can be used to explain the current flowing through the device in dark conditions and serves as a basis to understand the generation of photocurrent. When illuminating the InSe photodetectors with external illumination, electron-hole pairs are generated and the density of free holes *p* and free electrons *n* increases. The separation of these electron-hole pairs due to the electric field related to the source-drain voltage gives rise to a photocurrent. This process is usually called “photoconducting effect” that does not show photogain. In fact, the maximum responsivity achievable in a photodetector working solely by PC for illumination can be calculated through the Eq. 3-6 and in the case of illumination at 405 nm the maximum responsivity is ~0.66 A W^{-1}. In absence of active traps in the photodetector, PC is typically the dominant photocurrent generation mechanism. On the other hand, if hole traping levels are present in the system, each photogenerated hole has a certain probability (related to τ_t^{-1}) of getting trapped in one of these levels for an average time τ_d. This trapping process for minority carriers can give rise to “photogating effect” (PG), a process that can show photogain and can give responsivities much larger than ~0.66 A W^{-1} at 405 nm. Actually, the photogating is a particular example of the photoconductive effect. For a InSe photodetector under illumination, the photogenerated electron-hole pairs will be separated and drift towards to the electrodes in opposite directions. During this process if holes are trapped in localized states, once the electron jumps into the drain electrode the channel will be charged. In order to keep charge neutrality another electron has to jump into the channel from the source electrode. This electron also feels the voltage and drifts into the drain electrode and the channel will be charged again. And then another electron has to jump from the source electrode…This process repeats until the hole gets de-trapped, and thus introduces photogain. The magnitude of the photogain is related to the ratio between the trapping time and the drift time (the trapping time can be many orders of magnitude larger than the drift time).[321,325] In the case of a pristine InSe photodetector measured in vacuum (stage **1**), the large responsivity values can be explained by PG. This mechanism also explains the large response times recorded for pristine photodetectors as in the PG mechanism the response speed is limited by the trapping time. The power dependency of the photocurrent also confirms this scenario. In fact, a photodetector without trap levels is expected to be characterized by a value of the exponent α equal to 1 while in a photodetector containing active traps, α is smaller than 1. For the pristine InSe devices, dominant by PG effect, the interface between gold and InSe is characterized by small Schottky barriers, consistent with the scanning photocurrent measurements of device #4, and the alignment between the Fermi level of InSe and of the gold electrodes is determined by the Fermi level pinning to the trap levels.[395,396]

The right panel of **Fig. 3-24** schematizes the evolution in the band structure after the exposure of InSe photodetectors to air (stage **2**). In this case, it can be proposed that a change in the trap levels induce a strong change in the photocurrent generation process. In fact, the interaction between the selenium vacancies and the oxygen or water molecules present in air leads to a passivation of the defects, as predicted by theoretical calculations,[376-378] thus reducing the trap densities N_t and P_t (in the simplified scheme the traps have been completely removed). The passivation process will eventually stop after all the available vacancy sites are neutralized, characterized by a trap density much smaller than the initial density P_t at stage **1**. At this stage of the evolution fewer holes can be trapped, effectively decreasing the photogain. The photodetector working principle shifts from PG to PC and the power dependency of the photocurrent illustrates well this evolution, with the aged InSe photodetectors showing a linear dependency of the photocurrent on the incident power. Once the InSe photodetectors reach this stage of evolution (stage **2**), they become much faster in responding to light (as the trapping time does not limit the photodetector speed anymore) but at the expense of a reduced responsivity. In this limit, the interface between gold and InSe is characterized by larger Schottky barriers and the alignment between InSe and gold can be calculated by the Schottky-Mott rule,[52,396] which predicts that the Schottky barrier formed at the interface has the value $\Phi_{\mathrm{SB,n}} = W_M - X_S \sim 0.5$ eV, where W_M is the work function of gold (~5.1 eV) and X_S is the electron affinity of InSe (~4.6 eV). The Schottky barriers are visible in **Fig. 3-24d** in the line-profile of the aged InSe photodetector. Importantly, the final state of the photodetector seems to be stable both in the air and in vacuum suggesting that the passivation is a self-limiting process. A final feature of the model is the change of the relative alignment of the Fermi energy with respect to CB and VB during the evolution of InSe. In fact, the reduction of the density of trap levels is expected to induce a shift of the Fermi energy away from the conduction band, effectively introducing p-doping in the InSe channel.[394,397] The consequences of the p-doping can be observed in the reduction of the dark current in the air compared to the pristine one as shown in **Fig 3-17b** and in the shift of the threshold voltage in **Fig 3-21**.

3.3 Conclusions

In summary, the studies of the environmental and laser-induced degradation on thin GaSe flakes and the photocurrent generation process in InSe as well as its evolution in air/vacuum have been presented, which are both related to the presence of defects in the materials, especially, selenium vacancies. It was found that the environmental degradation of thin GaSe takes place in two main stages. At first, the exposure to air induces degradation of the pristine GaSe creating α-Se and Ga_2Se_3, accompanied by a photocurrent increase. In the second stage, Ga_2O_3 appears and its concentration increases in the samples resulting in a drop of the photocurrent leading to the final failure of the GaSe photodetectors. It was also found that capping the exfoliated GaSe flakes with a top h-BN flake is an effective way to passivate it, preventing its environmental degradation as well laser-induced damage.

Conversely, the selenium vacancies in InSe can be healed after exposure of InSe to air, which reduces the photogain and increases the operation speed of the photodetecting devices, and finally reach a long-term environmentally stable InSe. The statistical analyses based on all the investigated thin InSe devices suggest that photoresponsivity, response time and the photocurrent scaling law exponent α are all strongly correlated quantities. The proposed band diagram model indicates that the high photoresponsivity in pristine thin InSe photodetectors can be attributed to the photogating effect, which mainly originates from the hole-trapping levels induced by selenium vacancies. The air-induced passivation of defects may reduce the traps density in thin InSe photodetectors, thus shifting the photocurrent generation mechanism from photogating to photoconductive. This change is accompanied by a decrease in photoresponse time and photoresponsivity as well as the growth of exponent α.

4

INSE OPTOELECTRONIC DEVICES WITH ENGINEERED VDW CONTACTS

Metal-semiconductor junctions are characterized by an energy barrier known as the Schottky barrier, whose height can, in the ideal case, be predicted by the Schottky-Mott rule on the basis of the relative alignment of energy levels. However, such ideal physics has rarely been experimentally realized because of the inevitable chemical disorder and Fermi-level pinning at typical metal-semiconductor interfaces introduced by conventional fabrication process. Thanks to the dangling-bond-free surface of 2D semiconductors and deterministic transfer methods, the van der Waals (vdW) metal-semiconductor interfaces without direct chemical covalent bonding, thus less chemical disorder and Fermi-level pinning (FLP), which introduce a high-quality Schottky junction, will be discussed in this chapter. Firstly, a background of vdW contacts versus conventional metallization will be briefly introduced. Then the transport properties of Schottky diodes based on engineered asymmetric van der Waals contacts of thin InSe, including Au-InSe-Gr (graphite) and Pt-InSe-Gr, will be investigated. Finally, novel optoelectronic applications, i.e., optoelectronic memory effect, based on the Pt-InSe-Gr

Schottky diodes will be developed.

4.1 VdW contacts vs. conventional metallization

To fabricate devices with optimal electrical properties, it is crucial to have both high-quality semiconducting crystals and ideal contacts at metal-semiconductor interfaces.[52] Thanks to the mechanical exfoliation of van der Waals crystals, atomically-thin high-quality single-crystals can easily be obtained in a laboratory. However, the difficulty of forming high-quality ohmic or Schottky contact to 2D semiconductors limits investigations of their fundamental properties and hinders fabrication of high-performance devices.

Theoretically, in an ideal metal-2D semiconductor junction, Schottky barrier height Φ_{SB} can be well predicted by the Schottky-Mott rule,[398,399] a law first proposed in the 1930s and governed by the electrostatics in all types of problem that involve energy-level alignments:

$$\Phi_{\mathrm{SB,\,n}} = \Phi_{\mathrm{M}} - X_{\mathrm{S}} \tag{4-1}$$

$$\Phi_{\mathrm{SB,\,p}} = I_{\mathrm{S}} - \Phi_{\mathrm{M}} \tag{4-2}$$

Where Φ_{M} is the work function of the metal, X_{S} and I_{S} are the electron affinity and ionization potential of the semiconductor, correspondingly, and $\Phi_{\mathrm{SB,\,n}}$ and $\Phi_{\mathrm{SB,\,p}}$ are the Schottky barrier heights for electrons and holes, respectively. These quantities are the intrinsic properties of the isolated materials before they form the junction, and the Schottky-Mott model implies that Φ_{SB} is linearly dependent on the metal work function with a slope of unity. However, in practical experiments, Φ_{SB} is usually insensitive to Φ_{M}, and the Fermi level of the system in typically pinned to a nearly fixed position within the semiconductor bandgap, varying little with respect to different metals used, as first noted by Bardeen.[400] Thus, the Schottky-Mott limit is hardly experimentally achieved in traditional metal-semiconductor junctions.[401]

This striking discrepancy between theory and experiments arises because the Schottky-Mott model neglects several types of chemical interaction that are hard to avoid at the interface of two dissimilar materials. In the case of bulk metal (3D) connected to 3D semiconductors, firstly, owing to the termination of the crystal structure (see **Fig. 1-2a**) and incomplete covalent bonds, surface dangling bonds or surface reconstructions, lead to surface states within the semiconductor bandgap and result in FLP at these energy levels.[400] Second, the interface of the contact is rarely an atomically sharp discontinuity between the metal and semiconductor crystal, where chemical bonds takes place and modify their original energy levels. Chemical bonding between the metal and the semiconductor, and their interdiffusion, can also create large strain in both crystal lattices and change the band structures, as well as the resulting barrier height.[19,402,403] Fortunately, above mentioned challenges can be solved by fabricating pure top-contact geometry interface between 3D metal and 2D semiconductors thanks to their dangling-bond-free surface and low defects density nature (see **Fig. 1-2b**). Contrary to the case of bulk (3D) semiconductors, the pristine surface of 2D materials do not tend to form covalent bonds (see **Fig. 4-1a**). The interfaces between metals and 2D materials in the top-contacted configuration can therefore only formed by a van der Waals (vdW) gap in most situations. As shown in **Fig. 4-1b**, the vdW gap in such top-contact interfaces acts as an additional 'tunnel barrier' for carriers, before the inherent Schottky barrier (SB). However, the typical conventional processes for 2D semiconductors integration and device fabrication usually lead to additional chemical disorders and defect-induced gap states that serve as a reservoir for electrons or holes and therefore pin the Fermi level.[404] For example, **Fig. 4-1c** shows that 'high-energy' metal deposition processes usually involve atom or cluster bombardment and strong local heating to the interface;[405] moreover, the resist development process could also leave polymer residue within the interface that causes the overall measured barrier height to deviate from the predicted value. In addition, metal-induced gap states, formed in the junction owing to the decaying metallic wave function, penetrate to nanometer depth into the 2D semiconductors.[406]

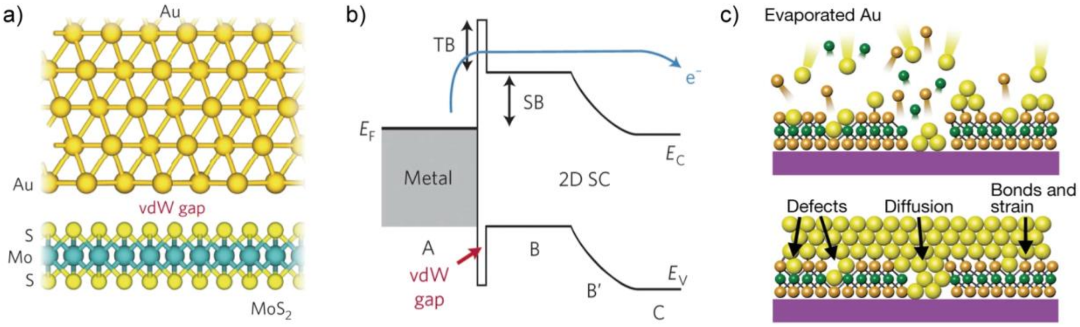

Fig. 4-1 a, b) Metal/2D semiconductor interface with vdW gap (a) and corresponding band diagram (b) (for example, Au–MoS_2 contact). c) Schematics of Au- 2D interface of conventional electron-beam-deposited Au electrodes on top of MoS_2.[395,396]

Therefore, the motivation design and creation of van der Waals (vdW) connected 3D metal and 2D semiconductor junctions have been developed to prevent the dangling-bond-free surface from being damaged using deterministic transfer techniques, in which pre-fabricated metal electrodes with atomically flat surfaces are physically laminated onto dangling-bond-free 2D semiconductors or transferring the exfoliated 2D semiconducting flakes bridging onto the pre-patterned electrodes.[396,407] Thus, without direct chemical bonding and avoiding the associated chemical disorder and defects-induced gap states, the high-quality Schottky diode based on the high-quality metal-2D semiconductor interface can be achieved based on the Au-, Pt-InSe Schottky barrier in this chapter.

4.2 Au-InSe-Gr Schottky photodiode

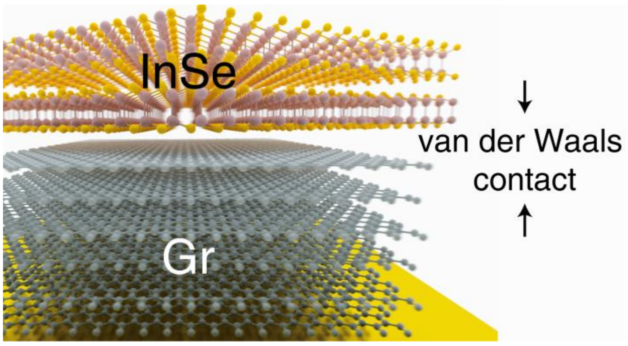

The characteristics of gold (Au) and graphite (Gr) vdW electrical contacts on indium selenide (InSe) have been studied. It was found that the Au-InSe interface is dominated by a large Schottky barrier that is estimated to be approximately 460 meV while the Gr-InSe interface shows a negligible barrier (smaller than 100 meV). Exploiting this difference in the barriers, Schottky diodes based on asymmetrically contacted InSe flakes by van der Waals stacking have been fabricated, which does not require any lithographic process or metallization on 2D semiconductors. The diodes show good performances and follow closely the ideal Schokley equation with a series resistance. Interestingly, these Schottky diodes do not need different metals for the source and drain electrodes, and thus they can be produced using only one metal evaporation step. Note that this section is mainly based on the published paper “InSe Schottky Diodes Based on Van Der Waals Contacts” in Advanced Functional Materials where I am the first author.[408]

4.2.1 Sample fabrication

To investigate the properties of thin InSe photodetectors contacted by gold or graphite electrodes, the devices are fabricated using the deterministic transfer method, and a Au-InSe-Au device with symmetric geometry was firstly fabricated by bridging a thin

InSe flake onto the pre-patterned Au electrodes, which is similar to the fabrication process demonstrated in **Fig. 2-16**. In a second class of devices, mechanically exfoliated flakes from natural graphite crystals (HQ Graphene, The Netherlands) have been used to contact an InSe flake on both sides, thereby creating a graphite-InSe-graphite device (Gr-InSe-Gr). Note that graphite (thickness > 12 layers) instead of graphene electrodes were employed during this fabrication to avoid the introduction of a gate dependency and/or a thickness dependency in the work function of the electrodes.[409,410] As shown in **Fig. 4-2a**, these Gr-InSe-Gr devices can be fabricated in three transfer steps. Graphite flakes with uniform appearance and having at least one long straight edge are firstly selected. Then one of graphite flakes will be transferred contacting only one electrode and the second graphite flake will be transferred contacting only the other electrode. And a spatial gap between the two electrodes can be obtained that can accommodate an InSe flake that can bridge over the gap and contact the two Gr flakes. **Fig. 4-2b** shows two transfer steps of the fabrication of the final devices, which is based on an InSe flake contacted on one side by a Gr flake and on the other side with a gold electrode (Au-InSe-Gr). A Gr flake is firstly transferred contacting only one pre-patterned gold electrode and the subsequent transfer of an InSe flake contacting the Gr flake and the free gold electrode.

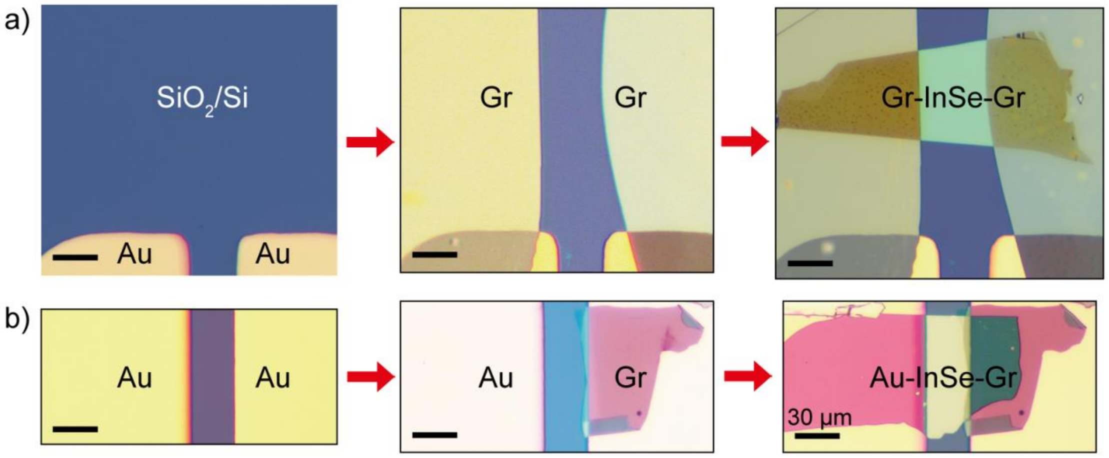

Fig. 4-2 Devices with the geometries of Gr-InSe-Gr (a) and Au-InSe-Gr (b) fabrication processes.

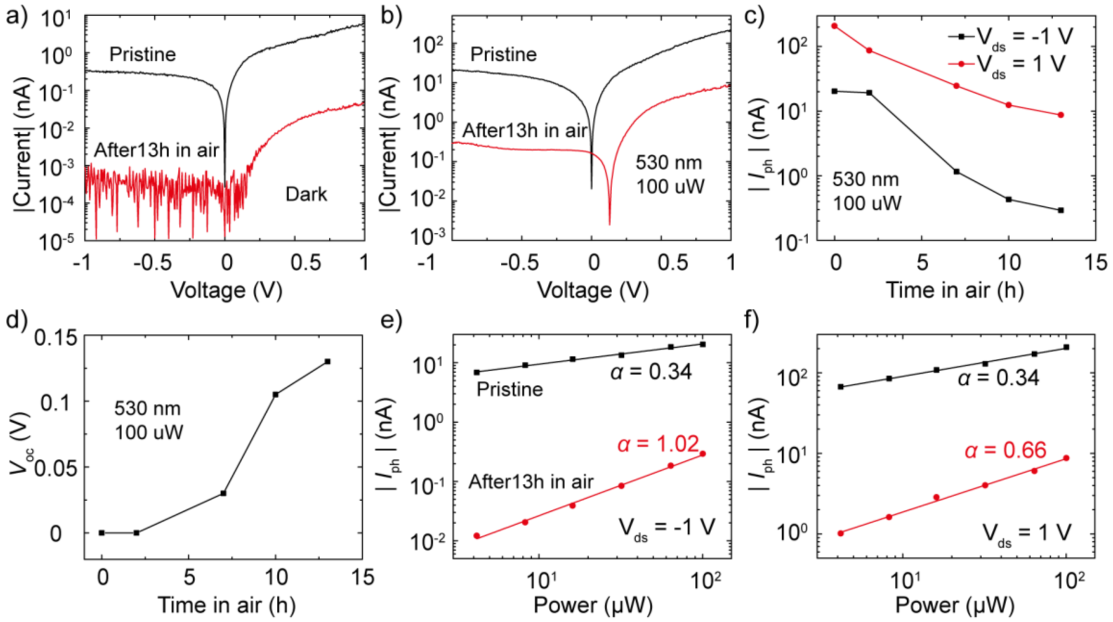

Fig. 4-3 Performance evolution of a Au-InSe-Gr Schottky diode as a function of air-exposure time. a-b) The *I*-*V* curves plotted in semi-logarithmic scale recorded in dark conditions (a) and under illumination with 530 nm light source (b) with the states of pristine (black line) and after 13 hours air exposure (red line). c-d) The variation of photocurrent at 1V (red) and -1 V (black) (c), and open circuit voltage (V_{oc}) extracted from *I*-*V* curves recorded as a function of air exposure time. e-f) The power dependent photocurrent recorded at -1 V (e) and 1 V (f) of the Au-InSe-Gr device in pristine state and after 13 hours air exposure.

Before performing the optoelectronic characterizations of the devices, all the devices were kept in air for 24 hours in order to reach their air-stable photodetecting operations. As has been discussed in chapter 3, the optoelectronic performance evolution of Au-InSe-Au and Gr-InSe-Gr photodetectors in air as a function of time, which decreases the trap density in InSe crystals thanks to air passivation,[370] can increase the Au-InSe Schottky barrier by weakening the fermi level pinning at the Au-InSe interface. **Fig. 4-3** shows the optoelectronic characterizations of a Au-InSe-Gr device performed in its pristine state and after being exposed to air. **Fig. 4-3a** shows the current-voltage characteristics of the device recorded in dark in pristine conditions (black curve) and after 13 hours in air (red curve) presented with semi-logarithmic scale. The current decreases around three orders of magnitude after the exposure to air and the current observed at negative voltages become comparable to the noise level of the measurement (from ~0.5 nA to lower than 1 pA). **Fig. 4-3b** shows similar measurements performed while keeping the device under external illumination (wavelength 530 nm). Also in this case a clear decrease of the total current can be observed in the aged device compared to the pristine state both at positive and negative biased condition. Interestingly the device after 13 hours of exposure to air develops an open circuit voltage (V_{OC}) that is absent in the pristine state. The decrease in photocurrent as a function of exposure to air can be better observed in **Fig. 4-3c**. **Fig. 4-3d** shows the increase in the open circuit voltage, which in the pristine device is 0 V and reaches 0.13 V after 13 hours in air. Both the decrease in photocurrent and the increase in the open circuit voltage (V_{OC}) can be explained by an increase in the height of the Schottky barrier formed at the Au-InSe interface. **Fig. 4-3e-f** shows the power dependency of the photocurrent at negative (panel e) and positive (panel f) voltages for the pristine device and after 13 hours in air. In all cases, the data appear to follow a linear trend in the log-log graphs that can be also mathematically described by a power law equation (3-5) $I_{ph} = A \bullet P^{\alpha}$, where A is a constant that is related to photoresponsivity, P is the optical power and the exponent α is the fitting parameter. Interestingly, in the case of the pristine device the power law exponent has a value of 0.34 ± 0.01 both for negative and positive voltages, while the aged device shows an asymmetric α, which is equal to 1.02 ± 0.03 at negative voltages and 0.66 ± 0.02 for positive voltages. The low value of α in the pristine state can be explained by the presence of traps in the system and negligible Schottky barrier, which also can explain the large photoresponsivity observed in this state. In the aged state, the two different values of α for positive and negative voltages indicate the presence of a sizeable Schottky barrier at one of the electrodes, which induces an intrinsic electric field in the device. In the following text, the Au-InSe-Gr Schottky diode properties will be discussed in detail.

4.2.2 *I*-*V* characteristics of Au-InSe-Au, Gr-InSe-Gr and Au-InSe-Gr photodetectors

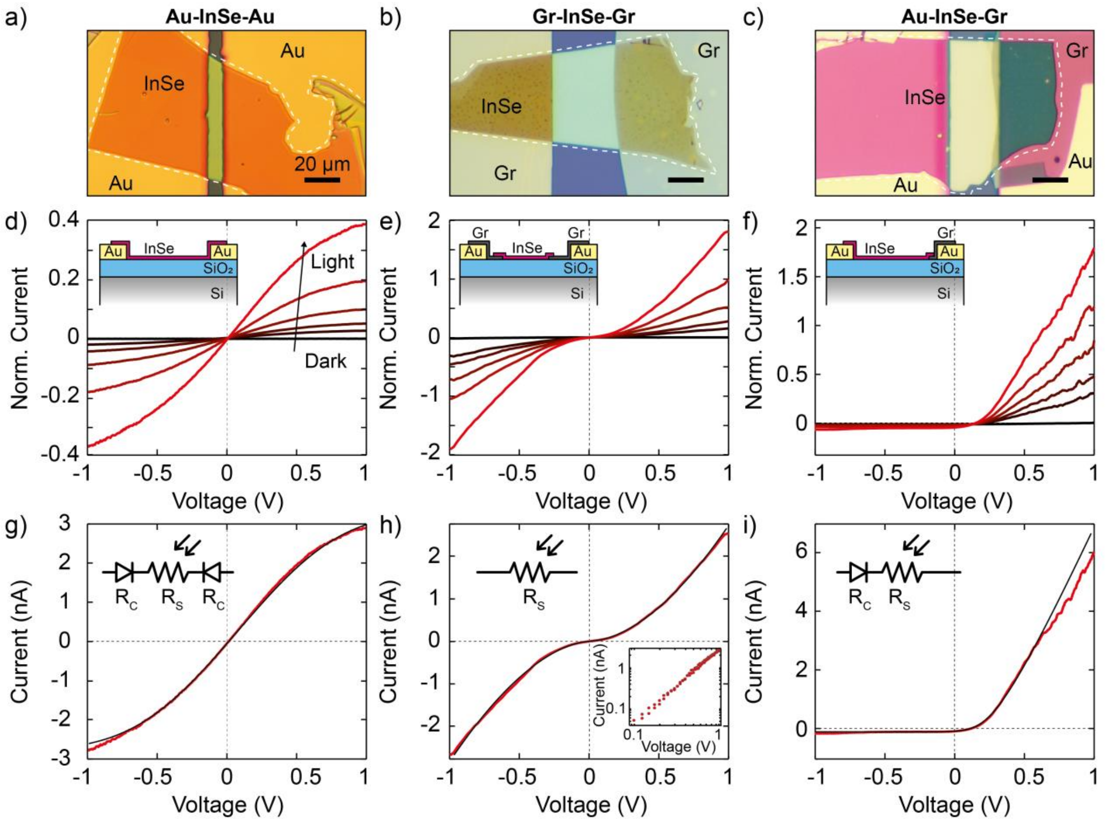

Fig. 4-4 a-c) Optical pictures of symmetric and asymmetric devices based on few-layer InSe, gold electrodes (Au) and graphite (Gr). d-f) Current-voltage characteristics of the three devices shown in panels (a-c) in dark and under 530 nm illumination with different intensity (from 1.2 $\mathrm{mW/cm^2}$ to 18 $\mathrm{mW/cm^2}$). g-i) Experimental *I*-*V* curves recorded with the largest illumination density (red curve) and theoretical fit (black curve). The *I*-*V* of Au-InSe-Au is adjusted to the back-to-back Schottky diode model, the one of Gr-InSe-Gr to a power law with exponent between 1 and 2 and the *I*-*V* of Au-InSe-Gr is fitted to a Schottky diode with series resistance model.

After fabrication, the optoelectronic measurements were performed in a home-built probe station kept in high-vacuum ($\approx 10^{-6}$ mbar), the setup has been introduced in section 2.5 in chapter 2. **Figs. 4-4a-c** show the optical pictures of fabricated Au-InSe-Au, Gr-InSe-Gr, and Au-InSe-Gr devices and the corresponding current-voltage (*I*-*V*) characteristics of the three devices kept in dark (black curves) and under illumination at 530 nm with increasing power density (red curves) are shown in panels d-f, respectively. Note that all *I*-*V*s have been recorded leaving the Si back-gate electrically floating. The inset of each panel in d-f shows a schematic of the device under study. In order to compare the characteristics of devices with different geometry all the *I*-*V*s have been normalized by multiplying the current by the dimensionless factor L/W, where L is the channel length (calculated from the distance from one electrode edge to the other) and W is the channel width. From the figures one can see that all the three devices show a negligible current in dark (the corresponding semi-logarithmic representations have been shown in **Fig. 4-5**), and that the current increases with the illumination intensity. The behavior of the *I*-*V*s for each device is very different and the magnitude of the current is the largest in the Au-InSe-Gr (at positive voltages) and in the Gr-InSe-Gr devices and the smallest in the Au-InSe-Au device.

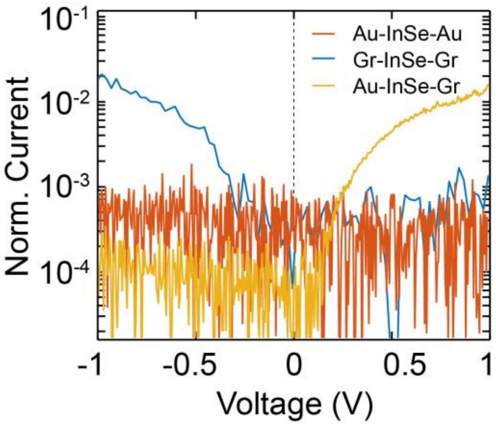

Fig. 4-5 Semi-logarithmic representation of the experimental *I*-*V*s of the three devices discussed in **Fig. 4-4d-f** recorded in dark.

Starting the discussion from the Au-InSe-Au device *I*-*V*s, it can be seen in **Fig. 4-4d** that current is symmetric in voltage and has negative curvature, approaching saturation both for large positive and large negative bias voltages. These *I*-*V*s can be explained by the presence of a Schottky barrier at the Au-InSe interface,[411] with a model composed by two Schottky diodes (one for each gold electrode) connected back-to-back with a series resistance, as shown in **Fig. 4-4g** and in the schematic inset.[412,413] In such a circuit, the voltage drops across the left (V^L) and the right (V^R) Schottky diodes can be written as:

$$V^L = -\frac{nkT}{q}\ln\left(1 - \frac{I}{I_0^L}\right) \quad \text{and} \quad V^R = \frac{nkT}{q}\ln\left(1 + \frac{I}{I_0^R}\right), \qquad (4\text{-}3)$$

where n is the ideality factor of the diodes, T is the absolute temperature, I is the total current flowing through the metal-semiconductor-metal (M-S-M) device and I_0^L (I_0^R) is the reverse saturation current of the left (right) diode.[322,323,414] These saturation currents are related to the Schottky barrier height between gold and InSe $\phi_{B,Au}^0$

according to:

$$I_0^{L/R} = A\,A^*\,T^2 \exp\left(-\frac{q\,\phi_{B,Au}^0}{kT}\right), \tag{4-4}$$

where A is the active area (the channel part is assumed as the active area) of the device and A^* is the Richardson constant of InSe. The total voltage drop across the the M-S-M device is related to the two voltage drops V^L and V^R and to the series resistance R_S through:

$$V = V^L + V^R + I\,(V)R_S, \tag{4-5}$$

By substituting Equation 4-3 in Equation 4-5 and adding a current source in series I_{Photo} to take into account the photocurrent generation in the two diodes, the total current $I(V)$ can be written as:

$$I(V) = \frac{I_0^L I_0^R \exp\left[\frac{q\left(V-I(V)\,R_S\right)}{nkT}\right] - I_0^L I_0^R}{I_0^L + I_0^R \exp\left[\frac{q\left(V-I(V)\,R_S\right)}{nkT}\right]} + I_{Photo}, \tag{4-6}$$

To solve Equation 4-6 as a function of voltage V, a numerical method has been employed to perform a minimization of the difference between the left and the right side of Equation 4-6, and the detailed discussion of the fitting model that how the single parameter takes charge of the final fitting result has been shown in **Fig. 4-6**. **Fig. 4-4g** shows one of the experimental *I*-*V*s of the Au-InSe-Au device recorded at room temperature (T = 296 K) and with incident power density P = 18 mW/cm^2, fitted to Equation 4-4 using the following parameters: $I_0^L = (6.2 \pm 0.4)$ nA, $I_0^R = (5.1 \pm 0.3)$ nA, $n = (6.2 \pm 1.0)$, $R_S = (60 \pm 10)$ MΩ and $I_{Photo} = (0.03 \pm 0.01)$ nA. From the good quality of the fit one can see that the model reproduce well the experimental data indicating that the Au-InSe-Au device has a M-S-M geometry and its behavior is dominated by the Schottky barriers located at the InSe/electrodes interfaces. In general the observed large value of *n*, larger than 2, which could be due to various sources of non-idealities such as tunneling processes, recombination through mid-gap and traps states in the junction region or image force effects.[323,415,416]

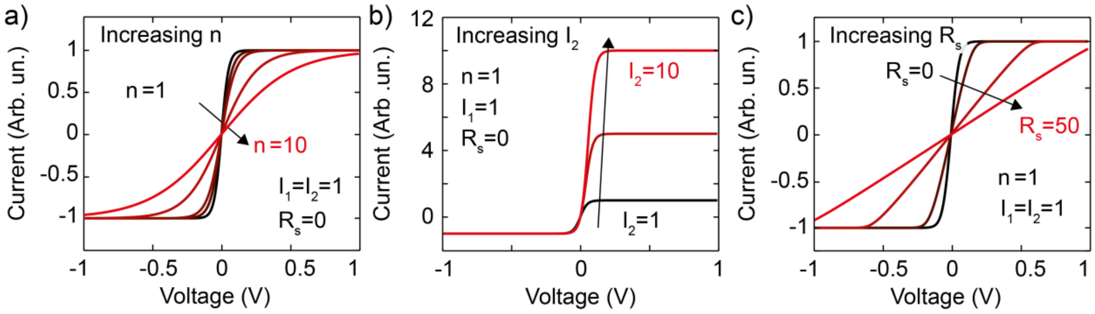

Fig. 4-6 a-c) Theoretical *I*-*V*s calculated from the back-to-back diode model using Equation 4-6 of the main text for different parameters values. each panel varies one of

the parameters of the model (n, I_1, I_2 or R_S) while keeping the other parameters fixed to show the influence of each parameter on the *I*-*V* curves predicted by the back-to-back diode model.

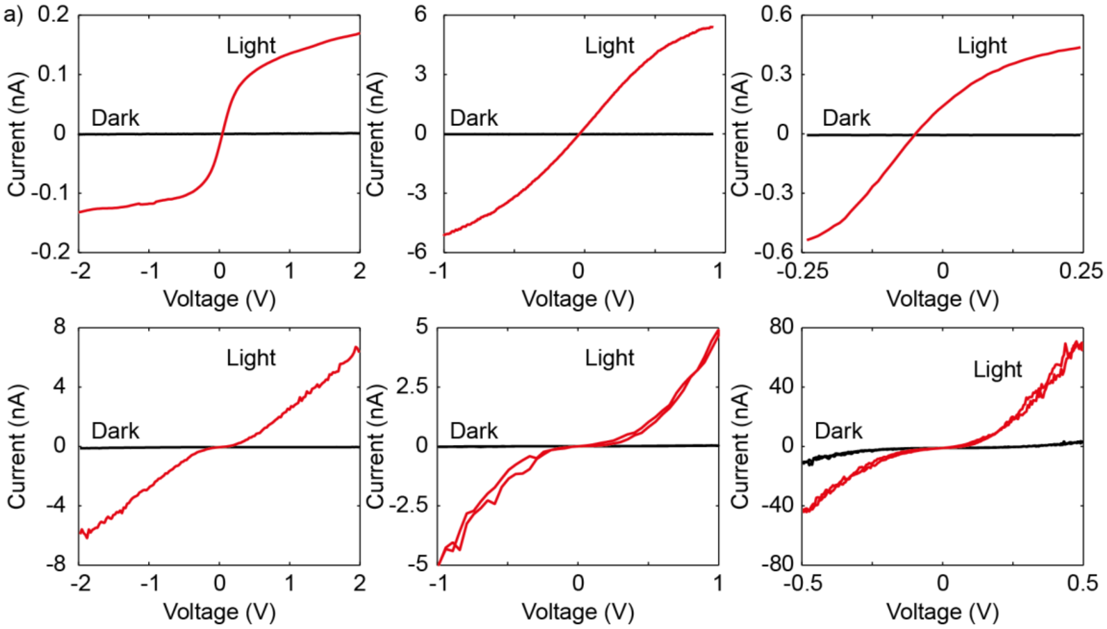

Fig. 4-7 Experimental *I*-*V*s of different symmetrically contacted InSe devices: Au-InSe-Au back-to-back Schottky diodes devices (top row) and Gr-InSe-Gr (bottom row).

Similarly to the Au-InSe-Au device, the *I*-*V*s measured on the Gr-InSe-Gr device, shown in **Fig. 4-4e**, are symmetric in voltage reflecting the symmetric electrodes configuration in the device geometry. Notably, in the Gr-InSe-Gr case the curvature of the current versus voltage is positive, meaning that the differential conductance $G(V) = dI/dV$ increases with the voltage and no saturation is observed. Also, the magnitude of the normalized current is approximately one order of magnitude larger in the Gr-InSe-Gr compared to the Au-InSe-Au device in the same conditions. The positive curvature in the *I*-*V*s and the larger current both indicate a better injection from the Gr electrodes into InSe compared to Au electrodes. By analyzing the *I*-*V*s of the Gr-InSe-Gr device one can find that the current-voltage dependency follows a power law $I \approx V^{\beta}$. The exponent β takes values between 1 and 2,[417] **Fig. 4-4h** shows one of the *I*-*V*s fitted with an exponent $\beta = 1.67$ and the inset shows a log-log plot of the same *I*-*V*. These results indicate that the Gr-InSe interface is not rectifying and that the contact is either ohmic or characterized by a small Schottky barrier $\phi^0_{B,Gr}$. A statistic collection of *I*-*V* characteristics recorded from symmetrically contacted Au-InSe-Au (top row) and Gr-InSe-Gr (bottom row) devices has been shown in **Fig. 4-7**, which further confirmed that the Au-InSe interface is dominant by a large

Schottky barrier while Gr-InSe is not a rectified contact interface or characterized by a small Schottky barrier.[417-419]

After having determined that the Au-InSe interface shows a rectifying behavior characterized by Schottky barriers $\phi_{B,Au}^{0}$ one can exploit the better injection from the Gr-InSe contact to fabricate Schottky diodes, based on asymmetrically contacted InSe flakes, which present rectifying *I*-*V*s and photovoltaic characteristics. **Fig. 4-4f** shows the normalized *I*-*V*s of such a Au-InSe-Gr device. The shape of the *I*-*V*s is strongly asymmetric in voltage showing a rectifying behavior and the magnitude of the normalized current for positive voltage is comparable with the one of the Gr-InSe-Gr device. These *I*-*V*s can be described by the following diode equation:[52]

$$I(V) = I_0\left\{\exp\left[\frac{q(V-I(V)R_S)}{nkT}\right]-1\right\}-I_{SC}, \tag{4-7}$$

where I_0 is the saturation current described by Equation 4-6. **Fig. 4-4g** shows one of the experimental *I*-*V*s of the Au-InSe-Gr device fitted to Equation 4-5 using the following fitting parameters: $I_0 = (22 \pm 2)$ pA, $n = (2.7 \pm 0.2)$, $R_S = (76 \pm 10)$ MΩ and $I_{SC} = (0.11 \pm 0.02)$ nA. The theoretical curves match perfectly the experimental *I*-*V* for voltages between -0.5 V and 0.5 V and starts to deviate at larger positive voltages where the experimental current-voltage curve diverges from the linear relation given by $I \approx V/R_S$. Such behavior, which happens after the flat-band condition of the Au-InSe interface, can be described by a dependency of R_S on the inverse of the voltage. The series resistance at the flat-band condition is given by the sum of two components, the sheet resistance of the InSe flake R_{InSe} and the Gr-InSe contact resistance. Assuming that R_{InSe} is constant in this voltage range, the voltage dependency of R_S can then be attributed to the Gr-InSe interface, which is known to have a voltage-dependent density of state and Fermi level or to the onset of space charge limited conduction in graphite as was previously reported.[419,420]

4.2.3 Scanning photocurrent microscopy and band diagram of Au-InSe-Au and Au-InSe-Gr

The planar geometry of thin InSe based devices allows directly probing the internal electric fields, which should be present at the heterointerfaces, through scanning photocurrent microscopy (SPCM).[421] The SPCM maps were obtained by raster scanning a light source with wavelength 660 nm focused in a ∼1 μm diameter circular spot onto the device surface with the device mounted on a motorized x-y stage, as schematized in **Fig. 2-30**. Simultaneously the current at a fixed voltage V_{SD} and the intensity of the reflected light will be recorded. More details about this technique can be found in chapter 2 experimental method section. **Fig. 4-8a** shows a map of the 660 nm light reflected from a Au-InSe-Au device investigated with SPCM measurements. All the different features of the device have been highlighted using the black dashed contours, used also to align the SPCM maps. **Figs. 4-8b-d** show the scanning photocurrent maps recorded at three different voltages (V_{SD} = -0.5 V, 0 V and 0.5 V). The map recorded at negative voltage, with the Schottky barrier at left Au/InSe interface forward biased and right one in reverse mode (**Fig. 4-8b**), shows a negative photocurrent (blue counts) that is mostly generated at the right contact edges. Also, a similar positive photocurrent is generated at the left contact region in **Fig. 4-8d** when the map was recorded at a positive voltage. The map recorded at V_{SD} = 0 V (**Fig. 4-8c**) shows two regions with positive (left) and negative (right) photocurrent centered at the both Au-InSe contact edges indicating that two electric fields with opposite directions are naturally present at both Au/InSe interfaces. Such symmetry observed in scanning photocurrent microscopy is consistent with the *I*-*V*s characteristics shown in **Fig. 4-4d**, which can be explained by two Schottky diodes connected in a back-to-back geometry.

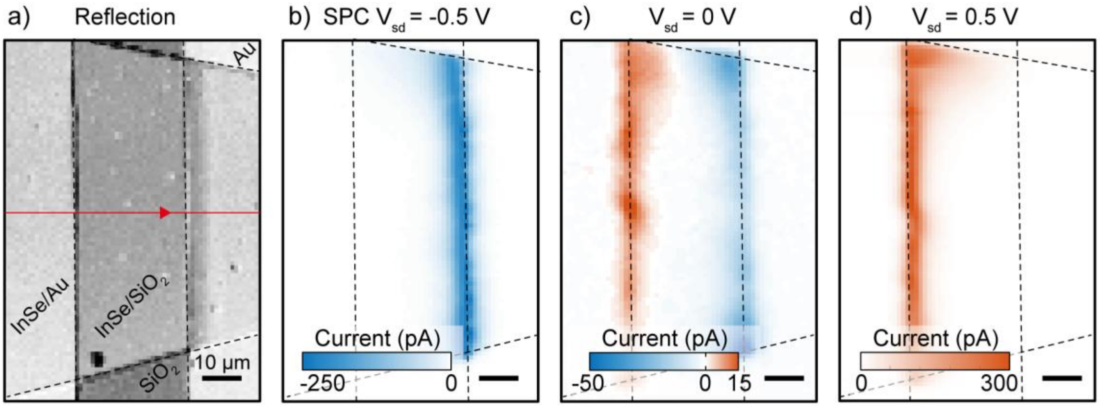

Fig. 4-8 a) Laser reflection map recorded with 660 nm light spot at the same time of the photocurrent of a Au-InSe-Au device. b-d) Scanning photocurrent maps of the device recorded for three different bias voltages.

The Au-InSe-Gr Schottky diode is also investigated using scanning photocurrent microscopy in **Fig. 4-9**. **Fig. 4-9a** shows the optical picture of the area of the Au-InSe-Gr Schottky diode investigated with SPCM measurements and a map of the 660 nm light reflected from the corresponding region has been shown in **Fig. 4-9b**. **Figs. 4-9c-e** show the scanning photocurrent maps recorded at V_{SD} = 1 V, 0 V and -1 V, respectively. The map recorded at positive voltage, with the diode biased in forward mode (**Fig. 4-9c**), shows a positive photocurrent (red counts) that is mostly generated at the two contact edges, both at the Au/InSe and at the Gr/InSe interface. Also, a smaller photocurrent is generated in the InSe channel region located between the two electrodes (visible in the in the map as a lighter red shaded region). The rest of the map shows only counts coming from the dark current (I_{Dark} = 0.55 nA at V_{SD} = 1 V). The map recorded at V_{SD} = 0 V (**Fig. 4-9d**) shows only a region with negative photocurrent centered at the Au-InSe contact edge indicating that an electric field is naturally present at this interface even in absence of an external bias voltage, while the absence of the current at the Gr/InSe contact edge indicates that the Schottky barrier should be too small to be able to separate the photogenerated carriers. Notice that the map recorded at zero bias can also be interpreted as a mapping of the short circuit current of the diode. Similar to the previous case, the SPCM map recorded at negative bias in **Fig. 4-9e** (with the diode biased in reverse mode) shows only a region of negative photocurrent generated at the Au-InSe interface with no photocurrent coming from the Gr-InSe interface or from the InSe channel.

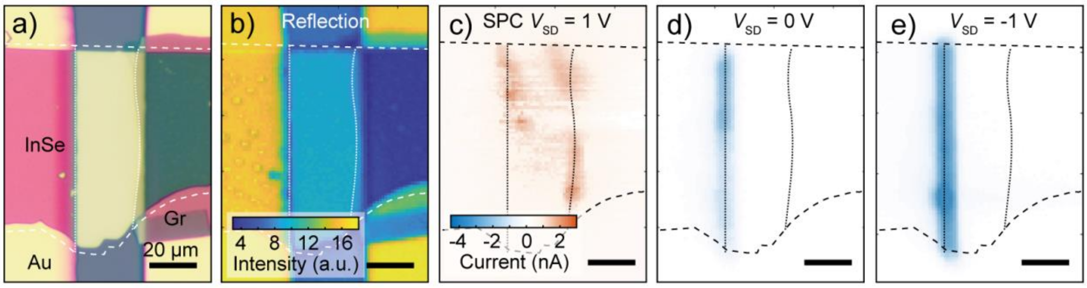

Fig. 4-9 a) Optical picture of the area of the Au-InSe-Gr studied with SPC. b) Laser reflection map recorded with 660 nm light spot at the same time of the photocurrent. c-e) Photocurrent maps of the device recorded in three different biasing conditions: forward voltage (1 V) (d), zero bias (e) and reverse voltage (-1 V) (f).

Using information from the *I*-*V*s (**Fig. 4-4**) and the SPCM maps (**Fig. 4-8**, **Fig. 4-9**) of the Au-InSe-Au and Au-InSe-Gr devices, a schematic band structure of the devices under investigation has been proposed in **Fig. 4-10**. **Fig. 4-10a** shows the band structure of the symmetric Au-InSe-Au device at zero external voltage (black curve) and with positive (FV) and negative voltage (RV). The gold electrodes are represented by Fermi distributions with Fermi energy E_F and the InSe by its conductance band minimum. From the *I*-*V*s of **Figs. 4-4d** and **f** and from the SPCM maps shown in **Fig. 4-8** and **Fig. 4-9** one can infer the presence of a Schottky barrier for electrons between n-type InSe and Au. The conductance band minimum of InSe shows a spatial dependence that arises from the charge transfer between metal and semiconductor.

Moving from the center of the semiconductor channel toward the electrodes, the band shows an upward bending (in a region generally called depletion layer or space charge region) reaching the highest point at the M-S interface, where the intrinsic electric field is expected to be the largest. The barrier height $\phi^0_{B,Au} \approx 0.5$ eV, which corresponds to the Schottky barrier height at zero bias, can be calculated according to the Schottky-Mott rule considering the work function of Au $W_{Au} \approx 5.1$ eV and the electron affinity of InSe $\chi_{InSe} \approx (4.55 \sim 4.60)$ eV.[395,398,415,422-425] The application of a bias voltage V_{SD} shifts the Fermi energy of each electrode in opposite directions and the voltage drop across each element in the device (left electrode/InSe, InSe channel and right electrode/InSe) depends on the resistance of the particular element (which can in turn depend on the voltage). The width of the depletion layer of the left (right) Schottky barrier is expected to increase (decrease) for RV biasing conditions and to decrease (increase) for FV. Also, the total voltage is expected to drop more across the reversely biased electrode/InSe than the other. In such a device, both at positive and negative voltages, the electrons have to overcome a strong barrier at the electrode reversely biased (the right electrode at positive voltage FV and the left electrode at negative voltage RV). The current is thus limited both for positive and for negative voltages giving rise to the current saturation observed in the *I*-*V*s at both large positive and negative bias.

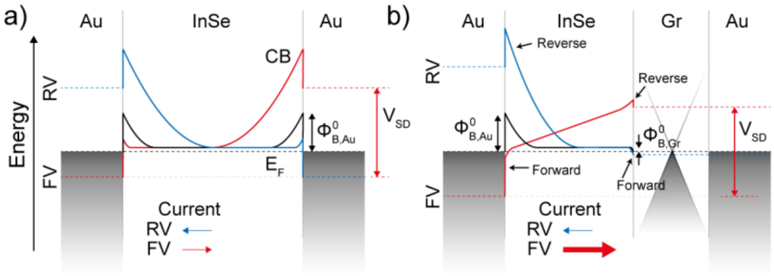

Fig. 4-10 a-b) Band diagram of a Au-InSe-Au (a) and Au-InSe-Gr (b) device at zero voltage (black curve), at positive voltage (red curve, FV) and at negative voltage (blue curve, RV). The dashed line shows the Fermi level energy (E_F) and there are indicated the Schottky barriers of InSe with gold $\Phi^0_{B,Au}$ and with graphite $\Phi^0_{B,Gr}$.

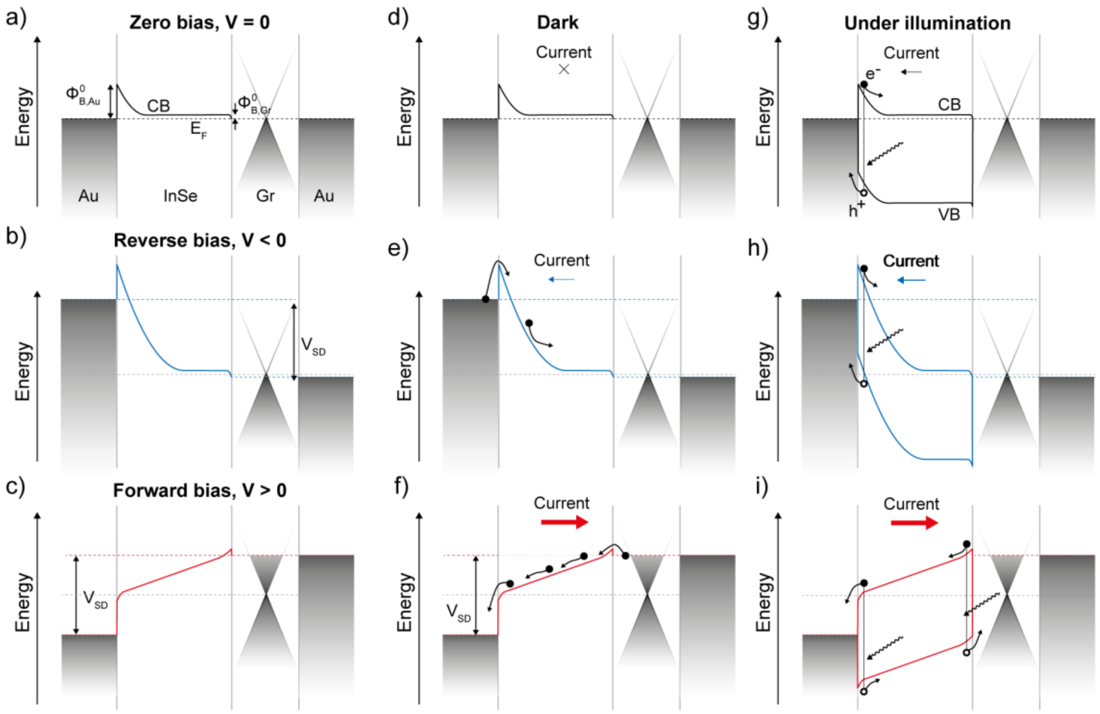

Fig. 4-11 a-c) Band diagram of an Au-InSe-Gr device at zero voltage (black curve), at reverse or negative voltage (blue curve) and at positive or forward voltage (blue curve). The dashed line shows the Fermi level energy (E_F) and there are indicated the Schottky barriers of InSe with gold $\Phi^0_{B,Au}$ and with graphite $\Phi^0_{B,Gr}$. d-f) Same diagrams of panels (a-c) with indicated the electron injection and the current flow in dark conditions. g-i) Same as panels (d-f) but under illumination conditions.

Conversely, in the case of graphite electrodes the reported work function values are $\chi_{Gr} \approx (4.5\sim4.7)$ eV,[426] and thus the expected contact with InSe falls in the range from not rectifying ($\phi^0_{B,Gr} \approx -0.1$ eV) to slightly rectifying (0.15 eV). Considering the variation in the predicted barrier values, a small Schottky barrier $\phi^0_{B,Gr} \approx 0.05$ eV has been chosen considering that a small variation of this value would not change the experimental results. **Fig.4-10b** shows the schematic band structure of the Au-InSe-Gr device with three different bias voltages (see also **Fig. 4-11** for a more detailed version of the band diagram). In this case the asymmetry in the contact barriers with the two different electrodes generates a preferred direction for the current flow. In the forward voltage (FV) mode the Au-InSe contact is forward biased while the Gr-InSe is reversely biased. In such configuration the electrons can flow easily since the only barrier is small and is located at the Gr-InSe reversely biased contact and the total resistance of the device is small and should be limited by the sheet resistance of InSe (the total voltage in this situation drops across the InSe channel and at the InSe/electrode interfaces).[52,415] In the SPCM map recorded at V_{SD} = 1 V shown in **Fig. 4-9c** the observation of a positive photocurrent located at both the

Au-InSe and the Gr-InSe interfaces is consistent with the band diagram of **Fig. 4-10b** in FV voltage configuration (see also **Fig. 4-11**). On the other hand, in the reverse voltage (RV) biasing the strong Schottky barrier $\phi^0_{B,Au}$ is reversely biased and thus only a small current can flow through the device, which is characterized by a large resistance dominated by the Au-InSe contact resistance (with the voltage dropping mostly across this interface).

4.2.4 Determination of Au/InSe Schottky barrier height

In order to estimate the barrier height $\phi^0_{B,Au}$ the study of temperature dependency *I*-*V*s of the device kept in dark has been carried out and reported in **Fig. 4-12a**. The *I*-*V*s recorded while increasing the temperature from room temperature (T = 297 K) to T = 452 K show a current increase both in the forward bias and in reverse bias and a decrease of the rectification. All these *I*-*V*s have been fitted using Equation 4-7 and based on the results the saturation current I_0 and the temperature are used to make Richardson plot of $\ln(I_0/T^2)$ vs. $1000/T$ shown in **Fig. 4-12b**. By rewriting Equation 4-4 as:

$$\ln(I_0/T^2) = \ln(A\,A^*) - \frac{q\,\phi^0_{B,Au}}{kT}, \tag{4-8}$$

one can see that the slope in the Richardson plot gives the barrier height $\phi^0_{B,Au}$. From the fit shown in **Fig. 4-12b** a barrier height of $\phi^0_{B,Au} = (0.46\ \pm 0.06)$ eV can be extracted, which is comparable to the value ~0.5 eV predicted by the Schottky-Mott rule.[52,398,422]

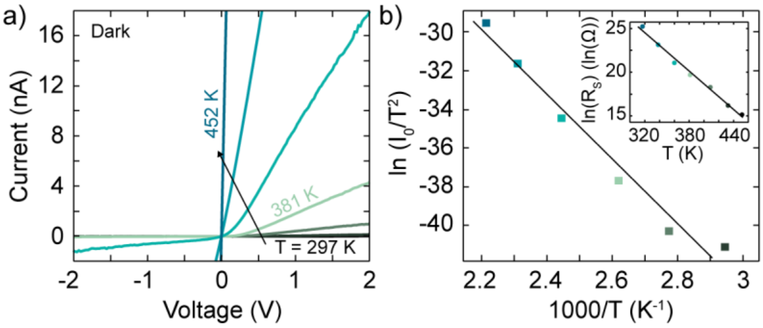

Fig. 4-12 a) Current-voltage characteristics of Au-InSe-Gr recorded at different temperatures in dark conditions. b) Richardson plot of the saturation current of Au-InSe-Gr extracted from fits to the *I*-*V*s in panel (c). Inset: natural logarithm of the series resistance (R_S) extracted as a function of temperature.

4.2.5 Optoelectronic performance

After having established the energetic of the devices under study, the characterizations of the optoelectronic performances of the Schottky diode are followed. **Fig. 4-13a** shows the current recorded as function of time *I*-*t*s with the device kept under a square wave modulated illumination at 530 nm. At the beginning of the traces, when the device is kept in dark, the current flowing through it is on the order of few pA both in FV and in RV bias (V_{SD} = 2 V and V_{SD} = -2 V respectively). After switching on the illumination a positive photocurrent at V_{SD} = 2 V and a negative photocurrent at V_{SD} = -2 V can be observed. The photodiode geometry allows detecting an external illumination also in absence of an applied voltage as can be seen in the *I*-*t* recorded at zero bias that shows a negative photocurrent under illumination. From the plot it is evident that both the magnitude of the photocurrent and the response time change dramatically under FV and RV biasing. To better appreciate this fact, **Fig. 4-13b** plots the previous *I*-*t* in a semi-logarithmic representation with the current in absolute value. The dark current recorded at the beginning of the trace, at zero bias and at -2 V, is on the order of 1 pA (comparable to the noise floor of the setup), while at 2 V is about two orders of magnitude larger. After switching on the illumination, the photocurrent with the device in FV biasing grows to of approximately 3 nA, which is about one order of magnitude larger than the current generated at zero bias and in RV both showing a similar photocurrent of 300 and 400 pA respectively.

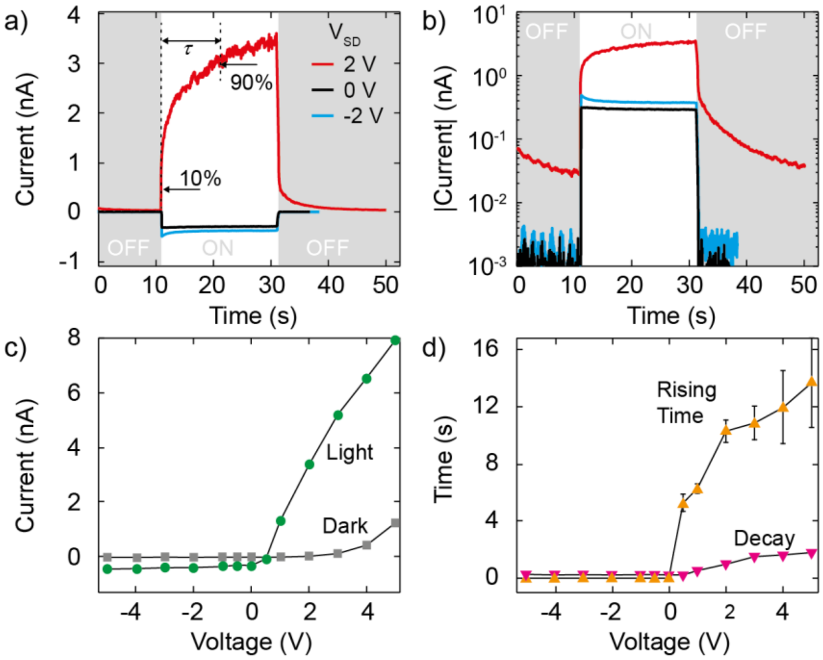

Fig. 4-13 a-b) Current in linear scale (a) and current absolute value in logarithm scale (b) at different V_{SD} (-2 V, 0 V, 2V) recorded in an Au-InSe-Gr Schottky diode as a function of time (*I-t* curves) while turning on and off a 530 nm light source with a power density of 33.4 mW/cm^2. c) Light (green) and dark (gray) current extracted from a series of *I-t* curves as a function of bias from -5 V to 5 V while the 530 nm light source under on and off state. d) Rising time (yellow) and decay time (purple) as a function of bias from -5 V to 5 V extracted from *I-t* curves.

The strong bias dependency of the photocurrent can be seen in **Fig. 4-13c** where the total current flowing through the device has been collected in dark and under illumination extracted from *I-t*s recorded at different bias in the range -5 V to 5 V. At negative voltages the photocurrent shows only a weak dependency on the applied voltage, going from -0.42 nA at -5 V to -0.30 nA at 0 V corresponding to an increase rate of ~0.03 nA/V. At positive voltages the rise is much faster and one can extract a rate of ~2 nA/V, approximately two orders of magnitude larger than the reverse biased regime. This large change in the magnitude of the photocurrent is accompanied by a change in the time response of the device. According to the definition of the rising time τ_r and the decay time τ_d using the 10%-90% rule,[321] in which the time that takes for the signal to go from 10% of the saturation to 90% of this value can be extracted, as shown in **Fig. 4-13a**, in the case of τ_r. Already inspecting the traces in **Fig. 4-13a** and **b** one can see that both rising and decay times are much faster when the device is operated at zero bias and at -2 V compared to 2 V. This fact is clearly visualized in **Fig. 4-13d** where the extracted rising and decay times are plotted as a function of voltage. For negative voltages the extracted rising times of 40 ms are probably upper bounds limited by the time resolution of the measurement setup while the decay times are on the order of 280 ms, contrarily when a positive voltage is applied the rising times increase to more than 13 s and the decay time can reach 1.8 s, showing a change in response time of more than one order of magnitude when passing from FV to RV biasing.

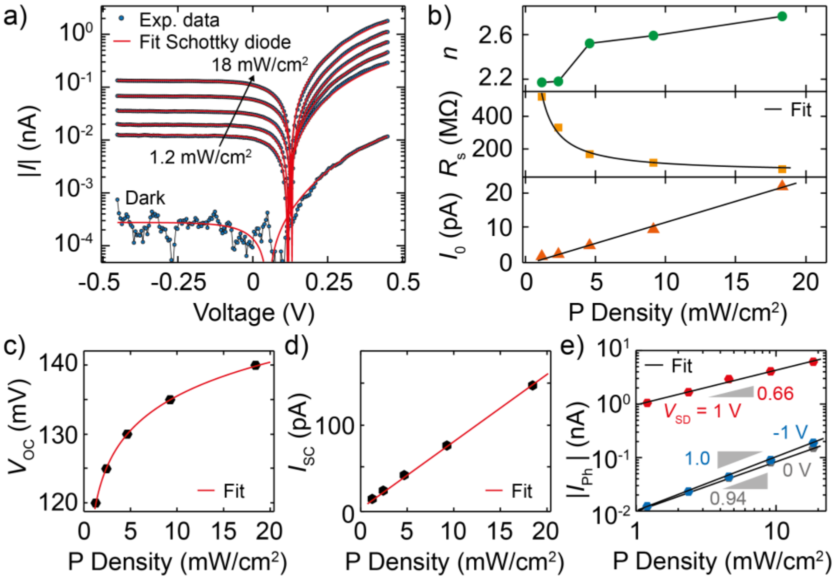

Fig. 4-14 a) Experimental (blue dots) and fitted (red curves) dark and under various 530 nm illumination powers *I*-*V* curves plotted in semi-logarithmic scale based on current absolute value. b-d) The fitted parameters I_0, series resistance R_s, ideal factor n (b), open circuit voltage (V_{oc}) (c) and short circuit current I_{sc} (d) as a function of 530 nm illumination power density extracted from panel a. f) Experimental photocurrent as a function of illumination power at 530 nm recorded at three different bias (-1 V, 0 V, 1 V).

The illumination power dependency of the device was also investigated. **Fig. 4-14a** shows a set of *I*-*V*s plotted in semi-logarithmic scale and recorded at room temperature with the device kept in dark and under illumination at 530 nm with power densities going from 1.2 mW/cm^2 to 18 mW/cm^2. The *I*-*V*s can be fitted using equation 4-5 and the results are shown in **Fig. 4-14a** and **b**. As can be seen from **Fig. 4-14a** the agreement between the *I*-*V*s predicted by the Schottky model and the experimental *I*-*V*s is excellent, which can reproduce well the increase in both the saturation current in reverse biasing and in the forward voltage current. **Fig. 4-14b** shows the dependency of the Schottky diode ideal factor, series resistance and reverse saturation current on the incident optical power. When increasing the illumination power the ideal factor n, which is related to the recombination mechanism of the free charge carriers in the device, increases from 2.2 to 2.7, at the same time the series resistance decreases of approximately one order of magnitude, going from 500 MΩ to 70 MΩ and the reverse saturation current increases linearly with the illumination power going from 2 pA to 20 pA. The linear increase in I_0 can be explained by the lowering of the Schottky barrier $\phi_{B,Au}^{0}$ under illumination,[427,428] also confirmed by the lower value of the Schottky barrier estimated using the temperature dependency of the I-Vs under illumination shown in **Fig. 4-15**. The increase in the ideality factor is consistent with the lower barrier and indicates the activation of additional non-ideal recombination paths under high light intensity and large number of photogenerated charge carriers. The higher illumination power also induces a decrease of R_s, which can be understood from an increase of the carrier density in InSe. Writing the current flowing in a semiconductor assuming only drift processes, $I = (N + P)\, q\, v$,[52] where $(N + P)$ is the density of free carriers and v is the drift velocity, one can see that the resistance, which is proportional to $(N + P)^{-1}$, is expected to be inversely proportional to the optical power P_{Opt}. The middle panel of **Fig. 4-14b** shows the excellent agreement between the experimental R_s values and the theoretical function $R_s\,(P_{\mathrm{Opt}}) = a \cdot P_{\mathrm{Opt}}^{-1} + b$ with a and b as fitting parameters equal to respectively 570 MΩ·cm^2/mW and 55 MΩ.

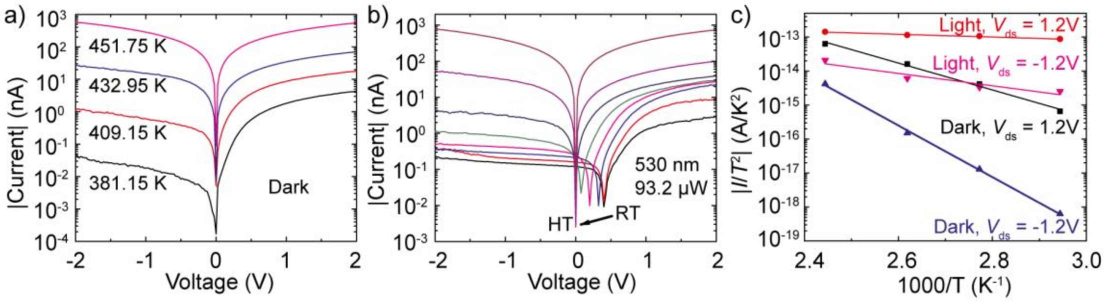

Fig. 4-15 Temperature dependent I-V curves recorded in dark (a) and under 530 nm illumination with the power of 93.2 µW (b) with a high condition of ~10^{-6} mbar. c) The Schottky barrier extraction at the bias of 1.2 V and -1.2 V in dark and light conditions, clear observation is that the Schottky barriers ($\Phi_{\mathrm{B,\ light,\ 1.2\ V}}$ = 35.2 meV, $\Phi_{\mathrm{B,\ light,\ -1.2\ V}}$ = 163.8 meV) under illumination both at 1.2 V and -1.2 V bais smaller than them in dark ($\Phi_{\mathrm{B,\ dark,\ 1.2\ V}}$ = 342.9 meV, $\Phi_{\mathrm{B,\ light,\ -1.2\ V}}$ = 657.1 meV).

Apart from the fitting parameters defined by the diode current-voltage equation, two important quantities especially relevant in solar cells and photodiodes are the open-circuit voltage V_{OC} and short-circuit current I_{SC}. **Fig. 4-14d** and **e** show the power dependency of these two quantities. As can be seen from the good agreement between the fit and the experimental plots, V_{OC} depends logarithmically on the incident power and I_{SC} depends linearly on the power. These two dependencies confirm that the photocurrent is predominantly caused by the photovoltaic effect as opposed to thermoelectric effects (that can be also the source of photocurrent at zero bias). The linearity of the short-circuit current is also evident in the log-log plot of the photocurrent generated at zero bias voltage versus illumination power, shown in **Fig. 4-14f**. From a power law fit to the equation 3-5, $I_{\mathrm{ph}} = A{\bullet}P^{\alpha}$,[321] using the exponent α

as the only fitting parameters, it can be determined that at 0 V α = 0.94 and that in reverse bias at -1 V α = 1. Contrarily, at 1 V in the forward voltage regime the photocurrent shows a sublinear dependency on the incident power with α = 0.66. The voltage dependency of α can be explained by the different photocurrent generation mechanism in reverse and forward bias.[321,370] In the reverse bias (and zero bias) cases, the presence of an (intrinsic) electric field in the device promotes the formation of a depletion region that causes the photodetector to operate as a normal photodiode with fast operation speed, but limited responsivity. In this case, the photogenerated electron-hole pairs in InSe can be efficiently separated by the electric field present at the Au/InSe interface and the minority carriers can quickly drift away from the InSe and can be collected into the Au electrode. This fast removal of the photogenerated minority carriers from the InSe channel prevents the trapping of these carriers and the subsequent photogain mechanism that can result in lower response speed. For forward bias the external electric field is applied in the opposite direction in respect to the intrinsic one, thus reducing the depletion layer width. In absence of such a space charge region, the minority carriers can get trapped by holes trapping centers. The trapping processes effectively increase the lifetime of the majority carriers and introduce photogain in the system, which can increase the responsivity at the expenses of the response speed. The value close to 1 assumed by α in the reverse biasing and zero bias conditions confirms that hole trapping centers are not effective in these regimes, corresponding to a linear dependency of the photocurrent on the illumination power (and a power independent responsivity). On the other hand, the participation of traps in the FV regime reduces the value of α to 0.66, which indicates that the rate of carriers trapping increases with the illumination power and thus at high injection level fewer carriers participate to the total current as compared to low injection. This is consistent with the voltage dependency of the response time and responsivity of the device which shows slower photodetection with higher responsivity in the FV biasing and faster photodetection but with lower responsivity in the RV biasing.

4.3 Pt-InSe-Gr Schottky diode

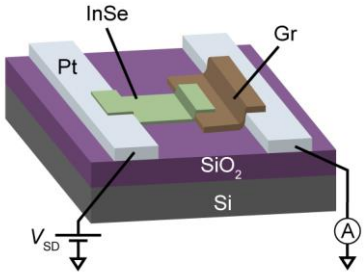

Following a similar fabrication routine of Au-InSe-Gr Schottky diode and taking advantage of the larger work function of Pt ($W_{Pt} \approx 5.5$ eV),[395] Pt-InSe-Gr diodes with larger Schottky barrier height have been demonstrated. After fabrication, the optoelectronic performance evolution of a Pt-InSe-Gr device has been followed in time when exposed to air and finally it can achieve a robust and stable Schottky diode behavior. According to the scanning photocurrent mapping and temperature-dependent characterization, the Schottky barrier height of diodes is determined to be ~540 meV with an open circuit voltage of ~0.6 V. The hysteresis in *I-V* characteristics of Pt-InSe-Gr Schottky diodes also has been discussed.

4.3.1 Sample fabrication

The Pt-InSe-Gr devices also are fabricated using an all-dry deterministic transfer technique (see section 2.4) to stack thin mechanically exfoliated graphite and InSe flakes onto pre-patterned platinum electrodes. Briefly, bulk graphite (HQ Graphene, The Netherlands) and InSe (grown by the Bridgman method) are mechanically exfoliated onto Gel-Film (WF 4 x 6.0 mil Gel-Film from Gel-Pak, Hayward, CA, USA). After optical identification with a microscope, a graphite flake with at least one long straight edge and uniform thickness of ≈ 15 layers, is firstly transferred onto a 280 nm SiO_2/Si substrate covering only one of the previously evaporated platinum electrodes (Pt/Cr thickness 45 nm/5 nm, electrode separation 30 μm). Then a homogeneous InSe flake (≈ 20-30 layers) is deposited bridging on one side the uncovered platinum electrode and on the other the graphite flake. **Fig. 4-16** shows the microscope photographs of five Pt-InSe-Gr devices investigated in section 4.3 and 4.4. In the case under investigation, by exploiting the electron affinity of InSe ($\chi_{InSe} \approx 4.6$ eV) and the large difference in work function between graphite ($W_{Gr} \approx 4.5$-4.7 eV) and platinum ($W_{Pt} \approx 5.5$ eV),[395,398,415,422-425] one can achieve a large barrier difference between the Gr-InSe contact and the Pt-InSe one, the first being ohmic and the second yielding a finite Schottky barrier.

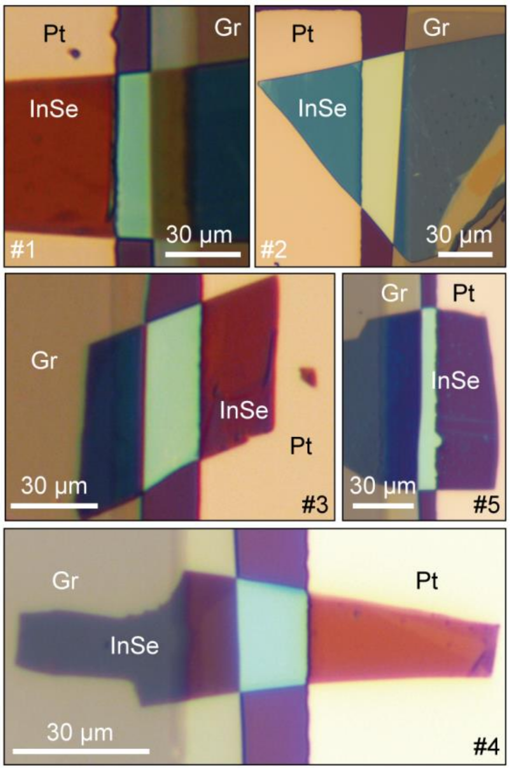

Fig. 4-16 Five Pt-InSe-Gr devices fabricated on SiO_2/Si substrates based on asymmetric Gr-Pt electrodes.

4.3.2 How the Pt-InSe-Gr devices evolve into Schottky diodes

After the fabrication of such a device, the evolution of its electrical and optoelectronics characteristics can be followed by recording current-voltage characteristics (I-Vs) in dark and under controlled illumination. Since it is known that InSe is sensitive to the environmental conditions, all the electrical and optoelectronic characterizations discussed in this section were recorded under high vacuum condition (~10^{-6} mbar) while the device aging was carried out in ambient conditions.[370] The top panel of **Fig. 4-17a** shows the I-Vs of pristine sample 1 recorded in dark (black curve) and under controlled illumination at 530 nm (green curve) with power density 0.05 W/cm^{-2} and a spot size of diameter ≈ 600 µm. The pristine I-V recorded in dark is slightly asymmetric with maximum a current of the order of 1 nA, while under illumination at 530 nm the current increases significantly both at positive and negative bias, reaching respectively 1000 nA and -1300 nA. From the photocurrent one can calculate the responsivity of the device using the formula $R = I_{Ph} \,/\, P_{Dev}$,[321] where

P_{Dev} is the total optical power hitting the device, finding R = 6 A/W for a bias voltage of 1 V. The bottom panel of **Fig. 4-17a** shows the *I*-*V* characteristics of the same Pt-InSe-Gr device after being passivated for two weeks in air, which present marked differences from the pristine state ones. Both the current recorded in dark and that under illumination are much lower in the aged state than these in the pristine state, with a maximum current of 4 pA at 1 V and 0.5 pA at -1 V in dark and 0.8 nA at 1 V under illumination. At zero voltage, one can observe a current of -0.3 nA flowing in the device, usually referred to short circuit current I_{SC}, and similarly, one can also find an open circuit voltage V_{OC} (defined as the voltage for which no current flows in the device) of ~0.6 V. Importantly both I_{SC} and V_{OC} were absent in the *I*-*V*s under illumination of the device in pristine state. These observations together with the reduction of the absolute current indicate the evolution of the device into a Schottky photodiode. This phenomenon can be attributed to a passivation of the defects in InSe due to the interaction with air-species as have been discussed in chapter 3,[370] which leads to the formation of a sizeable Schottky barrier by promoting a Fermi level pinning. Additional optoelectronic measurements on device 1 in its pristine state and after passivation can be found in **Fig. 4-18 and Fig. 4-19**, respectively.

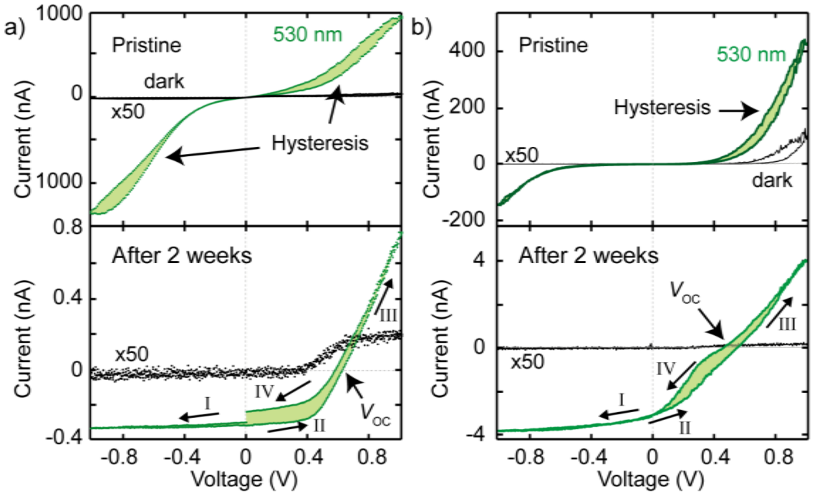

Fig. 4-17 Current-voltage characteristics of a Pt-InSe-Gr device (sample 1 (a) and sample 5 (b)) recorded in dark (black curve) and under 530 nm illumination with power density 0.05 W/cm^{-2} (green curve) just after fabrication (top panel) and after two weeks (bottom panel). In the graph there are indicated the hysteresis region, the open circuit voltage V_{OC} and the roman numbers that indicate the consecutive measurement steps (I-IV).

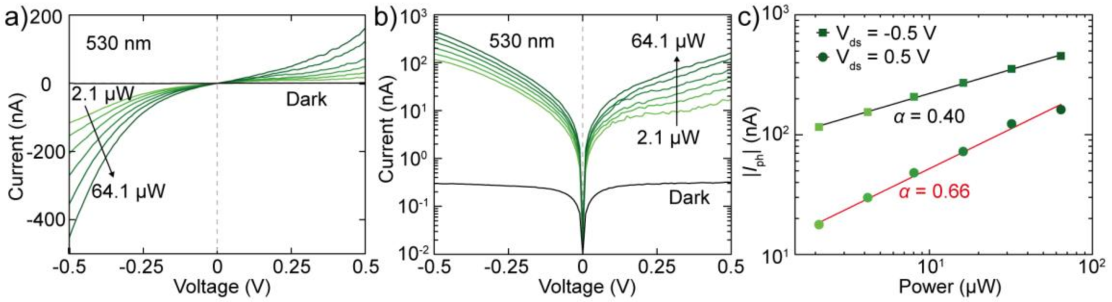

Fig. 4-18 The characterization of a Pristine Pt-InSe-Gr device. a-b) Current-voltage characteristics of a Pt-InSe-Gr Schottky diode just after fabrication in dark and under illumination with increasing power in linear scale (a) and semi-logarithmic scale (b). The optical picture of the device is shown by inset panel in (a). c) Absolute value of the photocurrent generated in the device as a function of optical power recorded at two different bias voltages. The solid lines represent power law fits to the data with the exponent α indicated in the plot.

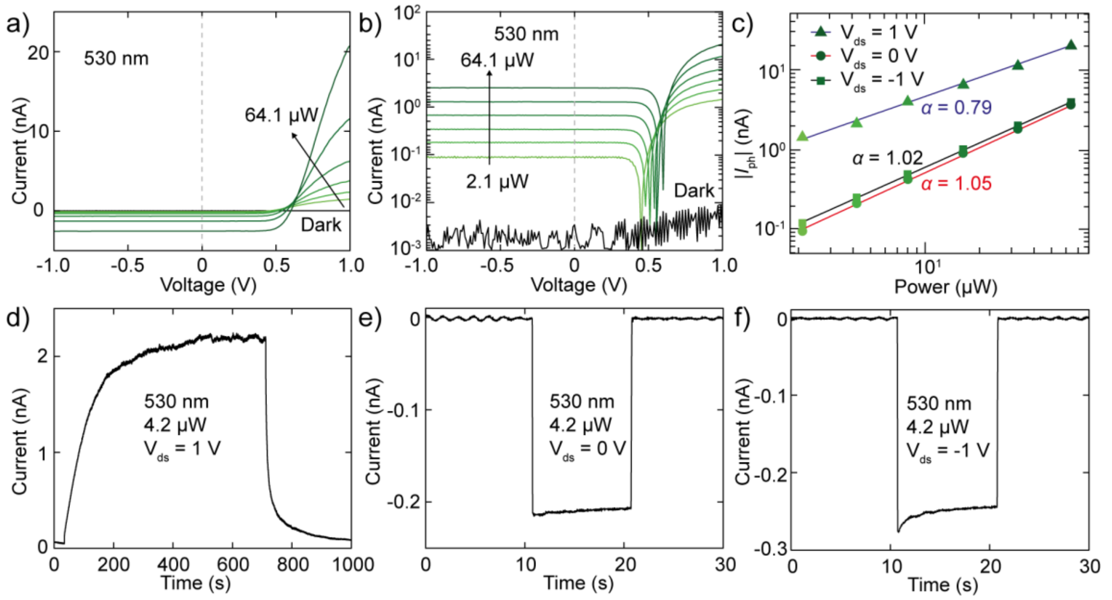

Fig. 4-19 The characterization of a Pt-InSe-Gr Schottky diode after degradation. a-b) Current-voltage characteristics of a Pt-InSe-Gr Schottky diode after air passivation in dark and under illumination with increasing power in linear scale (a) and semi-logarithmic (b). c) Absolute value of the photocurrent generated in the device as a function of optical power recorded at three different bias voltages. The solid lines represent power law fits to the data with the exponent α indicated in the plot. d-f) Current-time curves recorded respectively at V_{ds} = 1 V (d), 0 V (e) and -1 V (f) under a square-wave modulated illumination.

Another important feature of these devices visible in the *I-V* under illumination of **Fig. 4-17a** is the presence of a counterclockwise hysteresis in the forward voltage region. In fact, when the bias is swept from 0 V to 1 V a lower current (corresponding to larger resistance) flows through the device as compared to the sweep from 1 V to 0 V (the difference between the curves is highlighted by the light green shaded region). It is important to note that both the Schottky diode electrical behavior and the counterclockwise hysteresis are reproducible phenomena that can be observed in all the five devices investigated. In a second example, **Fig. 4-17b** shows the *I*-*V*s of sample 5 in pristine state and after passivation, which shows a similar behavior.

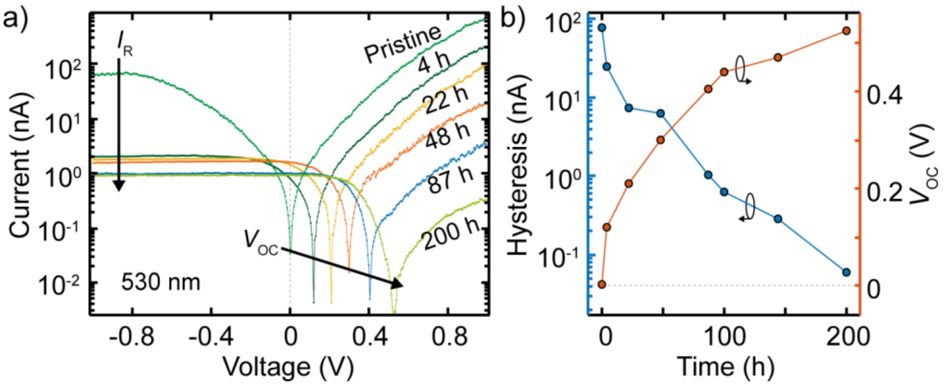

Fig. 4-20 a) Current-voltage characteristics of the device recorded under 530 nm illumination as a function of air exposure time (sample 3). b) Evolution of the current hysteresis (extracted at V_{DS} = 0.7 V) and the open circuit voltage as a function of air exposure time.

Fig. 4-20a shows a set of the *I*-*V*s recorded from -1 V to 1 V under 530 nm illumination during the passivation in air of sample 3 plotted in a semi-logarithmic scale. Both the reduction of current (the reverse current I_R at negative bias decaying rapidly to few nA and the forward current also decreasing from hundreds of nA to less than 1 nA) and the development of the open circuit voltage (V_{oc}, from ≈ 0 V to more than 0.5 V) and short circuit current (I_{sc}) can be obviously followed in several days, which indicates that the change of device is not abrupt and that the intermediate states can be investigated. Though the magnitude of this current hysteresis depends on the passivation time (among other variables such as voltage bias range and temperature), even in the passivated state it can be observed (see bottom panel of **Fig. 4-17a-b**). The evolution of the V_{oc} and current hysteresis at a fixed forward voltage is further summarized, shown in **Fig. 4-20b** as a function of passivating time, which suggests an interplay effect between Schottky barriers, whose height determines among other properties the magnitude of V_{OC}, and charge trapping/detrapping processes in the device. From these data one can find that between 50 and 150 hours, the device presents a sizeable V_{OC} larger than 0.2 V and hysteresis values around 0.1-10 nA, which can be used for an optoelectronic memory (will be discussed in section 4.4).

4.3.3 Scanning photocurrent microscopy and band diagram structure

After air passivation, the scanning photocurrent microscopy (SPCM) is employed to establish the band diagram structure of Pt-InSe-Gr Schottky diode. The details of the system can be found in section 2.6 in chapter 2. **Fig. 4-21a** shows the current maps recorded with bias voltages of 0 V (left), 0.6 V (center) and 1 V (right), where blue indicate negative current and red positive (the current of the map taken at 0.6 V has been multiplied by a factor 5 for better comparison). **Fig. 4-21b** shows the map of the light reflected during a SPCM measurement (see **Fig. 4-16** for a microscope optical picture of sample 2) with contours highlighting the important features (green InSe flake, grey Pt electrode edge, yellow Gr electrode edge). From these maps one can see that the photocurrent is generated inside the InSe flake area, indicating that the photoresponse observed depends on InSe and not on other effects (*e.g.* Pt-SiO_2 interface, Pt electrodes). The map taken at 0 V (and similarly the maps recorded at negative voltages, not shown here) shows only a negative photocurrent generated at the Pt-InSe interface, without any contribution from the Gr-InSe side. When increasing the voltage to 0.6 V (comparable to the value of V_{OC} estimated in “global” illumination), apart from the negative photocurrent generated at the Pt-InSe interface, the appearance of a second region of positive photocurrent can be observed at the Gr-InSe interface. The total photocurrent, which can be found by integrating the current map in x and y directions after removing the dark current (estimated from the average current generated when the laser illuminates the regions outside the InSe flake), at 0.6 V is approximately 0 since the positive and negative contributions cancel each other. In the rightmost current map taken at 1 V, one can observe only a positive photocurrent at the Gr-InSe and the disappearance of the negative photocurrent region at the Pt-InSe side.

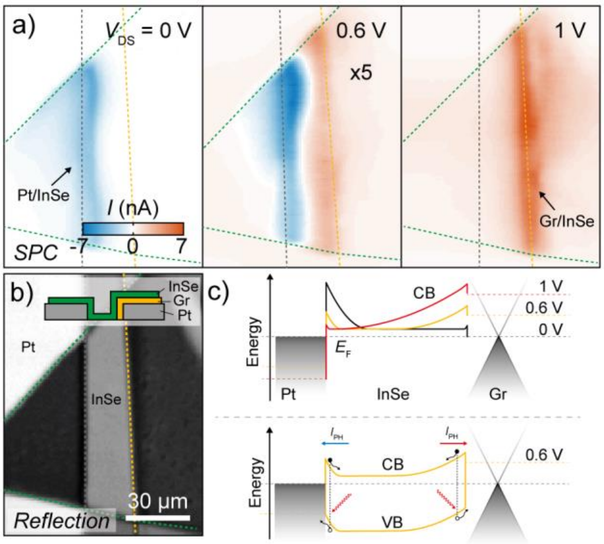

Fig. 4-21 Scanning photocurrent microscopy of a Pt-InSe-Gr Schottky diode and band description. a) Scanning photocurrent microscopy (SPCM) image of the Pt-InSe-Gr sample 2 device with zero bias voltage applied (left), 0.6 V approximately the open circuit voltage (middle) and 1 V (right). b) Spatial map of the intensity of the reflected light from the device collected during the SPCM measurement at 0 V. c) Top: schematic band diagram of the device in the three biasing conditions shown in panel (a). Bottom: schematic of the local photocurrent generation at 0.6 V.

From the SPCM measurements discussed above, a schematic band diagram of the device has been proposed and shown in the top panel of **Fig. 4-21c** at the three bias conditions. The generation of negative photocurrents on the Pt side observed up to 0.6 V indicates the presence of a Schottky barrier between Pt and InSe $\Phi_{B,Pt}$, which is reversely polarized for negative voltages. This barrier induces an intrinsic electric field that can separate electron-hole pairs in absence of an external field and generate a short circuit current at 0 V (visible in the SPCM map taken at 0 V). On the other hand, the absence of photocurrent at the Gr-InSe interface indicates an ohmic or low barrier contact on this side. The bottom panel of **Fig. 4-21c** shows a scheme of the local photocurrent generation at 0.6 V, a bias condition close to the open circuit voltage.

4.3.4 Determination of Schottky barrier height of Pt/InSe

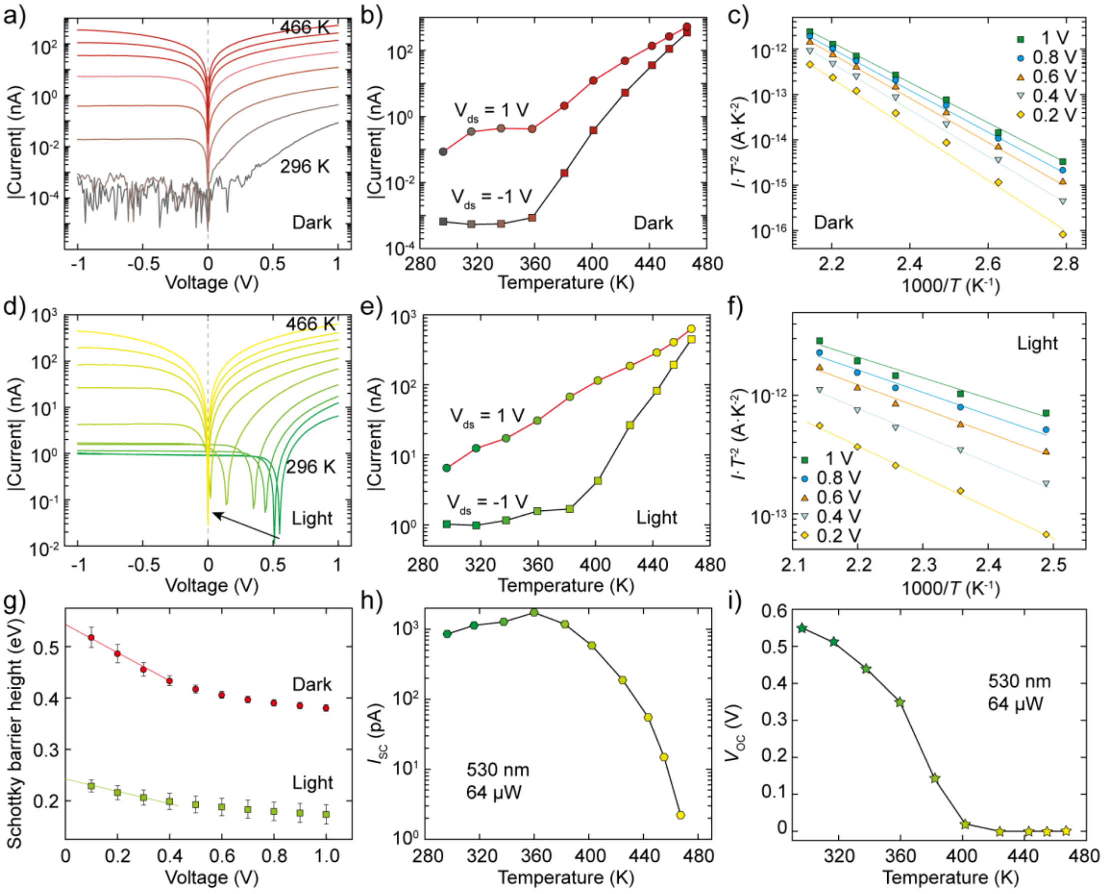

Fig. 4-22 Temperature-dependent characterization of Pt-InSe-Gr Schottky diodes. a-c) *I*-*V*s as a function of temperature (a), current absolute value at 1 V and -1 V extracted from the *I*-*V*s in Panel a (b), and the Richardson plot as a function of forward bias (c) in dark. d-f) *I*-*V*s as a function of temperature (d), current absolute value at 1 V and -1 V extracted from the *I*-*V*s in Panel a (e), and the Richardson plot as a function of forward bias (f) under 530 nm illumination. g) Schottky barrier heights of Pt-InSe in dark and under 530 nm illumination vary upon the applied forward voltage. h-i) Short circuit current (I_{cs}, h) and open circuit voltage (V_{oc}, i) as a function of temperature.

In **Fig. 4-22**, the temperature-dependent electrical and optoelectronic measurements have been performed on the Pt-InSe-Gr Schottky diode, which are employed to estimate the Schottky barrier height of Pt-InSe interface both in dark and under illumination. The *I*-*V*s recorded as a function of temperature of the device kept in dark and illuminated by 530 nm LED has been presented in **Fig. 4-22a** and **Fig. 4-22d**, respectively. All the *I*-*V*s recorded while increasing the temperature from room temperature (T = 296 K) to T = 466 K show a current increase both in the forward bias and in reverse bias and a decrease of the rectification. This behavior can be observed more obviously by plotting the current absolute value extracted at 1 V and

-1 V as a function temperature in **Fig. 4-22b** and **Fig. 4-22e**. Based on the current value extracted at various voltages from the temperature-dependent *I*-*V*s and the temperature, the Richardson plot in dark and under illumination have been shown in **Fig. 4-22c** and **Fig. 4-22f**. Using Equation 4-6, one can calculate that the slope in the Richardson plot gives the barrier height at different bias. From the plot shown in **Fig. 4-22g** the barrier height of Pt-InSe at 0 V in dark and under illumination are determined to be 542 ± 6 meV and 238 ± 2 meV. **Fig. 4-22h-i** show both the short circuit current (I_{sc}) and open circuit voltage (V_{oc}) tend to decrease with the growth of temperature, which corresponds to a Schottky barrier shrinking while heating up the device

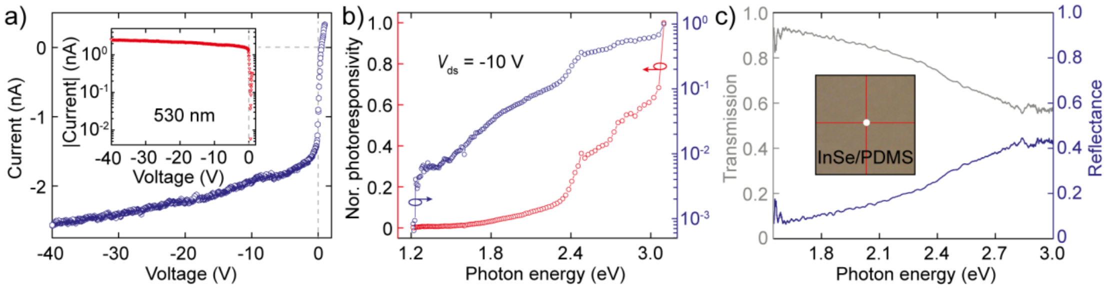

Fig. 4-24 a) Voltage-current characteristics of a Pt-InSe-Gr Schottky diode at large reverse biased condition (-40 V) under illumination of 530 nm LED. The inset shows a semi-logarithmic presentation reproduced based on the current absolute value. b) Normalized photoresponsivity as a function of illumination wavelength of a Pt-InSe-Gr Schottky diode recorded at reverse bias regime and plotted in linear (left axis) and semi-logarithmic scale (right axis). c) Transmission (left axis) and reflectance (right axis) spectrum of a thin InSe flake. The inset shows the optical picture of the thin InSe flake deposited onto the PDMS substrate and the white spot indicates the illumination position.

To further identify the quality of Pt-InSe-Gr Schottky diode, two additional characterizations under larger reverse bias regime also have been performed on these devices. **Fig. 4-24a** shows a *I*-*V* recorded from -40 V to 1 V, which indicates a robust Schottky rectification behavior without breakdown. Taking advantage of the ultrafast operation speed under reversely biased condition, one can determined the electrical band gap without considering the influence of the traps existing in the devices. **Fig. 4-24b** shows the normalized photoresponsivity as a function of incident photon energy in linear (right axis) which indicates the generated photocurrent originates the photons absorbed by InSe (see **Fig. 4-24c**), and semi-logarithmic scale (left axis), from which the electrical band gap of InSe can be determined to be ~1.23 eV.

4.4 Optoelectronic memory effect based on Pt-InSe-Gr Schottky diode

By utilizing the trapping/detrapping operation mechanism, optoelectronic memories also can be realized employing these 2D Schottky diodes based on the metal semiconductor (M-S) junction between Pt and InSe and the ohmic contact between graphite and InSe. These devices are capable of switching between a low resistance state (LRS) and high resistance state (LRS) thanks to the application of an external voltage together with illumination. In this way one can store information with a retention time of the order thousands of seconds and a switching ratio up to 100. This work will pave the way to the investigation of 2D optoelectronic memories based on Schottky diodes. Note that this section is mainly based on the submitted paper "Optoelectronic memories based on InSe Schottky diodes" where I am the first contributor.

4.4.1 Background

Information technology, which deals with storing, retrieving, transmitting, and manipulating data or information, has strongly shaped our society in the last decades. This profound change was made possible by the invention of novel devices, such as smartphones and personal computers. In order to deal with larger and larger quantity of data, great research efforts have been dedicated to investigate memory elements and nowadays novel memory technologies based on various nanoscale phenomena are generating interest both in the scientific community and in the industry.[429-433] One interesting device is the optoelectronic memory (OEM), which is a multi-functional device capable of optical sensing, data storage and data processing.[434,435] In this device external illumination and applied voltages are used to store and manipulate bits of information. This combination of both optical stimuli and electrical readout voltage has potential for developing a larger switching ratio between a low resistance state (LRS) and a high resistance state (HRS) and also to perform additional functions apart from storing information.

As introduced in chapter 1, two-dimensional (2D) materials, have exhibited attractive electrical and optical properties for the fabrication of optoelectronic memories, thanks to their broadband photo-detection ability (from ultraviolet to infrared regime), excellent photoresponsivity and gate tunability.[374,429,436,437] Moreover, their mechanical flexibility, optical transparency and the easiness of fabrication of van der Waals heterostructures make 2D materials suited for the production of memory devices on flexible and transparent substrates.[66,214,438,439] In literature, various optoelectronic memory effects mechanisms that can take place in planar 2D materials devices have been reported, including charge trapping/detrapping,[440-452] Schottky barriers and grain-boundaries.[453-456] Among these different operation mechanisms, one of the most studied is the charge trapping/detrapping that has been demonstrated in different ways. One of the first example of 2D material based OEM was reported by Roy et al. using a graphene/MoS_2 van der Waals heterostructure that showed both highly sensitive photodetection and gate-tunable persistent photoconductivity (PPC), functioning as a rewritable OEM.[457] Alternatively, Bertolazzi and coauthors demonstrated a 2D floating gate memory device based on a MoS_2-graphene heterostructure in a field-effect transistor geometry.[446] Other 2D memories, based on localized electronic levels, have also been reported.[440,442,458-462] Sangwan and coauthors reported a memory effects originating at the grain boundaries in single-layer MoS_2.[455] A symmetric back-to-back Schottky diode based on $CuIn_7Se_{11}$ and Au electrodes has been used both to store information and to perform image sensing by Lei and coauthors.[454] However, despite these previous works, to our knowledge an investigation on 2D based Schottky diode OEMs devices (that have the advantage of a simple device geometry) is still lacking in the literature.

4.4.2 Optoelectronic memory basis and operation

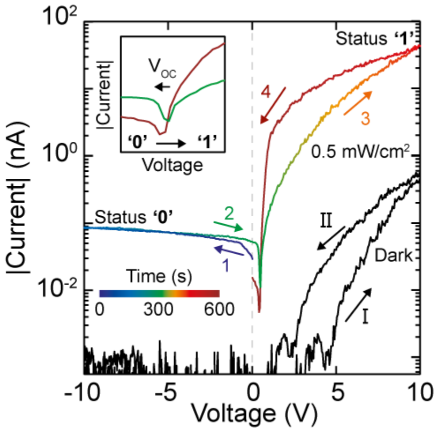

Fig. 4-24 Current-voltage characteristics of sample 3 in dark and under illumination at 530 nm and power density 0.5 mW/cm^2. The colors in the curve under illumination indicate the time at which each point was collected according to the color bar in the top left corner.

As previously discussed in section 4.3, the Pt-InSe-Gr Schottky diodes present both an obvious current hysteresis and a robust rectification behavior at large reverse condition, which thus motivates to think how the hysteresis evolves at larger bias range. **Fig. 4-24** shows *I-V* curves recorded from sample 3 from -10 V to 10 V in dark and under illumination. A counterclockwise hysteresis can be observed in both *I-V*s, while the hysteresis of *I-V*s under illumination is much larger than that in dark conditions. Based on the observation that the application of a negative (positive) voltage in presence of illumination brings the device to a high (low) resistance state, one can define the application of a large negative voltage as an “erase” operation (E, writing of a logic ‘0’) and a large positive voltage as a “write” operation (W, writing of a logic ‘1’). Additionally, an “idle” state (i) in absence of voltage and a “read” state (R) where a small positive voltage is applied both in dark condition are defined, in which the high or low resistance can be assessed.

A first example of a OEM operation has been shown in **Fig. 4-25a** where the Pt-InSe-Gr device (sample 4) is subjected to three consecutive “write”, “read”, “erase”, “read” cycles (with “idle” states in between each operation) with an operation time *T* of 150 s. The top panel shows the voltages applied to the device in the different states, 10 V for “write”, -5 V “erase”, 3 V “read” and 0 V “idle”. The middle panel shows the current flowing through the device as a function of time in the range between -0.05 nA and 0.3 nA. Starting from the left, in the first “write” operation (0-150 s) the current jumps to positive values larger than the current meter saturation (10 nA) and in the “idle” operation (150-300 s), and also in all the subsequent ones, the current is close to zero with the device being at rest. In the first “read” operations (300-450 s) an initial increase in current has been observed, which saturates around 200 pA. During the “erase” operation (600-750 s), the current jumps to large negative values, and in the subsequent “read” (900-1050 s), the current increases to a maximum value of 3 pA. The large difference in the current observed during the “read” operations when the device is a logic status of ‘**1**’ or ‘**0**’ (200 pA and 3 pA respectively), indicates a change in the device resistance as shown in the bottom panel of **Fig. 4-25a** in a semi-logarithmic scale. The resistance of the device (calculated dividing the voltage applied by the current observed) shows a difference of two orders of magnitude between the ‘**1**’ state and the ‘**0**’, respectively characterized by resistances of ≈ 15 GΩ and ≈ 1000 GΩ giving a ratio between HRS and LRS equal to 67. In the remaining two “write”, “read”, “erase”, “read” cycles the device shows a similar behavior and the overall performance can be assessed through the histograms of the current and of the resistance shown on the right side of **Fig. 4-25a**. The clear separation between the peaks in the histograms corresponding to the '**1**' and '**0**' states demonstrates that through the application of large positive or negative voltages together with illumination at 530 nm, one can reliably tune the resistance of the sample between two states and store information.

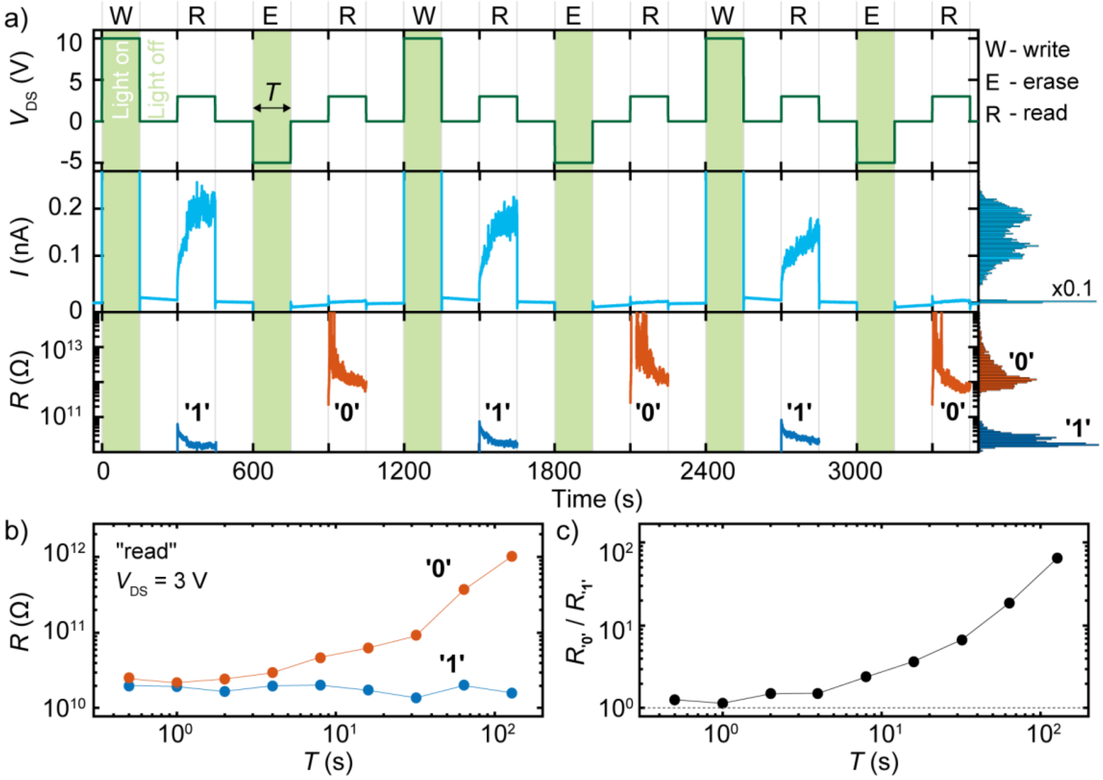

Fig. 4-25 Pt-InSe-Gr Schottky operated as a photomemory. a) Three consecutive "write"/"read"/"erase"/"read" cycles of the Pt-InSe-Gr device (sample 4). The "write", "erase" and "read" operations are performed applying respectively a voltage of 10 V, -5 V and 3 V, in between different operations in an idle state the device is kept at 0 V. During the "write" and the "erase" operations 530 nm illumination is applied onto the device (power density 0.5 W/cm^2). The top panel shows the source-drain voltage as a function of time, the central panel shows the current recorded and the bottom panel shows the resistance of the device in semi-logarithmic scale. b) Resistance of the device recorded at 3 V ("read") after writing (blue circles) and erasing (red circles) the photomemory as a function of the operation cycle time *T*. c) Ratio between the resistance of the '**0**' status and that of the '**1**' status as a function of *T*.

In the previous working example of the InSe-based OEM, an operation time *T* of 150 s resulted in a switching ratio of ≈ 67 between the resistances corresponding to the '**1**' and '**0**' states. Then now one can turn to the investigation of the performance of OEM for shorter *T*, since the "write" and "erase" time could determine the final resistance achieved by the system. The same measurements shown in **Fig. 4-25a** have been repeated for values of *T* ranging from 0.5 s to 150 s. **Fig. 4-25b** shows a logarithmic plot of the average resistance of the system extracted at 3 V (“read”) in the ‘**0**’ and ‘**1**’ states as a function of *T* (called respectively $R_{'\mathbf{0}'}$ and $R_{'\mathbf{1}'}$). Starting from values of *T* smaller than 10 s, one can see that the resistances in both the ‘**1**’ and ‘**0**’ states have similar values around 20 GΩ. After the initial plateaus, for larger *T* the resistance of the ‘**0**’ state increases reaching a value of 1000 GΩ at *T* = 150 s, while the resistance of the ‘**1**’ states fluctuates between 10 and 20 GΩ. From this measurement it is evident that the resistance of the ‘**0**’ state determines the dependency of the ratio $R_{'\mathbf{0}'}/R_{'\mathbf{1}'}$ on *T*, as also shown in **Fig. 4-25c**, and ultimately the performance of the OEM (the smallest operation time for this OEM, sample 3, to function is 8 s, with a ratio $R_{'\mathbf{0}'}/R_{'\mathbf{1}'}$ larger than 2). Note that this characteristic time present variations between different samples, *e.g.* sample 4 shows a slightly faster operation time of 4s. See additional measurements of samples 1 and 3 under memory operation cycling in **Fig. 4-26**.

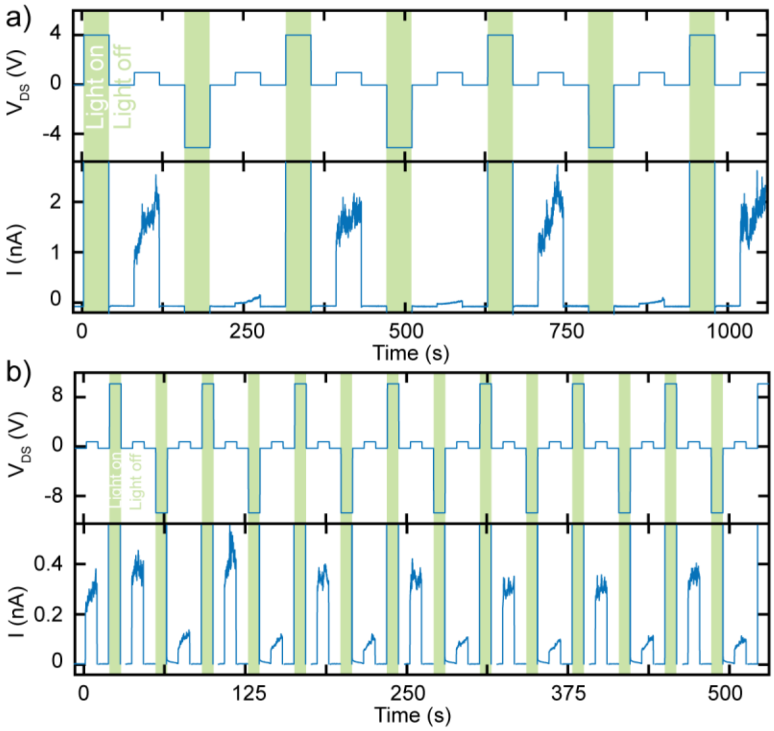

Fig. 4-26 Memory operations of sample 1 (a) and sample 3 (b).

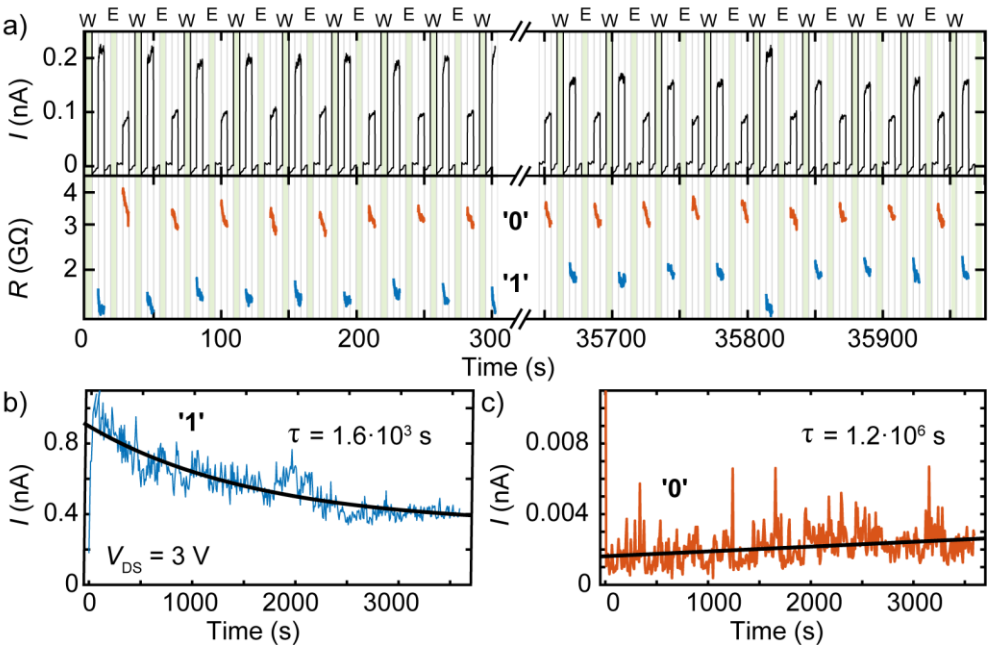

Fig. 4-27 Long-term operation of the photomemory. a) Long term operation of the Pt-InSe-Gr device (sample 5) with 900 "write"/"read"/"erase"/"read" consecutive cycles demonstrated. Top: current recorded and the bottom panel, bottom: resistance of the device in semi-logarithmic scale. b-c) Retention time during a "read" operation of the logic state **'1'** (b) and **'0'** (c).

After discussing the basic operations of the OEM, which can encode 1 bit of information by switching between a low resistance state and a high resistance one, the investigation of the long-term operation and reproducibility is carried out. To perform this test, sample 5 was used, which shows similar characteristics to sample 4. **Fig. 4-27a** shows a long-term measurement in which 900 consecutive memory operations (W-i-R-i-E-i-R-i) with T = 5 s for a total time of 36000 s have been performed. The top panel shows the current flowing through the device recorded during the first ~20 cycles and the last ~20 cycles while the bottom panel shows the extracted resistance. From the plots one can see that the switch between the HRS and the LRS is very reproducible and that the memory continues to function properly even after 900 consecutive "write"-"erase" operations. The values of the resistance in the two states do not change substantially during the measurement demonstrating the reliability of the device as a memory.

Additionally, the retention time of the memory to store either a '**1**' or a '**0**' also have been tested. To do this the memory device was kept in "write" or "erase" state for 1 hour, then in "idle" state for 1 hour and finally a "read" operation was performed for an additional hour. **Figs. 4-27b-c** show the current recorded during the "read" operations in the two logic states. At 0 s the difference between the current corresponding to the ‘$\mathbf{1}$’ and to the ‘$\mathbf{0}$’ states is large being approximately 1 nA in the ‘$\mathbf{1}$’ and 1 pA in the ‘$\mathbf{0}$’, respectively a low resistance state and high resistance one. After applying the “read” voltage of 3 V both a monotonous decrease in the current of the ‘$\mathbf{1}$’ state and an increase in the current of the ‘$\mathbf{0}$’ state have been observed. One can expect that after waiting for a large enough time these two currents should converge to the same value (a value comprised between 1 pA and 1 nA) thereby losing the information stored in the logic status of the memory. To model this process these two curves have been simultaneously fitted to an exponential decay or growth (respectively for the ‘$\mathbf{1}$’ and ‘$\mathbf{0}$’) by imposing the same saturation value for the current at infinite time. From the best fits shown in **Figs. 4-27b-c** one can find that the time constants in the ‘$\mathbf{1}$’ and ‘$\mathbf{0}$’ cases are respectively equal to 1.6×10^3 s and 1.2×10^6 s. The lower of these two quantities is the one that determines the retention time of the memory, which demonstrates that it is capable of storing information for at least 1 hour in the “idle” state and for more than 1000 s in the “read” giving a total retention time of more than 5000 s.

4.4.3 Transport mechanism

Finally, a transport mechanism has been proposed to explain the OEM operation based on the experimental findings. The device evolution in air discussed in **Fig. 4-20** shows a clear increase of the open circuit voltage of the device as a function of air exposition time. This observation indicates that the Pt-InSe Schottky barrier height is affected by the InSe air-induced passivation process, *i.e.* the interaction between the intrinsic defect in the exfoliated InSe flakes and oxygen species present in air.[370,377,463] Interestingly, in the literature there are various examples of systems where oxygen and chalcogen vacancies determine the Schottky barrier properties and give rise to memory effects.[453] Here, the memory effect in Schottky diode devices can be attributed to the trapping and detrapping of charge carriers, promoted by the application of an external voltage together with illumination. In general, the Schottky barrier height is related to the total charges trapped at distance δ from the interface by:[323,464]

$$\Phi_{\mathrm{B,Pt}} = W_{Pt} - \chi_{InSe} - \frac{\delta Q}{\varepsilon}, \qquad (4\text{-}9)$$

where Q is the trapped charge per unit of area and ε is the permittivity of the material. According to this equation a decrease in the number of negative charges trapped induces a lowering of the barrier height, which in turn leads to a decrease in the resistance of the device according to the formula of the current density of a diode:

$$J(V) = A^* T^2 \exp\left(-\frac{\Phi_{\mathrm{B,Pt}}}{kT}\right)\left[\exp\left(\frac{V}{nkT}\right) - 1\right], \tag{4-10}$$

where A^* is the Richardson constant, T is the temperature and n is the diode ideal factor.[415]

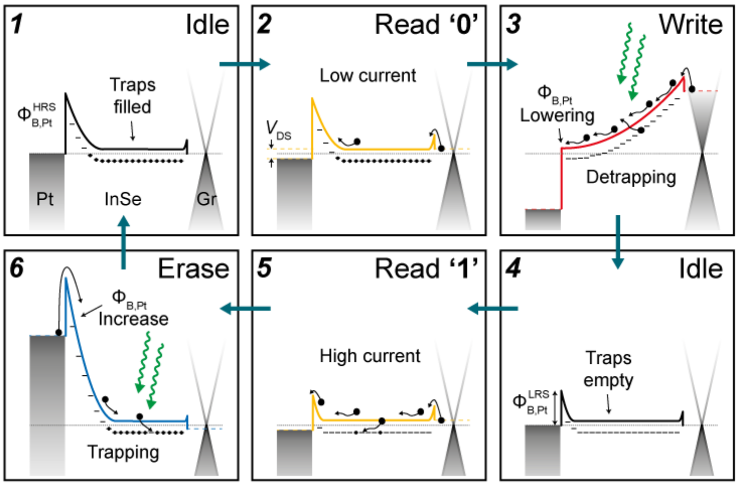

Fig. 4-28 Model of the photomemory operation. a) Proposed schematic band diagram of the Pt-InSe-Gr photomemory starting from the memory in state '**0**' under idle conditions in the top left panel.

A proposed schematic band diagram of the system has been shown in **Fig. 4-28**, with a set of donor trap levels localized close to the conduction band of InSe (see also **Fig. 4-21**). **(*1*)** The top leftmost panel of **Fig. 4-28** shows the diagram of the device at zero bias in the "idle" state (and logic state '**0**'). In this configuration InSe presents a larger barrier with Pt with height $\Phi^{HRS}_{\mathrm{B,Pt}}$ and a negligible one with Gr. It has been assumed that most of the traps are filled, except from the ones located in the space charge region close to the Pt-InSe interface where an electric field is present. **(*2*)** By increasing the voltage to small positive values ("read") the Pt-InSe Schottky barrier becomes forwardly polarized and the relative depletion region shrinks. Conversely, in the reversely-biased Gr-InSe contact a depletion region starts to form. In such a configuration most of the voltage drops at the two interfaces and the electrons injected from the graphite have to overcome an extended positively charged depletion region at the Pt-InSe side giving rise to a small current (HRS). **(*3*)** In the "write" configuration the Pt-InSe Schottky barrier is in forward biasing and the voltage can drop in the InSe channel in addition to the two interfaces between InSe and electrodes. The electric field can destabilize the donor traps and reduce the trap occupation, which in turn reduces the Pt-InSe barrier height according to Equation 4-9 and the size of the associated depletion region. Moreover, the presence of illumination can promote this charge detrapping process by introducing trap-to-band transitions. **(*4*-*5*)** In the subsequent "idle" and "read" operations, the device presents a small barrier on the Pt side $\Phi_{\mathrm{B,Pt}}^{LRS} < \Phi_{\mathrm{B,Pt}}^{HRS}$, which allows more current to flow through the device according to Equation 4-10 (LRS). In equilibrium, in absence of strong electric fields, the traps can get occupied again in time and the device slowly evolves to the HRS. This is compatible with the smaller retention time observed for in the LRS in respect to HRS (see **Figs. 4-27b-c**). **(*6*)** In the last "erase" step, a large negative voltage puts the Pt-InSe Schottky barrier in reverse bias, which causes the voltage to drop at the Pt-InSe side. The traps in the InSe channel and at the Gr-InSe interface are filled, thereby increasing the Pt-InSe Schottky barrier and increasing the resistance of the device (HRS).

4.5 Conclusions

In summary, thanks to the air passivation effect of the defects in thin InSe, various Schottky devices based on thin InSe with different van der Waals electrical contacts have been investigated. In the case of Au electrodes, a rectifying Schottky contact with a sizeable barrier between InSe and Au bas been found and estimated to be ≈ 460 meV by temperature dependent measurements, which is consistent with Schottky–Mott rule. While in the case of graphite, the contact gives rise to a negligible contact barrier (smaller than 100 meV) thanks to the similar electron affinity of thin InSe and graphite. Exploiting this strong contact barrier difference, a Au–InSe–Gr Schottky diode, based on symmetric pre-patterned gold electrodes and with asymmetric van der Waals contacts, has been fabricated. The asymmetric contacted device shows *I*–*V* curves that follow perfectly the Schottky diode equation in a large bias range. Furthermore, also the optoelectronic measurement of the devices is in agreement with the predicted Schottky diodes behaviors under reverse and forward biasing conditions. Following a similar fabrication routine of Au-InSe-Gr Schottky diode and taking advantage of the larger work function of Pt (W_{Pt} ≈ 5.5 eV), Pt-InSe-Gr devices also have been designed and demonstrated. Interestingly, it is found that after the fabrication of such a device, its electrical characteristics evolve in time when exposed to air and finally can achieve a robust and stable Schottky diode behavior, with a Pt-InSe Schottky barrier height of ≈ 540 meV and an open circuit voltage of ≈ 0.6 V, which are confirmed by scanning photocurrent microscopy and temperature-dependent measurements.

Another important feature of Pt-InSe-Gr Schottky diodes is the presence of a counterclockwise hysteresis in the *I-V*s in the forward voltage region. Based on the observation that the devices take a larger hysteresis under illumination than that of in dark, the investigations of optoelectronic memory effect based on Pt-InSe-Gr Schottky diodes has been introduced. It is found that these devices are capable of switching between a low resistance state and a high resistance one thanks to the application of an external voltage together with illumination, which can store information with a retention time of the order thousands of seconds and a switching ratio up to 100.

These results show the reliability of electronic and optoelectronic properties of van der Waals Schottky contacts. The easiness of fabrication, which comes from the van der Waals stacking by dry deterministic transfer, and the reproducible Schottky barrier formation are important factors for future applications of 2D semiconductors–metal systems.

5

MECHANICAL PROPERTIES AND STRAIN ENGINEERING OF THIN INSE

This chapter is devoted to the study of the mechanical properties of InSe and the use of strain engineering to tune the electrical and optical properties of InSe through controlled mechanical deformations. First, the Young's modulus of InSe, which describes the "stiffness" of the material, will be experimentally determined using buckling metrology method. Subsequently, biaxial strain is used to tune the electrical and optical properties of thin InSe flakes, including piezoresponse, band gap modulation, and strain engineered optoelectronic devices will be also investigated.

5.1 Flexibility of thin InSe: determination of Young's modulus

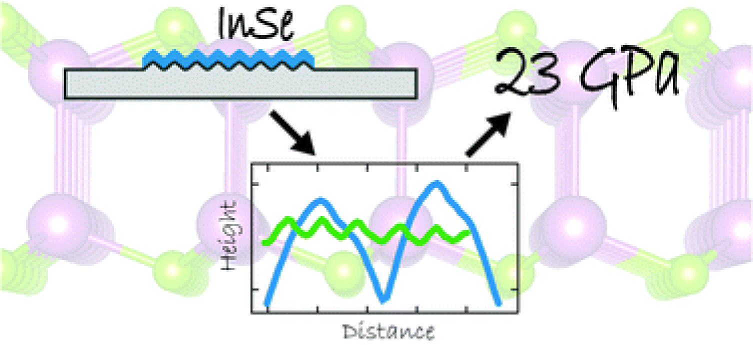

The buckling-based metrology method has been employed to experimentally determine the Young's modulus of thin InSe, and a value $E = 23.1 \pm 5.2$ GPa has been obtained. Moreover, a comparison between thin InSe Young's modulus and that of the other 2D semiconductors indicates that thin InSe is one order of magnitude more flexible than transition metal dichalcogenides (TMDCs), which contributes to an efficient strain transfer from flexible substrates to InSe flakes. Note that this section is mainly based on the published paper "InSe: a two-dimensional semiconductor with superior flexibility" in Nanoscale where I am the first author.[465]

5.1.1 Background: the challenge for determination the flexibility of 2D flakes

As has been introduced in chapter 1, 2D materials are promising candidates for future flexible electronics and optoelectronics applications due to their combination of remarkable mechanical, electrical and optical properties.[466] In fact, from the mechanical point of view, 2D materials are similar to polymers, as they are very elastic and resilient to large deformations,[225,467] while keeping electronic performance comparable to that of crystalline 3D materials.[179,214]

While the electrical and optical properties of 2D materials can be explored with conventional experimental tools developed to test 3D materials and thin film devices, probing the mechanical properties of 2D materials is more challenging, as neither bending nor tensile test macroscopic setups can be employed. Nanoindentation,[467-470] the analysis of the dynamics of the nanomechanical resonators,[471] and the microscopic adaptation of tensile tests setups or Brillouin scattering have been developed to characterize the fundamental mechanical properties of 2D materials such as their Young's modulus.[472-475] Although powerful, these techniques require dedicated setups and rather complex data acquisition and/or analysis. Alternative to these methods, Stafford and coauthors introduced the buckling metrology method,[476] a simple and elegant way to measure the Young's modulus of thin polymeric films by studying the buckling instability, which arises when the film is deposited onto a compliant substrate, and it is subjected to uniaxial compression.[477] Under these conditions, the trade-off between the adhesive forces between film and the bending rigidity of the film leads to a rippling of the thin film with a characteristic wavelength that depends on the elastic properties of the film and the substrates. This elegant method to characterize the mechanical properties of thin films has been extensively used to study coatings and organic semiconducting materials.[476,478] However, it has been scarcely employed to study 2D materials,[479-482] and it seems that it has been mostly overlooked by the 2D materials community until Nestor Iguiñiz and coauthors revisited this method to determine the Young's modulus of 2D transition metal dichalcogenides (TMDCs) flakes.[483] Compared with conventionally employed approaches,[467-475] *i.e.*,nanoindentation, nanomechanical resonators, blister test, and micro-Brillouin light scattering, the buckling metrology method provides a way with simplicity, fast measurement speed, and straightforwardness of the data analysis for measuring the mechanical properties of 2D materials, which thus also can be used for the determination of thin InSe flakes Young's modulus.

5.1.2 Determination Young's modulus of thin InSe

2D thin InSe flakes were mechanically isolated from high quality single crystalline InSe ingots grown by Bridgman method. The details about the bulk crystal growth, characterizations, and exfoliation process have been shown in sections 2.2 – 2.4 of chapter 2. In order to measure the mechanical properties of thin InSe flakes through the buckling metrology method, the InSe flakes have to be deposited onto a very complaint substrate and subjected to uniaxial compression. In the case of InSe deposited on top of Gel-Film (by Gel-Pak®), the flakes undertake a buckling instability when the compression strain in the InSe is above a critical value of approximately 0.07%. Due to the competition between the buckling of the flakes and the adhesion with the substrate, a wavy pattern (ripples) appears on the flakes.[484]

Interestingly, the period of these ripples (λ) is independent on the initial pre-stress of the elastomeric substrate and depends only on the mechanical properties of the flake and substrate:[476,484,485]

$$\lambda = h\left[\frac{8\pi^3(1-\nu_s^2)E_f}{3(1-\nu_f^2)E_s}\right]^{1/3} \qquad 5\text{-}1$$

where h is the thickness of the flake, ν_s and ν_f are the Poisson’s ratio of substrate and flake, E_s and E_f respectively correspond to the Young’s modulus of the substrate and flake. It is very important to point out that this equation is valid under certain assumptions:[483] a) the flake should follow a sinusoidal rippling, b) $E_f / E_s >> 1$, c) the substrate should be much thicker than the flake, d) the amplitude of the ripples should be much smaller than their wavelength (thus the shear forces are neglected), e) the adhesion between the flake and substrate is strong enough to prevent slippage, and f) all the deformations are assumed to be elastic. Therefore, for a known substrate one can extract the Young’s modulus of InSe by measuring the period of ripples for flakes with different thickness.

Fig. 5-1a shows a schematic drawing of the fabrication process followed to apply the uniaxial compression to InSe flakes. Firstly, a Gel-Film substrate with rectangular shape is slightly bent to induce a uniaxial expansion on its topmost surface. Then thin InSe flakes are transferred onto the bent surface by mechanical exfoliation with Nitto tape (see section 2.3 of chapter 2) and releasing the substrate stress to yield the desired uniaxial compression. A transmission mode optical microscopy image of an isolated InSe flake fabricated following this approach has been shown in **Fig. 5-1b**. Due to the buckling instability induced ripples, one can see that the flake presents a marked wavy pattern. The corresponding atomic force microscopy (AFM) topography image is shown in **Fig. 5-1c** with the thickness ranging from 9.4 nm to 24 nm which correspond to ~5L to ~27L. Note that the height extracted from the AFM dynamic mode measurements contains a systematic offset that was determined to be 4.9 ± 0.5 nm in the case of InSe (this value should be subtracted from the AFM data in order to find the real flake thickness, see section 2.3 in chapter 2). This offset, which has been reported also for other 2D materials, can be explained by the different interaction between the tip and either the substrate or the flake.[296] It is important to notice that this offset does not influence the determination of the Young’s modulus of InSe and thus it wasn’t subtracted from the data presented in this section. **Fig. 5-1d** shows the sinusoidal line profile shape of the ripples. From **Figs. 5-1c-d**, one can see that the wavelength λ of the ripples presents a strong dependency on InSe flake thickness.

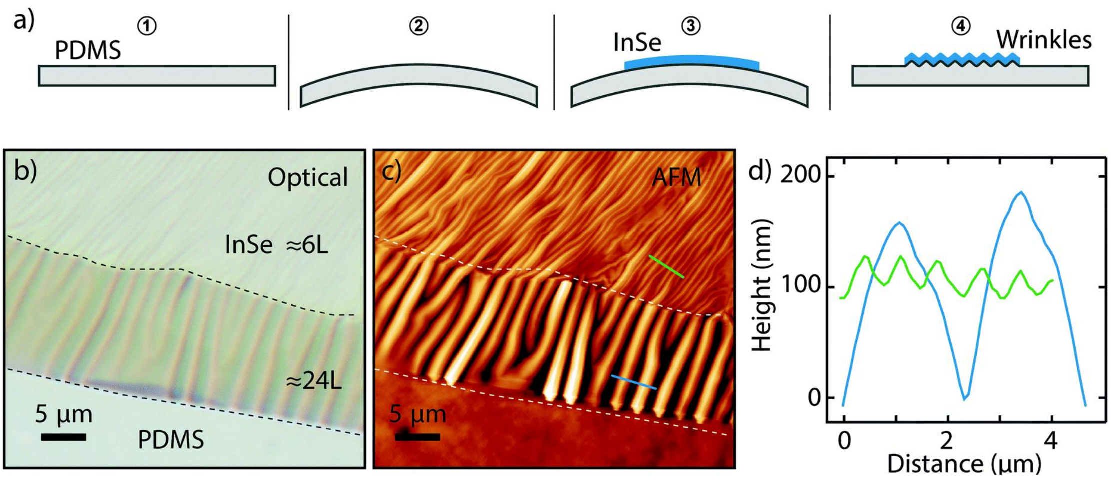

Fig. 5-1 The wrinkled thin InSe flakes. a) The schematic diagram of fabricating wrinkled InSe flakes on the Gel-Film substrate by using the buckling metrology method. b-c) Transmission mode optical pictures (b) and surface morphology recorded by AFM (c) of a wrinkled InSe flake with thicknesses (*h*) of ~6L and ~24L. d) The line profiles of the wrinkles with different thicknesses recorded at the positions marked in panel c (green line, 6L; blue line, 24L).

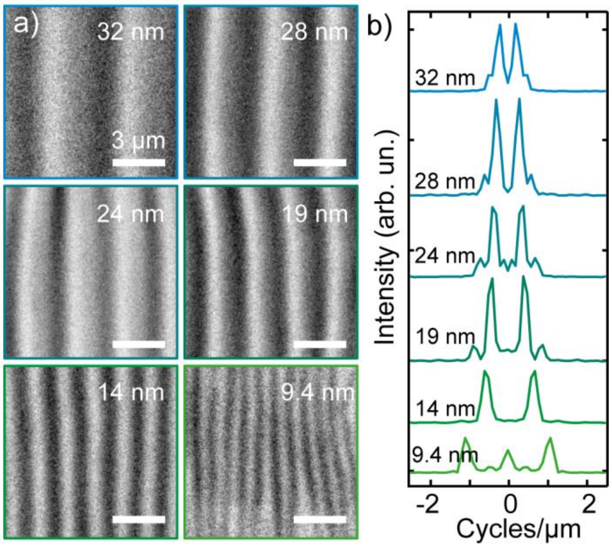

Fig. 5-2 The determination of Young's modulus of thin InSe flakes. a) Grayscale transmission mode optical microscopy images of wrinkled patterns on InSe flakes with thicknesses ranging from 9.4 nm to 32 nm. b) The line cuts along the FFT maxima extracted from the optical images in panel a.

As shown in Equation (5-1), the Young's modulus of thin InSe can be determined by measuring the wavelength of the buckling induced ripples as a function of flakes thickness. **Fig. 5-2a** shows six grayscale transmission mode optical images of the ripples produced on InSe flakes with different thicknesses. The wavelength of the ripples can be accurately extracted through the fast Fourier transform (FFT) of these images which has been shown in **Fig. 5-2b**. Note that rippled patterns with wavelengths smaller than ~0.8 μm and amplitude <10 nm cannot be well-resolved with optical microscopy.[483] In **Fig. 5-3**, it presents how the wavelength of the ripples can be determined in such cases. **Figs. 5-3a-b** show the optical pictures of an ultrathin wrinkled InSe flake (1-3 layers) that has been deposited onto the Gel-film substrate recorded respectively with reflection mode (a) and transmission mode (b). One can see that the ripple wavelengths of InSe flakes with different thickness cannot be well resolved directly based on these optical photographs. Panel c shows the intensity of the blue channel of the transmission image shown in **Fig. 5-3b**. The line with arrows indicates the position of the shown line profiles of the transmission. **Fig. 5-3d** shows the surface morphology of the same region in the panels a and b recorded using atomic force microscopy (AFM) that is capable of resolving the ripples in the thin regions of the flake, and the ripple wavelengths are obtained from 1L to 3L InSe flakes.

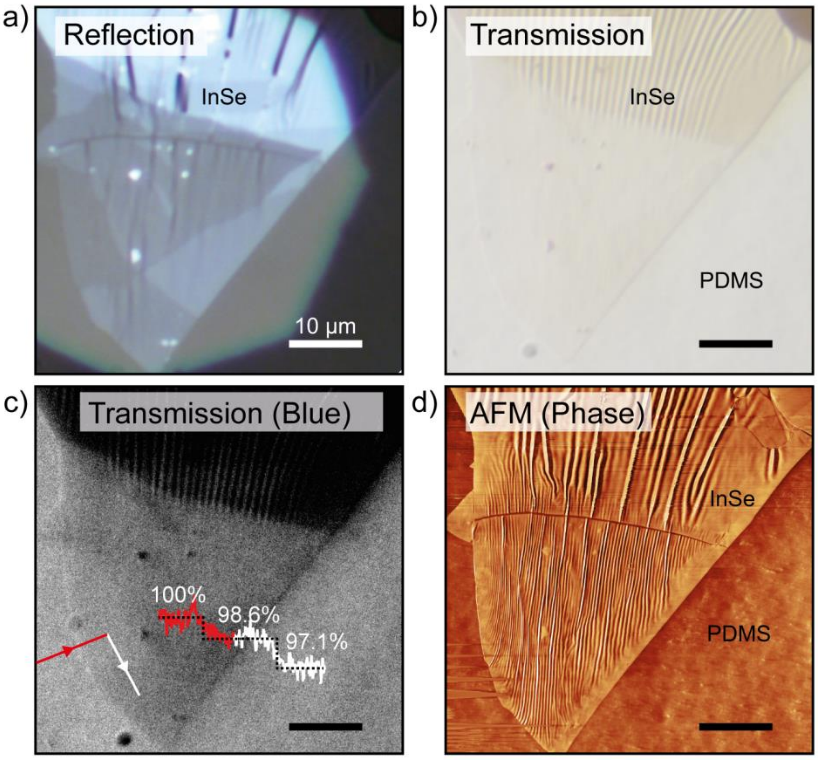

Fig. 5-3 a-b) Optical pictures of a wrinkled InSe flake deposited onto Gel-film in reflection illumination mode (a) and transmission (b). c) Intensity of the blue channel of the transmission image. The line with arrows indicates the position of the shown line profiles. d) AFM phase topology. Notice that the wrinkles (with wavelength < 800 nm) in the thinnest regions, which are visible in the AFM image, could not be observed optically.

Fig. 5-4 shows a summary of the wavelength values measured from 20 InSe flakes with thicknesses (measured by atomic force microscope) ranging from 6.4 nm to 32 nm (~1-2 layers to 27 layers). The experimental data points follow a marked linear trend, as expected from Equation (5-1). Based on the slope $\lambda/h = 146 \pm 11$ one can determine the Young's modulus of InSe. Using the known values of the Poisson's ratio of PDMS (Gel-Film) $\nu_s = 0.5$ and InSe flake $\nu_f = 0.27$,[486,487] and the Young's modulus of Gel-Film $E_s = 492 \pm 11$ kPa,[483] the Young's modulus of thin InSe flakes is determined to be $E = 23.1 \pm 5.2$ GPa, a value much smaller than the reported Young's modulus of other 2D materials.

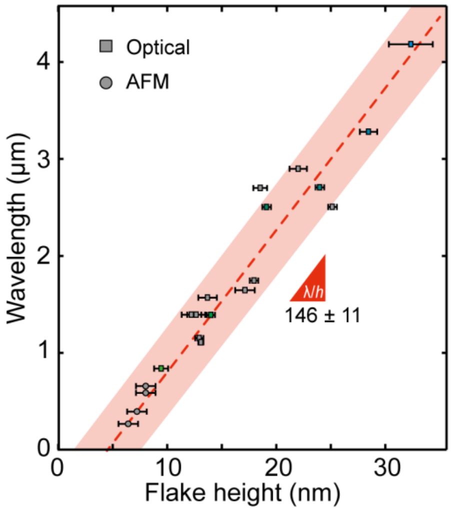

Fig. 5-4 Relationship between the wavelength of the wrinkles and the thickness of the InSe flakes. The red dashed line represents the linear fit based on the data and the light red shaded area indicates the uncertainty of the fitting. The squares indicate the wavelengths of the ripples are extracted using optical method and the circles indicate the wavelengths of the ripples are extracted based on the atomic force microscope measurements.

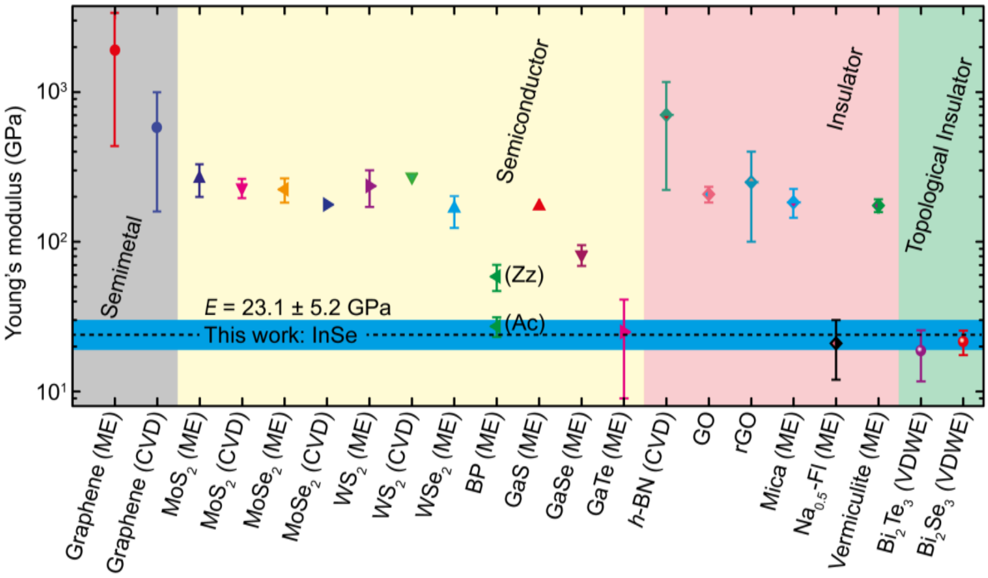

Fig. 5-5 Summary of the experimentally measured Young's modulus values of isolated two-dimensional species (semimetals, semiconductors, insulators and topological insulators). The different values of the Young's modulus of 2D materials reported in the literature are compared with the value of InSe obtained in this work E = 23.1 ±5.2 GPa (centered at the black dashed line with the blue shaded area indicating the experimental uncertainty).

In order to put this value in a more general context of 2D materials, a graphical comparison between the Young's modulus values for various isolated 2D materials available in the literature with a semi-logarithmic scale plot in **Fig. 5-5**. The highest and lowest Young's modulus values reported in the literature for each material are indicated through the error bar. The four differently colored regions are employed to indicate semimetal, semiconductor, insulator and topological insulator groups, respectively. The value determined with buckling method of thin InSe Young's modulus is shown with a black dashed line with a surrounding blue shadow (that represents the uncertainty of the measurement result). According to the plot, the thin InSe flakes have a Young's modulus value which is around two orders of magnitude smaller than that of graphene and one order of magnitude lower than MoS_2 flakes. This value of the Young's modulus is among the lowest values reported for 2D materials up to date and is comparable only with that of metal-organic frameworks (MOFs, ~5 GPa).[488] Notably, this small value for the Young's modulus of InSe is in agreement with theoretical calculations, which predicts an isotropic Young's modulus for monolayer InSe of 57 GPa, which is also much smaller than the predicted values for MoS_2 and graphene.[486] All the details displayed in **Fig. 5-5** are also summarized in **Table 15** to facilitate a quantitative comparison between different materials.

Table 15 The comparison of Young's modulus of two-dimensional (2D) materials measured at room temperature and ambient environments. Legend: "Isolation method"; ME: mechanical exfoliation, CVD: chemical vapor deposition, VDWE: Van der Waals epitaxy. "Testing method"; (1) Spring constant scaling, (2) Nano-indentation, (3) Compliance maps, (4) Electrostatic deflection, (5) Blister test, (6) Constant force maps, (7) Nano-resonator, (8) Bimodal AFM, (9) buckling metrology method, (10) Micro-tensile method.

Type	Materials	Isolation method	# of layers/ thickness	Young's modulus (GPa) (Testing method) highest	lowest	Ref.
	InSe	ME	~1-2L to 27L	23.1±5.2 (9)		This work
Semi-metal	Graphene	ME	1-100L	1000±100 (2)	430 (1)	467,489
		CVD	1L	1000±50 (2)	160 (2)	490,491
semiconductor	MoS_2	ME	1-108L	330±70 (2)	200 (7)	190,492
		CVD	1-2L	264±18 (2)	197±31 (5)	493,494
	$MoSe_2$	ME	5-10L	224±41 (9)		483
		CVD	1-2L	177.2±9.3 (10)		472
	WS_2	ME	3-8L	236±65 (9)		483
		CVD	1L	272±18 (2)		493
	WSe_2	ME	4-12L	167±7 (2)	163±39 (9)	483,495
	BP	ME	15-25 nm	Zz:58.6±11.7, Ac: 27.2±4.1 (2)		496
	GaS	ME	~5-20 nm	173±15 (2)	~50 (2)	497
	GaSe	ME	~10-30 nm	82±13 (2)		497
	GaTe	ME	~10-30 nm	~75 (2)	25±16 (2)	497
Insulator	h-BN	CVD	1, 15 nm	1160±100 (2)	223±16 (2)	117,498
	Graphene	-	1L	207.6±23.4 (6)		499
	oxide	reduced	1L	250±150 (1)		469
	Mica	ME	2-14L	200±30 (2)	170±40 (1)	500
	$Na_{0.5}$ – Fluo	ME	12-90L	21±9 (1)		501
	Vermiculite	ME	>2L	175±16 (6)		502
Topological	Bi_2Te_3	VDWE	5-14 nm	11.7-25.7 (2)		503
	Bi_2Se_3	VDWE	7-12L	17.48-25.45 (2)		504

The low Young's modulus value of thin InSe has implications in its applicability in flexible electronics, strain engineering or sensors. For example, applying or transferring strain to a 2D material with low Young's modulus requires less force than transferring the same amount of strain to a stiffer 2D material. To understand the role of the Young's modulus in the transfer of strain to a 2D materials deposited on a substrate, a three-dimensional axisymmetric finite element analysis (FEA) using the software COMSOL Multiphysics (version 5.1) has been performed. The solver that was used in COMSOL is MUMPS (Multifrontal Massively Parallel Sparse direct Solver). To model the system composed of a three-dimensional substrate and an atomically thin flake, the geometry with a very large aspect-ratio has been employed in the simulation. The system was modelled in an axisymmetric representation, and the substrate was modelled with a cylinder and the flake by another cylinder located on the top-center of the substrate. The complete mesh consists of 72214 elements (Minimum quality: 0.335, average quality: 0.9758). **Fig. 5-6** shows some cross sections of the model with superimposed the mesh elements and **Fig. 5-7** shows the three dimensional visualization of the model.

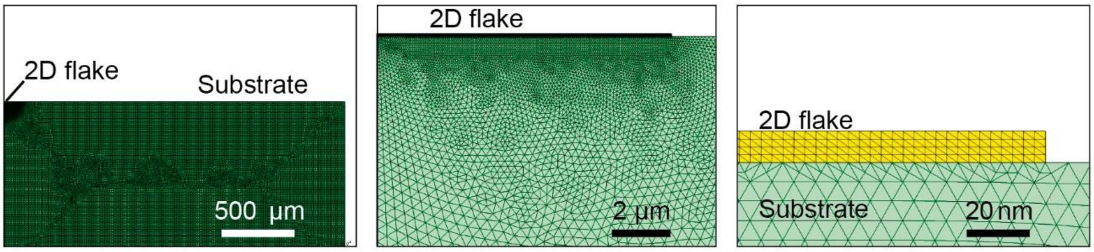

Fig. 5-6 Pictures of the axisymmetric geometry used in COMSOL to simulate the train transfer from a substrate (green) to a flake deposited on top (yellow) taken at different magnifications.

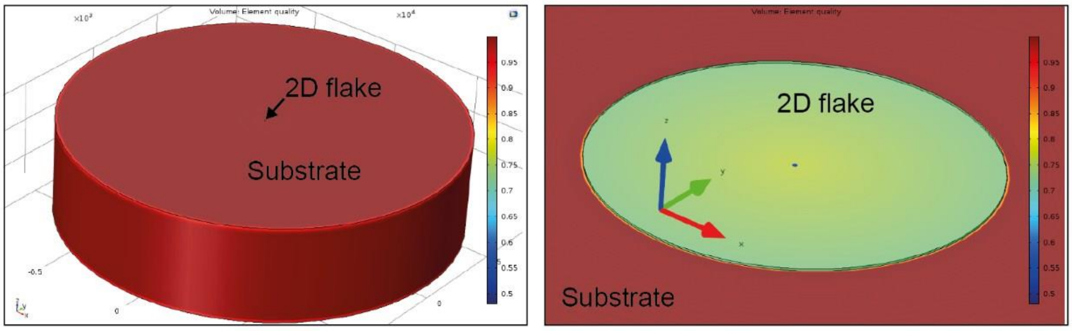

Fig. 5-7 Pictures of the final 3D geometry used in COMSOL to simulate the strain transfer from a substrate to a flake deposited on top taken at two different magnifications.

The results shown in **Fig. 5-8** are calculated for a thin InSe with a thickness of 10 nm, diameter 20 μm and Young's modulus E_{InSe} = 23.1 GPa, placed on a substrate with a thickness of 1000 μm and a diameter of 10000 μm. The interface between the InSe flake and the substrate is modeled using perfect bonding. In each step of the simulation the substrate is firstly expanded and then the total expansion induced in the InSe flake can be extracted, from which the strain transfer for all the different substrate Young's modulus values are calculated. The calculations for MoS_2 (E_{MoS2} =

250 GPa) and graphene ($E_{Graphene}$ = 1 TPa) also have been presented,[467,483,490] which show that, independently from the Young's modulus of the 2D material, for very small values of the substrate Young's modulus no strain is transferred from the substrate to the 2D flake, while for very large values the strain transfer approaches 100%. In between these two limits one can see that the strain transfer present in all three cases a similar sigmoidal shape and is shifted along the horizontal axis. The onset of transfer of each curve depends on the 2D material Young's modulus being the lowest for InSe and the largest for graphene. For 2D flakes with lower Young's modulus the strain transfer is larger than for flakes with larger Young's modulus (given the same substrate Young's modulus). Since no atomistic details are taken into account in the simulation, the real absolute value of strain transfer for a given substrate Young's modulus can differ from the calculated one. Nevertheless, the general shape of the strain transfer curve and the trend observed should hold true for all the different 2D materials.

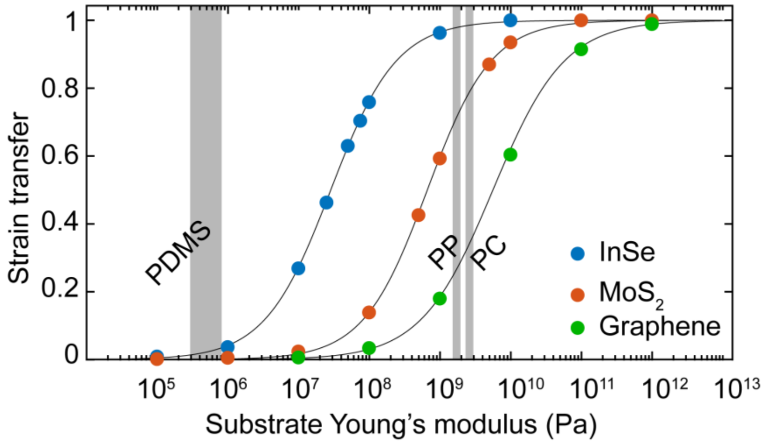

Fig. 5-8 Strain transfer as a function of the substrate Young's modulus calculated from finite element analysis for InSe, MoS_2 and graphene. The grey shaded regions indicate the Young's modulus values of polymer substrates typically used in flexible and printed electronics.

5.2 Biaxial strain tunability in ultrathin InSe

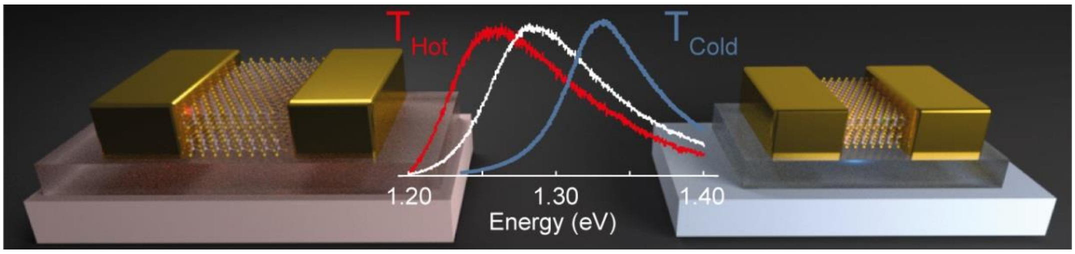

InSe flakes are subjected to biaxial strain through the substrate expansion upon temperature increase. The effective strain transfer from the substrate to the thin InSe is confirmed by Raman spectroscopy. The band gap change upon biaxial strain is determined through photoluminescence measurements, finding a gauge factor of up to ~200 meV/%. Furthermore, the effect of biaxial strain on the electrical properties of the InSe devices has also been characterized. In the dark state, a large increase of the current is observed upon applied strain which gives a piezoresistive gauge factor value of ~450-1000, ~5-12 times larger than that of other 2D materials and of state-of-the-art silicon strain gauges. Moreover, the biaxial strain tuning of the InSe band gap also translates in a strain-induced redshift of the spectral response of our InSe photodetectors with $\Delta E_{\text{cut-off}}$ ~173 meV at a rate of ~360 meV/% of strain, indicating a strong strain tunability of the spectral bandwidth of the photodetectors. Note that this section is mainly based on the published paper “Giant Piezoresistive Effect and Strong Bandgap Tunability in Ultrathin InSe upon Biaxial Strain” in Advanced Science where I am the first author.[505]

5.2.1 Background

Strain engineering, the modification of the optical, magnetic, electrical, and optoelectronic properties of a given material by applying an external mechanical deformation to its crystal lattice, is establishing itself as one of the most prospective strategies to controllably modify the properties of two-dimensional (2D) materials.[506-510] In fact, the lack of dangling bonds on their surface makes them extremely resilient to the mechanical deformation without fracture,[225] even approaching the theoretical limit (predicted by Griffith) for defect-free materials.[511,512] The capability of applying very large deformations together with strain sensitive band-structures makes 2D materials a very suitable family of materials for strain engineering.

During the last years, multiple works studying the strain tunability of the bandgap of several 2D semiconductors, including transition metal dichalcogenides (TMDCs), black phosphorus (bP) and other 2D semiconductors, have been reported (see **Table 16**).[283,513-549] Very recently, InSe has shown sizeable larger strain tunability with respect to transition metal chalcogenides (TMDCs) and black phosphorus upon uniaxial strain loading and local strain modification.[283,547,550-552] According to the works reported for TMDCs and bP, biaxial strain usually yields stronger bandgap tunability than uniaxial strain because of the larger lattice deformation in both crystal orientations.[549] Although recent calculations also predicted that biaxial strain should have a stronger effect on the InSe band structure than uniaxial strain,[486,553,554] its experimental realization was still lacking.

5.2.2 Sample fabrication

The Au-InSe-Au devices are obtained by following a fabrication process similar to the one described in previous chapters. Briefly, the selected InSe flake is first deterministically placed to bridge a pair of gold electrodes that have been pre-patterned on target polycarbonate (PC) substrates. Subsequently, a larger thin h-BN flake (30-50 layers) is placed on the top of the active region in the device to provide a full insulating encapsulation to slow down the environmental induced degradation of InSe. **Fig. 5-9** shows a comparison of current evolution of the InSe devices with and without h-BN degradation as a function of time under continuous illumination at a fixed bias of 1 V. To prevent the influence of contamination in the air all these fabrication steps are carried out under ambient conditions within 30 minutes. In **Fig. 5-10**, one can find the details of a Au-InSe-Au device fabricated on the PC substrate. **Fig. 5-10a** shows the schematic (top panel) and optical images obtained with reflection (middle panel) and transmission (bottom panel) mode of a selected ultrathin ~20 nm InSe flake (shown by inset picture) deterministically transferred bridging two Au / Ti (50 nm / 5 nm) electrodes pre-patterned on the surface of PC substrate. **Fig. 5-10b** shows the geometry (top panel) and pictures (middle and bottom panels) of the final devices after top encapsulation with h-BN. Thanks to the combination of high thermal expansion coefficient $\alpha = 64 \cdot 10^{-6}$ ℃$^{-1}$ and large Young's modulus (E = 2.5 GPa) which can introduce a good strain transfer (see **Fig. 5-8**),[513,531] the PC has been chosen as a substrate. A set of InSe devices on SiO_2/Si substrates with similar geometries of the devices on PC substrate but with negligible thermal expansion coefficient ($\alpha < 1 \cdot 10^{-6}$ ℃$^{-1}$) also have been fabricated and are shown in **Fig. 5-11**.[555] This set of devices is employed as control samples to determine the role of the intrinsic temperature increase, without biaxial strain, on the observed features. This allows for the disentanglement of the temperature and strain effects on the observed features during the measurements.

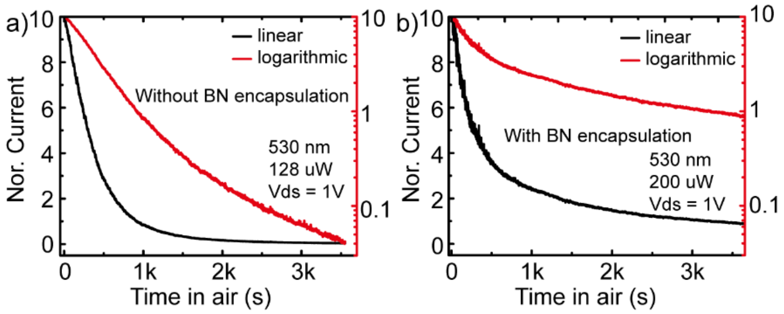

Fig. 5-9 The current evolution during the *in situ* annealing of InSe devices without (a) and with (b) h-BN encapsulation.

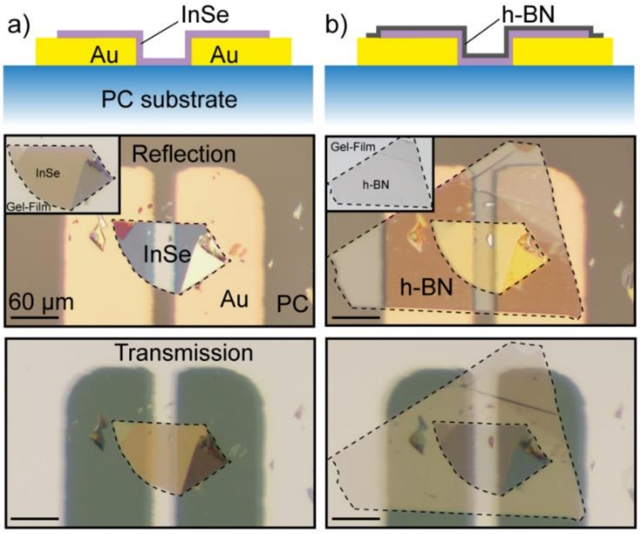

Fig. 5-10 Fabrication of Au-InSe-Au device on polycarbonate (PC) substrate. a, b) Schematics (top) and optical microscopy images of a Au-InSe-Au device before (a) and after (b) encapsulating a h-BN flake on the surface with optical microscope reflection (middle) and transmission (bottom) mode. Insets: the optical microscopy images of selected thin InSe flake and h-BN fabricated on Gel-Film observed with transmission mode.

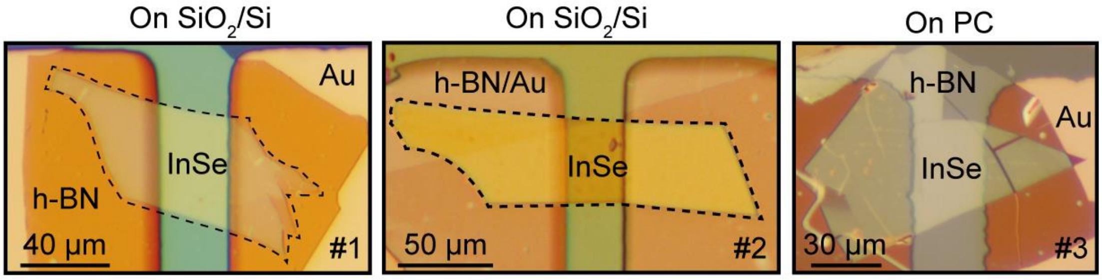

Fig. 5-11 Optical pictures of three additional Au-InSe-Au devices respectively fabricated on 280 nm SiO_2/Si (#1 and #2) and on PC (#3) substrate.

In order to minimize the influence of the traps during the temperature-dependent device characterization, all the Au-InSe-Au devices discussed in this section have been annealed *in situ* in air at ~100 ℃ for around 2 hours on the micro-heater mounted on probe station before carrying out the Raman spectroscopy and optoelectronic characterizations. This process yields the passivation of the defects existing in thin InSe flakes, thanks to the air species trapped at the interfaces, and helps to reach a long-term stable working state with fast photodetection operation.[370] **Fig. 5-12** shows how the photocurrent flowing through the devices evolves in time under 530 nm LED continuous illumination during the annealing process both on PC and SiO_2/Si substrates, as expected for a defects passivation process in InSe photodetector. Raman spectroscopy measurement in **Fig. 5-13** indicates there is no structural change before and after annealing. The typical fast-operated optoelectronic performance of the devices on SiO_2/Si and PC substrate after annealing have been respectively shown in **Fig. 5-14** and **Fig. 5-15**. Particularly, the passivated devices both exhibit the same unitary power exponent α at room temperature and 100 ℃, which indicates there is no active traps playing a role during the temperature dependent measurements.

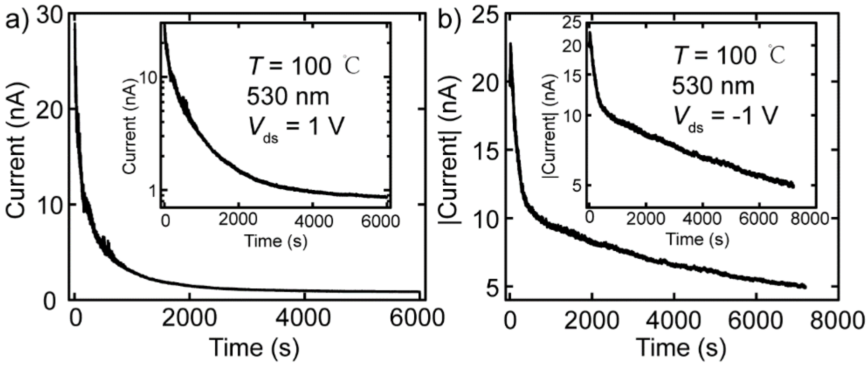

Fig. 5-12 The current evolution during the *in situ* annealing. a, b) The current flowing through the device #1 at 1 V (a) and device #3 at -1 V (b) as a function of *in situ* annealing time in linear and semi-logarithmic (inset) scale.

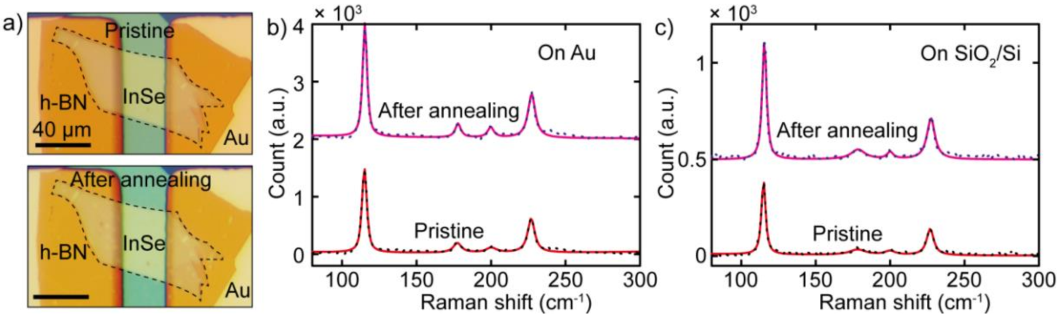

Fig. 5-13 Structural stability before and after *in situ* annealing of Au-InSe-Au device. a) The optical picture of a Au-InSe-Au devices fabricated on SiO_2/Si substrate before and after annealing. b, c) Raman Spectra of InSe flake on Au (b) and on SiO_2/Si (c) recorded in pristine state and after annealing at room temperature.

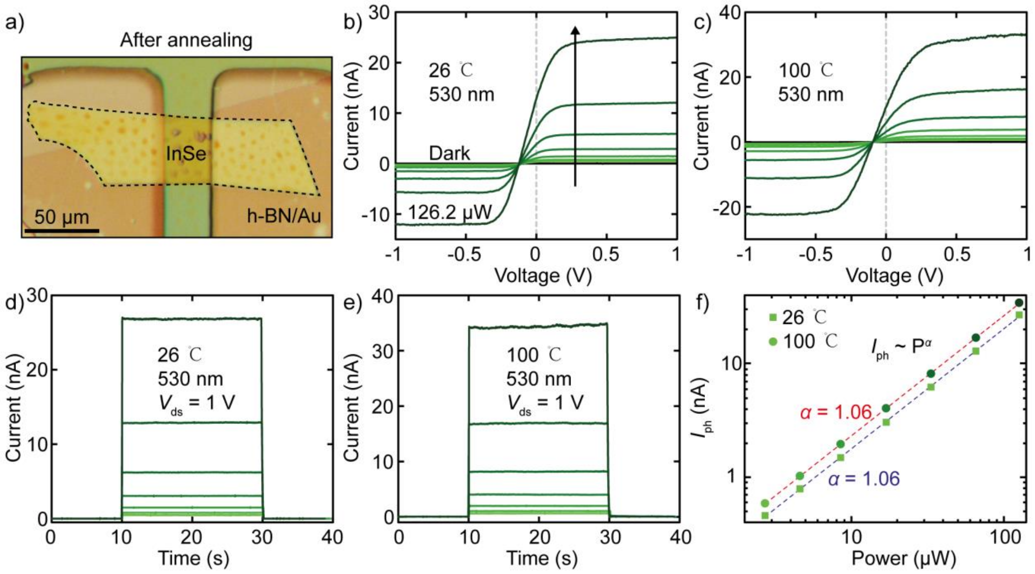

Fig. 5-14 Optoelectronic characterization of device #2 after *in situ* annealing. a) The optical picture of device #2 after annealing. b, c) *I*-*V* curves recorded in dark condition and as a function of 530 nm illumination power at 26 ℃ and 100 ℃. d, e) *I*-*t* curves at 1 V recorded as a function of 530 nm illumination power at 26 ℃ and 100 ℃. f) Photocurrent value in the device at 1 V at 26 ℃ (square) and 100 ℃ (circle) *versus* illumination power plot in log-log scale.

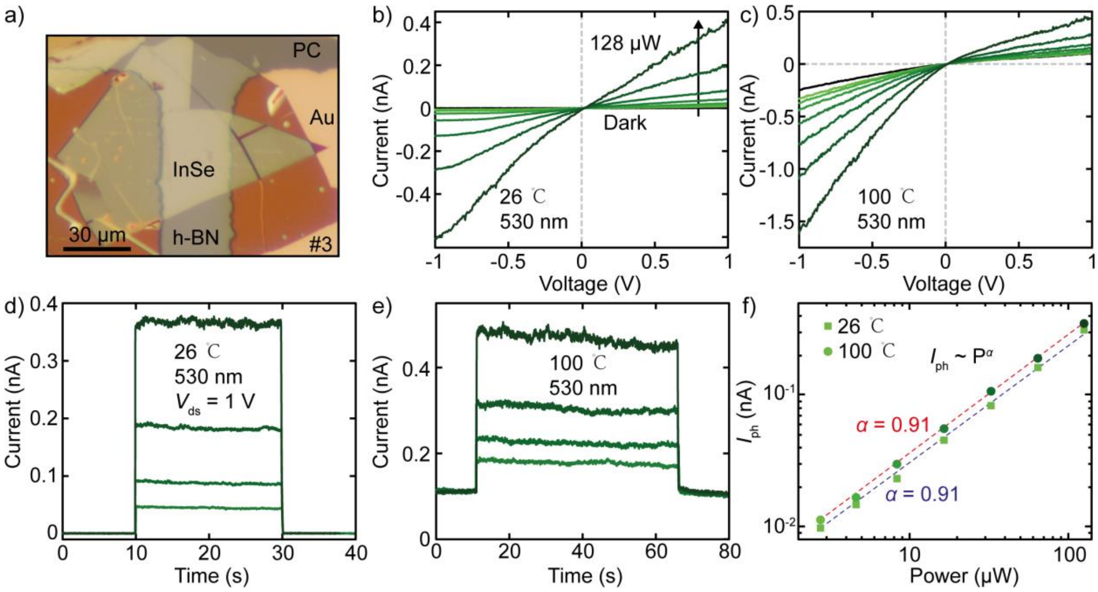

Fig. 5-15 Optoelectronic characterization of device #3 after *in situ* annealing. a) The optical picture of device #3. b, c) *I*-*V* curves recorded in dark condition and as a function of 530 nm illumination power at 26 ℃ and 100 ℃. d, e) *I*-*t* curves at 1 V recorded as a function of 530 nm illumination power at 26 ℃ and 100 ℃. f) Photocurrent value in the device at 1 V at 26 ℃ (square) and 100 ℃ (circle) *versus* illumination power plot in log-log scale.

5.2.3 Raman characterization

Raman spectroscopy is employed to characterize the strain transfer from the PC substrate to the InSe flake upon thermal expansion. **Fig. 5-16a** shows Raman spectra acquired in the 20 nm thick InSe device at different PC substrate temperatures (from ~26 ℃ to ~100 ℃), corresponding to a biaxial thermal expansion ranging from 0% up to 0.48%.[513,531] To demonstrate the reproducibility of the thermal induced biaxial straining approach, **Fig. 5-17** addresses a second set of Raman measurements acquired on the same sample during another heating cycle. Three Raman active in-plane modes A_1'(1), A_2''(1) and A_2'(1) located at ~113 cm^{-1}, ~198 cm^{-1} and ~226 cm^{-1}, and one out-of-plane E''(2) located at ~176 cm^{-1} are observed, which is consistent with hexagonal crystal structure of ultrathin InSe with ε stacking sequence.[556] With the increase of temperature, all Raman peaks shift towards lower Raman shifts, which is similar to recently reported experimental works on uniaxial strained InSe due to phonon softening.[547,550,557] That is the increase of the covalent bonds length introduced by the applied tensile strain results in a weaker restoring force of vibrations, and thus lower phonon frequencies. As a control experiment the same measurements are also repeated on an InSe device fabricated on SiO_2/Si (with negligible thermal expansion). In this control sample the Raman peaks position shift at much lower rate upon SiO_2/Si substrate temperature increase (see **Fig. 5-16b**), indicating that the shift observed in the PC based device can be mostly attributed to the effect of biaxial strain. By subtracting the shift obtained on the SiO_2/Si substrate to that of the PC substrate, the redshift rate due to biaxial strain: -1.48 cm^{-1}/%, -4.84 cm^{-1}/%, -5.32 cm^{-1}/% and -5.77 cm^{-1}/% of biaxial strain for the A_1'(1), E''(2), A_2''(1) and A_2'(1) Raman modes, can be determined, respectively and are shown in **Fig. 5-16c**. Interestingly, another dataset in **Fig. 5-18** acquired on a 13 nm thick InSe flake showing very similar Raman peak shift upon straining, demonstrating that a similar strain transfer is achieved for the 20 nm and the 13 nm InSe flakes. This good strain transfer, even for relatively thick InSe flakes, can be attributed to the low Young's modulus of InSe (E = 23 ± 5 GPa,[465] as shown in **Fig. 5-5** and **Table 15**) as strain transfer from the substrate to the flake is inversely proportional to the Young's modulus of the flake. Indeed, this result is consistent with that shown by finite element calculations in **Fig. 5-8**, which predicts a strain transfer of ~100% for InSe on PC substrates.[465] Furthermore, in order to probe if the top h-BN encapsulation has any effect on the strain transfer, as a complementary part, a control straining experiment on a ~13 layers InSe flake partially encapsulated with h-BN has been performed in **Fig. 5-19**, both finding very similar results on the parts with and without encapsulation.

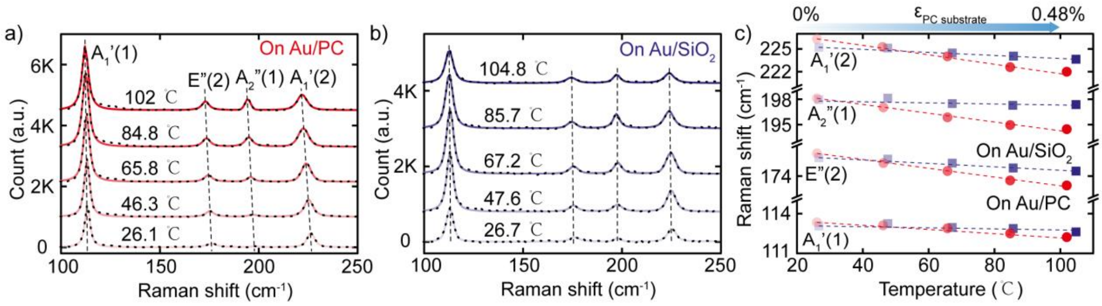

Fig. 5-16 Temperature-dependent Raman Spectroscopy of thin InSe flakes deposited on Au/PC and on Au/SiO_2/Si substrates. a, b) Raman spectra of thin InSe recorded on Au/PC (a) and on Au/280 nm SiO_2/Si (b) substrates with 50× objective as a function of temperature (from ~26 ℃ to ~100 ℃). c) Temperature-dependency of four Raman active modes (A_1'(1), E''(2), A_2''(1) and A_1'(1)) of thin InSe on PC (red) and on Au/280 nm SiO_2/Si (blue) substrate. The top axis in (c) indicates the biaxial strain induced by the thermal expansion of the PC substrate.

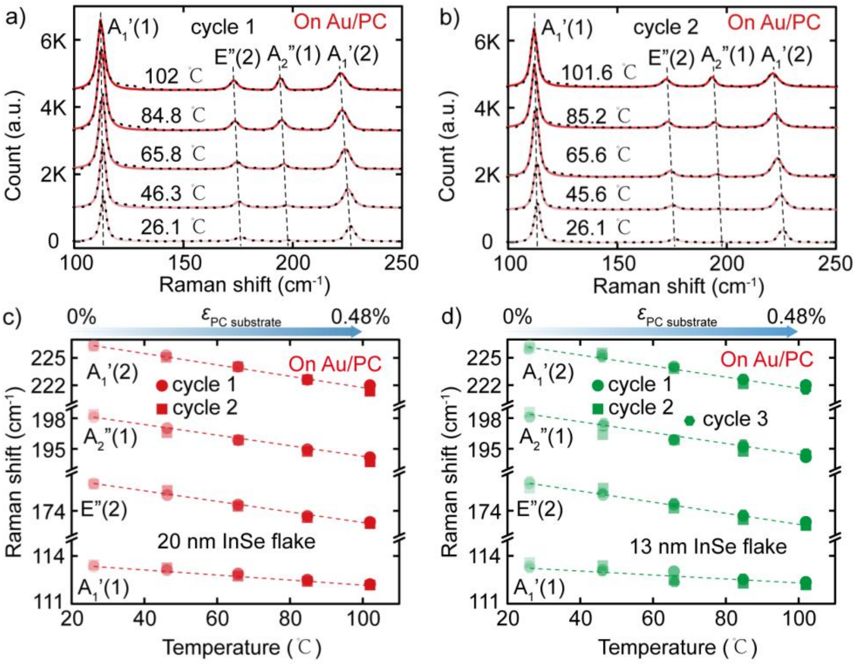

Fig. 5-17 Temperature-dependent Raman Spectroscopy of thin InSe flakes recorded during different heating cycles. a, b) Raman spectra of thin InSe (~20 nm) recorded on Au/PC substrates during heating cycle 1 (a) and cycle 2 (b) with 50× objective as a function of temperature (from ~26 ℃ to ~100 ℃). c-d) Temperature-dependency of four Raman active modes (A_1'(1), E''(2), A_2''(1) and A_1'(1)) of 20 nm InSe (c) and 13 nm InSe (d) on PC substrate during different heating cycles. The top axis indicates the biaxial strain induced by the thermal expansion of the PC substrate.

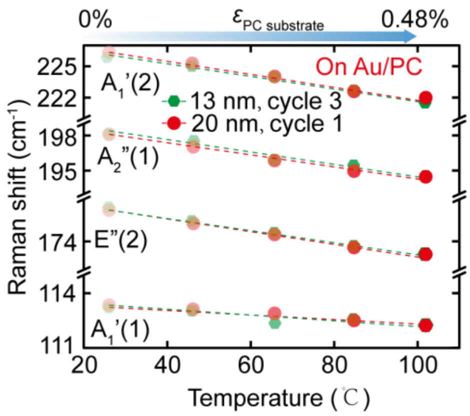

Fig. 5-18 Temperature-dependency of four Raman active modes (A_1'(1), E''(2), A_2''(1) and A_1'(1)) of two thin InSe flakes with the thicknesses of 13 nm (green) and 20 nm (red) on PC substrate. The top axis indicates the biaxial strain induced by the thermal expansion of the PC substrate.

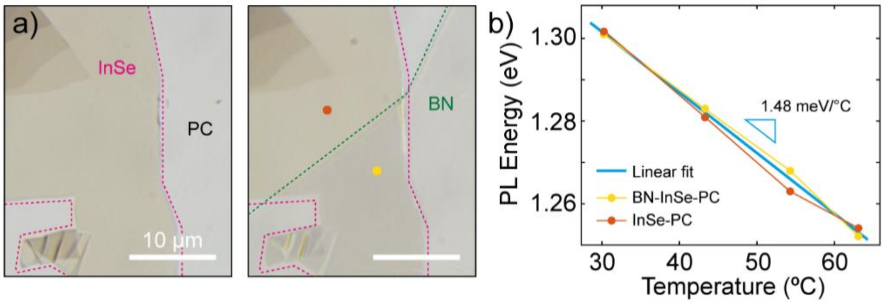

Fig. 5-19 The effects of h-BN encapsulation on bandgap tunability of biaxial strained InSe. a) A thin InSe flake (~13 layers) deposited on PC substrate before (left) and after (right) being half encapsulated with h-BN. b) The PL energy as a function of temperature of the InSe flake recorded at the two positions indicated by the colored circles in panel (a) corresponding to InSe-PC and BN-InSe-PC. The blue line is a linear fit to the data with slope 1.48 meV/℃.

The redshift rates of the Raman peaks are around 2 times larger than the value reported for uniaxial strained thin InSe.[283,547,550] This information can be highly valuable as Raman spectroscopy is commonly used to monitor residual or built-in strains during the device fabrication and/or growth of other 2D materials. More interestingly, the Grüneisen parameters,[558] that describes the effect of a volume change on the vibrational properties, of the A_1'(1), E''(2), A_2''(1) and A_2'(1) Raman modes by using the obtained Raman mode shift rate, which take the values of 0.65, 1.38, 1.34 and 1.28, also can be extracted for InSe. These values are comparable with the results in the literature reported for uniaxial strained InSe.[547] The determination of the Grüneisen parameters through biaxial straining, however, has the advantage that (unlike in uniaxial strain) no need for assumptions about the Poisson's ratio value of thin InSe.

5.2.4 Photoluminescence

The effect of the applied biaxial strain on the band gap of InSe is studied through photoluminescence (PL). **Fig. 5-20a** shows PL spectra acquired on InSe flakes transferred onto a PC substrate and onto a SiO_2/Si substrate at different temperatures. The PL spectra show a peak corresponding to the direct band gap transition at the Γ point of the Brillouin zone and it is thus a good probe of the band gap of InSe.[258,290,540] Similar to the Raman experiments, the measurements on the SiO_2/Si substrates are also used as a control experiment to probe the intrinsic shift of the PL peaks upon temperature increase (without biaxial strain). This allows determining the biaxial strain induced PL shift, subtracting the PL shift measured on SiO_2/Si substrates (only thermal contribution) to the PL shift measured on PC substrates (thermal + biaxial strain contribution). **Fig. 5-20a** shows how the PL shift on PC substrates is much larger than that measured on SiO_2/Si substrates, indicating that biaxial strain strongly modifies the band gap of InSe. Interestingly, it is also found a clear thickness dependence on the band gap strain tunability: thinner flakes (7-10 layers) are more sensitive to strain than thicker flakes (15-20 layers). To further demonstrate this thickness-dependent band gap tunability, **Fig. 5-20b** summarizes the PL shift rate measured for 19 InSe flakes (10 on PC and 9 on SiO_2/Si) with the thickness ranging from 5 to 30 layers. By subtracting the two trends obtained for the PC and the SiO_2/Si substrates, the thickness dependent band gap gauge factor, i.e., the change of bandgap per % of biaxial strain, of InSe that ranges from 195 ± 20 meV/% (for 5 layers thick InSe) to 63 ± 6 meV/% (for 30 layers thick InSe) can be obtained in **Fig. 5-20c**. This value is among one of the largest reported values for 2D semiconducting materials so far, as shown in **Table 16** and **Fig. 5-20d**. Interestingly, for ultrathin flakes our bandgap gauge factor is nearly twice that of uniaxial strained InSe,[283,547] in very good agreement with recent DFT predictions.[486]

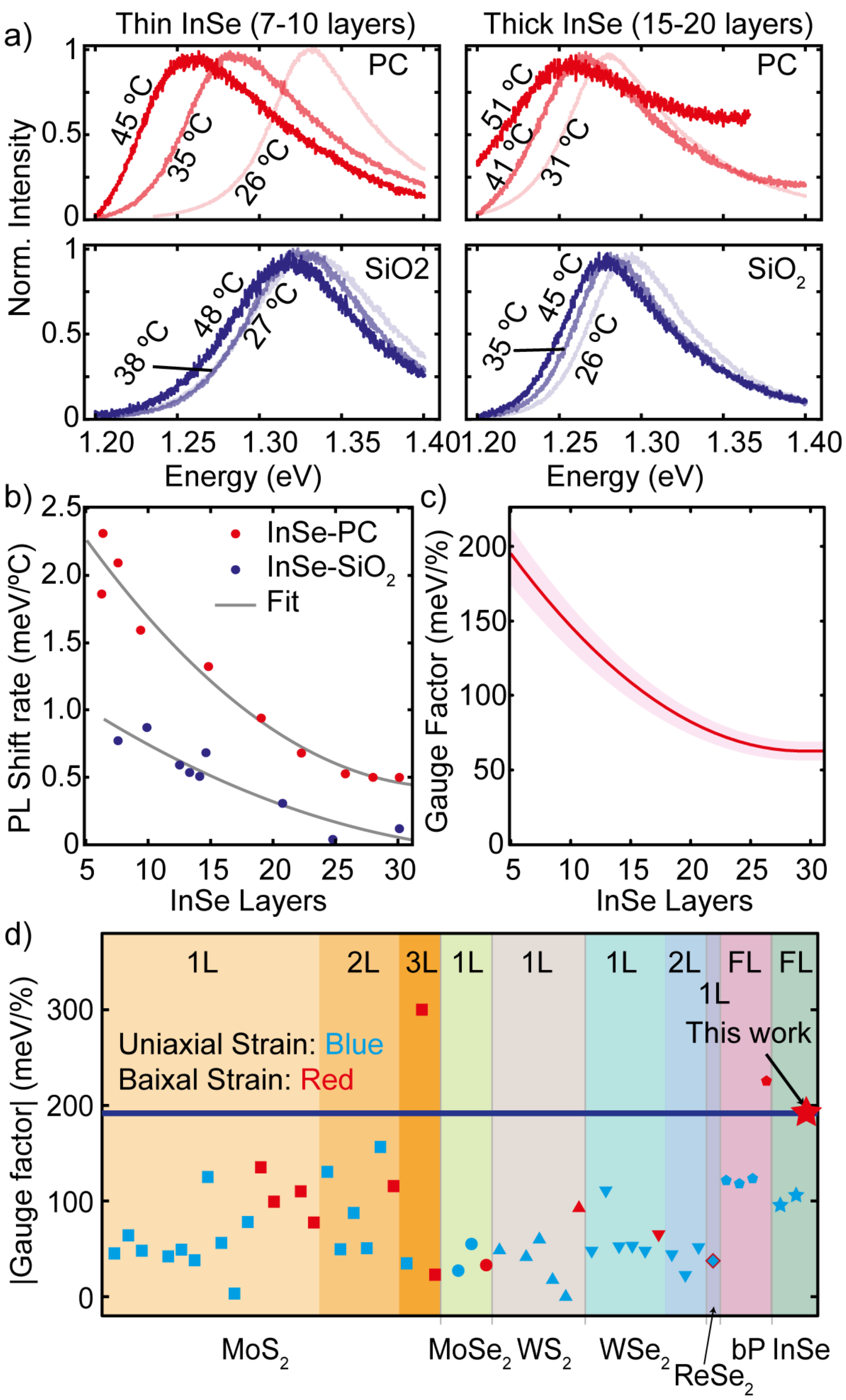

Fig. 5-20 Gauge factor of biaxial strained InSe. a) Photoluminescence spectra of thin (7-10 layers, left) and thick (15-20 layers, right) InSe flakes deposited on PC substrate (top) and on 280 nm SiO_2/Si substrate (bottom) recorded as a function of temperature (from RT to ~50 °C). b) PL energy shift rate versus thickness of InSe flakes deposited on PC substrate (red) and on 280 nm SiO_2/Si (blue) substrate. The solid lines represent the best fit for each dataset to a second order polynomial function. c) Calculated gauge factor of biaxial strained InSe flakes as a function of layer numbers. d) The different values of the strain tunability gauge factors of 2D semiconducting

flakes reported in the literature with various approaches are compared with the value of biaxial strained InSe obtained in this work (~200 meV/%).

TABLE 16 Summarized comparison of bandgap tunability of two-dimensional semiconductors under strain engineering. The ε^{max} refers to the maximum strain applied on the flexible substrate or directly on a suspended 2D flake or induced by a pre-patterned substrate. $^{(D)}$ and $^{(I)}$ indicate direct and indirect bandgap, respectively. * Data obtained in a polyvynilacetate (PVA) encapsulated sample. ** Data obtained based on CVD grown 2D materials.

Materials	Strain type	Method/substrate	ΔE_g^{max}, ε^{max}	Gauge factor (meV/%)	Ref.
1L MoS_2	Uniaxial	Mechanical bending, PC	-81 meV, 1.8%	-45 ±7	520
		Mechanical bending, PMMA	-33 meV, 0.52%	-64 ±5	521
		Mechanical bending, PET	-38.4 meV, 0.8%	-48	522
		Mechanical bending, PC	-57.5 meV, 1.37%	-42	523
		Mechanical bending, PC	-44.5 meV, 1.06%	-42	524
		MEMS mechanics, suspended	-49.4 meV, 1.3%	-38 ±1**	525
		Mechanical bending, PVA	-300 meV, 1.7%	-125*, -61	526
		Mechanical bending, PET	-36 meV, 0.64%	-56	527
		Substrate stretching, PDMS	-15 meV, 4.8%	-3**	528
		Mechanical bending, PI	-31 meV, 0.4%	-78 ±4	529
	Biaxial	Thermal expansion, PC	-65 meV, 0.48%	-135	513
		Pressurized membranes, suspended	-500 meV, 5%	-99	530
		Thermal expansion, PDMS, PP	-12.5 meV, -51.1 meV, 1%	-12.5, -51.1	531
		Pre-patterned substrate, SiO_2	-50 meV, 0.565%	-110	533
		AFM indentation, suspended	--, 7%	-77.3±10	519
2L MoS_2	Uniaxial	Mechanical bending, PC	-32 meV$^{(D)}$, -77 meV$^{(I)}$, 0.6%	-53±10$^{(D)}$, -129 ± 20$^{(I)}$	520
		Mechanical bending, PMMA	-25 meV, 0.52%	-48 ±5	521
		Mechanical bending, PET	-36.8 meV$^{(D)}$, -68.8 meV$^{(I)}$, 0.8%	-46$^{(D)}$,-86$^{(I)}$	522
		Mechanical bending, PC	-78 meV, 1.6%	-49 ±1	548
		Mechanical bending, PI	-12 meV$^{(D)}$, 56 meV$^{(I)}$, 0.36%	-34 ±3$^{(D)}$, -155 ± 11$^{(I)}$	529
	Biaxial	AFM indentation, suspended	--, 7%	-116.7±10	519
3L MoS_2	Uniaxial	Pre-strained substrate, Gel-Film	-90 meV, 2.5%	-36	534
	Biaxial	piezoelectric substrate, PMN-PT	-60 meV, 0.2%	-300	532
		AFM indentation, suspended	--, 7%	-22.7±6	519
1L $MoSe_2$	Uniaxial	Mechanical bending, PC	-40.7 meV, 1.07%	-38 ±2	523
		Mechanical bending, PC	-30 meV, 1.1%	-27 ±2	535
		Mechanical bending, PEN	-28 meV, 0.5%	-54.8 ±5.8	536
	Biaxial	Thermal expansion, PP	-33 meV, 1%	-33	531

1L WS_2	Uniaxial	Mechanical bending, PC	-69 meV, 1.26%	-55 ±2	523
		Mechanical bending, PVA	-253 meV, 5.68%	-43**	526
		Mechanical bending, PET	-27.5 meV, 0.64%	-43	527
		Mechanical bending, PEN	-31 meV, 0.5%	-61.2 ±3.8	536
		Mechanical bending, PET	-44 meV$^{(D)}$, -76 meV$^{(I)}$, 4%	-11**$^{(D)}$, -19** $^{(I)}$	541
		Substrate stretching, PDMS	-20 meV, 16%	-1.3**	538
	Biaxial	Thermal expansion, PP	-95 meV, 1%	-95	531
1L WSe_2	Uniaxial	Mechanical bending, PC	-72.5 meV, 1.48%	-49 ±2	523
		Mechanical bending, PVA	-176 meV, 1.7%	-109	526
			-137 meV, 2.56%	-53**	
		Mechanical bending, PEN	-20 meV, 0.35%	-53 ±3.1	536
		Mechanical bending, PC	-75.5 meV, 1.4%	-54	539
		Mechanical bending, PETG	101 meV, 2.1%	-48	540
	Biaxial	Thermal expansion, PP	-63 meV, 1%	-63	531
2L WSe_2	Uniaxial	Mechanical bending, PETG	-68 meV, 1.51%	-45	541
		Mechanical bending, PET	-45 meV$^{(D)}$, -40 meV$^{(I)}$, 2%	-22.5$^{(D)}$, 20$^{(I)}$	542
		Mechanical bending, PETG	-110 meV, 2.1%	-52	543
1L $ReSe_2$	Uniaxial	Pre-strained substrate, Gel-Film	-70 meV, 1.64%	-43	544
6L bP	Uniaxial	Mechanical bending, PET	110 meV, 0.92%	120	545
18L bP	Uniaxial	Pre-strained substrate, Gel-Film	700 meV, 5%	100-140	546
6L bP	Uniaxial	Mechanical bending, PP	132 meV, 1%	132	549
	Biaxial	Thermal expansion, PP	67 meV, 0.3%	222	
4-8L InSe	Uniaxial	Mechanical bending, PP	-110 meV, 1.15%	-(90-100)	283
4-35 nm InSe	Uniaxial	Mechanical bending, PET	-118 meV, 1.06%	-(80-150)	547
5L InSe	Biaxial	Thermal expansion, PC	-26 meV, 0.13%	-200	This work

5.2.5 Piezoresistance

The effect of biaxial strain on the electronic properties on the Au-InSe-Au photodetector devices in the dark state is also studied. **Fig. 5-21a** shows the current *vs*. voltage characteristics (*I*-*V*s hereafter) in linear scale as a function of the PC substrate temperature from ~23 ℃ to ~100 ℃, leading to a biaxial strain in the 0% - 0.48% range.[513] A significant increase in the slope of *I*-*V*s with temperature increase is observed, indicating an increase of conductivity of the device upon substrate thermal expansion (in good agreement with the observed bandgap reduction under biaxial tension). The data is also plotted in semi-logarithmic scale (with current absolute value) to facilitate the quantitative comparison between different datasets. The current at V = -1 V increases dramatically: from -0.6 pA at ~23 ℃ (0% strain) to -0.33 nA at ~100 ℃ (0.48% strain), see inset in **Fig. 5-21a**. In order to estimate the intrinsic contribution of the temperature increase (without strain) on the observed current change the same measurement also is repeated on a control device fabricated on a SiO_2/Si substrate (with very small thermal expansion) where finding a negligible current change (**Fig. 5-21b** and inset). A minor increase of the current value from -0.46 pA to -2.6 pA at -1 V, due to the increase of thermal excited carriers, is observed. The observed larger current change in the PC device thus can be mostly attributed to a piezoresistive response of InSe to biaxial strain. In order to quantify this piezoresistive response, and to compare it with that of other materials, in **Fig. 5-21c**, the current absolute values flowing through the devices at 1 V and -1 V both on PC and SiO_2/Si substrate as a function of temperature have been extracted. The calculated electrical gauge factor in the investigated device, $\mathrm{GF} = (I - I_0)/\varepsilon I_0$, reaches values of ~450 at 1 V and ~1076 at -1 V, ~5-12 times larger than that found for InSe under uniaxial strain loading and other strained 2D materials. In fact, GF values of ~150, ~220 and ~40 have been reported for single-, bi- and tri-layer MoS_2, respectively,[519] upon biaxial strain and GF ~15-30 for tri-layer MoS_2 upon uniaxial strain.[559] For graphene sensors GF values up to ~125 has been reported.[560] Moreover, the large gauge factor and mechanical resilience of 2D InSe makes it even more suitable as a biaxial strain sensor than state-of-the-art silicon strain sensors (GF ~200) with a fracture strain limit of ~0.7%.[561,562]

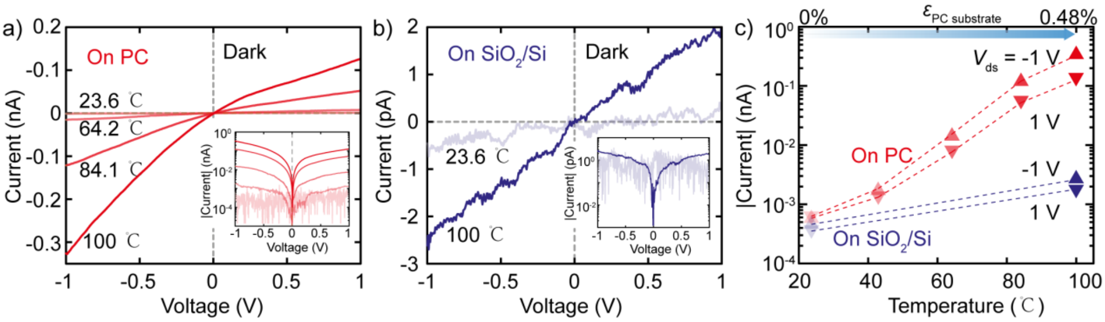

Fig. 5-21 Temperature-dependent dark current-voltage (*I*-*V*) characteristics of InSe device fabricated on PC and on 280 nm SiO_2/Si substrate. a, b) *I*-*V* curves of Au-InSe-Au device on PC substrate (a) and on 280 nm SiO_2/Si substrate (b) recorded in dark conditions as a function of temperature (from ~23 ℃ to ~100 ℃) in linear scale and semi-logarithmic scale (insets). c) Temperature-dependency of absolute values of the current flow through Au-InSe-Au devices at 1 V and -1 V on PC (red) and on 280 nm SiO_2/Si (blue) substrate. The top axis in (c) indicates the biaxial strain induced by the thermal expansion of the PC substrate.

5.2.6 Optoelectronic performance

The strong PL emission energy shift upon biaxial straining indicates that biaxial strain could be an efficient strategy to tune the spectral bandwidth of InSe based photodetectors. In order to study this possibility, the photocurrent of the InSe photodetector upon illumination with different wavelengths at a fixed bias of 1 V and power density of 35.4 mW/cm^2 has been measured. **Fig. 5-22a** shows the photocurrent spectra measured at various temperatures between ~23 ℃ and ~100 ℃ (corresponding to a biaxial strain range of 0% to 0.48%) in the InSe photodetector fabricated on PC. The overall spectra redshift upon biaxial strain, which is consistent with the strain-induced reduction of the bandgap observed in the PL measurements. This can be seen more clearly in the Tauc plot representation (see inset) that allows for an estimation of the energy cut-off ($\Delta E_{\text{cut-off}}$) of the photodetector (the minimum detectable photon energy). The theoretical foundation of Tauc plot extrapolation is based on the energy dependence of the above-band-gap absorption, which appears either as a square relation (direct-allowed-transition dominant) or a square-rooted relation (indirect-allowed-transition dominated) and due to the direct bandgap a squared plot relation can be taken for InSe.[258,563,564] In order to determine whether the observed bandgap reduction is mainly caused by the biaxial strain induced by substrate expansion, and not by the temperature increase, another set of control measurement was performed on an InSe device fabricated on a SiO_2/Si substrate. From **Fig. 5-22b**, one can see that in the control device (with negligible thermal expansion) the redshift of the spectra is less pronounced. Therefore, one can reliably extract the biaxial strain tunability of the energy cut-off ($\Delta E_{\text{cut-off}}$) directly from the measurements on the InSe device fabricated on PC. **Fig. 5-22c** summarizes the energy cut-off ($\Delta E_{\text{cut-off}}$) values extracted for the different biaxial strain levels showing a marked linear trend. The slope of this linear relationship is higher than the bandgap gauge factor giving a value of ~360 meV/%. This could be due to the intrinsic higher uncertainty in the Tauc plot extrapolation method (given the reduced number of data points at the absorption edge part of the spectra).

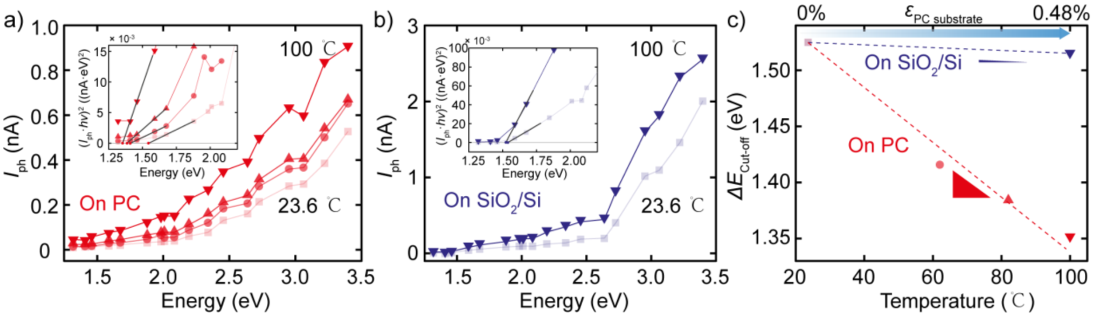

Fig. 5-22 Temperature-dependence of photocurrent spectra of InSe devices on PC and on 280 nm SiO_2/Si substrate. a, b) Photocurrent (I_{ph}) *versus* illumination photon energy spectra recorded under a fixed illumination power intensity (35.4 mW/cm^2) at 1 V as a function of temperature (from ~23 ℃ to ~100 ℃) of Au-InSe-Au device on PC (a) and on 280 nm SiO_2/Si substrate (b). Insets: Tauc plots: $(I_{ph}\,\hbar v)^2$ *vs*. photon energy. c) Temperature-dependence of bandgap values extracted from the Tauc plots as a function of temperature based on the Au-InSe-Au devices on PC (red) and on 280 nm SiO_2/Si (blue) substrate. The top axis in (c) indicates the biaxial strain induced by the thermal expansion of the PC substrate.

5.3 Conclusions

In conclusion, the experimental value of the Young's modulus of thin InSe flakes using the buckling metrology method has been found to be in the range of 18 - 28 GPa, which makes thin InSe one of the most flexible two-dimensional materials. Motivated from this point, the effects of biaxial strain on the vibrational, photoluminescence, electrical and optoelectronic properties of ultrathin InSe are studied. A strong shift of the photoluminescence spectra upon biaxial strain with a gauge factor ranging from 195 meV/% for 5 thick layers InSe to 63 meV/% for 30 layers thick InSe and a giant piezoresponse with an electrical gauge factor of ~1000 in the dark state have been determined. Interestingly, it is further demonstrated that how the strain tunable band gap can be exploited to tune the spectral response of InSe photodetectors. These results indicate thin InSe is a promising candidate for future straintronic and flexible optoelectronic applications.

6

CONCLUSIONS AND OUTLOOK

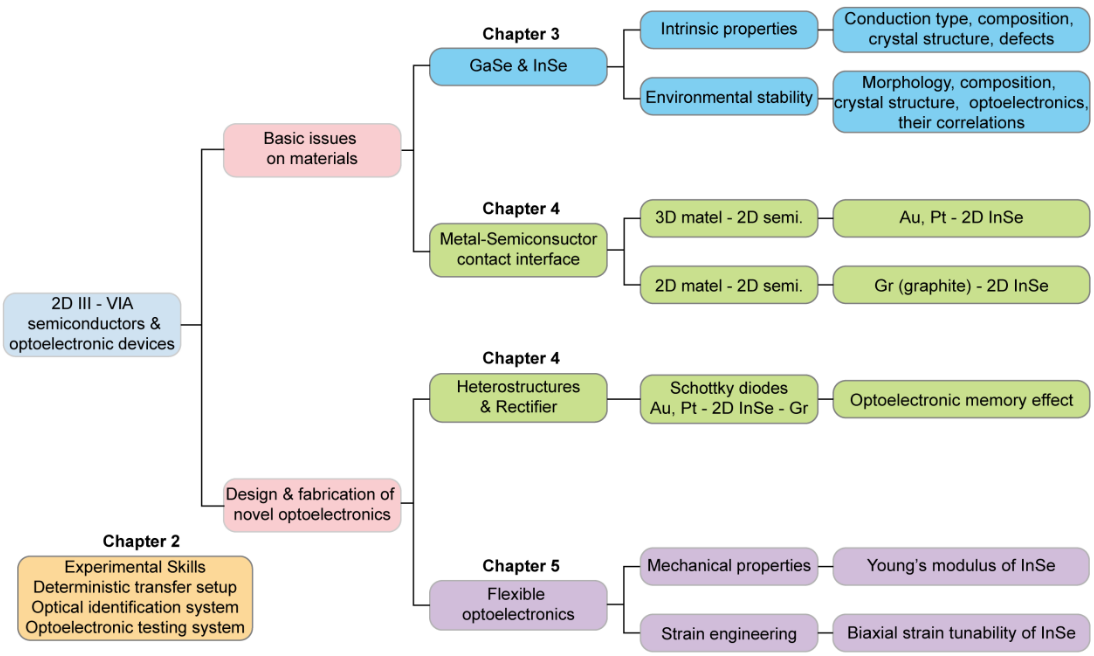

Fig. 6-1 Scheme of the topics addressed in this thesis.

In this thesis, two-dimensional (2D) III - VIA semiconducting materials (in particular GaSe and InSe) and optoelectronic devices have been investigated. To carry out the planed research, a whole set of experimental techniques and tools: a deterministic transfer setup, several optical-microscopy based methods to identify flakes, and electrical/optoelectronic testing system, have been developed and implemented. Based on the experimental observations and theoretical analysis, the main conclusions have been shown in **Fig. 6-1** and are summarized as follows:

1) Thin GaSe flakes and photodetectors are not stable in ambient conditions and h-BN encapsulation is an effective way to passivate this process. The environmental degradation of thin GaSe, which is accompanied by the variation of surface morphology, chemical composition, crystal structure and performance of the devices as a function of time, takes place in two main stages. At first, the exposure to air induces degradation of the pristine GaSe creating α-Se and Ga_2Se_3, accompanied by a photocurrent increase flowing through the devices. In the second stage, Ga_2O_3 appears and its concentration increases in the samples resulting in a drop of the photocurrent and leading to the final failure of the GaSe photodetectors. It was also found that capping the exfoliated GaSe flakes with a top h-BN flake is an effective way to prevent its environmental degradation as well laser-induced damage (chapter 3).
2) Thin InSe photodetectors can reach long-term environmental stability in air. No obvious changes can be observed on InSe surface morphology, chemical

composition, and crystal structure after air exposure. However, the performance of InSe photodetectors is strongly modified upon air exposure. This performance variation can be attributed to the modification of the hole-trapping, induced by selenium vacancies, upon air exposure. The pristine InSe photodetectors, with large density of traps, present large response time and high photoresponsivity which can be explained by the photogating effect. After air exposure, the InSe photodetectors can work with fast operation speed and low photogain, and finally reach a long-term environmentally stable behavior. The observed InSe device performance change is accompanied by a decrease in photoresponse time and photoresponsivity as well as the growth of exponent α. A statistical analysis indicates that photoresponsivity, response time and the photocurrent scaling law exponent α of InSe photodetectors are strongly correlated. All this can be explained by the passivation of selenium vacancies with atmospheric species, reducing the traps density in thin InSe photodetectors, and thus shifting the photocurrent generation mechanism from photogating to photoconductive effect (and making the devices to work as a back-to-back Schottky diode (chapter 3)).

3) The defects passivation in thin InSe introduced by air species can further reduce the fermi level pinning at the metal-InSe contact interface, thus various Schottky contact based on thin InSe with different van der Waals electrical contacts have been investigated. In the case of Au electrodes, a rectifying Schottky contact with a sizeable barrier between InSe and Au has been found and estimated to be ≈ 460 meV by temperature dependent measurements, which is consistent with Schottky–Mott rule. While in the case of graphite, the contact gives rise to a negligible contact barrier (smaller than 100 meV) thanks to the similar electron affinity of thin InSe and graphite. Exploiting this strong contact barrier difference, a Au–InSe–Gr Schottky diode, based on symmetric pre-patterned gold electrodes and with asymmetric van der Waals contacts, has been fabricated. The asymmetric contacted device shows *I*–*V* curves that follow perfectly the Schottky diode equation in a wide bias range. Furthermore, also the optoelectronic measurement of the devices is in agreement with the predicted Schottky diodes behaviors under reverse and forward biasing conditions (chapter 4).
4) Following a similar fabrication routine of Au-InSe-Gr Schottky diode and taking advantage of the larger work function of Pt ($W_{Pt} \approx 5.5$ eV), Pt-InSe-Gr devices also have been designed and demonstrated. Interestingly, it is found that after the fabrication of such a device, its electrical characteristics evolve in time when

exposed to air and finally can achieve a robust and stable Schottky diode behavior, with a Pt-InSe Schottky barrier height of ≈ 540 meV and an open circuit voltage of ≈ 0.6 V, which are confirmed by scanning photocurrent microscopy and temperature-dependent measurements. It is worth to note that the Pt-InSe-Gr Schottky diodes can work at large reverse bias condition (chapter 4).

5) Another important feature of Pt-InSe-Gr Schottky diodes is the presence of a counterclockwise hysteresis in the *I-V*s at the forward regime. Based on the observation that the devices take a larger hysteresis under illumination than that of in dark, the investigations of optoelectronic memory effect based on Pt-InSe-Gr Schottky diodes has been introduced. It is found that these devices are capable of switching between a low resistance state and a high resistance one thanks to the application of an external voltage together with illumination, which can store information with a retention time of the order thousands of seconds and a switching ratio up to 100 (chapter 4).
6) The experimental value of the Young's modulus of thin InSe flakes using the buckling metrology method has been found to be in the range of 18 - 28 GPa, which makes thin InSe one of the most flexible two-dimensional materials (chapter 5).
7) Motivated from the superior flexibility of thin InSe, the effects of biaxial strain on the vibrational, photoluminescence, electrical and optoelectronic properties of ultrathin InSe are studied. A strong shift of the photoluminescence spectra upon biaxial strain with a gauge factor ranging from 195 meV/% for 5 layers thick InSe to 63 meV/% for 30 layers thick InSe and a giant piezo response with an electrical gauge factor of ~1000 in the dark state have been determined. Interestingly, it is further demonstrated that how the strain tunable band gap can be exploited to tune the spectral response of InSe photodetectors (chapter 5).

In general, these results demonstrate great promise, such as the high-quality van der Waals Schottky diode, superior mechanical properties and strain tunability. But this thesis also pinpoints some of the most urgent challenges in the future research of 2D III-VIA semiconductors, like environmental degradation and property modification. These results, on the one hand, can promote the development of this field, on the other hand, are able to continuously inspire the enthusiasm from the researchers on 2D materials. However, it is important to point out that most of the works in this thesis are still at initial stages, the following subjects require further efforts.

The role of defects/traps in the thin GaSe/InSe-based photodetecting system requires further investigation. The interaction between air species and thin GaSe/InSe photodetectors demonstrates how significant roles that the traps play during the device operations. Controllable modification of traps levels in the 2D semiconductor is very important for future electrical and optoelectronic applications. It is necessary to present a systematic study of how the role of the starting InSe bulk could give shed more light about the variability observed in the literature.

Considering the practical industry application, it is necessary to clarify that how the O_2 and/or H_2O interact with defect sites during this passivation processes and carry out the quantitative investigations under control conditions, thus one can engineer the device performance under a control manner.

Novel 2D van der Waals heterostructures design and fabrication will continue to get attention. The successes of InSe-based diodes show the reliability of electronic and optoelectronic properties of van der Waals Schottky contacts. The easiness of fabrication, which comes from the van der Waals stacking by dry deterministic transfer, and the reproducible Schottky barrier formation are important factors for future applications of 2D semiconductors–metal systems. Moreover, at present, most of the 2D semiconductor-based Schottky contact investigations are focused on the 3D metal – 2D semiconductor system, whose tunability is usually limited by the effect of strong fermi level pinning. This problem can be overcome by using 2D metals, which are bounded with 2D semiconductors through van der Waals interaction. The future work will uncover the great potential of 2D metals for device applications.

Novel flexible optoelectronics should be included in the future work plan. The superior mechanical properties of thin InSe, *i.e.* ultralow Young’s modulus, allows efficient strain transfer from the flexible substrates to flakes. Until now, most strain engineering discussions of thin InSe are based on the symmetrically contact devices, the investigations about how the strain influence the transport properties of rectifying devices, such as Schottky diodes and p-n junctions, remain further exploration.

CONCLUSIONES Y PERSPECTIVAS

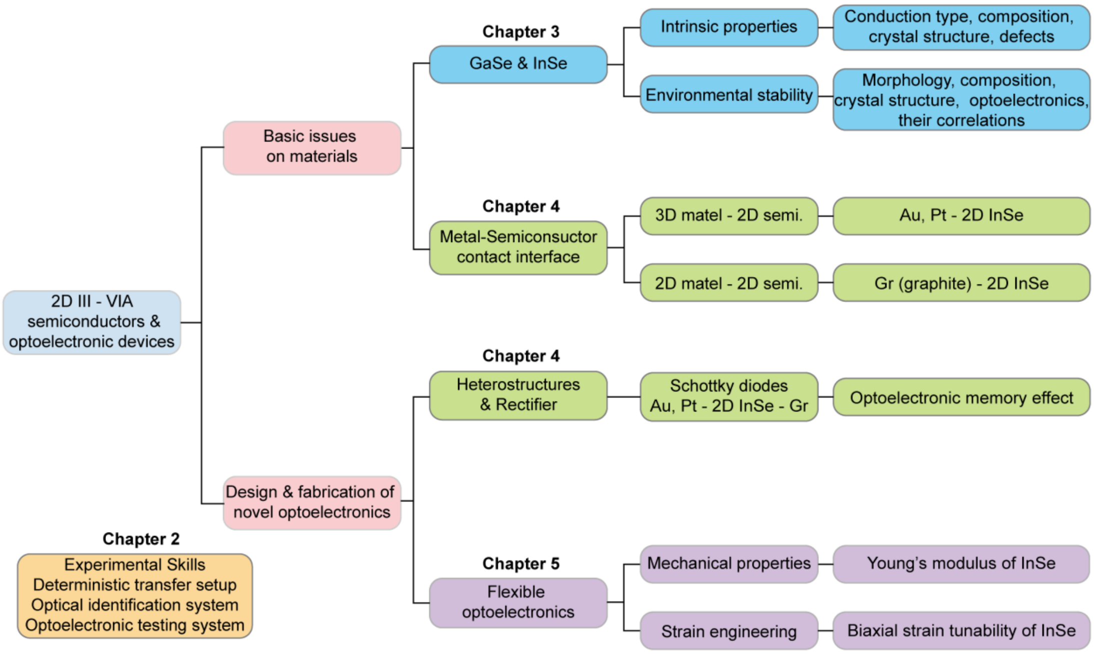

Fig. 6-1 Esquema de los temas tratados en esta tesis.

En esta tesis, se han investigado materiales semiconductores bidimensionales (2D) III - VIA (en particular GaSe e InSe) y dispositivos optoelectrónicos. Para llevar a cabo la investigación planificada, se ha desarrollado e implementado un conjunto completo de técnicas y herramientas experimentales: un sistema de transferencia determinista, varios métodos basados en microscopía óptica para identificar los copos y un sistema de medición eléctrico/optoelectrónico. Con base en las observaciones experimentales y el análisis teórico, las principales conclusiones se muestran en la **Fig. 6-1** y se resumen a continuación:

1) Los fotodetectores y los copos delgados de GaSe no son estables en condiciones ambientales y la encapsulación de h-BN es una forma eficaz de pasivar su degradación. La degradación ambiental del GaSe delgado, que va acompañada de la variación de la morfología de la superficie, la composición química, la estructura cristalina y el rendimiento de los dispositivos en función del tiempo, tiene lugar en dos etapas principales. Al principio, la exposición al aire induce la degradación del GaSe prístino creando α-Se y Ga_2Se_3, acompañado de un aumento de la fotocorriente que fluye a través de los dispositivos. En la segunda etapa, aparece Ga_2O_3 y su concentración aumenta en las muestras dando como resultado una caída de la fotocorriente y conduciendo al fallo final de los

fotodetectores de GaSe. También se descubrió que cubrir los copos de GaSe exfoliados con un copo de h-BN superior es una forma eficaz de prevenir su degradación ambiental, así como el daño inducido por láser (capítulo 3).

2) Los fotodetectores basados en copos delgados de InSe pueden alcanzar una estabilidad ambiental a largo plazo en el aire. No se pueden observar cambios obvios en la morfología de la superficie de InSe, la composición química y la estructura cristalina después de la exposición al aire. Sin embargo, el rendimiento de los fotodetectores de InSe se modifica considerablemente con la exposición al aire. Esta variación de rendimiento se puede atribuir a la modificación del atrapamiento de huecos, inducido por las trampas debidas a vacantes de selenio, tras la exposición al aire. Los fotodetectores de InSe prístinos, con gran densidad de trampas, presentan un tiempo de respuesta elevado y una alta fotorrespuesta que se puede explicar por el efecto "fotogating". Después de la exposición al aire, los fotodetectores InSe pueden trabajar con una velocidad de operación rápida y una baja ganancia de fotocorriente, y alcanzan un comportamiento ambientalmente estable a largo plazo. El cambio observado en el rendimiento de los dispositivos de InSe se acompaña de una disminución en el tiempo de respuesta y la magnitud de la fotorrespuesta, así como el crecimiento del exponente α. Un análisis estadístico indica que la fotorreactividad, el tiempo de respuesta y el exponente α de la ley de escalamiento de la fotocorriente de los fotodetectores de InSe están fuertemente correlacionados. Todo esto puede explicarse por la pasivación de las vacantes de selenio con especies atmosféricas, reduciendo la densidad de trampas en los fotodetectores delgados de InSe, y cambiando así el mecanismo de generación de fotocorriente de "fotogating" a efecto fotoconductivo (y haciendo que los dispositivos funcionen como un diodo Schottky tipo "back-to-back" (capítulo 3)).

3) La pasivación de defectos en copos delgados de InSe, introducidos por especies atmosféricas, pueden reducir aún más la fijación del nivel de Fermi en la interfaz del contacto metal-InSe, por lo que se han investigado varios contactos Schottky basados en InSe delgado con diferentes contactos eléctricos de tipo van der Waals. En el caso de los electrodos de Au, se ha encontrado un contacto Schottky rectificador con una barrera considerable entre InSe y Au y se ha estimado que es ≈ 460 meV mediante mediciones dependientes de la temperatura, lo cual es consistente con la regla de Schottky-Mott. En el caso del grafito, sin embargo, el contacto da lugar a una barrera de contacto insignificante (menor de 100 meV)

gracias a la afinidad electrónica similar de InSe delgado y grafito. Aprovechando esta fuerte diferencia de barrera de contacto, se han fabricado diodos Schottky Au-InSe-Gr, basados en electrodos de oro simétricos pre-fabricados y con contactos asimétricos de tipo van der Waals. Los dispositivos con contactos asimétricos muestran curvas IV que siguen perfectamente la ecuación del diodo Schottky en un amplio rango de voltaje. Además, también la medición optoelectrónica de los dispositivos está de acuerdo con los comportamientos predichos para los diodos Schottky en condiciones de polarización inversa y directa (capítulo 4).

4) Siguiendo un protocolo de fabricación similar al del diodo Schottky Au-InSe-Gr, y aprovechando la función de trabajo más grande de Pt ($W_{Pt} \approx 5.5$ eV), también se han diseñado y demostrado dispositivos Pt-InSe-Gr. Curiosamente, se encuentra que después de la fabricación de dicho dispositivo, sus características eléctricas evolucionan con el tiempo cuando se exponen al aire y finalmente pueden lograr un comportamiento de diodo Schottky robusto y estable, con una altura de barrera Pt-InSe Schottky de $\approx$ 540 meV y una Voltaje de circuito abierto de 0.6 V, que se confirma mediante microscopía de fotocorriente de barrido y mediciones dependientes de la temperatura. Vale la pena señalar que los diodos Schottky Pt-InSe-Gr pueden funcionar en condiciones de polarización inversa grande (capítulo 4).
5) Otra característica importante de los diodos Schottky Pt-InSe-Gr es la presencia de una histéresis en sentido antihorario en las curvas *I-V* en el régimen directo. Basándose en la observación de que los dispositivos toman una histéresis mayor bajo iluminación que en la oscuridad, se ha investigado el efecto de memoria optoelectrónica basadas en diodos Schottky Pt-InSe-Gr. Se ha encuentrado que estos dispositivos son capaces de conmutar entre un estado de baja resistencia y uno de alta resistencia gracias a la aplicación de un voltaje externo junto con iluminación, que puede almacenar información con un tiempo de retención del orden de miles de segundos y una relación de conmutación de hasta 100 (capítulo 4).
6) Se ha encontrado que el valor experimental del módulo de Young de los copos delgados de InSe utilizando el método de metrología de pandeo está en el rango de 18-28 GPa, lo que hace que el InSe sea uno de los materiales bidimensionales más flexibles (capítulo 5).
7) Motivado por la flexibilidad superior de copos delgados de InSe, se han estudiado

los efectos de la deformación biaxial sobre las propiedades vibratorias, fotoluminiscentes, eléctricas y optoelectrónicas de copos de InSe ultradelgados. Se ha observado un fuerte cambio de los espectros de fotoluminiscencia con la aplicación de deformación biaxial con un factor de galga ("gauge factor") que va desde 195 meV /% para 5 capas de InSe de espesor a 63 meV /% para 30 capas de InSe de espesor y una respuesta piezoresistiva gigante con un factor de galga eléctrico de ~1000 en el estado oscuro. Curiosamente, se demuestra además cómo se puede aprovechar la sintonización con deformación de la banda prohibida para ajustar la respuesta espectral de los fotodetectores de InSe (capítulo 5).

En general, estos resultados demuestran una gran promesa, como el diodo Schottky con contactos tipo van der Waals de alta calidad, las propiedades mecánicas superiores y capacidad de ajuste de la banda de energía prohibida con la deformación. Pero esta tesis también señala algunos de los desafíos más urgentes en la investigación futura de semiconductores 2D III-VIA, como la degradación ambiental y la modificación de propiedades. Estos resultados, por un lado, pueden promover el desarrollo de este campo, por otro lado, son capaces de inspirar continuamente el entusiasmo de los investigadores por los materiales 2D. Sin embargo, es importante señalar que la mayoría de los trabajos de esta tesis aún se encuentran en etapas iniciales, los siguientes temas requieren mayores esfuerzos.

El papel de los defectos/trampas en los fotodetectores basados en GaSe / InSe requiere más investigación. La interacción entre las especies ambientales y los fotodetectores basados en copos delgados de GaSe/InSe demuestra la importancia que tienen las trampas durante la operación de los dispositivos. La modificación controlable de los niveles de trampas en los semiconductores 2D es muy importante para futuras aplicaciones eléctricas y optoelectrónicas. Es necesario un estudio sistemático en el futuro de cuál es el papel del InSe en volumen inicial dado que podría arrojar más luz sobre la variabilidad observada en la literatura.

Teniendo en cuenta las aplicaciones prácticas en la industria, es necesario aclarar cómo el O_2 y/o H_2O interactúan con los sitios de defectos durante estos procesos de pasivación y llevar a cabo las investigaciones cuantitativas en condiciones de control, por lo que se puede diseñar el rendimiento del dispositivo de manera controlada.

El novedoso diseño y fabricación de heteroestructuras 2D de van der Waals continuará recibiendo atención. Los éxitos de los diodos Schottky basados en InSe muestran la fiabilidad de las propiedades electrónicas y optoelectrónicas de los contactos de tipo van der Waals. La facilidad de fabricación, que proviene del apilamiento de materiales de van der Waals por transferencia determinista seca, y la formación reproducible de la barrera de Schottky son factores importantes para las aplicaciones futuras de los sistemas de metal y semiconductores 2D. Además, en la actualidad, la mayoría de las investigaciones de contacto de Schottky basadas en semiconductores 2D se centran en el sistema de semiconductores 2D de metal 3D, cuya sintonización suele estar limitada por el efecto de una fuerte fijación de nivel fermi. Este problema puede superarse mediante el uso de metales 2D, en contacto con semiconductores 2D a través de la interacción de van der Waals. El trabajo futuro se centrará en investigar el gran potencial de los metales 2D para aplicaciones de dispositivos.

En el plan de trabajo futuro deberá incluirse una nueva optoelectrónica flexible. Las propiedades mecánicas superiores del InSe delgado, es decir, el módulo de Young ultrabajo, permite una transferencia de deformación eficiente desde los sustratos flexibles a los copos. Hasta ahora, la mayoría de las discusiones sobre ingeniería de deformaciones de InSe delgado se basan en los dispositivos con contactos eléctricos simétricos, las investigaciones sobre cómo la deformación influye en las propiedades de transporte de los dispositivos rectificadores, como los diodos Schottky y las uniones p-n, requieren una exploración más profunda en el futuro.

REFERENCES

1 Ashby, M. F., Shercliff, H. & Cebon, D. *Materials: engineering, science, processing and design*. (Butterworth-Heinemann, 2018).

2 Callister, W. D. *Fundamentals of materials science and engineering*. Vol. 471660817 (Wiley London, 2000).

3 Buzea, C., Pacheco, I. I. & Robbie, K. Nanomaterials and nanoparticles: sources and toxicity. *Biointerphases* **2**, MR17-MR71 (2007).

4 Drexler, E. There's Plenty of Room at the Bottom. *Richard Feynman, Pasadena* **29** (2009).

5 Tiwari, J. N., Tiwari, R. N. & Kim, K. S. Zero-dimensional, one-dimensional, two-dimensional and three-dimensional nanostructured materials for advanced electrochemical energy devices. *Progress in Materials Science* **57**, 724-803, doi:https://doi.org/10.1016/j.pmatsci.2011.08.003 (2012).

6 Kroto, H. W., Heath, J. R., O'Brien, S. C., Curl, R. F. & Smalley, R. E. C60: Buckminsterfullerene. *Nature* **318**, 162-163 (1985).

7 Iijima, S. Helical microtubules of graphitic carbon. *Nature* **354**, 56-58, doi:10.1038/354056a0 (1991).

8 Kuchibhatla, S. V. N. T., Karakoti, A. S., Bera, D. & Seal, S. One dimensional nanostructured materials. *Progress in Materials Science* **52**, 699-913, doi:https://doi.org/10.1016/j.pmatsci.2006.08.001 (2007).

9 Tan, C. *et al.* Recent Advances in Ultrathin Two-Dimensional Nanomaterials. *Chemical Reviews* **117**, 6225-6331, doi:10.1021/acs.chemrev.6b00558 (2017).

10 Mas-Ballesté, R., Gómez-Navarro, C., Gómez-Herrero, J. & Zamora, F. 2D materials: to graphene and beyond. *Nanoscale* **3**, 20-30, doi:10.1039/C0NR00323A (2011).

11 Novoselov, K. S. *et al.* Electric Field Effect in Atomically Thin Carbon Films. *Science* **306**, 666, doi:10.1126/science.1102896 (2004).

12 Allen, M. J., Tung, V. C. & Kaner, R. B. Honeycomb Carbon: A Review of Graphene. *Chemical Reviews* **110**, 132-145, doi:10.1021/cr900070d (2010).

13 Feynman, R. P., Leighton, R. B. & Sands, M. (Addison-Wesley. pp, 1965).

14 Cahay, M. (The Electrochemical Society).

15 in *Applied Nanophotonics* (eds Hilmi Volkan Demir & Sergey V. Gaponenko) 52-91 (Cambridge University Press, 2018).

16 Pereira, R. M. S., Borges, J., Smirnov, G. V., Vaz, F. & Vasilevskiy, M. I.

Surface Plasmon Resonance in a Metallic Nanoparticle Embedded in a Semiconductor Matrix: Exciton–Plasmon Coupling. *ACS Photonics* **6**, 204-210, doi:10.1021/acsphotonics.8b01430 (2019).

17 Haus, J. W., Zhou, H. S., Honma, I. & Komiyama, H. Quantum confinement in semiconductor heterostructure nanometer-size particles. *Physical Review B* **47**, 1359-1365, doi:10.1103/PhysRevB.47.1359 (1993).

18 Zhu, K. *et al.* Magnetic Nanomaterials: Chemical Design, Synthesis, and Potential Applications. *Accounts of Chemical Research* **51**, 404-413, doi:10.1021/acs.accounts.7b00407 (2018).

19 Kang, J., Liu, W., Sarkar, D., Jena, D. & Banerjee, K. Computational Study of Metal Contacts to Monolayer Transition-Metal Dichalcogenide Semiconductors. *Physical Review X* **4**, 031005, doi:10.1103/PhysRevX.4.031005 (2014).

20 Peierls, R. Bemerkungen über umwandlungstemperaturen. *Helv. Phys. Acta* **7**, 81 (1934).

21 Peierls, R. in *Annales de l'institut Henri Poincaré* 177-222.

22 LD, L. Zur Theorie der Phasenumwandlungen. *II. Phys Z. Sowjetunion* **11**, 26-35 (1937).

23 Landau, L. & Lifshitz, E. (Pergamon, Oxford, 1980).

24 Born, M. & Huang, K. *Dynamical theory of crystal lattices*. (Clarendon press, 1954).

25 Mermin, N. D. Crystalline Order in Two Dimensions. *Physical Review* **176**, 250-254, doi:10.1103/PhysRev.176.250 (1968).

26 Mermin, N. D. & Wagner, H. Absence of Ferromagnetism or Antiferromagnetism in One- or Two-Dimensional Isotropic Heisenberg Models. *Physical Review Letters* **17**, 1133-1136, doi:10.1103/PhysRevLett.17.1133 (1966).

27 Venable, J., Spiller, G. & Hanbucken, M. Nucleation and growth of thin film. *Rep. Prog. Phys.* **47**, 399-459 (1984).

28 Zinke-Allmang, M., Feldman, L. C. & Grabow, M. H. Clustering on surfaces. *Surface Science Reports* **16**, 377-463 (1992).

29 Evans, J. W., Thiel, P. A. & Bartelt, M. C. Morphological evolution during epitaxial thin film growth: Formation of 2D islands and 3D mounds. *Surface Science Reports* **61**, 1-128, doi:https://doi.org/10.1016/j.surfrep.2005.08.004 (2006).

30 Novoselov, K. S. *et al.* Two-dimensional atomic crystals. *Proceedings of the National Academy of Sciences of the United States of America* **102**, 10451, doi:10.1073/pnas.0502848102 (2005).

31 Meyer, J. C. *et al.* The structure of suspended graphene sheets. *Nature* **446**, 60-63, doi:10.1038/nature05545 (2007).

32 Fasolino, A., Los, J. H. & Katsnelson, M. I. Intrinsic ripples in graphene. *Nature Materials* **6**, 858-861, doi:10.1038/nmat2011 (2007).

33 Moore, G. E. in *2003 IEEE International Solid-State Circuits Conference, 2003. Digest of Technical Papers. ISSCC.* 20-23 vol.21.

34 Schaller, R. R. Moore's law: past, present and future. *IEEE Spectrum* **34**, 52-59, doi:10.1109/6.591665 (1997).

35 Moore, G. E. Cramming more components onto integrated circuits, Reprinted from Electronics, volume 38, number 8, April 19, 1965, pp.114 ff. *IEEE Solid-State Circuits Society Newsletter* **11**, 33-35, doi:10.1109/N-SSC.2006.4785860 (2006).

36 Mistry, K. *et al.* in *2007 IEEE International Electron Devices Meeting.* 247-250.

37 Davari, B., Dennard, R. H. & Shahidi, G. G. CMOS scaling for high performance and low power - the next ten years. *Proceedings of the IEEE* **83**, 595-606, doi:10.1109/5.371968 (1995).

38 Cartwright, J. Intel enters the third dimension. *Nature* **6** (2011).

39 Auth, C. *et al.* in *2012 Symposium on VLSI Technology (VLSIT).* 131-132.

40 Thompson, S. E. & Parthasarathy, S. Moore's law: the future of Si microelectronics. *Materials Today* **9**, 20-25, doi:https://doi.org/10.1016/S1369-7021(06)71539-5 (2006).

41 del Alamo, J. A. Nanometre-scale electronics with III–V compound semiconductors. *Nature* **479**, 317-323, doi:10.1038/nature10677 (2011).

42 Waldrop, M. M. The chips are down for Moore’s law. *Nature News* **530**, 144 (2016).

43 Thompson, S. in *Intel Technology Journal.* (Citeseer).

44 Haron, N. Z. & Hamdioui, S. in *2008 3rd International Design and Test Workshop.* 98-103.

45 Frank, D. J. Power-constrained CMOS scaling limits. *IBM Journal of Research and Development* **46**, 235-244, doi:10.1147/rd.462.0235 (2002).

46 Kim, Y.-B. Challenges for nanoscale MOSFETs and emerging nanoelectronics.

Transactions on Electrical and Electronic Materials **11**, 93-105 (2010).

47 Horowitz, M. *et al.* in *IEEE InternationalElectron Devices Meeting, 2005. IEDM Technical Digest.* 7 pp.-15.

48 Kuhn, K. J. Considerations for Ultimate CMOS Scaling. *IEEE Transactions on Electron Devices* **59**, 1813-1828, doi:10.1109/TED.2012.2193129 (2012).

49 Skotnicki, T., Hutchby, J. A., Tsu-Jae, K., Wong, H. P. & Boeuf, F. The end of CMOS scaling: toward the introduction of new materials and structural changes to improve MOSFET performance. *IEEE Circuits and Devices Magazine* **21**, 16-26, doi:10.1109/MCD.2005.1388765 (2005).

50 Cavin, R. K., Lugli, P. & Zhirnov, V. V. Science and Engineering Beyond Moore's Law. *Proceedings of the IEEE* **100**, 1720-1749, doi:10.1109/JPROC.2012.2190155 (2012).

51 Kuhn, K. J. *et al.* in *2012 International Electron Devices Meeting.* 8.1.1-8.1.4.

52 Sze, S. M. & Ng, K. K. *Physics of semiconductor devices*. (John wiley & sons, 2006).

53 Das, S., Robinson, J. A., Dubey, M., Terrones, H. & Terrones, M. Beyond Graphene: Progress in Novel Two-Dimensional Materials and van der Waals Solids. *Annual Review of Materials Research* **45**, 1-27, doi:10.1146/annurev-matsci-070214-021034 (2015).

54 Schwierz, F. Graphene transistors. *Nature Nanotechnology* **5**, 487-496, doi:10.1038/nnano.2010.89 (2010).

55 Schwierz, F. Graphene Transistors: Status, Prospects, and Problems. *Proceedings of the IEEE* **101**, 1567-1584, doi:10.1109/JPROC.2013.2257633 (2013).

56 Song, I., Park, C. & Choi, H. C. Synthesis and properties of molybdenum disulphide: from bulk to atomic layers. *RSC Advances* **5**, 7495-7514, doi:10.1039/C4RA11852A (2015).

57 Xu, M., Liang, T., Shi, M. & Chen, H. Graphene-Like Two-Dimensional Materials. *Chemical Reviews* **113**, 3766-3798, doi:10.1021/cr300263a (2013).

58 Schwierz, F. Flat transistors get off the ground. *Nature Nanotechnology* **6**, 135-136, doi:10.1038/nnano.2011.26 (2011).

59 Lembke, D., Bertolazzi, S. & Kis, A. Single-Layer MoS_2 Electronics. *Accounts of Chemical Research* **48**, 100-110, doi:10.1021/ar500274q (2015).

60 Ganatra, R. & Zhang, Q. Few-Layer MoS_2: A Promising Layered

Semiconductor. *ACS Nano* **8**, 4074-4099, doi:10.1021/nn405938z (2014).

61 Venkata Subbaiah, Y. P., Saji, K. J. & Tiwari, A. Atomically Thin MoS_2: A Versatile Nongraphene 2D Material. *Advanced Functional Materials* **26**, 2046-2069, doi:10.1002/adfm.201504202 (2016).

62 Wang, F. *et al.* Progress on Electronic and Optoelectronic Devices of 2D Layered Semiconducting Materials. *Small* **13**, 1604298, doi:10.1002/smll.201604298 (2017).

63 Cao, W. *et al.* in *2013 Proceedings of the European Solid-State Device Research Conference (ESSDERC).* 37-44.

64 Velický, M. & Toth, P. S. From two-dimensional materials to their heterostructures: An electrochemist's perspective. *Applied Materials Today* **8**, 68-103, doi:https://doi.org/10.1016/j.apmt.2017.05.003 (2017).

65 Gupta, A., Sakthivel, T. & Seal, S. Recent development in 2D materials beyond graphene. *Progress in Materials Science* **73**, 44-126, doi:https://doi.org/10.1016/j.pmatsci.2015.02.002 (2015).

66 Geim, A. K. & Grigorieva, I. V. Van der Waals heterostructures. *Nature* **499**, 419-425, doi:10.1038/nature12385 (2013).

67 Yi, M. & Shen, Z. A review on mechanical exfoliation for the scalable production of graphene. *Journal of Materials Chemistry A* **3**, 11700-11715, doi:10.1039/C5TA00252D (2015).

68 Novoselov, K. S. & Castro Neto, A. H. Two-dimensional crystals-based heterostructures: materials with tailored properties. *Physica Scripta* **T146**, 014006, doi:10.1088/0031-8949/2012/t146/014006 (2012).

69 Li, H., Wu, J., Yin, Z. & Zhang, H. Preparation and Applications of Mechanically Exfoliated Single-Layer and Multilayer MoS_2 and WSe_2 Nanosheets. *Accounts of Chemical Research* **47**, 1067-1075, doi:10.1021/ar4002312 (2014).

70 Li, H. *et al.* Fabrication of Single- and Multilayer MoS_2 Film-Based Field-Effect Transistors for Sensing NO at Room Temperature. *Small* **8**, 63-67, doi:10.1002/smll.201101016 (2012).

71 Late, D. J., Doneux, T. & Bougouma, M. Single-layer $MoSe_2$ based NH_3 gas sensor. *Applied Physics Letters* **105**, 233103, doi:10.1063/1.4903358 (2014).

72 Late, D. J., Shirodkar, S. N., Waghmare, U. V., Dravid, V. P. & Rao, C. N. R. Thermal Expansion, Anharmonicity and Temperature-Dependent Raman Spectra of Single- and Few-Layer $MoSe_2$ and WSe_2. *ChemPhysChem* **15**,

1592-1598, doi:10.1002/cphc.201400020 (2014).

73 Li, H. *et al.* Mechanical Exfoliation and Characterization of Single- and Few-Layer Nanosheets of WSe_2, TaS_2, and $TaSe_2$. *Small* **9**, 1974-1981, doi:10.1002/smll.201202919 (2013).

74 Pezeshki, A. *et al.* Static and Dynamic Performance of Complementary Inverters Based on Nanosheet α-$MoTe_2$ p-Channel and MoS_2 n-Channel Transistors. *ACS Nano* **10**, 1118-1125, doi:10.1021/acsnano.5b06419 (2016).

75 Liu, F. *et al.* Highly Sensitive Detection of Polarized Light Using Anisotropic 2D ReS_2. *Advanced Functional Materials* **26**, 1169-1177, doi:10.1002/adfm.201504546 (2016).

76 Chen, Y. *et al.* Tunable Band Gap Photoluminescence from Atomically Thin Transition-Metal Dichalcogenide Alloys. *ACS Nano* **7**, 4610-4616, doi:10.1021/nn401420h (2013).

77 Dumcenco, D. O., Kobayashi, H., Liu, Z., Huang, Y.-S. & Suenaga, K. Visualization and quantification of transition metal atomic mixing in $Mo_{1-x}W_xS_2$ single layers. *Nature Communications* **4**, 1351, doi:10.1038/ncomms2351 (2013).

78 Chen, Y. *et al.* Composition-dependent Raman modes of $Mo_{1-x}W_xS_2$ monolayer alloys. *Nanoscale* **6**, 2833-2839, doi:10.1039/C3NR05630A (2014).

79 Liu, F. *et al.* Optoelectronic properties of atomically thin ReSSe with weak interlayer coupling. *Nanoscale* **8**, 5826-5834, doi:10.1039/C5NR08440G (2016).

80 Goyal, V., Teweldebrhan, D. & Balandin, A. A. Mechanically-exfoliated stacks of thin films of Bi_2Te_3 topological insulators with enhanced thermoelectric performance. *Applied Physics Letters* **97**, 133117, doi:10.1063/1.3494529 (2010).

81 Shahil, K. M. F., Hossain, M. Z., Goyal, V. & Balandin, A. A. Micro-Raman spectroscopy of mechanically exfoliated few-quintuple layers of Bi_2Te_3, Bi_2Se_3, and Sb_2Te_3 materials. *Journal of Applied Physics* **111**, 054305, doi:10.1063/1.3690913 (2012).

82 Sotor, J. *et al.* Mode-locking in Er-doped fiber laser based on mechanically exfoliated Sb_2Te_3 saturable absorber. *Opt. Mater. Express* **4**, 1-6, doi:10.1364/OME.4.000001 (2014).

83 Liu, F. *et al.* Room-temperature ferroelectricity in $CuInP_2S_6$ ultrathin flakes.

Nature Communications **7**, 12357, doi:10.1038/ncomms12357 (2016).

84 Castellanos-Gomez, A. *et al.* Isolation and characterization of few-layer black phosphorus. *2D Materials* **1**, 025001, doi:10.1088/2053-1583/1/2/025001 (2014).

85 Buscema, M. *et al.* Fast and Broadband Photoresponse of Few-Layer Black Phosphorus Field-Effect Transistors. *Nano Letters* **14**, 3347-3352, doi:10.1021/nl5008085 (2014).

86 Chen, Y. *et al.* Mechanically exfoliated black phosphorus as a new saturable absorber for both Q-switching and Mode-locking laser operation. *Opt. Express* **23**, 12823-12833, doi:10.1364/OE.23.012823 (2015).

87 Li, L. *et al.* Black phosphorus field-effect transistors. *Nature Nanotechnology* **9**, 372-377, doi:10.1038/nnano.2014.35 (2014).

88 Ares, P. *et al.* Mechanical Isolation of Highly Stable Antimonene under Ambient Conditions. *Advanced Materials* **28**, 6332-6336, doi:10.1002/adma.201602128 (2016).

89 Du, K.-z. *et al.* Weak Van der Waals Stacking, Wide-Range Band Gap, and Raman Study on Ultrathin Layers of Metal Phosphorus Trichalcogenides. *ACS Nano* **10**, 1738-1743, doi:10.1021/acsnano.5b05927 (2016).

90 Alem, N. *et al.* Atomically thin hexagonal boron nitride probed by ultrahigh-resolution transmission electron microscopy. *Physical Review B* **80**, 155425, doi:10.1103/PhysRevB.80.155425 (2009).

91 Dean, C. R. *et al.* Boron nitride substrates for high-quality graphene electronics. *Nature Nanotechnology* **5**, 722-726, doi:10.1038/nnano.2010.172 (2010).

92 Hernandez, Y. *et al.* High-yield production of graphene by liquid-phase exfoliation of graphite. *Nature Nanotechnology* **3**, 563-568, doi:10.1038/nnano.2008.215 (2008).

93 Coleman, J. N. *et al.* Two-Dimensional Nanosheets Produced by Liquid Exfoliation of Layered Materials. *Science* **331**, 568, doi:10.1126/science.1194975 (2011).

94 Paton, K. R. *et al.* Scalable production of large quantities of defect-free few-layer graphene by shear exfoliation in liquids. *Nature Materials* **13**, 624-630, doi:10.1038/nmat3944 (2014).

95 Xu, F. *et al.* Scalable shear-exfoliation of high-quality phosphorene nanoflakes with reliable electrochemical cycleability in nano batteries. *2D Materials* **3**,

025005, doi:10.1088/2053-1583/3/2/025005 (2016).

96 Dines, M. B. Lithium intercalation via n-Butyllithium of the layered transition metal dichalcogenides. *Materials Research Bulletin* **10**, 287-291, doi:https://doi.org/10.1016/0025-5408(75)90115-4 (1975).

97 Joensen, P., Frindt, R. F. & Morrison, S. R. Single-layer MoS_2. *Materials Research Bulletin* **21**, 457-461, doi:https://doi.org/10.1016/0025-5408(86)90011-5 (1986).

98 Osada, M. & Sasaki, T. Nanosheet architectonics: a hierarchically structured assembly for tailored fusion materials. *Polymer Journal* **47**, 89-98, doi:10.1038/pj.2014.111 (2015).

99 Sasaki, T., Watanabe, M., Hashizume, H., Yamada, H. & Nakazawa, H. Macromolecule-like Aspects for a Colloidal Suspension of an Exfoliated Titanate. Pairwise Association of Nanosheets and Dynamic Reassembling Process Initiated from It. *Journal of the American Chemical Society* **118**, 8329-8335, doi:10.1021/ja960073b (1996).

100 Liu, Z., Ma, R., Ebina, Y., Takada, K. & Sasaki, T. Synthesis and Delamination of Layered Manganese Oxide Nanobelts. *Chemistry of Materials* **19**, 6504-6512, doi:10.1021/cm7019203 (2007).

101 Adachi-Pagano, M., Forano, C. & Besse, J.-P. Delamination of layered double hydroxides by use of surfactants. *Chemical Communications*, 91-92, doi:10.1039/A908251D (2000).

102 Geng, F. *et al.* General Synthesis and Structural Evolution of a Layered Family of $Ln_8(OH)_{20}Cl_4$ nH2O (Ln = Nd, Sm, Eu, Gd, Tb, Dy, Ho, Er, Tm, and Y). *Journal of the American Chemical Society* **130**, 16344-16350, doi:10.1021/ja807050e (2008).

103 Zhu, Y. *et al.* Graphene and Graphene Oxide: Synthesis, Properties, and Applications. *Advanced Materials* **22**, 3906-3924, doi:10.1002/adma.201001068 (2010).

104 Tan, C., Huang, X. & Zhang, H. Synthesis and applications of graphene-based noble metal nanostructures. *Materials Today* **16**, 29-36, doi:https://doi.org/10.1016/j.mattod.2013.01.021 (2013).

105 Lukatskaya, M. R. *et al.* Cation Intercalation and High Volumetric Capacitance of Two-Dimensional Titanium Carbide. *Science* **341**, 1502, doi:10.1126/science.1241488 (2013).

106 Wang, X. *et al.* Pseudocapacitance of MXene nanosheets for high-power

sodium-ion hybrid capacitors. *Nature Communications* **6**, 6544, doi:10.1038/ncomms7544 (2015).

107 Boota, M. *et al.* Pseudocapacitive Electrodes Produced by Oxidant-Free Polymerization of Pyrrole between the Layers of 2D Titanium Carbide (MXene). *Advanced Materials* **28**, 1517-1522, doi:10.1002/adma.201504705 (2016).

108 Backes, C. *et al.* Production of Highly Monolayer Enriched Dispersions of Liquid-Exfoliated Nanosheets by Liquid Cascade Centrifugation. *ACS Nano* **10**, 1589-1601, doi:10.1021/acsnano.5b07228 (2016).

109 Nicolosi, V., Chhowalla, M., Kanatzidis, M. G., Strano, M. S. & Coleman, J. N. Liquid Exfoliation of Layered Materials. *Science* **340**, 1226419, doi:10.1126/science.1226419 (2013).

110 Yu, J., Li, J., Zhang, W. & Chang, H. Synthesis of high quality two-dimensional materials via chemical vapor deposition. *Chemical Science* **6**, 6705-6716, doi:10.1039/C5SC01941A (2015).

111 Platz, R. & Wagner, S. Intrinsic microcrystalline silicon by plasma-enhanced chemical vapor deposition from dichlorosilane. *Applied Physics Letters* **73**, 1236-1238, doi:10.1063/1.122138 (1998).

112 Zhang, Y., Zhang, L. & Zhou, C. Review of Chemical Vapor Deposition of Graphene and Related Applications. *Accounts of Chemical Research* **46**, 2329-2339, doi:10.1021/ar300203n (2013).

113 Somani, P. R., Somani, S. P. & Umeno, M. Planer nano-graphenes from camphor by CVD. *Chemical Physics Letters* **430**, 56-59, doi:https://doi.org/10.1016/j.cplett.2006.06.081 (2006).

114 Pollard, A. J. *et al.* Formation of Monolayer Graphene by Annealing Sacrificial Nickel Thin Films. *The Journal of Physical Chemistry C* **113**, 16565-16567, doi:10.1021/jp906066z (2009).

115 Li, X. *et al.* Large-Area Synthesis of High-Quality and Uniform Graphene Films on Copper Foils. *Science* **324**, 1312, doi:10.1126/science.1171245 (2009).

116 Shi, Y. *et al.* Synthesis of Few-Layer Hexagonal Boron Nitride Thin Film by Chemical Vapor Deposition. *Nano Letters* **10**, 4134-4139, doi:10.1021/nl1023707 (2010).

117 Song, L. *et al.* Large Scale Growth and Characterization of Atomic Hexagonal Boron Nitride Layers. *Nano Letters* **10**, 3209-3215, doi:10.1021/nl1022139

(2010).

118 Kong, D. & Cui, Y. Opportunities in chemistry and materials science for topological insulators and their nanostructures. *Nature Chemistry* **3**, 845-849, doi:10.1038/nchem.1171 (2011).

119 Kong, D. *et al.* Few-Layer Nanoplates of Bi_2Se_3 and Bi_2Te_3 with Highly Tunable Chemical Potential. *Nano Letters* **10**, 2245-2250, doi:10.1021/nl101260j (2010).

120 Yan, K., Peng, H., Zhou, Y., Li, H. & Liu, Z. Formation of Bilayer Bernal Graphene: Layer-by-Layer Epitaxy via Chemical Vapor Deposition. *Nano Letters* **11**, 1106-1110, doi:10.1021/nl104000b (2011).

121 Xu, C. *et al.* Large-area high-quality 2D ultrathin Mo_2C superconducting crystals. *Nature Materials* **14**, 1135-1141, doi:10.1038/nmat4374 (2015).

122 Gogotsi, Y. Transition metal carbides go 2D. *Nature Materials* **14**, 1079-1080, doi:10.1038/nmat4386 (2015).

123 Fleurence, A. *et al.* Experimental Evidence for Epitaxial Silicene on Diboride Thin Films. *Physical Review Letters* **108**, 245501, doi:10.1103/PhysRevLett.108.245501 (2012).

124 Feng, B. *et al.* Experimental realization of two-dimensional boron sheets. *Nature Chemistry* **8**, 563-568, doi:10.1038/nchem.2491 (2016).

125 Ji, J. *et al.* Two-dimensional antimonene single crystals grown by van der Waals epitaxy. *Nature Communications* **7**, 13352, doi:10.1038/ncomms13352 (2016).

126 Shi, Y., Li, H. & Li, L.-J. Recent advances in controlled synthesis of two-dimensional transition metal dichalcogenides via vapour deposition techniques. *Chemical Society Reviews* **44**, 2744-2756, doi:10.1039/C4CS00256C (2015).

127 Hofmann, W. K. Thin films of molybdenum and tungsten disulphides by metal organic chemical vapour deposition. *Journal of Materials Science* **23**, 3981-3986, doi:10.1007/BF01106824 (1988).

128 Liu, K.-K. *et al.* Growth of Large-Area and Highly Crystalline MoS_2 Thin Layers on Insulating Substrates. *Nano Letters* **12**, 1538-1544, doi:10.1021/nl2043612 (2012).

129 Zhan, Y., Liu, Z., Najmaei, S., Ajayan, P. M. & Lou, J. Large-Area Vapor-Phase Growth and Characterization of MoS_2 Atomic Layers on a SiO_2 Substrate. *Small* **8**, 966-971, doi:10.1002/smll.201102654 (2012).

130 Lee, Y.-H. *et al.* Synthesis of Large-Area MoS_2 Atomic Layers with Chemical Vapor Deposition. *Advanced Materials* **24**, 2320-2325, doi:10.1002/adma.201104798 (2012).

131 Najmaei, S. *et al.* Vapour phase growth and grain boundary structure of molybdenum disulphide atomic layers. *Nature Materials* **12**, 754-759, doi:10.1038/nmat3673 (2013).

132 Liu, B. *et al.* High-Performance Chemical Sensing Using Schottky-Contacted Chemical Vapor Deposition Grown Monolayer MoS_2 Transistors. *ACS Nano* **8**, 5304-5314, doi:10.1021/nn5015215 (2014).

133 Zhang, Y. *et al.* Controlled Growth of High-Quality Monolayer WS_2 Layers on Sapphire and Imaging Its Grain Boundary. *ACS Nano* **7**, 8963-8971, doi:10.1021/nn403454e (2013).

134 Gutiérrez, H. R. *et al.* Extraordinary Room-Temperature Photoluminescence in Triangular WS_2 Monolayers. *Nano Letters* **13**, 3447-3454, doi:10.1021/nl3026357 (2013).

135 Wang, X. *et al.* Chemical Vapor Deposition Growth of Crystalline Monolayer $MoSe_2$. *ACS Nano* **8**, 5125-5131, doi:10.1021/nn501175k (2014).

136 Shaw, J. C. *et al.* Chemical vapor deposition growth of monolayer $MoSe_2$ nanosheets. *Nano Research* **7**, 511-517, doi:10.1007/s12274-014-0417-z (2014).

137 Docherty, C. J. *et al.* Ultrafast Transient Terahertz Conductivity of Monolayer MoS_2 and WSe_2 Grown by Chemical Vapor Deposition. *ACS Nano* **8**, 11147-11153, doi:10.1021/nn5034746 (2014).

138 Eichfeld, S. M. *et al.* Highly Scalable, Atomically Thin WSe_2 Grown via Metal–Organic Chemical Vapor Deposition. *ACS Nano* **9**, 2080-2087, doi:10.1021/nn5073286 (2015).

139 Zhang, M. *et al.* Controlled Synthesis of ZrS_2 Monolayer and Few Layers on Hexagonal Boron Nitride. *Journal of the American Chemical Society* **137**, 7051-7054, doi:10.1021/jacs.5b03807 (2015).

140 Wang, X. *et al.* Large scale ZrS_2 atomically thin layers. *Journal of Materials Chemistry C* **4**, 3143-3148, doi:10.1039/C6TC00254D (2016).

141 Keyshar, K. *et al.* Chemical Vapor Deposition of Monolayer Rhenium Disulfide (ReS_2). *Advanced Materials* **27**, 4640-4648, doi:10.1002/adma.201501795 (2015).

142 He, X. *et al.* Chemical Vapor Deposition of High-Quality and Atomically

Layered ReS_2. *Small* **11**, 5423-5429, doi:10.1002/smll.201501488 (2015).

143 Zhou, L. *et al.* Large-Area Synthesis of High-Quality Uniform Few-Layer $MoTe_2$. *Journal of the American Chemical Society* **137**, 11892-11895, doi:10.1021/jacs.5b07452 (2015).

144 Naylor, C. H. *et al.* Monolayer Single-Crystal 1T′-$MoTe_2$ Grown by Chemical Vapor Deposition Exhibits Weak Antilocalization Effect. *Nano Letters* **16**, 4297-4304, doi:10.1021/acs.nanolett.6b01342 (2016).

145 Xie, L. M. Two-dimensional transition metal dichalcogenide alloys: preparation, characterization and applications. *Nanoscale* **7**, 18392-18401, doi:10.1039/C5NR05712D (2015).

146 Liu, H., Antwi, K. K. A., Chua, S. & Chi, D. Vapor-phase growth and characterization of $Mo_{1-x}W_xS_2$ ($0 \leq x \leq 1$) atomic layers on 2-inch sapphire substrates. *Nanoscale* **6**, 624-629, doi:10.1039/C3NR04515C (2014).

147 Gong, Y. *et al.* Band Gap Engineering and Layer-by-Layer Mapping of Selenium-Doped Molybdenum Disulfide. *Nano Letters* **14**, 442-449, doi:10.1021/nl4032296 (2014).

148 Li, H. *et al.* Growth of Alloy $MoS_{2x}Se_{2(1-x)}$ Nanosheets with Fully Tunable Chemical Compositions and Optical Properties. *Journal of the American Chemical Society* **136**, 3756-3759, doi:10.1021/ja500069b (2014).

149 Mann, J. *et al.* 2-Dimensional Transition Metal Dichalcogenides with Tunable Direct Band Gaps: $MoS_{2(1-x)}Se_{2x}$ Monolayers. *Advanced Materials* **26**, 1399-1404, doi:10.1002/adma.201304389 (2014).

150 Feng, Q. *et al.* Growth of $MoS_{2(1-x)}Se_{2x}$ ($x = 0.41$–1.00) Monolayer Alloys with Controlled Morphology by Physical Vapor Deposition. *ACS Nano* **9**, 7450-7455, doi:10.1021/acsnano.5b02506 (2015).

151 Han, J. H., Lee, S. & Cheon, J. Synthesis and structural transformations of colloidal 2D layered metal chalcogenide nanocrystals. *Chemical Society Reviews* **42**, 2581-2591, doi:10.1039/C2CS35386E (2013).

152 Tan, C. & Zhang, H. Wet-chemical synthesis and applications of non-layer structured two-dimensional nanomaterials. *Nature Communications* **6**, 7873, doi:10.1038/ncomms8873 (2015).

153 Zhuang, Z., Peng, Q. & Li, Y. Controlled synthesis of semiconductor nanostructures in the liquid phase. *Chemical Society Reviews* **40**, 5492-5513, doi:10.1039/C1CS15095B (2011).

154 Shi, W., Song, S. & Zhang, H. Hydrothermal synthetic strategies of inorganic

semiconducting nanostructures. *Chemical Society Reviews* **42**, 5714-5743, doi:10.1039/C3CS60012B (2013).

155 Sun, Z. *et al.* Generalized self-assembly of scalable two-dimensional transition metal oxide nanosheets. *Nature Communications* **5**, 3813, doi:10.1038/ncomms4813 (2014).

156 Xie, J. *et al.* Defect-Rich MoS_2 Ultrathin Nanosheets with Additional Active Edge Sites for Enhanced Electrocatalytic Hydrogen Evolution. *Advanced Materials* **25**, 5807-5813, doi:10.1002/adma.201302685 (2013).

157 Schliehe, C. *et al.* Ultrathin PbS Sheets by Two-Dimensional Oriented Attachment. *Science* **329**, 550, doi:10.1126/science.1188035 (2010).

158 Simon, P. *et al.* Interconnection of Nanoparticles within 2D Superlattices of PbS/Oleic Acid Thin Films. *Advanced Materials* **26**, 3042-3049, doi:10.1002/adma.201305667 (2014).

159 Acharya, S. *et al.* A Bottom-Up Approach toward Fabrication of Ultrathin PbS Sheets. *Nano Letters* **13**, 409-415, doi:10.1021/nl303568d (2013).

160 Fan, Z. & Zhang, H. Template Synthesis of Noble Metal Nanocrystals with Unusual Crystal Structures and Their Catalytic Applications. *Accounts of Chemical Research* **49**, 2841-2850, doi:10.1021/acs.accounts.6b00527 (2016).

161 Liu, Y., Goebl, J. & Yin, Y. Templated synthesis of nanostructured materials. *Chemical Society Reviews* **42**, 2610-2653, doi:10.1039/C2CS35369E (2013).

162 Huang, X. *et al.* Synthesis of hexagonal close-packed gold nanostructures. *Nature Communications* **2**, 292, doi:10.1038/ncomms1291 (2011).

163 Murray, C., Norris, D. J. & Bawendi, M. G. Synthesis and characterization of nearly monodisperse CdE (E= sulfur, selenium, tellurium) semiconductor nanocrystallites. *Journal of the American Chemical Society* **115**, 8706-8715 (1993).

164 Son, J. S. *et al.* Large-Scale Soft Colloidal Template Synthesis of 1.4 nm Thick CdSe Nanosheets. *Angewandte Chemie* **121**, 6993-6996 (2009).

165 Bauer, T. *et al.* Synthesis of free-standing, monolayered organometallic sheets at the air/water interface. *Angewandte Chemie* **123**, 8025-8030 (2011).

166 Xu, L. *et al.* Surface-Confined Crystalline Two-Dimensional Covalent Organic Frameworks via on-Surface Schiff-Base Coupling. *ACS Nano* **7**, 8066-8073, doi:10.1021/nn403328h (2013).

167 Yue, J.-Y., Liu, X.-H., Sun, B. & Wang, D. The on-surface synthesis of imine-based covalent organic frameworks with non-aromatic linkage.

Chemical Communications **51**, 14318-14321, doi:10.1039/C5CC05689F (2015).

168 Dappe, Y. J., Basanta, M. A., Flores, F. & Ortega, J. Weak chemical interaction and van der Waals forces between graphene layers: A combined density functional and intermolecular perturbation theory approach. *Physical Review B* **74**, 205434, doi:10.1103/PhysRevB.74.205434 (2006).

169 Tributsch, H. & Bennett, J. C. Electrochemistry and photochemistry of MoS_2 layer crystals. I. *Journal of Electroanalytical Chemistry and Interfacial Electrochemistry* **81**, 97-111, doi:https://doi.org/10.1016/S0022-0728(77)80363-X (1977).

170 Fivaz, R. & Mooser, E. Mobility of Charge Carriers in Semiconducting Layer Structures. *Physical Review* **163**, 743-755, doi:10.1103/PhysRev.163.743 (1967).

171 Mattheiss, L. F. Band Structures of Transition-Metal-Dichalcogenide Layer Compounds. *Physical Review B* **8**, 3719-3740, doi:10.1103/PhysRevB.8.3719 (1973).

172 Fleischauer, P. D., Lince, J. R., Bertrand, P. & Bauer, R. Electronic structure and lubrication properties of molybdenum disulfide: a qualitative molecular orbital approach. *Langmuir* **5**, 1009-1015 (1989).

173 Bromley, R. A., Murray, R. B. & Yoffe, A. D. The band structures of some transition metal dichalcogenides. III. Group VIA: trigonal prism materials. *Journal of Physics C: Solid State Physics* **5**, 759-778, doi:10.1088/0022-3719/5/7/007 (1972).

174 Lin, Y.-C., Dumcenco, D. O., Huang, Y.-S. & Suenaga, K. Atomic mechanism of the semiconducting-to-metallic phase transition in single-layered MoS_2. *Nature Nanotechnology* **9**, 391-396, doi:10.1038/nnano.2014.64 (2014).

175 Kappera, R. *et al.* Phase-engineered low-resistance contacts for ultrathin MoS_2 transistors. *Nature Materials* **13**, 1128-1134, doi:10.1038/nmat4080 (2014).

176 Geim, A. K. Nobel Lecture: Random walk to graphene. *Reviews of Modern Physics* **83**, 851-862, doi:10.1103/RevModPhys.83.851 (2011).

177 Novoselov, K. S. Nobel Lecture: Graphene: Materials in the Flatland. *Reviews of Modern Physics* **83**, 837-849, doi:10.1103/RevModPhys.83.837 (2011).

178 Novoselov, K. S. *et al.* Two-dimensional gas of massless Dirac fermions in graphene. *Nature* **438**, 197-200, doi:10.1038/nature04233 (2005).

179 Radisavljevic, B., Radenovic, A., Brivio, J., Giacometti, V. & Kis, A.

Single-layer MoS$_2$ transistors. *Nature Nanotechnology* **6**, 147-150, doi:10.1038/nnano.2010.279 (2011).

180 Kim, S. *et al.* High-mobility and low-power thin-film transistors based on multilayer MoS$_2$ crystals. *Nature Communications* **3**, 1011, doi:10.1038/ncomms2018 (2012).

181 Cui, X. *et al.* Multi-terminal transport measurements of MoS$_2$ using a van der Waals heterostructure device platform. *Nature Nanotechnology* **10**, 534-540, doi:10.1038/nnano.2015.70 (2015).

182 Jeon, J. *et al.* Layer-controlled CVD growth of large-area two-dimensional MoS$_2$ films. *Nanoscale* **7**, 1688-1695, doi:10.1039/C4NR04532G (2015).

183 Withers, F., Bointon, T. H., Hudson, D. C., Craciun, M. F. & Russo, S. Electron transport of WS$_2$ transistors in a hexagonal boron nitride dielectric environment. *Scientific Reports* **4**, 4967, doi:10.1038/srep04967 (2014).

184 Lee, H. S. *et al.* MoS$_2$ Nanosheet Phototransistors with Thickness-Modulated Optical Energy Gap. *Nano Letters* **12**, 3695-3700, doi:10.1021/nl301485q (2012).

185 Das, S., Chen, H.-Y., Penumatcha, A. V. & Appenzeller, J. High Performance Multilayer MoS$_2$ Transistors with Scandium Contacts. *Nano Letters* **13**, 100-105, doi:10.1021/nl303583v (2013).

186 Braga, D., Gutiérrez Lezama, I., Berger, H. & Morpurgo, A. F. Quantitative Determination of the Band Gap of WS$_2$ with Ambipolar Ionic Liquid-Gated Transistors. *Nano Letters* **12**, 5218-5223, doi:10.1021/nl302389d (2012).

187 Mak, K. F., Lee, C., Hone, J., Shan, J. & Heinz, T. F. Atomically Thin MoS$_2$: A New Direct-Gap Semiconductor. *Physical Review Letters* **105**, 136805, doi:10.1103/PhysRevLett.105.136805 (2010).

188 Splendiani, A. *et al.* Emerging Photoluminescence in Monolayer MoS$_2$. *Nano Letters* **10**, 1271-1275, doi:10.1021/nl903868w (2010).

189 Zhao, W. *et al.* Evolution of Electronic Structure in Atomically Thin Sheets of WS$_2$ and WSe$_2$. *ACS Nano* **7**, 791-797, doi:10.1021/nn305275h (2013).

190 Castellanos-Gomez, A. *et al.* Elastic Properties of Freely Suspended MoS$_2$ Nanosheets. *Advanced Materials* **24**, 772-775, doi:10.1002/adma.201103965 (2012).

191 Chernikov, A. *et al.* Electrical Tuning of Exciton Binding Energies in Monolayer WS$_2$. *Physical Review Letters* **115**, 126802, doi:10.1103/PhysRevLett.115.126802 (2015).

192 Tongay, S. *et al.* Defects activated photoluminescence in two-dimensional semiconductors: interplay between bound, charged and free excitons. *Scientific Reports* **3**, 2657, doi:10.1038/srep02657 (2013).

193 Zhu, X. *et al.* Charge Transfer Excitons at van der Waals Interfaces. *Journal of the American Chemical Society* **137**, 8313-8320, doi:10.1021/jacs.5b03141 (2015).

194 Chernikov, A. *et al.* Exciton Binding Energy and Nonhydrogenic Rydberg Series in Monolayer WS_2. *Physical Review Letters* **113**, 076802, doi:10.1103/PhysRevLett.113.076802 (2014).

195 Mak, K. F. *et al.* Tightly bound trions in monolayer MoS_2. *Nature Materials* **12**, 207-211, doi:10.1038/nmat3505 (2013).

196 You, Y. *et al.* Observation of biexcitons in monolayer WSe_2. *Nature Physics* **11**, 477-481, doi:10.1038/nphys3324 (2015).

197 Kheng, K. *et al.* Observation of negatively charged excitons X^- in semiconductor quantum wells. *Physical Review Letters* **71**, 1752-1755, doi:10.1103/PhysRevLett.71.1752 (1993).

198 High, A. A., Novitskaya, E. E., Butov, L. V., Hanson, M. & Gossard, A. C. Control of Exciton Fluxes in an Excitonic Integrated Circuit. *Science* **321**, 229, doi:10.1126/science.1157845 (2008).

199 Lv, H. Y. *et al.* Perfect charge compensation in WTe_2 for the extraordinary magnetoresistance: From bulk to monolayer. *EPL (Europhysics Letters)* **110**, 37004, doi:10.1209/0295-5075/110/37004 (2015).

200 Keum, D. H. *et al.* Bandgap opening in few-layered monoclinic $MoTe_2$. *Nature Physics* **11**, 482-486, doi:10.1038/nphys3314 (2015).

201 Wang, L. *et al.* One-Dimensional Electrical Contact to a Two-Dimensional Material. *Science* **342**, 614, doi:10.1126/science.1244358 (2013).

202 Allain, A. & Kis, A. Electron and Hole Mobilities in Single-Layer WSe_2. *ACS Nano* **8**, 7180-7185, doi:10.1021/nn5021538 (2014).

203 Soule, D. E. Magnetic Field Dependence of the Hall Effect and Magnetoresistance in Graphite Single Crystals. *Physical Review* **112**, 698-707, doi:10.1103/PhysRev.112.698 (1958).

204 Augustin, J. *et al.* Electronic band structure of the layered compound Td-WTe_2. *Physical Review B* **62**, 10812-10823, doi:10.1103/PhysRevB.62.10812 (2000).

205 Tonndorf, P. *et al.* Photoluminescence emission and Raman response of monolayer MoS_2, $MoSe_2$, and WSe_2. *Opt. Express* **21**, 4908-4916 (2013).

206 Kam, K. & Parkinson, B. Detailed photocurrent spectroscopy of the semiconducting group VIB transition metal dichalcogenides. *The Journal of Physical Chemistry* **86**, 463-467 (1982).

207 Ruppert, C., Aslan, O. B. & Heinz, T. F. Optical Properties and Band Gap of Single- and Few-Layer $MoTe_2$ Crystals. *Nano Letters* **14**, 6231-6236, doi:10.1021/nl502557g (2014).

208 Yun, W. S., Han, S. W., Hong, S. C., Kim, I. G. & Lee, J. D. Thickness and strain effects on electronic structures of transition metal dichalcogenides: 2H-MX_2 semiconductors (M = Mo, W; X = S, Se, Te). *Physical Review B* **85**, 033305, doi:10.1103/PhysRevB.85.033305 (2012).

209 Coehoorn, R. *et al.* Electronic structure of $MoSe_2$, MoS_2, and WSe_2. I. Band-structure calculations and photoelectron spectroscopy. *Physical Review B* **35**, 6195-6202, doi:10.1103/PhysRevB.35.6195 (1987).

210 Wilson, J. A. & Yoffe, A. D. The transition metal dichalcogenides discussion and interpretation of the observed optical, electrical and structural properties. *Advances in Physics* **18**, 193-335, doi:10.1080/00018736900101307 (1969).

211 Lewerenz, H., Heller, A. & DiSalvo, F. Relationship between surface morphology and solar conversion efficiency of tungsten diselenide photoanodes. *Journal of the American Chemical Society* **102**, 1877-1880 (1980).

212 Coehoorn, R., Haas, C. & de Groot, R. A. Electronic structure of $MoSe_2$, MoS_2, and WSe_2. II. The nature of the optical band gaps. *Physical Review B* **35**, 6203-6206, doi:10.1103/PhysRevB.35.6203 (1987).

213 Kadantsev, E. S. & Hawrylak, P. Electronic structure of a single MoS_2 monolayer. *Solid State Communications* **152**, 909-913, doi:https://doi.org/10.1016/j.ssc.2012.02.005 (2012).

214 Wang, Q. H., Kalantar-Zadeh, K., Kis, A., Coleman, J. N. & Strano, M. S. Electronics and optoelectronics of two-dimensional transition metal dichalcogenides. *Nature Nanotechnology* **7**, 699-712, doi:10.1038/nnano.2012.193 (2012).

215 Greenaway, D. L. & Nitsche, R. Preparation and optical properties of group IV–VI_2 chalcogenides having the CdI_2 structure. *Journal of Physics and Chemistry of Solids* **26**, 1445-1458, doi:https://doi.org/10.1016/0022-3697(65)90043-0 (1965).

216 Gong, C. *et al.* Band alignment of two-dimensional transition metal

dichalcogenides: Application in tunnel field effect transistors. *Applied Physics Letters* **103**, 053513, doi:10.1063/1.4817409 (2013).

217 Frindt, R. F. The optical properties of single crystals of WSe_2 and $MoTe_2$. *Journal of Physics and Chemistry of Solids* **24**, 1107-1108, doi:https://doi.org/10.1016/0022-3697(63)90024-6 (1963).

218 Beal, A. R., Liang, W. Y. & Hughes, H. P. Kramers-Kronig analysis of the reflectivity spectra of 3R-WS_2 and 2H-WSe_2. *Journal of Physics C: Solid State Physics* **9**, 2449-2457, doi:10.1088/0022-3719/9/12/027 (1976).

219 Beal, A. R. & Hughes, H. P. Kramers-Kronig analysis of the reflectivity spectra of 2H-MoS_2, 2H-$MoSe_2$ and 2H-$MoTe_2$. *Journal of Physics C: Solid State Physics* **12**, 881-890, doi:10.1088/0022-3719/12/5/017 (1979).

220 Jäger-Waldau, A., Lux-Steiner, M. C. & Bucher, E. MoS_2, $MoSe_2$, WS_2 and WSe_2 Thin Films for Photovoltaics. *Solid State Phenomena* **37-38**, 479-484, doi:10.4028/www.scientific.net/SSP.37-38.479 (1994).

221 Bernardi, M., Palummo, M. & Grossman, J. C. Extraordinary Sunlight Absorption and One Nanometer Thick Photovoltaics Using Two-Dimensional Monolayer Materials. *Nano Letters* **13**, 3664-3670, doi:10.1021/nl401544y (2013).

222 Beal, A. R., Hughes, H. P. & Liang, W. Y. The reflectivity spectra of some group VA transition metal dichalcogenides. *Journal of Physics C: Solid State Physics* **8**, 4236-4234, doi:10.1088/0022-3719/8/24/015 (1975).

223 Nair, R. R. *et al.* Fine Structure Constant Defines Visual Transparency of Graphene. *Science* **320**, 1308, doi:10.1126/science.1156965 (2008).

224 Frindt, R. F., Yoffe, A. D. & Bowden, F. P. Physical properties of layer structures: optical properties and photoconductivity of thin crystals of molybdenum disulphide. *Proceedings of the Royal Society of London. Series A. Mathematical and Physical Sciences* **273**, 69-83, doi:10.1098/rspa.1963.0075 (1963).

225 Bertolazzi, S., Brivio, J. & Kis, A. Stretching and Breaking of Ultrathin MoS_2. *ACS Nano* **5**, 9703-9709, doi:10.1021/nn203879f (2011).

226 Miró, P., Ghorbani-Asl, M. & Heine, T. Spontaneous Ripple Formation in MoS_2 Monolayers: Electronic Structure and Transport Effects. *Advanced Materials* **25**, 5473-5475, doi:10.1002/adma.201301492 (2013).

227 Luo, S. *et al.* Formation of ripples in atomically thin MoS_2 and local strain engineering of electrostatic properties. *Nanotechnology* **26**, 105705,

doi:10.1088/0957-4484/26/10/105705 (2015).

228 Wu, W. *et al.* Piezoelectricity of single-atomic-layer MoS_2 for energy conversion and piezotronics. *Nature* **514**, 470-474, doi:10.1038/nature13792 (2014).

229 Khare, H. S. & Burris, D. L. The Effects of Environmental Water and Oxygen on the Temperature-Dependent Friction of Sputtered Molybdenum Disulfide. *Tribology Letters* **52**, 485-493, doi:10.1007/s11249-013-0233-8 (2013).

230 Kim, Y. *et al.* Anomalous Raman scattering and lattice dynamics in mono- and few-layer WTe_2. *Nanoscale* **8**, 2309-2316, doi:10.1039/C5NR06098B (2016).

231 Fernelius, N. C. Properties of gallium selenide single crystal. *Progress in Crystal Growth and Characterization of Materials* **28**, 275-353, doi:https://doi.org/10.1016/0960-8974(94)90010-8 (1994).

232 Ikari, T., Shigetomi, S. & Hashimoto, K. Crystal Structure and Raman Spectra of InSe. *physica status solidi (b)* **111**, 477-481, doi:10.1002/pssb.2221110208 (1982).

233 Plucinski, L. *et al.* Electronic band structure of GaSe (0001): Angle-resolved photoemission and ab initio theory. *Physical Review B* **68**, 125304, doi:10.1103/PhysRevB.68.125304 (2003).

234 Han, G., Chen, Z.-G., Drennan, J. & Zou, J. Indium Selenides: Structural Characteristics, Synthesis and Their Thermoelectric Performances. *Small* **10**, 2747-2765, doi:10.1002/smll.201400104 (2014).

235 Lei, S. *et al.* Evolution of the Electronic Band Structure and Efficient Photo-Detection in Atomic Layers of InSe. *ACS Nano* **8**, 1263-1272, doi:10.1021/nn405036u (2014).

236 Gürbulak, B. *et al.* Structural characterizations and optical properties of InSe and InSe:Ag semiconductors grown by Bridgman/Stockbarger technique. *Physica E: Low-dimensional Systems and Nanostructures* **64**, 106-111, doi:https://doi.org/10.1016/j.physe.2014.07.002 (2014).

237 Mudd, G. W. *et al.* Quantum confined acceptors and donors in InSe nanosheets. *Applied Physics Letters* **105**, 221909, doi:10.1063/1.4903738 (2014).

238 Late, D. J., Liu, B., Matte, H. S. S. R., Rao, C. N. R. & Dravid, V. P. Rapid Characterization of Ultrathin Layers of Chalcogenides on SiO_2/Si Substrates. *Advanced Functional Materials* **22**, 1894-1905, doi:10.1002/adfm.201102913 (2012).

239 Lei, S. *et al.* Synthesis and Photoresponse of Large GaSe Atomic Layers.

Nano Letters **13**, 2777-2781, doi:10.1021/nl4010089 (2013).

240 Zhou, Y. *et al.* Epitaxy and Photoresponse of Two-Dimensional GaSe Crystals on Flexible Transparent Mica Sheets. *ACS Nano* **8**, 1485-1490, doi:10.1021/nn405529r (2014).

241 Li, X. *et al.* Van der Waals Epitaxial Growth of Two-Dimensional Single-Crystalline GaSe Domains on Graphene. *ACS Nano* **9**, 8078-8088, doi:10.1021/acsnano.5b01943 (2015).

242 Yuan, X. *et al.* Arrayed van der Waals Vertical Heterostructures Based on 2D GaSe Grown by Molecular Beam Epitaxy. *Nano Letters* **15**, 3571-3577, doi:10.1021/acs.nanolett.5b01058 (2015).

243 Mahjouri-Samani, M. *et al.* Pulsed Laser Deposition of Photoresponsive Two-Dimensional GaSe Nanosheet Networks. *Advanced Functional Materials* **24**, 6365-6371, doi:10.1002/adfm.201401440 (2014).

244 Zhou, J. *et al.* InSe monolayer: synthesis, structure and ultra-high second-harmonic generation. *2D Materials* **5**, 025019, doi:10.1088/2053-1583/aab390 (2018).

245 Mudd, G. W. *et al.* Tuning the Bandgap of Exfoliated InSe Nanosheets by Quantum Confinement. *Advanced Materials* **25**, 5714-5718, doi:10.1002/adma.201302616 (2013).

246 Yang, Z. *et al.* Wafer-Scale Synthesis of High-Quality Semiconducting Two-Dimensional Layered InSe with Broadband Photoresponse. *ACS Nano* **11**, 4225-4236, doi:10.1021/acsnano.7b01168 (2017).

247 Petroni, E. *et al.* Liquid-Phase Exfoliated Indium–Selenide Flakes and Their Application in Hydrogen Evolution Reaction. *Small* **14**, 1800749, doi:10.1002/smll.201800749 (2018).

248 Li, Z. *et al.* High-Performance Photo-Electrochemical Photodetector Based on Liquid-Exfoliated Few-Layered InSe Nanosheets with Enhanced Stability. *Advanced Functional Materials* **28**, 1705237, doi:10.1002/adfm.201705237 (2018).

249 Fan, Y., Bauer, M., Kador, L., Allakhverdiev, K. R. & Salaev, E. Y. Photoluminescence frequency up-conversion in GaSe single crystals as studied by confocal microscopy. *Journal of Applied Physics* **91**, 1081-1086, doi:10.1063/1.1421215 (2002).

250 Hu, P., Wen, Z., Wang, L., Tan, P. & Xiao, K. Synthesis of Few-Layer GaSe Nanosheets for High Performance Photodetectors. *ACS Nano* **6**, 5988-5994,

doi:10.1021/nn300889c (2012).

251 Jung, C. S. *et al.* Red-to-Ultraviolet Emission Tuning of Two-Dimensional Gallium Sulfide/Selenide. *ACS Nano* **9**, 9585-9593, doi:10.1021/acsnano.5b04876 (2015).

252 Late, D. J. *et al.* GaS and GaSe Ultrathin Layer Transistors. *Advanced Materials* **24**, 3549-3554, doi:10.1002/adma.201201361 (2012).

253 Yin, Z. *et al.* Single-Layer MoS_2 Phototransistors. *ACS Nano* **6**, 74-80, doi:10.1021/nn2024557 (2012).

254 Li, X. *et al.* Controlled Vapor Phase Growth of Single Crystalline, Two-Dimensional GaSe Crystals with High Photoresponse. *Scientific Reports* **4**, 5497, doi:10.1038/srep05497 (2014).

255 Cao, Y. *et al.* Strong enhancement of photoresponsivity with shrinking the electrodes spacing in few layer GaSe photodetectors. *Scientific Reports* **5**, 8130, doi:10.1038/srep08130 (2015).

256 Wasala, M. *et al.* Recent advances in investigations of the electronic and optoelectronic properties of group III, IV, and V selenide based binary layered compounds. *Journal of Materials Chemistry C* **5**, 11214-11225, doi:10.1039/C7TC02866K (2017).

257 Feng, W., Zheng, W., Cao, W. & Hu, P. Back Gated Multilayer InSe Transistors with Enhanced Carrier Mobilities via the Suppression of Carrier Scattering from a Dielectric Interface. *Advanced Materials* **26**, 6587-6593, doi:10.1002/adma.201402427 (2014).

258 Bandurin, D. A. *et al.* High electron mobility, quantum Hall effect and anomalous optical response in atomically thin InSe. *Nature Nanotechnology* **12**, 223-227, doi:10.1038/nnano.2016.242 (2017).

259 Lei, S. *et al.* An Atomically Layered InSe Avalanche Photodetector. *Nano Letters* **15**, 3048-3055, doi:10.1021/acs.nanolett.5b00016 (2015).

260 Tamalampudi, S. R. *et al.* High Performance and Bendable Few-Layered InSe Photodetectors with Broad Spectral Response. *Nano Letters* **14**, 2800-2806, doi:10.1021/nl500817g (2014).

261 Wells, S. A. *et al.* Suppressing Ambient Degradation of Exfoliated InSe Nanosheet Devices via Seeded Atomic Layer Deposition Encapsulation. *Nano Letters* **18**, 7876-7882, doi:10.1021/acs.nanolett.8b03689 (2018).

262 Feng, W. *et al.* Ultrahigh photo-responsivity and detectivity in multilayer InSe nanosheets phototransistors with broadband response. *Journal of Materials*

Chemistry C **3**, 7022-7028, doi:10.1039/C5TC01208B (2015).

263 Luo, W. *et al.* Gate Tuning of High-Performance InSe-Based Photodetectors Using Graphene Electrodes. *Advanced Optical Materials* **3**, 1418-1423, doi:10.1002/adom.201500190 (2015).

264 Yang, H.-W. *et al.* Ultraefficient Ultraviolet and Visible Light Sensing and Ohmic Contacts in High-Mobility InSe Nanoflake Photodetectors Fabricated by the Focused Ion Beam Technique. *ACS Applied Materials & Interfaces* **10**, 5740-5749, doi:10.1021/acsami.7b15106 (2018).

265 Mudd, G. W. *et al.* High Broad-Band Photoresponsivity of Mechanically Formed InSe–Graphene van der Waals Heterostructures. *Advanced Materials* **27**, 3760-3766, doi:10.1002/adma.201500889 (2015).

266 Eng, P. C., Song, S. & Ping, B. State-of-the-art photodetectors for optoelectronic integration at telecommunication wavelength. *Nanophotonics* **4**, 277-302 (2015).

267 Feng, W., Zheng, W., Chen, X., Liu, G. & Hu, P. Gate Modulation of Threshold Voltage Instability in Multilayer InSe Field Effect Transistors. *ACS Applied Materials & Interfaces* **7**, 26691-26695, doi:10.1021/acsami.5b08635 (2015).

268 Feng, W., Zhou, X., Tian, W. Q., Zheng, W. & Hu, P. Performance improvement of multilayer InSe transistors with optimized metal contacts. *Physical Chemistry Chemical Physics* **17**, 3653-3658, doi:10.1039/C4CP04968C (2015).

269 Chen, Z., Biscaras, J. & Shukla, A. A high performance graphene/few-layer InSe photodetector. *Nanoscale* **7**, 5981-5986, doi:10.1039/C5NR00400D (2015).

270 Karvonen, L. *et al.* Investigation of Second- and Third-Harmonic Generation in Few-Layer Gallium Selenide by Multiphoton Microscopy. *Scientific Reports* **5**, 10334, doi:10.1038/srep10334 (2015).

271 Jie, W. *et al.* Layer-dependent nonlinear optical properties and stability of non-centrosymmetric modification in few-layer GaSe sheets. *Angewandte Chemie* **127**, 1201-1205 (2015).

272 Zhou, X. *et al.* Strong Second-Harmonic Generation in Atomic Layered GaSe. *Journal of the American Chemical Society* **137**, 7994-7997, doi:10.1021/jacs.5b04305 (2015).

273 Hao, Q. *et al.* Phase Identification and Strong Second Harmonic Generation in

Pure ε-InSe and Its Alloys. *Nano Letters* **19**, 2634-2640, doi:10.1021/acs.nanolett.9b00487 (2019).

274 Wang, T. *et al.* High-quality GaSe single crystal grown by the Bridgman method. *Materials* **11**, 186 (2018).

275 Singh, N. B. *et al.* Growth and characterization of gallium selenide crystals for far-infrared conversion applications. *Journal of Crystal Growth* **163**, 398-402, doi:https://doi.org/10.1016/0022-0248(95)00983-3 (1996).

276 Kokh, K. A., Andreev, Y. M., Svetlichnyi, V. A., Lanskii, G. V. & Kokh, A. E. Growth of GaSe and GaS single crystals. *Crystal Research and Technology* **46**, 327-330, doi:10.1002/crat.201100055 (2011).

277 Ni, Y. *et al.* Growth and quality of gallium selenide (GaSe) crystals. *Journal of Crystal Growth* **381**, 10-14, doi:https://doi.org/10.1016/j.jcrysgro.2013.06.030 (2013).

278 Kolesnikov, N. N., Borisenko, E. B., Borisenko, D. N. & Gartman, V. K. Influence of growth conditions on microstructure and properties of GaSe crystals. *Journal of Crystal Growth* **300**, 294-298, doi:https://doi.org/10.1016/j.jcrysgro.2007.01.001 (2007).

279 Xiong, X. *et al.* One-step synthesis of p-type GaSe nanoribbons and their excellent performance in photodetectors and phototransistors. *Journal of Materials Chemistry C* **4**, 7817-7823, doi:10.1039/C6TC02700H (2016).

280 Bereznaya, S. A. *et al.* Formation of native oxide crystallites on GaSe (001) surface. *Infrared Physics & Technology* **76**, 126-130, doi:https://doi.org/10.1016/j.infrared.2016.02.002 (2016).

281 Dai, M. *et al.* A Dual-Band Multilayer InSe Self-Powered Photodetector with High Performance Induced by Surface Plasmon Resonance and Asymmetric Schottky Junction. *ACS Nano* **12**, 8739-8747, doi:10.1021/acsnano.8b04931 (2018).

282 Liu, G., Chen, K. & Li, J. Combustion synthesis of InSe, In_2Se_3, and GaSe. *Journal of the American Ceramic Society* **101**, 36-39, doi:10.1111/jace.15223 (2018).

283 Song, C. *et al.* Largely Tunable Band Structures of Few-Layer InSe by Uniaxial Strain. *ACS Applied Materials & Interfaces* **10**, 3994-4000, doi:10.1021/acsami.7b17247 (2018).

284 Wu, M. *et al.* Crystal structure and optical performance in bulk γ-InSe single crystals. *AIP Advances* **9**, 025013, doi:10.1063/1.5086492 (2019).

285 Malard, L. M., Alencar, T. V., Barboza, A. P. M., Mak, K. F. & de Paula, A. M. Observation of intense second harmonic generation from MoS_2 atomic crystals. *Physical Review B* **87**, 201401, doi:10.1103/PhysRevB.87.201401 (2013).

286 Li, D. *et al.* Multimodal Nonlinear Optical Imaging of MoS_2 and MoS_2-Based van der Waals Heterostructures. *ACS Nano* **10**, 3766-3775, doi:10.1021/acsnano.6b00371 (2016).

287 Brebner, J., Steiner, T. & Thewalt, M. Time-resolved photoluminescence study of InSe. *SSCom* **56**, 929-931 (1985).

288 Paraskevopoulos, K. M., Julien, C. & Balkanski, M. Fine Structure in the Free Exciton Region of the Emission Spectrum of γ-InSe. *physica status solidi (b)* **143**, 741-748, doi:10.1002/pssb.2221430234 (1987).

289 Imai, K. Excitonic photoluminescence properties of InSe. *Journal of Luminescence* **43**, 121-124, doi:https://doi.org/10.1016/0022-2313(89)90034-3 (1989).

290 Ho, C.-H. & Chu, Y.-J. Bending Photoluminescence and Surface Photovoltaic Effect on Multilayer InSe 2D Microplate Crystals. *Advanced Optical Materials* **3**, 1750-1758, doi:10.1002/adom.201500390 (2015).

291 Shigetomi, S., Ikari, T., Koga, Y. & Shigetomi, S. Annealing behavior of electrical properties of n-InSe single crystals. *Physica Status Solidi A, Applied Research* **86**, K69-K72 (1984).

292 Ishii, T. High quality single crystal growth of layered InSe Semiconductor by Bridgman Technique. *Journal of Crystal Growth* **89**, 459-462, doi:https://doi.org/10.1016/0022-0248(88)90206-0 (1988).

293 Giessibl, F. J. Advances in atomic force microscopy. *Reviews of Modern Physics* **75**, 949-983, doi:10.1103/RevModPhys.75.949 (2003).

294 Casiraghi, C. *et al.* Rayleigh Imaging of Graphene and Graphene Layers. *Nano Letters* **7**, 2711-2717, doi:10.1021/nl071168m (2007).

295 Li, X.-L. *et al.* Layer number identification of intrinsic and defective multilayered graphenes up to 100 layers by the Raman mode intensity from substrates. *Nanoscale* **7**, 8135-8141, doi:10.1039/C5NR01514F (2015).

296 Nemes-Incze, P., Osváth, Z., Kamarás, K. & Biró, L. P. Anomalies in thickness measurements of graphene and few layer graphite crystals by tapping mode atomic force microscopy. *Carbon* **46**, 1435-1442, doi:https://doi.org/10.1016/j.carbon.2008.06.022 (2008).

297 Shearer, C. J., Slattery, A. D., Stapleton, A. J., Shapter, J. G. & Gibson, C. T.

Accurate thickness measurement of graphene. *Nanotechnology* **27**, 125704, doi:10.1088/0957-4484/27/12/125704 (2016).

298 Zheng, T. *et al.* Layer-number dependent and structural defect related optical properties of InSe. *RSC Advances* **7**, 54964-54968, doi:10.1039/C7RA09370E (2017).

299 Chen, X. *et al.* How Universal Is the Wetting Aging in 2D Materials. *Nano Letters* **20**, 5670-5677, doi:10.1021/acs.nanolett.0c00855 (2020).

300 Niu, Y. *et al.* Thickness-dependent differential reflectance spectra of monolayer and few-layer MoS_2, $MoSe_2$, WS_2 and WSe_2. *Nanomaterials* **8**, 725 (2018).

301 Li, H. *et al.* Rapid and Reliable Thickness Identification of Two-Dimensional Nanosheets Using Optical Microscopy. *ACS Nano* **7**, 10344-10353, doi:10.1021/nn4047474 (2013).

302 Papadopoulos, N. *et al.* Large birefringence and linear dichroism in TiS_3 nanosheets. *Nanoscale* **10**, 12424-12429, doi:10.1039/C8NR03616K (2018).

303 Gant, P. *et al.* Optical contrast and refractive index of natural van der Waals heterostructure nanosheets of franckeite. *Beilstein journal of nanotechnology* **8**, 2357-2362 (2017).

304 Rubio-Bollinger, G. *et al.* Enhanced visibility of MoS_2, $MoSe_2$, WSe_2 and black-phosphorus: making optical identification of 2D semiconductors easier. *Electronics* **4**, 847-856 (2015).

305 Castellanos-Gomez, A. *et al.* Atomically Thin Mica Flakes and Their Application as Ultrathin Insulating Substrates for Graphene. *Small* **7**, 2491-2497, doi:10.1002/smll.201100733 (2011).

306 Hecht, J. *City of light: the story of fiber optics*. (Oxford University Press on Demand, 2004).

307 Anders, H. Thin films in optics. *tfo* (1967).

308 Manjon, F., Van der Vijver, Y., Segura, A. & Munoz, V. Pressure dependence of the refractive index in InSe. *Semiconductor science and technology* **15**, 806 (2000).

309 Schinke, C. *et al.* Uncertainty analysis for the coefficient of band-to-band absorption of crystalline silicon. *AIP Advances* **5**, 067168 (2015).

310 Malitson, I. H. Interspecimen comparison of the refractive index of fused silica. *Josa* **55**, 1205-1209 (1965).

311 Bandurin, D. A. *et al.* High electron mobility, quantum Hall effect and

anomalous optical response in atomically thin InSe. *Nature nanotechnology* **12**, 223-227 (2017).

312 Seo, Y. & Jhe, W. Atomic force microscopy and spectroscopy. *Reports on Progress in Physics* **71**, 016101, doi:10.1088/0034-4885/71/1/016101 (2007).

313 Long, D. A. Raman spectroscopy. *New York*, 1-12 (1977).

314 Frisenda, R. *et al.* Recent progress in the assembly of nanodevices and van der Waals heterostructures by deterministic placement of 2D materials. *Chemical Society Reviews* **47**, 53-68, doi:10.1039/C7CS00556C (2018).

315 Zomer, P. J., Dash, S. P., Tombros, N. & van Wees, B. J. A transfer technique for high mobility graphene devices on commercially available hexagonal boron nitride. *Applied Physics Letters* **99**, 232104, doi:10.1063/1.3665405 (2011).

316 Zomer, P. J., Guimarães, M. H. D., Brant, J. C., Tombros, N. & van Wees, B. J. Fast pick up technique for high quality heterostructures of bilayer graphene and hexagonal boron nitride. *Applied Physics Letters* **105**, 013101, doi:10.1063/1.4886096 (2014).

317 Pizzocchero, F. *et al.* The hot pick-up technique for batch assembly of van der Waals heterostructures. *Nature Communications* **7**, 11894, doi:10.1038/ncomms11894 (2016).

318 Castellanos-Gomez, A. *et al.* Deterministic transfer of two-dimensional materials by all-dry viscoelastic stamping. *2D Materials* **1**, 011002, doi:10.1088/2053-1583/1/1/011002 (2014).

319 Zhao, Q., Wang, T., Ryu, Y. K., Frisenda, R. & Castellanos-Gomez, A. An inexpensive system for the deterministic transfer of 2D materials. *Journal of Physics: Materials* **3**, 016001, doi:10.1088/2515-7639/ab6a72 (2020).

320 Zhao, Q. *et al.* A system to test 2D optoelectronic devices in high vacuum. *Journal of Physics: Materials* **3**, 036001, doi:10.1088/2515-7639/ab8781 (2020).

321 Buscema, M. *et al.* Photocurrent generation with two-dimensional van der Waals semiconductors. *Chemical Society Reviews* **44**, 3691-3718, doi:10.1039/C5CS00106D (2015).

322 Nouchi, R. Extraction of the Schottky parameters in metal-semiconductor-metal diodes from a single current-voltage measurement. *Journal of Applied Physics* **116**, 184505, doi:10.1063/1.4901467 (2014).

323 Rhoderick, E. H. Metal-semiconductor contacts. *IEE Proceedings I -*

Solid-State and Electron Devices **129**, 1, doi:10.1049/ip-i-1.1982.0001 (1982).

324 Ahn, J. *et al.* Transition metal dichalcogenide heterojunction PN diode toward ultimate photovoltaic benefits. *2D Materials* **3**, 045011, doi:10.1088/2053-1583/3/4/045011 (2016).

325 Furchi, M. M., Polyushkin, D. K., Pospischil, A. & Mueller, T. Mechanisms of Photoconductivity in Atomically Thin MoS_2. *Nano Letters* **14**, 6165-6170, doi:10.1021/nl502339q (2014).

326 Graham, R. & Yu, D. Scanning photocurrent microscopy in semiconductor nanostructures. *Modern Physics Letters B* **27**, 1330018, doi:10.1142/S0217984913300184 (2013).

327 Reuter, C. *et al.* A Versatile Scanning Photocurrent Mapping System to Characterize Optoelectronic Devices based on 2D Materials. *Small Methods* **1**, 1700119, doi:10.1002/smtd.201700119 (2017).

328 Zhao, Q. *et al.* Toward Air Stability of Thin GaSe Devices: Avoiding Environmental and Laser-Induced Degradation by Encapsulation. *Advanced Functional Materials* **28**, 1805304, doi:10.1002/adfm.201805304 (2018).

329 Chhowalla, M. *et al.* The chemistry of two-dimensional layered transition metal dichalcogenide nanosheets. *Nature Chemistry* **5**, 263-275, doi:10.1038/nchem.1589 (2013).

330 Boukhvalov, D. W. & Katsnelson, M. I. Chemical Functionalization of Graphene with Defects. *Nano Letters* **8**, 4373-4379, doi:10.1021/nl802234n (2008).

331 Island, J. O., Steele, G. A., Zant, H. S. J. v. d. & Castellanos-Gomez, A. Environmental instability of few-layer black phosphorus. *2D Materials* **2**, 011002, doi:10.1088/2053-1583/2/1/011002 (2015).

332 Favron, A. *et al.* Photooxidation and quantum confinement effects in exfoliated black phosphorus. *Nature Materials* **14**, 826-832, doi:10.1038/nmat4299 (2015).

333 Wood, J. D. *et al.* Effective Passivation of Exfoliated Black Phosphorus Transistors against Ambient Degradation. *Nano Letters* **14**, 6964-6970, doi:10.1021/nl5032293 (2014).

334 Xia, F., Wang, H. & Jia, Y. Rediscovering black phosphorus as an anisotropic layered material for optoelectronics and electronics. *Nature Communications* **5**, 4458, doi:10.1038/ncomms5458 (2014).

335 Qiao, J., Kong, X., Hu, Z.-X., Yang, F. & Ji, W. High-mobility transport

anisotropy and linear dichroism in few-layer black phosphorus. *Nature Communications* **5**, 4475, doi:10.1038/ncomms5475 (2014).

336 Yang, S. *et al.* Environmental stability of 2D anisotropic tellurium containing nanomaterials: anisotropic to isotropic transition. *Nanoscale* **9**, 12288-12294, doi:10.1039/C7NR02397A (2017).

337 Chen, B. *et al.* Environmental Changes in $MoTe_2$ Excitonic Dynamics by Defects-Activated Molecular Interaction. *ACS Nano* **9**, 5326-5332, doi:10.1021/acsnano.5b00985 (2015).

338 Wang, G., Pandey, R. & Karna, S. P. Physics and chemistry of oxidation of two-dimensional nanomaterials by molecular oxygen. *WIREs Computational Molecular Science* **7**, e1280, doi:10.1002/wcms.1280 (2017).

339 Gao, J. *et al.* Aging of Transition Metal Dichalcogenide Monolayers. *ACS Nano* **10**, 2628-2635, doi:10.1021/acsnano.5b07677 (2016).

340 Bergeron, A., Ibrahim, J., Leonelli, R. & Francoeur, S. Oxidation dynamics of ultrathin GaSe probed through Raman spectroscopy. *Applied Physics Letters* **110**, 241901, doi:10.1063/1.4986189 (2017).

341 Beechem, T. E. *et al.* Oxidation of ultrathin GaSe. *Applied Physics Letters* **107**, 173103, doi:10.1063/1.4934592 (2015).

342 Rahaman, M., Rodriguez, R. D., Monecke, M., Lopez-Rivera, S. A. & Zahn, D. R. T. GaSe oxidation in air: from bulk to monolayers. *Semiconductor Science and Technology* **32**, 105004, doi:10.1088/1361-6641/aa8441 (2017).

343 Pozo-Zamudio, D. *et al.* Photoluminescence and Raman investigation of stability of InSe and GaSe thin films. *arXiv preprint arXiv:1506.05619* (2015).

344 Andres-Penares, D., Cros, A., Martínez-Pastor, J. P. & Sánchez-Royo, J. F. Quantum size confinement in gallium selenide nanosheets: band gap tunability versus stability limitation. *Nanotechnology* **28**, 175701, doi:10.1088/1361-6528/aa669e (2017).

345 Susoma, J., Lahtinen, J., Kim, M., Riikonen, J. & Lipsanen, H. Crystal quality of two-dimensional gallium telluride and gallium selenide using Raman fingerprint. *AIP Advances* **7**, 015014, doi:10.1063/1.4973918 (2017).

346 Shi, L., Li, Q., Ouyang, Y. & Wang, J. Effect of illumination and Se vacancies on fast oxidation of ultrathin gallium selenide. *Nanoscale* **10**, 12180-12186, doi:10.1039/C8NR01533C (2018).

347 Currie, M. *et al.* Quantifying pulsed laser induced damage to graphene. *Applied Physics Letters* **99**, 211909, doi:10.1063/1.3663875 (2011).

348 Tonndorf, P. *et al.* Single-photon emitters in GaSe. *2D Materials* **4**, 021010, doi:10.1088/2053-1583/aa525b (2017).

349 Haigh, S. J. *et al.* Cross-sectional imaging of individual layers and buried interfaces of graphene-based heterostructures and superlattices. *Nature Materials* **11**, 764-767, doi:10.1038/nmat3386 (2012).

350 Kretinin, A. V. *et al.* Electronic Properties of Graphene Encapsulated with Different Two-Dimensional Atomic Crystals. *Nano Letters* **14**, 3270-3276, doi:10.1021/nl5006542 (2014).

351 De Sanctis, A., Amit, I., Hepplestone, S. P., Craciun, M. F. & Russo, S. Strain-engineered inverse charge-funnelling in layered semiconductors. *Nature Communications* **9**, 1652, doi:10.1038/s41467-018-04099-7 (2018).

352 Hoff, R. M., Irwin, J. C. & Lieth, R. M. A. Raman Scattering in GaSe. *Canadian Journal of Physics* **53**, 1606-1614, doi:10.1139/p75-203 (1975).

353 Jandl, S., Brebner, J. L. & Powell, B. M. Lattice dynamics of GaSe. *Physical Review B* **13**, 686-693, doi:10.1103/PhysRevB.13.686 (1976).

354 Wieting, T. J. & Verble, J. L. Interlayer Bonding and the Lattice Vibrations of beta-GaSe. *Physical Review B* **5**, 1473-1479, doi:10.1103/PhysRevB.5.1473 (1972).

355 Finkman, E., Tauc, J., Kershaw, R. & Wold, A. Lattice dynamics of tetrahedrally bonded semiconductors containing ordered vacant sites. *Physical Review B* **11**, 3785-3794, doi:10.1103/PhysRevB.11.3785 (1975).

356 Yamada, A., Kojima, N., Takahashi, K., Okamoto, T. & Konagai, M. Raman Study of Epitaxial Ga_2Se_3 Films Grown by Molecular Beam Epitaxy. *Japanese Journal of Applied Physics* **31**, L186-L188, doi:10.1143/jjap.31.l186 (1992).

357 Onuma, T. *et al.* Polarized Raman spectra in β-Ga_2O_3 single crystals. *Journal of Crystal Growth* **401**, 330-333, doi:https://doi.org/10.1016/j.jcrysgro.2013.12.061 (2014).

358 Carroll, P. J. & Lannin, J. S. Raman Scattering of amorphous selenium films. *Solid State Communications* **40**, 81-84, doi:https://doi.org/10.1016/0038-1098(81)90716-X (1981).

359 Baganich, A. A., Mikla, V. I., Semak, D. G., Sokolov, A. P. & Shebanin, A. P. Raman Scattering in Amorphous Selenium Molecular Structure and Photoinduced Crystallization. *physica status solidi (b)* **166**, 297-302, doi:10.1002/pssb.2221660133 (1991).

360 Chen, G. & Hui, P. Thermal conductivities of evaporated gold films on silicon and glass. *Applied Physics Letters* **74**, 2942-2944, doi:10.1063/1.123973 (1999).

361 Yamane, T., Nagai, N., Katayama, S.-i. & Todoki, M. Measurement of thermal conductivity of silicon dioxide thin films using a 3ω method. *Journal of Applied Physics* **91**, 9772-9776, doi:10.1063/1.1481958 (2002).

362 Ishida, K. & Tanaka, K. Photoinduced anisotropic crystallization of amorphous Se. *Physical Review B* **56**, 206-209, doi:10.1103/PhysRevB.56.206 (1997).

363 Poborchii, V. V., Kolobov, A. V. & Tanaka, K. An in situ Raman study of polarization-dependent photocrystallization in amorphous selenium films. *Applied Physics Letters* **72**, 1167-1169, doi:10.1063/1.121002 (1998).

364 Huang, W. *et al.* Controlled Synthesis of Ultrathin 2D β-In_2S_3 with Broadband Photoresponse by Chemical Vapor Deposition. *Advanced Functional Materials* **27**, 1702448, doi:10.1002/adfm.201702448 (2017).

365 Zhou, X. *et al.* Ultrathin 2D $GeSe_2$ Rhombic Flakes with High Anisotropy Realized by Van der Waals Epitaxy. *Advanced Functional Materials* **27**, 1703858, doi:10.1002/adfm.201703858 (2017).

366 Shi, L. *et al.* Oxidation Mechanism and Protection Strategy of Ultrathin Indium Selenide: Insight from Theory. *The Journal of Physical Chemistry Letters* **8**, 4368-4373, doi:10.1021/acs.jpclett.7b02059 (2017).

367 Kong, W.-Y. *et al.* Graphene-β-Ga_2O_3 Heterojunction for Highly Sensitive Deep UV Photodetector Application. *Advanced Materials* **28**, 10725-10731, doi:10.1002/adma.201604049 (2016).

368 Li, L. *et al.* Few-Layered PtS_2 Phototransistor on h-BN with High Gain. *Advanced Functional Materials* **27**, 1701011, doi:10.1002/adfm.201701011 (2017).

369 Rose, A. Recombination Processes in Insulators and Semiconductors. *Physical Review* **97**, 322-333, doi:10.1103/PhysRev.97.322 (1955).

370 Zhao, Q. *et al.* The role of traps in the photocurrent generation mechanism in thin InSe photodetectors. *Materials Horizons* **7**, 252-262, doi:10.1039/C9MH01020C (2020).

371 Qiu, H. *et al.* Hopping transport through defect-induced localized states in molybdenum disulphide. *Nature Communications* **4**, 2642, doi:10.1038/ncomms3642 (2013).

372 Park, W. *et al.* Oxygen environmental and passivation effects on molybdenum disulfide field effect transistors. *Nanotechnology* **24**, 095202, doi:10.1088/0957-4484/24/9/095202 (2013).

373 Fuhrer, M. S. & Hone, J. Measurement of mobility in dual-gated MoS_2 transistors. *Nature Nanotechnology* **8**, 146-147, doi:10.1038/nnano.2013.30 (2013).

374 Chhowalla, M., Jena, D. & Zhang, H. Two-dimensional semiconductors for transistors. *Nature Reviews Materials* **1**, 16052, doi:10.1038/natrevmats.2016.52 (2016).

375 Wang, H. *et al.* Origin of n-type conductivity in two-dimensional InSe: In atoms from surface adsorption and van der Waals gap. *Physica E: Low-dimensional Systems and Nanostructures* **98**, 66-73, doi:https://doi.org/10.1016/j.physe.2017.12.028 (2018).

376 Xiao, K. J., Carvalho, A. & Castro Neto, A. H. Defects and oxidation resilience in InSe. *Physical Review B* **96**, 054112, doi:10.1103/PhysRevB.96.054112 (2017).

377 Liu, Y., Stradins, P. & Wei, S. H. Air Passivation of Chalcogen Vacancies in Two-Dimensional Semiconductors. *Angewandte Chemie* **128**, 977-980 (2016).

378 Ma, D. *et al.* The role of the intrinsic Se and In vacancies in the interaction of O_2 and H_2O molecules with the InSe monolayer. *Applied Surface Science* **434**, 215-227, doi:https://doi.org/10.1016/j.apsusc.2017.10.204 (2018).

379 Hopkinson, D. G. *et al.* Formation and Healing of Defects in Atomically Thin GaSe and InSe. *ACS Nano* **13**, 5112-5123, doi:10.1021/acsnano.8b08253 (2019).

380 Wei, X., Dong, C., Xu, A., Li, X. & Macdonald, D. D. Oxygen-induced degradation of the electronic properties of thin-layer InSe. *Physical Chemistry Chemical Physics* **20**, 2238-2250, doi:10.1039/C7CP07446H (2018).

381 Ho, P.-H. *et al.* High-Mobility InSe Transistors: The Role of Surface Oxides. *ACS Nano* **11**, 7362-7370, doi:10.1021/acsnano.7b03531 (2017).

382 Huang, Y.-T. *et al.* High-Performance InSe Transistors with Ohmic Contact Enabled by Nonrectifying Barrier-Type Indium Electrodes. *ACS Applied Materials & Interfaces* **10**, 33450-33456, doi:10.1021/acsami.8b10576 (2018).

383 Chang, Y.-R. *et al.* Surface Oxidation Doping to Enhance Photogenerated Carrier Separation Efficiency for Ultrahigh Gain Indium Selenide Photodetector. *ACS Photonics* **4**, 2930-2936,

doi:10.1021/acsphotonics.7b01030 (2017).

384 Sucharitakul, S. *et al.* Intrinsic Electron Mobility Exceeding 10^3 $cm^2/(V s)$ in Multilayer InSe FETs. *Nano Letters* **15**, 3815-3819, doi:10.1021/acs.nanolett.5b00493 (2015).

385 Li, M. *et al.* High Mobilities in Layered InSe Transistors with Indium-Encapsulation-Induced Surface Charge Doping. *Advanced Materials* **30**, 1803690, doi:10.1002/adma.201803690 (2018).

386 Ayari, A., Cobas, E., Ogundadegbe, O. & Fuhrer, M. S. Realization and electrical characterization of ultrathin crystals of layered transition-metal dichalcogenides. *Journal of Applied Physics* **101**, 014507, doi:10.1063/1.2407388 (2007).

387 Choi, W. *et al.* High-Detectivity Multilayer MoS_2 Phototransistors with Spectral Response from Ultraviolet to Infrared. *Advanced Materials* **24**, 5832-5836, doi:10.1002/adma.201201909 (2012).

388 Choi, M. S. *et al.* Lateral MoS_2 p–n Junction Formed by Chemical Doping for Use in High-Performance Optoelectronics. *ACS Nano* **8**, 9332-9340, doi:10.1021/nn503284n (2014).

389 Fang, Y., Armin, A., Meredith, P. & Huang, J. Accurate characterization of next-generation thin-film photodetectors. *Nature Photonics* **13**, 1-4, doi:10.1038/s41566-018-0288-z (2019).

390 Huo, N. & Konstantatos, G. Recent Progress and Future Prospects of 2D-Based Photodetectors. *Advanced Materials* **30**, 1801164, doi:10.1002/adma.201801164 (2018).

391 Lopez-Sanchez, O., Lembke, D., Kayci, M., Radenovic, A. & Kis, A. Ultrasensitive photodetectors based on monolayer MoS_2. *Nature Nanotechnology* **8**, 497-501, doi:10.1038/nnano.2013.100 (2013).

392 Jin, H. *et al.* Ohmic contact in monolayer InSe-metal interface. *2D Materials* **4**, 025116, doi:10.1088/2053-1583/aa75eb (2017).

393 Shi, B. *et al.* n-Type Ohmic contact and p-type Schottky contact of monolayer InSe transistors. *Physical Chemistry Chemical Physics* **20**, 24641-24651, doi:10.1039/C8CP04615H (2018).

394 Kistanov, A. A., Cai, Y., Zhou, K., Dmitriev, S. V. & Zhang, Y.-W. Atomic-scale mechanisms of defect- and light-induced oxidation and degradation of InSe. *Journal of Materials Chemistry C* **6**, 518-525, doi:10.1039/C7TC04738J (2018).

395 Schulman, D. S., Arnold, A. J. & Das, S. Contact engineering for 2D materials and devices. *Chemical Society Reviews* **47**, 3037-3058, doi:10.1039/C7CS00828G (2018).

396 Liu, Y. *et al.* Approaching the Schottky–Mott limit in van der Waals metal–semiconductor junctions. *Nature* **557**, 696-700, doi:10.1038/s41586-018-0129-8 (2018).

397 Politano, A. *et al.* The influence of chemical reactivity of surface defects on ambient-stable InSe-based nanodevices. *Nanoscale* **8**, 8474-8479, doi:10.1039/C6NR01262K (2016).

398 Schottky, W. Zur halbleitertheorie der sperrschicht-und spitzengleichrichter. *Zeitschrift für Physik* **113**, 367-414 (1939).

399 Mott, N. F. The theory of crystal rectifiers. *Proceedings of the Royal Society of London. Series A. Mathematical and Physical Sciences* **171**, 27-38, doi:10.1098/rspa.1939.0051 (1939).

400 Bardeen, J. Surface States and Rectification at a Metal-SemiConductor Contact. *Physical Review* **71**, 717-727, doi:10.1103/PhysRev.71.717 (1947).

401 Cowley, A. M. & Sze, S. M. Surface States and Barrier Height of Metal-Semiconductor Systems. *Journal of Applied Physics* **36**, 3212-3220, doi:10.1063/1.1702952 (1965).

402 Saidi, W. A. Influence of strain and metal thickness on metal-MoS_2 contacts. *The Journal of Chemical Physics* **141**, 094707, doi:10.1063/1.4893875 (2014).

403 Tung, R. T. Chemical Bonding and Fermi Level Pinning at Metal-Semiconductor Interfaces. *Physical Review Letters* **84**, 6078-6081, doi:10.1103/PhysRevLett.84.6078 (2000).

404 Hasegawa, H. & Sawada, T. On the electrical properties of compound semiconductor interfaces in metal/insulator/semiconductor structures and the possible origin of interface states. *Thin Solid Films* **103**, 119-140, doi:https://doi.org/10.1016/0040-6090(83)90430-3 (1983).

405 Zan, R. *et al.* Control of Radiation Damage in MoS_2 by Graphene Encapsulation. *ACS Nano* **7**, 10167-10174, doi:10.1021/nn4044035 (2013).

406 Heine, V. Theory of Surface States. *Physical Review* **138**, A1689-A1696, doi:10.1103/PhysRev.138.A1689 (1965).

407 Jung, Y. *et al.* Transferred via contacts as a platform for ideal two-dimensional transistors. *Nature Electronics* **2**, 187-194, doi:10.1038/s41928-019-0245-y (2019).

408 Zhao, Q., Jie, W., Wang, T., Castellanos-Gomez, A. & Frisenda, R. InSe Schottky Diodes Based on Van Der Waals Contacts. *Advanced Functional Materials* **30**, 2001307, doi:10.1002/adfm.202001307 (2020).

409 Yu, Y.-J. *et al.* Tuning the Graphene Work Function by Electric Field Effect. *Nano Letters* **9**, 3430-3434, doi:10.1021/nl901572a (2009).

410 Rut'kov, E. V., Afanas'eva, E. Y. & Gall, N. R. Graphene and graphite work function depending on layer number on Re. *Diamond and Related Materials* **101**, 107576, doi:https://doi.org/10.1016/j.diamond.2019.107576 (2020).

411 Mamy, R., Zaoui, X., Barrau, J. & Chevy, A. Au/InSe Schottky barrier height determination. *Revue de physique appliqu ée* **25**, 947-950 (1990).

412 Di Bartolomeo, A. *et al.* A WSe_2 vertical field emission transistor. *Nanoscale* **11**, 1538-1548, doi:10.1039/C8NR09068H (2019).

413 Di Bartolomeo, A. *et al.* Asymmetric Schottky Contacts in Bilayer MoS_2 Field Effect Transistors. *Advanced Functional Materials* **28**, 1800657, doi:10.1002/adfm.201800657 (2018).

414 Luongo, G., Di Bartolomeo, A., Giubileo, F., Chavarin, C. A. & Wenger, C. Electronic properties of graphene/p-silicon Schottky junction. *Journal of Physics D: Applied Physics* **51**, 255305, doi:10.1088/1361-6463/aac562 (2018).

415 Di Bartolomeo, A. Graphene Schottky diodes: An experimental review of the rectifying graphene/semiconductor heterojunction. *Physics Reports* **606**, 1-58, doi:https://doi.org/10.1016/j.physrep.2015.10.003 (2016).

416 Tress, W. *et al.* Interpretation and evolution of open-circuit voltage, recombination, ideality factor and subgap defect states during reversible light-soaking and irreversible degradation of perovskite solar cells. *Energy & Environmental Science* **11**, 151-165, doi:10.1039/C7EE02415K (2018).

417 Joung, D., Chunder, A., Zhai, L. & Khondaker, S. I. Space charge limited conduction with exponential trap distribution in reduced graphene oxide sheets. *Applied Physics Letters* **97**, 093105, doi:10.1063/1.3484956 (2010).

418 Mahvash, F., Paradis, E., Drouin, D., Szkopek, T. & Siaj, M. Space-Charge Limited Transport in Large-Area Monolayer Hexagonal Boron Nitride. *Nano Letters* **15**, 2263-2268, doi:10.1021/nl504197c (2015).

419 Di Bartolomeo, A. *et al.* Tunable Schottky barrier and high responsivity in graphene/Si-nanotip optoelectronic device. *2D Materials* **4**, 015024, doi:10.1088/2053-1583/4/1/015024 (2016).

420 Das Sarma, S., Adam, S., Hwang, E. H. & Rossi, E. Electronic transport in two-dimensional graphene. *Reviews of Modern Physics* **83**, 407-470, doi:10.1103/RevModPhys.83.407 (2011).

421 Xiao, R., Hou, Y., Law, M. & Yu, D. On the Use of Photocurrent Imaging To Determine Carrier Diffusion Lengths in Nanostructured Thin-Film Field-Effect Transistors. *The Journal of Physical Chemistry C* **122**, 18356-18364, doi:10.1021/acs.jpcc.8b06734 (2018).

422 Mott, N. Proc. Roy. Soc. *London, Ser. A* **171**, 27 (1939).

423 Lang, O., Klein, A., Pettenkofer, C., Jaegermann, W. & Chevy, A. Band lineup of lattice mismatched InSe/GaSe quantum well structures prepared by van der Waals epitaxy: Absence of interfacial dipoles. *Journal of Applied Physics* **80**, 3817-3821, doi:10.1063/1.363335 (1996).

424 Hughes, H. P. & Starnberg, H. *Electron spectroscopies applied to low-dimensional structures*. Vol. 24 (Springer Science & Business Media, 2001).

425 Lang, O. *et al.* Thin film growth and band lineup of In_2O_3 on the layered semiconductor InSe. *Journal of Applied Physics* **86**, 5687-5691, doi:10.1063/1.371579 (1999).

426 Sque, S. J., Jones, R. & Briddon, P. R. The transfer doping of graphite and graphene. *physica status solidi (a)* **204**, 3078-3084, doi:10.1002/pssa.200776313 (2007).

427 Katz, O., Garber, V., Meyler, B., Bahir, G. & Salzman, J. Gain mechanism in GaN Schottky ultraviolet detectors. *Applied Physics Letters* **79**, 1417-1419, doi:10.1063/1.1394717 (2001).

428 Fan, Y. *et al.* Photoinduced Schottky Barrier Lowering in 2D Monolayer WS_2 Photodetectors. *Advanced Optical Materials* **4**, 1573-1581, doi:10.1002/adom.201600221 (2016).

429 Akinwande, D. *et al.* Graphene and two-dimensional materials for silicon technology. *Nature* **573**, 507-518, doi:10.1038/s41586-019-1573-9 (2019).

430 Liu, X. & Hersam, M. C. 2D materials for quantum information science. *Nature Reviews Materials* **4**, 669-684, doi:10.1038/s41578-019-0136-x (2019).

431 Hui, F. *et al.* Graphene and Related Materials for Resistive Random Access Memories. *Advanced Electronic Materials* **3**, 1600195, doi:10.1002/aelm.201600195 (2017).

432 Zhang, L., Gong, T., Wang, H., Guo, Z. & Zhang, H. Memristive devices based on emerging two-dimensional materials beyond graphene. *Nanoscale* **11**, 12413-12435, doi:10.1039/C9NR02886B (2019).

433 Bertolazzi, S. *et al.* Nonvolatile Memories Based on Graphene and Related 2D Materials. *Advanced Materials* **31**, 1806663, doi:10.1002/adma.201806663 (2019).

434 Zhou, F., Chen, J., Tao, X., Wang, X. & Chai, Y. 2D Materials Based Optoelectronic Memory: Convergence of Electronic Memory and Optical Sensor. *Research* **2019**, 9490413, doi:10.34133/2019/9490413 (2019).

435 Kang, S. *et al.* 2D semiconducting materials for electronic and optoelectronic applications: potential and challenge. *2D Materials* **7**, 022003, doi:10.1088/2053-1583/ab6267 (2020).

436 Manzeli, S., Ovchinnikov, D., Pasquier, D., Yazyev, O. V. & Kis, A. 2D transition metal dichalcogenides. *Nature Reviews Materials* **2**, 17033, doi:10.1038/natrevmats.2017.33 (2017).

437 Wang, C.-Y. *et al.* 2D Layered Materials for Memristive and Neuromorphic Applications. *Advanced Electronic Materials* **6**, 1901107, doi:10.1002/aelm.201901107 (2020).

438 Zhou, X. *et al.* 2D Layered Material-Based van der Waals Heterostructures for Optoelectronics. *Advanced Functional Materials* **28**, 1706587, doi:10.1002/adfm.201706587 (2018).

439 Frisenda, R., Molina-Mendoza, A. J., Mueller, T., Castellanos-Gomez, A. & van der Zant, H. S. J. Atomically thin p–n junctions based on two-dimensional materials. *Chemical Society Reviews* **47**, 3339-3358, doi:10.1039/C7CS00880E (2018).

440 He, G. *et al.* Thermally Assisted Nonvolatile Memory in Monolayer MoS_2 Transistors. *Nano Letters* **16**, 6445-6451, doi:10.1021/acs.nanolett.6b02905 (2016).

441 Lee, J. *et al.* Monolayer optical memory cells based on artificial trap-mediated charge storage and release. *Nature Communications* **8**, 14734, doi:10.1038/ncomms14734 (2017).

442 Huh, W. *et al.* Synaptic Barristor Based on Phase-Engineered 2D Heterostructures. *Advanced Materials* **30**, 1801447, doi:10.1002/adma.201801447 (2018).

443 Molina-Mendoza, A. J., Paur, M. & Mueller, T. Nonvolatile Programmable

WSe$_2$ Photodetector. *Advanced Optical Materials* **8**, 2000417, doi:10.1002/adom.202000417 (2020).

444 Zhang, E. *et al.* Tunable Charge-Trap Memory Based on Few-Layer MoS$_2$. *ACS Nano* **9**, 612-619, doi:10.1021/nn5059419 (2015).

445 Sup Choi, M. *et al.* Controlled charge trapping by molybdenum disulphide and graphene in ultrathin heterostructured memory devices. *Nature Communications* **4**, 1624, doi:10.1038/ncomms2652 (2013).

446 Bertolazzi, S., Krasnozhon, D. & Kis, A. Nonvolatile Memory Cells Based on MoS$_2$/Graphene Heterostructures. *ACS Nano* **7**, 3246-3252, doi:10.1021/nn3059136 (2013).

447 Kim, S. M. *et al.* Transparent and Flexible Graphene Charge-Trap Memory. *ACS Nano* **6**, 7879-7884, doi:10.1021/nn302193q (2012).

448 Lee, S. *et al.* Impact of gate work-function on memory characteristics in Al_2O_3/HfO_x/Al_2O_3/graphene charge-trap memory devices. *Applied Physics Letters* **100**, 023109, doi:10.1063/1.3675633 (2012).

449 Yu, W. J., Chae, S. H., Lee, S. Y., Duong, D. L. & Lee, Y. H. Ultra-Transparent, Flexible Single-walled Carbon Nanotube Non-volatile Memory Device with an Oxygen-decorated Graphene Electrode. *Advanced Materials* **23**, 1889-1893, doi:10.1002/adma.201004444 (2011).

450 Vu, Q. A. *et al.* Two-terminal floating-gate memory with van der Waals heterostructures for ultrahigh on/off ratio. *Nature Communications* **7**, 12725, doi:10.1038/ncomms12725 (2016).

451 Liu, C. *et al.* A semi-floating gate memory based on van der Waals heterostructures for quasi-non-volatile applications. *Nature Nanotechnology* **13**, 404-410, doi:10.1038/s41565-018-0102-6 (2018).

452 Li, D. *et al.* Nonvolatile Floating-Gate Memories Based on Stacked Black Phosphorus – Boron Nitride – MoS$_2$ Heterostructures. *Advanced Functional Materials* **25**, 7360-7365, doi:10.1002/adfm.201503645 (2015).

453 Sawa, A. Resistive switching in transition metal oxides. *Materials Today* **11**, 28-36, doi:https://doi.org/10.1016/S1369-7021(08)70119-6 (2008).

454 Lei, S. *et al.* Optoelectronic Memory Using Two-Dimensional Materials. *Nano Letters* **15**, 259-265, doi:10.1021/nl503505f (2015).

455 Sangwan, V. K. *et al.* Gate-tunable memristive phenomena mediated by grain boundaries in single-layer MoS$_2$. *Nature Nanotechnology* **10**, 403-406, doi:10.1038/nnano.2015.56 (2015).

456 Sangwan, V. K. *et al.* Multi-terminal memtransistors from polycrystalline monolayer molybdenum disulfide. *Nature* **554**, 500-504, doi:10.1038/nature25747 (2018).

457 Roy, K. *et al.* Graphene–MoS_2 hybrid structures for multifunctional photoresponsive memory devices. *Nature Nanotechnology* **8**, 826-830, doi:10.1038/nnano.2013.206 (2013).

458 Di Bartolomeo, A. *et al.* Electrical transport and persistent photoconductivity in monolayer MoS_2 phototransistors. *Nanotechnology* **28**, 214002, doi:10.1088/1361-6528/aa6d98 (2017).

459 Fang, H. & Hu, W. Photogating in Low Dimensional Photodetectors. *Advanced Science* **4**, 1700323, doi:10.1002/advs.201700323 (2017).

460 Liu, T. *et al.* Nonvolatile and Programmable Photodoping in $MoTe_2$ for Photoresist-Free Complementary Electronic Devices. *Advanced Materials* **30**, 1804470, doi:10.1002/adma.201804470 (2018).

461 Wang, Q. *et al.* Nonvolatile infrared memory in MoS_2/PbS van der Waals heterostructures. *Science Advances* **4**, eaap7916, doi:10.1126/sciadv.aap7916 (2018).

462 Xiang, D. *et al.* Two-dimensional multibit optoelectronic memory with broadband spectrum distinction. *Nature Communications* **9**, 2966, doi:10.1038/s41467-018-05397-w (2018).

463 Chen, Y.-H. *et al.* Oxidized-monolayer tunneling barrier for strong Fermi-level depinning in layered InSe transistors. *npj 2D Materials and Applications* **3**, 49, doi:10.1038/s41699-019-0133-3 (2019).

464 Nicholls, J. R., Dimitrijev, S., Tanner, P. & Han, J. The Role of Near-Interface Traps in Modulating the Barrier Height of SiC Schottky Diodes. *IEEE Transactions on Electron Devices* **66**, 1675-1680, doi:10.1109/TED.2019.2896216 (2019).

465 Zhao, Q., Frisenda, R., Wang, T. & Castellanos-Gomez, A. InSe: a two-dimensional semiconductor with superior flexibility. *Nanoscale* **11**, 9845-9850, doi:10.1039/C9NR02172H (2019).

466 Akinwande, D., Petrone, N. & Hone, J. Two-dimensional flexible nanoelectronics. *Nature Communications* **5**, 5678, doi:10.1038/ncomms6678 (2014).

467 Lee, C., Wei, X., Kysar, J. W. & Hone, J. Measurement of the Elastic Properties and Intrinsic Strength of Monolayer Graphene. *Science* **321**, 385,

doi:10.1126/science.1157996 (2008).

468 Poot, M. & van der Zant, H. S. J. Nanomechanical properties of few-layer graphene membranes. *Applied Physics Letters* **92**, 063111, doi:10.1063/1.2857472 (2008).

469 Gómez-Navarro, C., Burghard, M. & Kern, K. Elastic Properties of Chemically Derived Single Graphene Sheets. *Nano Letters* **8**, 2045-2049, doi:10.1021/nl801384y (2008).

470 Frank, I. W., Tanenbaum, D. M., van der Zande, A. M. & McEuen, P. L. Mechanical properties of suspended graphene sheets. *Journal of Vacuum Science & Technology B: Microelectronics and Nanometer Structures Processing, Measurement, and Phenomena* **25**, 2558-2561, doi:10.1116/1.2789446 (2007).

471 Bunch, J. S. *et al.* Electromechanical Resonators from Graphene Sheets. *Science* **315**, 490, doi:10.1126/science.1136836 (2007).

472 Yang, Y. *et al.* Brittle Fracture of 2D $MoSe_2$. *Advanced Materials* **29**, 1604201, doi:10.1002/adma.201604201 (2017).

473 Graczykowski, B. *et al.* Elastic Properties of Few Nanometers Thick Polycrystalline MoS_2 Membranes: A Nondestructive Study. *Nano Letters* **17**, 7647-7651, doi:10.1021/acs.nanolett.7b03669 (2017).

474 Castellanos-Gomez, A., Singh, V., van der Zant, H. S. J. & Steele, G. A. Mechanics of freely-suspended ultrathin layered materials. *Annalen der Physik* **527**, 27-44, doi:10.1002/andp.201400153 (2015).

475 Li, X., Sun, M., Shan, C., Chen, Q. & Wei, X. Mechanical Properties of 2D Materials Studied by In Situ Microscopy Techniques. *Advanced Materials Interfaces* **5**, 1701246, doi:10.1002/admi.201701246 (2018).

476 Stafford, C. M. *et al.* A buckling-based metrology for measuring the elastic moduli of polymeric thin films. *Nature Materials* **3**, 545-550, doi:10.1038/nmat1175 (2004).

477 Bowden, N., Brittain, S., Evans, A. G., Hutchinson, J. W. & Whitesides, G. M. Spontaneous formation of ordered structures in thin films of metals supported on an elastomeric polymer. *Nature* **393**, 146-149, doi:10.1038/30193 (1998).

478 Reyes-Martinez, M. A., Ramasubramaniam, A., Briseno, A. L. & Crosby, A. J. The Intrinsic Mechanical Properties of Rubrene Single Crystals. *Advanced Materials* **24**, 5548-5552, doi:10.1002/adma.201201749 (2012).

479 Feicht, P. *et al.* Systematic evaluation of different types of graphene oxide in

respect to variations in their in-plane modulus. *Carbon* **114**, 700-705, doi:https://doi.org/10.1016/j.carbon.2016.12.065 (2017).

480 Kunz, D. A. *et al.* In-Plane Modulus of Singular 2:1 Clay Lamellae Applying a Simple Wrinkling Technique. *ACS Applied Materials & Interfaces* **5**, 5851-5855, doi:10.1021/am4015204 (2013).

481 Kunz, D. A. *et al.* Space-Resolved In-Plane Moduli of Graphene Oxide and Chemically Derived Graphene Applying a Simple Wrinkling Procedure. *Advanced Materials* **25**, 1337-1341, doi:10.1002/adma.201204049 (2013).

482 Brennan, C. J., Nguyen, J., Yu, E. T. & Lu, N. Interface Adhesion between 2D Materials and Elastomers Measured by Buckle Delaminations. *Advanced Materials Interfaces* **2**, 1500176, doi:10.1002/admi.201500176 (2015).

483 Iguiñiz, N., Frisenda, R., Bratschitsch, R. & Castellanos-Gomez, A. Revisiting the Buckling Metrology Method to Determine the Young's Modulus of 2D Materials. *Advanced Materials* **31**, 1807150, doi:10.1002/adma.201807150 (2019).

484 Khang, D.-Y., Rogers, J. A. & Lee, H. H. Mechanical Buckling: Mechanics, Metrology, and Stretchable Electronics. *Advanced Functional Materials* **19**, 1526-1536, doi:10.1002/adfm.200801065 (2009).

485 Volynskii, A. L., Bazhenov, S., Lebedeva, O. V. & Bakeev, N. F. Mechanical buckling instability of thin coatings deposited on soft polymer substrates. *Journal of Materials Science* **35**, 547-554, doi:10.1023/A:1004707906821 (2000).

486 Hu, T., Zhou, J. & Dong, J. Strain induced new phase and indirect–direct band gap transition of monolayer InSe. *Physical Chemistry Chemical Physics* **19**, 21722-21728, doi:10.1039/C7CP03558F (2017).

487 Pritchard, R. H., Lava, P., Debruyne, D. & Terentjev, E. M. Precise determination of the Poisson ratio in soft materials with 2D digital image correlation. *Soft Matter* **9**, 6037-6045, doi:10.1039/C3SM50901J (2013).

488 Hermosa, C. *et al.* Mechanical and optical properties of ultralarge flakes of a metal–organic framework with molecular thickness. *Chemical Science* **6**, 2553-2558, doi:10.1039/C4SC03115F (2015).

489 Traversi, F. *et al.* Elastic properties of graphene suspended on a polymer substrate by e-beam exposure. *New Journal of Physics* **12**, 023034, doi:10.1088/1367-2630/12/2/023034 (2010).

490 Lee, G.-H. *et al.* High-Strength Chemical-Vapor–Deposited Graphene and

Grain Boundaries. *Science* **340**, 1073, doi:10.1126/science.1235126 (2013).

491 Ruiz-Vargas, C. S. *et al.* Softened Elastic Response and Unzipping in Chemical Vapor Deposition Graphene Membranes. *Nano Letters* **11**, 2259-2263, doi:10.1021/nl200429f (2011).

492 Lee, J., Wang, Z., He, K., Shan, J. & Feng, P. X. L. High Frequency MoS_2 Nanomechanical Resonators. *ACS Nano* **7**, 6086-6091, doi:10.1021/nn4018872 (2013).

493 Liu, K. *et al.* Elastic Properties of Chemical-Vapor-Deposited Monolayer MoS_2, WS_2, and Their Bilayer Heterostructures. *Nano Letters* **14**, 5097-5103, doi:10.1021/nl501793a (2014).

494 Lloyd, D. *et al.* Adhesion, Stiffness, and Instability in Atomically Thin MoS_2 Bubbles. *Nano Letters* **17**, 5329-5334, doi:10.1021/acs.nanolett.7b01735 (2017).

495 Zhang, R., Koutsos, V. & Cheung, R. Elastic properties of suspended multilayer WSe_2. *Applied Physics Letters* **108**, 042104, doi:10.1063/1.4940982 (2016).

496 Tao, J. *et al.* Mechanical and Electrical Anisotropy of Few-Layer Black Phosphorus. *ACS Nano* **9**, 11362-11370, doi:10.1021/acsnano.5b05151 (2015).

497 Chitara, B. & Ya'akobovitz, A. Elastic properties and breaking strengths of GaS, GaSe and GaTe nanosheets. *Nanoscale* **10**, 13022-13027, doi:10.1039/C8NR01065J (2018).

498 Kim, S. M. *et al.* Synthesis of large-area multilayer hexagonal boron nitride for high material performance. *Nature Communications* **6**, 8662, doi:10.1038/ncomms9662 (2015).

499 Suk, J. W., Piner, R. D., An, J. & Ruoff, R. S. Mechanical Properties of Monolayer Graphene Oxide. *ACS Nano* **4**, 6557-6564, doi:10.1021/nn101781v (2010).

500 Castellanos-Gomez, A. *et al.* Mechanical properties of freely suspended atomically thin dielectric layers of mica. *Nano Research* **5**, 550-557, doi:10.1007/s12274-012-0240-3 (2012).

501 Kunz, D. A. *et al.* Deformation Measurements on Thin Clay Tactoids. *Small* **5**, 1816-1820, doi:10.1002/smll.200801710 (2009).

502 Suk, J. W., Piner, R. D., An, J. & Ruoff, R. S. Evaluation of elastic modulus of ultra-thin vermiculite membranes by contact mode atomic force microscopy imaging. *Thin Solid Films* **527**, 205-209,

doi:https://doi.org/10.1016/j.tsf.2012.12.024 (2013).

503 Guo, L. *et al.* Elastic properties of van der Waals epitaxy grown bismuth telluride 2D nanosheets. *Nanoscale* **7**, 11915-11921, doi:10.1039/C5NR03282B (2015).

504 Yan, H. *et al.* Elastic behavior of Bi_2Se_3 2D nanosheets grown by van der Waals epitaxy. *Applied Physics Letters* **109**, 032103, doi:10.1063/1.4958986 (2016).

505 Zhao, Q., Wang, T., Frisenda, R. & Castellanos-Gomez, A. Giant Piezoresistive Effect and Strong Bandgap Tunability in Ultrathin InSe upon Biaxial Strain. *Advanced Science* **n/a**, 2001645, doi:10.1002/advs.202001645 (2020).

506 Dai, Z., Liu, L. & Zhang, Z. Strain Engineering of 2D Materials: Issues and Opportunities at the Interface. *Advanced Materials* **31**, 1805417, doi:10.1002/adma.201805417 (2019).

507 Deng, S., Sumant, A. V. & Berry, V. Strain engineering in two-dimensional nanomaterials beyond graphene. *Nano Today* **22**, 14-35, doi:https://doi.org/10.1016/j.nantod.2018.07.001 (2018).

508 Roldán, R., Castellanos-Gomez, A., Cappelluti, E. & Guinea, F. Strain engineering in semiconducting two-dimensional crystals. *Journal of Physics: Condensed Matter* **27**, 313201, doi:10.1088/0953-8984/27/31/313201 (2015).

509 Sun, Y. & Liu, K. Strain engineering in functional 2-dimensional materials. *Journal of Applied Physics* **125**, 082402, doi:10.1063/1.5053795 (2018).

510 Naumis, G. G., Barraza-Lopez, S., Oliva-Leyva, M. & Terrones, H. Electronic and optical properties of strained graphene and other strained 2D materials: a review. *Reports on Progress in Physics* **80**, 096501, doi:10.1088/1361-6633/aa74ef (2017).

511 Griffith, A. in *Ser A.* 163-198.

512 Cooper, R. C. *et al.* Nonlinear elastic behavior of two-dimensional molybdenum disulfide. *Physical Review B* **87**, 035423, doi:10.1103/PhysRevB.87.035423 (2013).

513 Gant, P. *et al.* A strain tunable single-layer MoS_2 photodetector. *Materials Today* **27**, 8-13, doi:https://doi.org/10.1016/j.mattod.2019.04.019 (2019).

514 Xie, C. & Yan, F. Flexible Photodetectors Based on Novel Functional Materials. *Small* **13**, 1701822, doi:10.1002/smll.201701822 (2017).

515 Kim, S. J., Choi, K., Lee, B., Kim, Y. & Hong, B. H. Materials for Flexible,

Stretchable Electronics: Graphene and 2D Materials. *Annual Review of Materials Research* **45**, 63-84, doi:10.1146/annurev-matsci-070214-020901 (2015).

516 Wu, W. *et al.* Piezophototronic Effect in Single-Atomic-Layer MoS_2 for Strain-Gated Flexible Optoelectronics. *Advanced Materials* **28**, 8463-8468, doi:10.1002/adma.201602854 (2016).

517 Zhang, Z. *et al.* Strain-Modulated Bandgap and Piezo-Resistive Effect in Black Phosphorus Field-Effect Transistors. *Nano Letters* **17**, 6097-6103, doi:10.1021/acs.nanolett.7b02624 (2017).

518 An, C. *et al.* The Opposite Anisotropic Piezoresistive Effect of ReS_2. *ACS Nano* **13**, 3310-3319, doi:10.1021/acsnano.8b09161 (2019).

519 Manzeli, S., Allain, A., Ghadimi, A. & Kis, A. Piezoresistivity and Strain-induced Band Gap Tuning in Atomically Thin MoS_2. *Nano Letters* **15**, 5330-5335, doi:10.1021/acs.nanolett.5b01689 (2015).

520 Conley, H. J. *et al.* Bandgap Engineering of Strained Monolayer and Bilayer MoS_2. *Nano Letters* **13**, 3626-3630, doi:10.1021/nl4014748 (2013).

521 He, K., Poole, C., Mak, K. F. & Shan, J. Experimental Demonstration of Continuous Electronic Structure Tuning via Strain in Atomically Thin MoS_2. *Nano Letters* **13**, 2931-2936, doi:10.1021/nl4013166 (2013).

522 Zhu, C. R. *et al.* Strain tuning of optical emission energy and polarization in monolayer and bilayer MoS_2. *Physical Review B* **88**, 121301, doi:10.1103/PhysRevB.88.121301 (2013).

523 Niehues, I. *et al.* Strain Control of Exciton–Phonon Coupling in Atomically Thin Semiconductors. *Nano Letters* **18**, 1751-1757, doi:10.1021/acs.nanolett.7b04868 (2018).

524 Niehues, I. *et al.* Strain transfer across grain boundaries in MoS_2 monolayers grown by chemical vapor deposition. *2D Materials* **5**, 031003, doi:10.1088/2053-1583/aaba9a (2018).

525 Christopher, J. W. *et al.* Monolayer MoS_2 Strained to 1.3% With a Microelectromechanical System. *Journal of Microelectromechanical Systems* **28**, 254-263, doi:10.1109/JMEMS.2018.2877983 (2019).

526 Li, Z. *et al.* Efficient strain modulation of 2D materials via polymer encapsulation. *Nature Communications* **11**, 1151, doi:10.1038/s41467-020-15023-3 (2020).

527 He, X. *et al.* Strain engineering in monolayer WS_2, MoS_2, and the WS_2/MoS_2

heterostructure. *Applied Physics Letters* **109**, 173105, doi:10.1063/1.4966218 (2016).

528 Liu, Z. *et al.* Strain and structure heterogeneity in MoS_2 atomic layers grown by chemical vapour deposition. *Nature Communications* **5**, 5246, doi:10.1038/ncomms6246 (2014).

529 John, A. P., Thenapparambil, A. & Thalakulam, M. Strain-engineering the Schottky barrier and electrical transport on MoS_2. *Nanotechnology* **31**, 275703, doi:10.1088/1361-6528/ab83b7 (2020).

530 Lloyd, D. *et al.* Band Gap Engineering with Ultralarge Biaxial Strains in Suspended Monolayer MoS_2. *Nano Letters* **16**, 5836-5841, doi:10.1021/acs.nanolett.6b02615 (2016).

531 Frisenda, R. *et al.* Biaxial strain tuning of the optical properties of single-layer transition metal dichalcogenides. *npj 2D Materials and Applications* **1**, 10, doi:10.1038/s41699-017-0013-7 (2017).

532 Hui, Y. Y. *et al.* Exceptional Tunability of Band Energy in a Compressively Strained Trilayer MoS_2 Sheet. *ACS Nano* **7**, 7126-7131, doi:10.1021/nn4024834 (2013).

533 Li, H. *et al.* Optoelectronic crystal of artificial atoms in strain-textured molybdenum disulphide. *Nature Communications* **6**, 7381, doi:10.1038/ncomms8381 (2015).

534 Castellanos-Gomez, A. *et al.* Local Strain Engineering in Atomically Thin MoS_2. *Nano Letters* **13**, 5361-5366, doi:10.1021/nl402875m (2013).

535 Island, J. O. *et al.* Precise and reversible band gap tuning in single-layer $MoSe_2$ by uniaxial strain. *Nanoscale* **8**, 2589-2593, doi:10.1039/C5NR08219F (2016).

536 Mennel, L., Paur, M. & Mueller, T. Second harmonic generation in strained transition metal dichalcogenide monolayers: MoS_2, $MoSe_2$, WS_2, and WSe_2. *APL Photonics* **4**, 034404, doi:10.1063/1.5051965 (2018).

537 Wang, Y. *et al.* Strain-induced direct–indirect bandgap transition and phonon modulation in monolayer WS_2. *Nano Research* **8**, 2562-2572, doi:10.1007/s12274-015-0762-6 (2015).

538 Zhang, Q. *et al.* Strain Relaxation of Monolayer WS_2 on Plastic Substrate. *Advanced Functional Materials* **26**, 8707-8714, doi:10.1002/adfm.201603064 (2016).

539 Schmidt, R. *et al.* Reversible uniaxial strain tuning in atomically thin WSe_2.

2D Materials **3**, 021011, doi:10.1088/2053-1583/3/2/021011 (2016).

540 Aslan, O. B., Deng, M. & Heinz, T. F. Strain tuning of excitons in monolayer WSe_2. *Physical Review B* **98**, 115308, doi:10.1103/PhysRevB.98.115308 (2018).

541 Desai, S. B. *et al.* Strain-Induced Indirect to Direct Bandgap Transition in Multilayer WSe_2. *Nano Letters* **14**, 4592-4597, doi:10.1021/nl501638a (2014).

542 Tang, N., Du, C., Wang, Q. & Xu, H. Strain engineering in bilayer WSe_2 over a large strain range. *Microelectronic Engineering* **223**, 111202, doi:https://doi.org/10.1016/j.mee.2019.111202 (2020).

543 Aslan, O. B., Deng, M., Brongersma, M. L. & Heinz, T. F. Strained bilayer WSe_2 with reduced exciton-phonon coupling. *Physical Review B* **101**, 115305, doi:10.1103/PhysRevB.101.115305 (2020).

544 Yang, S. *et al.* Tuning the Optical, Magnetic, and Electrical Properties of $ReSe_2$ by Nanoscale Strain Engineering. *Nano Letters* **15**, 1660-1666, doi:10.1021/nl504276u (2015).

545 Zhang, G. *et al.* Infrared fingerprints of few-layer black phosphorus. *Nature Communications* **8**, 14071, doi:10.1038/ncomms14071 (2017).

546 Quereda, J. *et al.* Strong Modulation of Optical Properties in Black Phosphorus through Strain-Engineered Rippling. *Nano Letters* **16**, 2931-2937, doi:10.1021/acs.nanolett.5b04670 (2016).

547 Li, Y. *et al.* Ultrasensitive tunability of the direct bandgap of 2D InSe flakes via strain engineering. *2D Materials* **5**, 021002, doi:10.1088/2053-1583/aaa6eb (2018).

548 Niehues, I., Blob, A., Stiehm, T., Michaelis de Vasconcellos, S. & Bratschitsch, R. Interlayer excitons in bilayer MoS_2 under uniaxial tensile strain. *Nanoscale* **11**, 12788-12792, doi:10.1039/C9NR03332G (2019).

549 Huang, S. *et al.* Strain-tunable van der Waals interactions in few-layer black phosphorus. *Nature Communications* **10**, 2447, doi:10.1038/s41467-019-10483-8 (2019).

550 Song, C. *et al.* Drastic enhancement of the Raman intensity in few-layer InSe by uniaxial strain. *Physical Review B* **99**, 195414, doi:10.1103/PhysRevB.99.195414 (2019).

551 Brotons-Gisbert, M. *et al.* Nanotexturing To Enhance Photoluminescent Response of Atomically Thin Indium Selenide with Highly Tunable Band Gap. *Nano Letters* **16**, 3221-3229, doi:10.1021/acs.nanolett.6b00689 (2016).

552 Li, Y. *et al.* Enhanced Light Emission from the Ridge of Two-Dimensional InSe Flakes. *Nano Letters* **18**, 5078-5084, doi:10.1021/acs.nanolett.8b01940 (2018).

553 Luo, K. *et al.* Ab-Initio Simulations of Monolayer InSe and MoS_2 Strain Effect: From Electron Mobility to Photoelectric Effect. *Journal of Electronic Materials* **49**, 559-565, doi:10.1007/s11664-019-07809-z (2020).

554 Shi, L.-B. *et al.* Theoretical prediction of intrinsic electron mobility of monolayer InSe: first-principles calculation. *Journal of Physics: Condensed Matter* **32**, 065306, doi:10.1088/1361-648x/ab534f (2019).

555 Okada, Y. & Tokumaru, Y. Precise determination of lattice parameter and thermal expansion coefficient of silicon between 300 and 1500 K. *Journal of Applied Physics* **56**, 314-320, doi:10.1063/1.333965 (1984).

556 Molas, M. R. *et al.* Raman spectroscopy of GaSe and InSe post-transition metal chalcogenides layers. *Faraday Discussions*, doi:10.1039/D0FD00007H (2020).

557 Huang, M. *et al.* Phonon softening and crystallographic orientation of strained graphene studied by Raman spectroscopy. *Proceedings of the National Academy of Sciences* **106**, 7304, doi:10.1073/pnas.0811754106 (2009).

558 Androulidakis, C. *et al.* Graphene flakes under controlled biaxial deformation. *Scientific Reports* **5**, 18219, doi:10.1038/srep18219 (2015).

559 Tsai, M.-Y. *et al.* Flexible MoS_2 Field-Effect Transistors for Gate-Tunable Piezoresistive Strain Sensors. *ACS Applied Materials & Interfaces* **7**, 12850-12855, doi:10.1021/acsami.5b02336 (2015).

560 Casiraghi, C. *et al.* Inkjet printed 2D-crystal based strain gauges on paper. *Carbon* **129**, 462-467, doi:https://doi.org/10.1016/j.carbon.2017.12.030 (2018).

561 Kanda, Y. Piezoresistance effect of silicon. *Sensors and Actuators A: Physical* **28**, 83-91, doi:https://doi.org/10.1016/0924-4247(91)85017-I (1991).

562 Petersen, K. E. Silicon as a mechanical material. *Proceedings of the IEEE* **70**, 420-457, doi:10.1109/PROC.1982.12331 (1982).

563 Feng, Y., Lin, S., Huang, S., Shrestha, S. & Conibeer, G. Can Tauc plot extrapolation be used for direct-band-gap semiconductor nanocrystals? *Journal of Applied Physics* **117**, 125701, doi:10.1063/1.4916090 (2015).

564 Tauc, J. Optical properties and electronic structure of amorphous Ge and Si. *Materials Research Bulletin* **3**, 37-46,

doi:https://doi.org/10.1016/0025-5408(68)90023-8 (1968).

PUBLICATION LIST

2020

[18] **Zhao Q.**, Wang T., Castellanos-Gomez A., et al. *Optoelectronic memories based on InSe Schottky diodes*, **2020**, Submitted.

[17] **Zhao Q.**, Puebla S., Zhang W., et al. *Thickness identification of thin InSe by optical microscopy methods* [J]. Advanced Photonics Research, **2020**, Accepted.

[16] **Zhao Q.**, Wang T., Frisenda R., et al. *Giant Piezoresistive Effect and Strong Bandgap Tunability in Ultrathin InSe upon Biaxial Strain* [J]. Advanced Science, **2020**: 2001645.

[15] **Zhao Q.**, Jie W., Wang T., et al. *InSe Schottky Diodes Based on Van Der Waals Contacts* [J]. Advanced Functional Materials, **2020**: 2001307.

[14] **Zhao Q.**, Carrascoso F., Gant P., et al. *A system to test 2D optoelectronic devices in high vacuum* [J]. Journal of Physics: Materials, **2020**, 3(3): 036001.

[13] Gant P., Carrascoso F., **Zhao Q.**, et al. *A system for the deterministic transfer of 2D materials under inert environmental conditions* [J]. 2D Materials, **2020**, 7(2): 025034.

[12] **Zhao Q.**, Wang T., Ryu Y., et al. *An inexpensive system for the deterministic transfer of 2D materials* [J]. Journal of Physics: Materials, **2020**, 3(1): 016001.

[11] **Zhao Q.**, Wang W., Carrascoso F., et al. *The role of traps in the photocurrent generation mechanism in thin InSe photodetectors* [J]. Materials Horizons, *2020*, 7(1): 252-262. (**ESI Highly Cited Paper**)

2019

[10] Wang T., Ai X., Yin Z., **Zhao Q.**, et al. *Study on a co-doped CdZnTe crystal containing Yb and In* [J]. CrystEngComm, **2019**, 21(16): 2620-2625.

[9] **Zhao Q.**, Frisenda R., Wang T., et al. *InSe: a two-dimensional semiconductor with superior flexibility* [J]. Nanoscale, **2019**, 11(20): 9845-9850.

[8] Mercado E., Zhou Y., Xie Y., **Zhao Q.**, et al. *Passivation of Layered Gallium Telluride by Double Encapsulation with Graphene* [J]. ACS omega, **2019**, 4(19): 18002-18010.

2018

[7] **Zhao Q.**, Frisenda R., Gant P., et al. *Toward Air Stability of Thin GaSe Devices: Avoiding Environmental and Laser-Induced Degradation by Encapsulation* [J]. Advanced Functional Materials, **2018**, 28(47): 1805304.

[6] Gan X., Zhao C., Hu S., Wang T., Song Y., Li J., **Zhao Q**, et al. *Microwatts continuous-wave pumped second harmonic generation in few-and mono-layer GaSe* [J]. Light: Science & Applications, **2018**, 7(1): 17126.

[5] Wang T., Li J., **Zhao Q.**, et al. *High-quality GaSe single crystal grown by the Bridgman method* [J]. Materials, **2018**, 11(2): 186.

[4] Wang T., **Zhao Q.**, Miao Y., et al. *Lattice vibration of layered GaTe single crystals* [J]. Crystals, **2018**, 8(2): 74.

[3] Fang L., Yuan Q., Fang H., Gan X., Li J., Wang T., **Zhao Q.**, et al. *Multiple Optical Frequency Conversions in Few-Layer GaSe Assisted by a Photonic Crystal Cavity* [J]. Advanced Optical Materials, **2018**, 6(22): 1800698.

2016-previous to this thesis

[2] **Zhao Q.**, Wang T., Miao Y., et al. *Thickness-induced structural phase transformation of layered gallium telluride* [J]. Physical Chemistry Chemical Physics, **2016**, 18(28): 18719-18726. (**Back cover**)

[1] Xi S., Jie W., Zha G., Yuan Y., Wang T., Zhang W., Zhu J., Xu L., Xu Y., Su J., Zhang H., Gu Y., Li J., Ren J., **Zhao Q.**. *Effects of Ga–Te interface layer on the potential barrier height of CdTe/GaAs heterointerface* [J]. Physical Chemistry Chemical Physics, **2016**, 18(4): 2639-2645.